Non-Crystalline Nitrogenated Carbon Electrode Materials: Bulk and Surface Doping Methods for Controlling Electrochemical Properties

A thesis presented to the University of Dublin, Trinity College for the degree of

Doctor of Philosophy in Chemistry

by

Md. Khairul Hoque

Under the supervision of Prof. Paula E. Colavita

School of Chemistry & CRANN

Trinity College Dublin

2020

Declaration

I declare that the work in this thesis it has not been submitted as an exercise for a degree at this or any other University and it is entirely my own work. Due acknowledgement and references are given to others were included in the text.

I agree that the TCD Library may lend or copy the thesis upon request, subject to the Irish Copyright Legislation.

Md. Khairul Hoque

December 2019

Acknowledgements

First and foremost, I would like to acknowledge my PhD supervisor Prof. Paula E. Colavita for her guidance, expert knowledge, research suggestion and valuable support all through my PhD candidature. Prof. Paula E. Colavita always there to offer suggestions which help me to improve my knowledges in the field of my PhD research. Without her help it would not have been possible to successfully done this project. I also would like to special thanks to Prof Tatiana S. Perova for her support and help during Raman Spectroscopy measurement. She has been supporting me for Raman measurement for four years.

I would also like to thank to the people, who have collaborated in this thesis work. I wish to thank my group members past and present Post Doc's, fellow PhD students: James, Adam, Joana, Federico, Guido, Leticia, Serban, Suoyuan, Carlota, Alessandro, Silvia, Swapnil and others. I also like thanks group member from Bob Baker groups specially Stefano, Saptarshi, Harrison, Farzana, Sam for their support. I would like to thank James creel for install plasma chamber.

I would like to thank all of the technical staff at the School of Chemistry for their assistance, particularly Patsy Greene for helping me when I started as JS lab demonstration, Fred Cowzer for training for shift gas cylinders. I also would like to thank administrative staffs at the School of Chemistry for their assistance. I am also grateful to Dr Cormac McGuinness for training me in XPS. I also would like to thank Dr. Niamh Mc Goldrick for her assistance in GNIB, Visa process.

Finally, my special gratitude goes to my parents and my brother, sisters, my wife who, despite the distance, never stopped supporting me during all these years. I would like to thank all my friends for their supports.

Summary

Carbon is ubiquitous as an electrode material and its electronic and capacitive properties and its surface chemistry are suitable for electrode materials for several applications such as fuel cells, capacitive storage devices and batteries. Carbon may be found as variety of allotropes and it can exhibit different properties and it represents a very attractive material for electrochemical applications especially as a material for energy storage and conversion. These carbon materials can be modified by doping or by employing physical/chemical treatment to achieve desirable electrochemical properties. The role of nitrogenation in carbons has gained huge attention in the materials science due to the electrocatalytic activity showed by nitrogen modified carbons in electrochemical reactions such as, oxygen reduction reaction (ORR) and the hydrogen evolution reaction (HER) for energy applications. The purpose of this thesis is to study the effects of nitrogen doping on the electronic, chemical and structural properties of amorphous carbon electrodes and to understand the role of nitrogenation in determining the electrochemical response of these materials.

Chapter I describes major allotropes of carbon materials with their method of preparation and applications. Nitrogen incorporated carbon materials are also discussed with their selected application in energy conversion technologies. Overview of amorphous carbon and nitrogen doped amorphous carbon is also described. The capacitive process in semiconducting electrodes are also discussed along with some theoretical model to understand the structure of double layer which applied to electrode/electrolyte interphase. Double layer properties of semiconducting electrodes and contributions to the double layer capacitance of carbon electrodes is discussed. Finally, overview of the oxygen reduction reaction along with carbon-based materials in the ORR catalytic application is presented.

The methods used to prepare amorphous carbon and nitrogen doped amorphous carbon films is briefly described in chapter II. In this chapter the DC magnetron sputtering technique is used to synthesize these films. The various characterization techniques used in this work to characterize these electrode materials are also describes including x-ray photoelectron spectroscopy, ultraviolet photoelectron spectroscopy, Raman spectroscopy, voltammetry, electrochemical impedance spectroscopy.

The results obtained from characterization of amorphous carbon and nitrogenated amorphous carbon films is described in Chapter III, where electronic and structural properties of these electrodes are directly correlated to the capacitive properties. Initial nitrogen incorporation significantly increases the capacitance of amorphous carbon electrode, resulting in an increase in metallic character. However, greater level of nitrogenation increases the disorder and it creates defects and localised N-sites.

Chapter IV discusses nitrogen doped and nitrogen free graphitized amorphous carbon which are prepared though thermal annealing of sputtered amorphous carbon films. A combination of spectroscopic and electrochemical techniques is used to investigate the effect of selective N-site incorporation in the organization of the carbon scaffolds. Electrochemical capacitive properties of these nitrogenated electrodes is correlated with the organization of the carbon scaffolds due to selective N-site incorporation.

Chapter V introduces a method, RF plasma system in order to incorporate nitrogen into graphitised amorphous carbon. The effect of surface nitrogenation through RF plasma system on the electronic properties of the graphitised amorphous carbon is investigated. It is shown that total N/C content and the distribution of N-sites are not varying with plasma exposer time thus suggesting that the chemical composition of the carbon surface reaches steady state within *ca.* 5 min of exposure. Effect of nitrogenation results in a significant restructuring of the carbon scaffold and it increases defects and amorphization. Electrochemical characterization results show that nitrogenation increases the capacitive storage significantly. The ORR performance of these materials also investigated. It is found that nitrogenation improves the onset potential and reduce H_2O_2 yields.

Finally, Chapter VI summarises the main conclusions of the thesis and describes possible future work.

Table of Contents

Chapter I

Introduction

Chapter II

Experimental Methods

Chapter III

Capacitive Storage at Nitrogenated Amorphous Carbon

Chapter IV

Electrochemical Capacitance Study on Graphitised N-Doped Carbon Electrodes

Chapter V

RF plasma N-Doped Amorphous Carbon

Chapter VI

Conclusions and Future work

List of Figures

Chapter I

Chapter II

Chapter III

Chapter IV

Chapter V

Chapter VI

List of Tables

Chapter I

Chapter III

Chapter IV

Chapter V

List of Abbreviations

a-C – Amorphous Carbon

a-C a900 – Amorphous Carbon annealed at 900 ^oC

anC- Amorphous Carbon annealed at 900 ^oC

a-C:N – Nitrogenated Amorphous Carbon

a-C:N a900-pl- annealed amorphous carbon treated with plasma

AES- Auger Electron spectroscopy

ASV- Anodic Stripping Voltammetry

C – Capacitance

CB - Carbon Blacks

CPE – Constant Phase Element

CV – Cyclic Voltammetry

CDs– Carbon Dots

CNT- Carbon Nanotubes

CVD- Chemical Vapor Deposition

CSV- Cathodic Stripping Voltammetry

C_{DL} -Double Layer Capacitance

C_{PZC}- Capacitance at Point of Zero Charge

D – Diffusion Coefficient

DLC – Diamond-like Carbon

E – Electrode Potential

$E^{0'}$ – Formal Potential

EIS – Electrochemical Impedance Spectroscopy

EDLC- Electrical Double Layer Capacitors

EC- Electrochemical Capacitors

FWHM- Full Width Half Maximum

F – Faraday's Constant

FC- fuel Cells

GFS - Gas Flow Sputtering

GC – Glassy Carbon

GQD- Graphene Quantum Dots

GO- Graphite Oxide

HOPG – Highly-Oriented Pyrolytic Graphite

HEV- Hybrid Electric Vehicles

HOR- Hydrogen Oxidation Reaction

i – Current

IBD - Ion Beam Sputtering

IAD - Ion Beam Assisted Deposition

j – Current Density

j_L – Limiting Current Density

LIB- Lithium Ion Battery

MWCNTs- Multi Walled Carbon Nanotubes

MOFs- Metal Organic Frameworks

NPMC- Non-Precious Metal Based Catalysts

ORR- Oxygen Reduction Reaction

OCP- Open Circuit Potential

PLD- Pulsed Laser Deposition

PTC- Positive Temperature Coefficient

R_{CT} - Charge Transfer Resistance

ORR – Oxygen Reduction Reaction

RHE – Reversible Hydrogen Electrode

RDS – Rate Determining Step

RMS – Root Mean Square

RDE- Rotating Disk Electrode

RRDE –Ring Disk Electrode

SWCNTs - Single Walled Carbon Nanotubes

SE – Spectroscopic Ellipsometry

SEM – Scanning Electron Microscopy

SHE – Standard Hydrogen Electrode

UPS- Ultraviolet Photoelectron Spectroscopy

V – Voltage

XPS – X-Ray Photoelectron Spectroscopy

α – Transfer Coefficient

ν – Scan Rate

ω – Angular Frequency

ϕ – Phase Angle

ϕ- Work function

Chapter 1

Introduction

In the chapter major allotropes of carbon materials are discussed with their electrochemical application. The properties of amorphous carbon and nitrogen doped amorphous carbon described along with their preparation and application in energy storage and electrocatalytic performances. Capacitive properties of semiconducting electrodes also discussed along with some theoretical models. Finally, the oxygen reduction reaction is explained and overview of carbon-based ORR catalysts is described.

1 Introduction

Carbon is one of the most abundant elements on Earth. For thousands of years, carbon has been an important source of energy and humankind has struggled to extract and utilize power from carbon materials [1]. Carbon is widely used in a large range of electrochemical applications due to its diverse morphologies and plays a significant role in the development of alternative clean and sustainable energy technologies [2-3]. Due to different allotropes (Diamond, Graphite, Lonsdaelite, fullerenes, amorphous carbon, and carbon nanotubes,) carbon can exhibit different properties and represents a very attractive material for electrochemical applications especially as a material for energy storage and conversion. [4].

Carbon displays electronic properties ranging from semi-metallic in graphite or glassy carbon to semi-conductive, e.g. in diamond. Carbon surfaces can adsorb a wide range of molecules via either chemisorption or physisorption and can also display a variety of functional surface groups. Carbon-based electrodes are capable of forming covalent bonds with a wide range of surface modifiers which make them attractive substrates for the fabrication of functional electrodes. Furthermore, selected electrochemical reactions are sluggish on carbon electrodes when compared to metals and this relative inertness in redox interfacial processes can be important for many applications in electrochemistry [5].

The aim of this thesis is to investigate the effects of nitrogen doping on the electronic, chemical and structural properties of non-crystalline carbon electrodes and to, in turn, understand how these physico-chemical changes affect their electrochemical response. The role of nitrogenation in carbons has gained prominence in the materials science literature due to the electrocatalytic activity displayed by these heteroatom-modified carbons in electrochemical reactions of importance for energy applications, such as the oxygen reduction reaction (ORR) and the hydrogen evolution reaction (HER). Despite the excellent results obtained through synthetic efforts there remain significant questions on what electronic, chemical and structural changes are responsible for enhanced activity of carbons and nanocarbons in these reactions. In this thesis the synthesis of nitrogen incorporated amorphous carbon thin films and their characterization in terms of chemistry, structure and charge storage properties is reported. These films were used as model systems to understand the role of nitrogenation in determining the electrochemical response of these materials. A combination of X-Ray Photoelectron Spectroscopy (XPS), Raman Spectroscopy and Electrochemical Impedance Spectroscopy (EIS) was used throughout the studies to connect chemical and structural probes to electrochemical performance with particular focus on fundamental capacitive response and electrocatalytic activity in the ORR. The following section will review the role of different carbon allotropes in electrochemical applications and how their capacitive properties are key for many of these applications.

1.1 Allotropes of Carbon as electrodes

Carbon and nanocarbon electrodes often display electronic properties in common with those of metals although their structures and chemistry are different from all metallic electrodes. Graphitic carbons dominate the electrochemical applications of carbon followed by doped diamond electrodes. Graphite consists of ideally infinite graphene layers; carbon atoms in graphite are trigonally bonded via σ- and π-bonds to three carbon atoms (often referred to as sp^2-hybridized), with an intraplanar C-C bond length of 1.42 Å and interplanar spacing of 3.354 Å. A vast family of electrode materials are based on sp^2-rich forms of carbon which includes many nanocarbon forms based on a variety of arrangements of graphene sheets, including for instance carbon nanotubes, nanohorns, nano-onions, nanoribbons, nanofibers, few-layer graphene and vertically aligned graphene, all of which find applications in electrochemistry. Diamond possesses tetrahedrally σ-bonded carbon (sp^3-hybridized) with a C-C bond length of 1.54 Å. Diamond is a wide-bandgap semiconductor but doping with e.g. boron enhances its conductivity and results in interesting properties that define its success in a variety of electrochemical applications. Figure 1.1 shows selected examples of the structure of the above materials, while their properties are discussed in greater detail in the following sections [6].

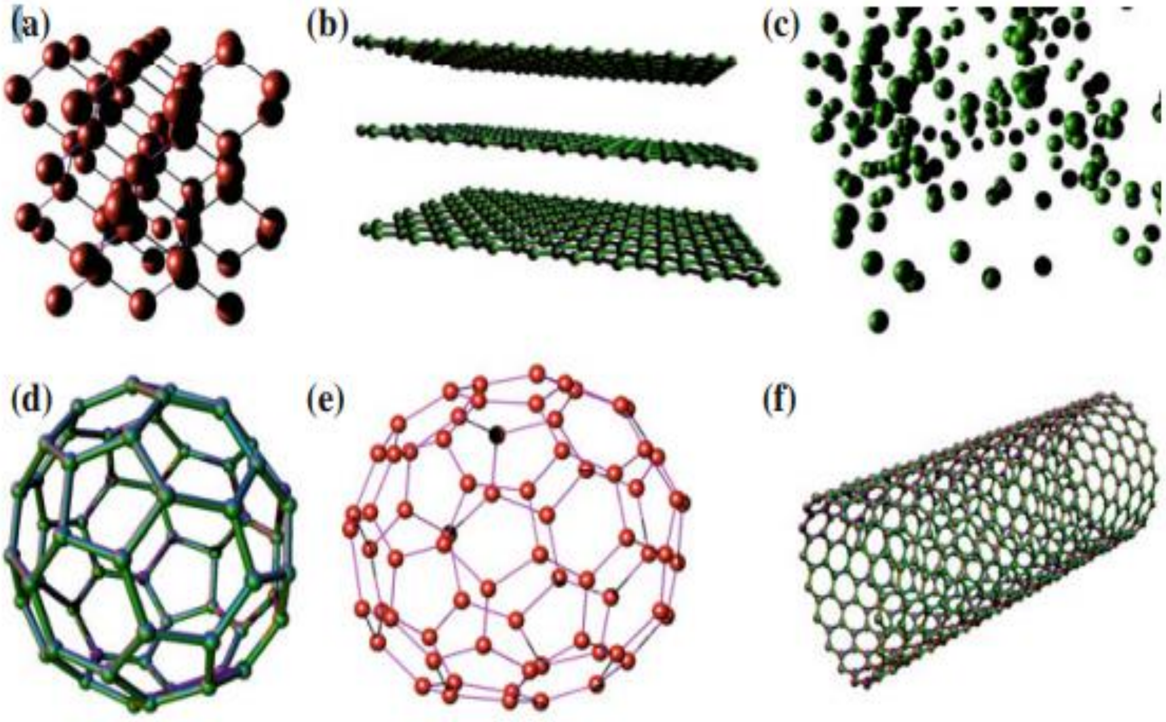

Figure 1.1: Allotropes of carbon. a) Diamond. b) Graphite, c) Amorphous carbon, Sphericalfullerene, C_{60}, e) Ellipsoidal fullerene, C_{70} and f) Tubular fullerene, SWCNT[6]. Reproduced from reference 6.

1.1.1 Graphite and Related sp^2 Hybridized Carbon

The simplest graphite material is a two-dimensional graphene sheet, which is essentially a very large polycyclic hydrocarbon. Ordered three-dimensional graphite materials consist of stacked graphene sheets; they comprise highly oriented pyrolytic graphite (HOPG), made by high temperature decomposition of gaseous hydrocarbons, and natural crystalline graphite [7-8]. HOPG is highly conductive and therefore suitable for electrode applications, however its conductivity is highly anisotropic with basal plane resistivity 30-40 µΩ cm and resistivity perpendicular to the basal plane of 0.15-0.20 Ω cm. Graphite materials are characterized by their crystallinity which is denoted by L where L_a and L_c describe crystal size in plane and perpendicular to the graphene plane, respectively. X-ray diffraction and Raman techniques are used to determine L_a and L_c parameters [9-11]. In HOPG the crystallites have their c axis aligned parallel but rotationally disordered relative to adjacent crystallites [12]. Natural graphite is rarely used for electrochemistry due to its metal impurities (*e.g.*, “ash”). Graphite consists of atomically ordered planes containing the “a” axis (basal plane) and irregular surface with sp^3 hybridized carbon parallel to ‘’c’’ axis (edge plane). Edge plane graphite contains a variety of sites with different geometry such as “armchair” or "zig-zag" edge terminations, as well as oxygen-containing functional groups. Edge-plane HOPG is a useful material for electroanalytical applications because of its electrical conductivity (S m^{-1}) combined with the availability of different reactive functional groups such carboxyl or hydroxyl along the edge plane [7], whose importance in graphite electrochemistry has been highlighted in several studies [13-14]. The electron transfer rate is reported to be much faster at edge-planes than at basal planes of HOPG; for instance the charge transfer rate constant of $Fe(CN)_6^{3-/4-}$ is reported to be k_0= 0.06 - 0.1 cms^{-1} and $<10^{-7}$ cms^{-1} at edge and basal plane electrodes, respectively [15].

An electrochemically important and common graphitic electrode is glassy carbon (GC), which is made by heat-treating polymers at 1000-3000 °C under inert atmosphere; this process pyrolysis the polymer, leading to elimination of heteroatoms into the gas phase until only a highly graphitic network of C-C bonds remains [16]. GC is approximately 60% as dense as HOPG and contains many voids with a structure often described as consisting of twisted and entangled graphitic microfibrils, while its surface is highly heterogeneous and displays a mixture of basal and edge plane sites. Depending on the pre-treatment, the electrochemistry of GC can differ greatly in terms of electron transfer rate constants. For example, laser activated GC exhibits a fast electron transfer rate constant of 0.46 cm s^{-1} for $Fe(CN)_6^{3-/4-}$. For eight quasi-reversible one-electron redox couples, electron transfer rates were found to be 1-3 orders of magnitude higher than those for HOPG basal plane [15, 17-18].

1.1.2 Fullerenes

Fullerenes are allotropes of carbon in the form of hollow spheres, tubes or ellipsoids. Spherical fullerenes are referred to as Buckminster fullerenes or buckyballs whereas cylindrical fullerenes are called carbon nanotubes (CNT). Buckminster fullerenes were discovered by Kroto et al. in 1985 [19-20], Kroto studied organic molecules in space using a telescope and discovered the presence of C_{60}; he collaborated with Smalley and Curl in order to recreate C_{60} molecules in the laboratory via laser vaporization of graphite and determined that C_{60} molecules consisted of sp^2-centers arranged in pentagonal and hexagonal rings [19-21]. Other forms of fullerenes such as C_{70}, C_{76}, C_{82}, and C_{84} have been discovered in soot and have been synthesized via arc discharges [22-26]. The fullerenes C_{60} and C_{70} have well-defined spheroid geometry with approximate diameter of 0.7 nm. and C_{60} consist of 12 pentagons and 20 hexagons where C_{70} consist of 12 pentagons and 25 hexagons. C_{60} Buckyballs obey Euler's theorem which defines that each closed cage geometry holds 12 pentagons in order to implement suitable curvature to lock the cage. The next most studied fullerene is C_{70} which is a rugby ball-shaped molecule [27]. The structure of C_{60} and C_{70} looks like a cage-like fused ring that is made up of pentagonal and hexagonal rings with a carbon atom situated at each polygon. The fullerene family, especially C_{60}, displays photochemical, electrochemical and physical properties which have been explored for various proposed practical applications in a wide range of areas such as pharmaceuticals, environmental, electronic devices, diagnostics, and energy conversion [28].

1.1.3 Carbon Dots

Carbon dots (denoted as CDs) are a relatively recent member of the nanocarbon family. These materials are considered as zero-dimensional carbon nanostructures with diameters less than 10 nm. CDs including graphene quantum dots (GQDs) were accidentally discovered by Xu et al.in 2014 during the purification of single walled carbon nanotubes (SWCNTs) via arc-discharge methods [29]. Since their discovery much attention has been given to CDs because of their versatile properties particularly photoluminescence, excellent biocompatibility, low-cost, the potential to be synthesized from abundant raw materials and their benign chemical toxicity [30-33]. Early studies of CDs were focused on controlling their photoluminescence (PL) yield and spectral characteristics. Approaches for the synthesis of CDs with high PL efficiency can be divided into two groups: top-down methods such as electrochemical synthesis [34] and chemical oxidation [35], and bottom-up methods such as microwave assisted synthesis [36] and the hydrothermal approach [37]. Different types of biological and chemical sensors have been developed based on photoluminescent CDs and their surface functional groups [38]. Some examples include Lai et al. [39] who synthesized polyethylene glycol (PEG) modified CDs for loading and delivery of the doxorubicin (DOX); and Chowdhuri et al. [40] who prepared CDs with metal organic frameworks (MOFs) to investigate drug delivery applications.

1.1.4 Carbon Blacks and Activated Carbons

Carbon black (CB) is an elemental carbon different from diamond, cokes, charcoal and graphite. CBs consist mostly of spherical and ellipsoidal particles and contain both amorphous and crystalline substructures [41]. The basic building blocks of CB are formed by stacked graphene layers where the stacking axis is randomly oriented and translated parallel to the layers. Carbon blacks are synthesised by the incomplete combustion of a heavy aromatic feedstock in a hot flame of air and natural gas. They are good electric conductors due to the overlapping graphene layers and the fused nature of the particles.

The electrical conductivity of CBs ranges from 1 to 10^4 S m^{-1} and thanks to their good electrical properties they are widely used as conductive fillers in polymers [42]. CB/polymer composites possess a wide range of applications such as solid electrolytes for batteries, room temperature gas sensors, conducting electrodes, electrical switching devices, and anti-reflection coatings. Chung et al [43], has investigated the electrical applications of CBs and noted that a sharp rise in electrical resistivity is observed with increasing temperature; this phenomenon is known as positive temperature coefficient (PTC) effect and is pronounced near the melting point [44-45]. Importantly for energy applications, CBs are widely used in low temperature fuel cells as electrocatalyst support materials [46].

Activated carbons are carbonaceous materials with high porosity which are mainly amorphous in nature. Based on studies carried out on the preparation and physicochemical properties of activated carbon, it has been evidenced that their high surface area, the pore structure and the chemical polarity of activated carbons depends largely on the activation process and precursor materials used [47]. These materials are synthesized from carbon-rich precursors such as wood, coconut shells, fossil fuels, pitch coal or selected polymers [48]. ACs are in demand for the fabrication of supercapacitor electrodes due to their high surface area and their low cost of manufacture [49]. The activation process leads to the high surface area which is obtained using thermal reactions in a furnace or a microwave under controlled atmosphere. The reported surface area of the AC materials in the literature is in the range of 1000-2000 m^2 g^{-1} although the theoretical Specific surface area (SSA) can be as high as 3000 m^2 g^{-1} [48]. Wang et al. [50-51] synthesized activated carbon cloth (ACC) with excellent electrochemical properties, namely specific capacitance of 8.8 mF g^{-1}. Beyond capacitive storage, AC-based materials find applications in other energy technologies, e.g. solar cells and batteries. For example, Zhang et al. [51] has synthesized a porous, ultrahigh activated carbon for Li-S battery application which showed high surface area (3164 m^2 g^{-1}) and superior electrochemical; properties with high specific capacity of 11.2 mF g^{-1} and excellent retention capacity (up to 51%) after 800 cycles.

1.1.5 Carbon Nanotubes (CNT) and Nanofibers (CNF)

The early history of CNTs had its beginnings in 1970: a PhD student, Morinobu Endo, at the University of Orleans in France synthesised carbon filaments together with Agnès Oberlin via benzene decomposition which were identified as hollow carbon tubes. The production of these carbon filaments is believed to be the first report of CNT fabrication [52]. They did not receive as much attention at that time however they received renewed interest in 1991 when Ijima brought them to the attention of the academic community once again thus establishing the most popular discovery date for CNTs [53]. Notably, some researchers believe that the initial invention of CNTs dates back to the 1950s, when Roger Bakon observed the first tubules with a high-powered electron microscope [53-55].

CNTs are generally categorized into single-walled carbon nanotubes (SWNTs) and multiwall carbon nanotubes (MWNTs). SWNT is a single layer of graphite rolled up in such a way that it becomes a one-dimensional cylindrical tube. On the other hand, MWNT consist of multiple layers of graphite rolled up concentrically, yielding a one-dimensional cylindrical tube [54, 56-58]. Length of the carbon nanotubes are on the micron scale depending on the number of graphenic layers in the walls of the cylindrical structure. The aspect ratios of carbon nanotubes surpasses 10,000 [59]. Nanotubes are synthesised either by the arc-discharge method [56] or via metal-catalysed chemical vapour deposition [60]. The electronic properties of SWNTs have been studied extensively and depend on their band structure [61]. SWNTs have nanometre-sized dimensions, high aspect ratio, good electrical conductivity along the main axis [62] and low capacitance in the pristine state [12, 63].

Surface modification of CNTs can significantly affect their electrochemical response. Gooding and co-workers have shown that oxygen-containing groups are important for the electrochemical properties of SWCNTs [64] and attributed fast charge transfer kinetics towards $[Fe(CN)_6]^{3-/4-}$ to the presence of particularly carboxylic acid groups[64-65]. Pumera and co-workers have shown the opposite for double-walled carbon nanotubes, observing slower heterogeneous electron-transfer towards $Fe(CN)_6]^{3-/4-}$ [66] for oxidised surfaces. Heteroatom -incorporated CNTs have been shown to display good activity in the ORR. In particular, N-doped CNTs are among the most studied metal free electrocatalyst for ORR [67-68]. Dai and co-workers have shown potential applications of N-doped CNTs as electrocatalysts for ORR [68].

CNFs are cylindrical and conical nanostructure with graphene sheets arranged as stacked cones or curve. They are described as non-continuous one dimensional carbon allotropes. The diameter of CNFs is in the range of 50-200 nm with a high aspect ratio exceeding 100. CNFs are commonly prepared using chemical vapor deposition method [60], electrospinning of polymer solutions [69]. CNTs can be modified or functionalized to improve the activity in electrocatalysis. Stevenson and co-workers have shown that N doped CNFs display a significant catalytic activity toward ORR [70].

1.1.6 Graphene and Graphene Nanoribbons

Graphene is a two-dimensional sheet of sp^2-hybridized carbon which is the basic building block of other important allotropes [71] Initially graphene was considered as building block which was used to study the formation of carbon nanotubes and also to describe the graphite crystal [72]. However, Geim and Novoselov demonstrated that it was possible to isolate single sheets of graphene thus opening the door to the investigation of its properties as a nanomaterial. Ruoff and co-workers demonstrated the solution-based synthesis of single layer graphene sheets [73-75], which involves chemical modification to produce graphite oxide (GO) followed by exfoliation of GO via mechanical energy [76-77]. Nanoribbons are narrow layer of graphene whose properties depend on chemical and magnetic properties, edge orientation and termination. Nanoribbons were categorised as one dimensional carbon materials and they possess a high aspect ratio. Most studied graphene nanoribbons are those which have zigzag and armchair edges. The methods available to synthesize carbon nanoribbons are CVD, unzipping of carbon nanotubes via oxidation method, chemical method, The catalytic cutting method [72].

Graphene and graphene nanoribbons are proposed for a range of applications including ultrafast transistors [78], support film for HRTEM [79], sensors, energy storage/conversion, electronics [80-82], membrane technologies [83], and optics [84] among others. Importantly for the work in this thesis, graphene can act as an electrocatalyst in the ORR and HER when doped/modified with heteroatoms such as nitrogen, boron phosphorous or sulfur. Liming Dai and co-workers [85] (Figure 1.2) demonstrated that nitrogen-doped graphene can serve as an efficient electrocatalyst for the ORR with improved activity compared to unmodified graphene. Several other groups have also reported on the activity of N-doped graphene as an electrocatalyst for ORR [86-88]. Modified or doped graphene has also attracted great attention as a potential anode material for batteries while Reddy et al. [89] have shown that the reversible discharge capacity of N-graphene has higher than that of pristine graphene.

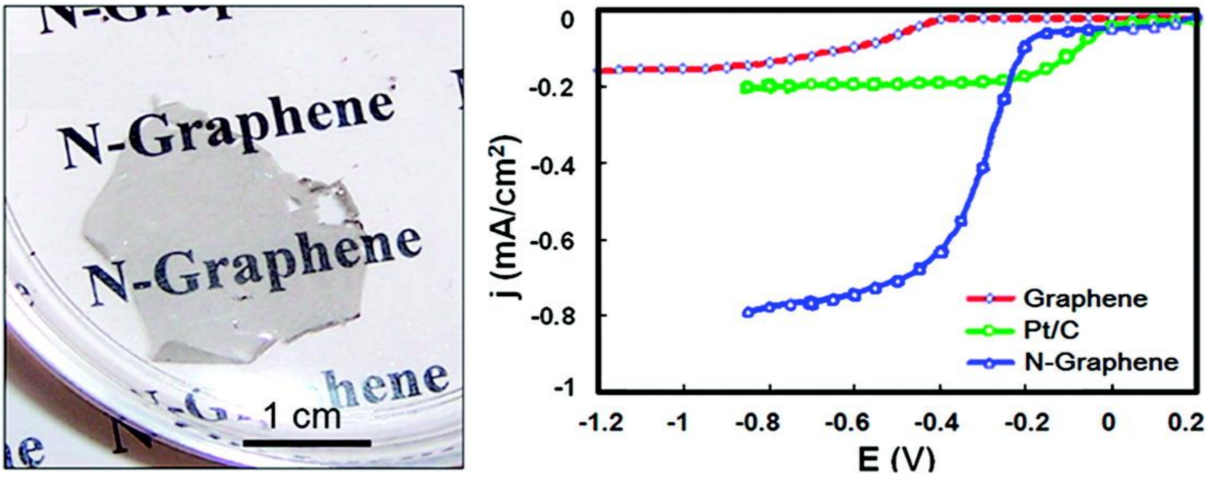

Figure 1.2: RRDE voltammograms for the ORR in air-saturated 0.1 M KOH at the C-graphene electrode (red line), Pt/C electrode (green line), and N-graphene electrode (blue line). Taken from Ref (85), Copyright © 2010 American Chemical Society.

1.1.7 Diamond

Diamond displays a cubic crystal structure and at room temperature and pressure it is metastable. Diamond is considered an excellent material for many applications due to its unusual physical and chemical properties such as high electrical resistivity, high thermal conductivity, high corrosion resistance, wide band gap, low coefficient of friction, chemical inertness, and optical transparency [90-91]. These properties are important for several technical applications such as high-power electronic devices, electrooptical devices and coatings for cutting tools etc. Impurity free and undoped diamond is a wide bandgap semiconductor(5.4-5.7 eV) with resistivity >10^8 Ω cm[92]. The electrical resistivity of diamond films strongly depends on the surface termination, with H-terminated diamond notably imparting high conductivity and negative electron affinity. Incorporation of impurities (for example boron, nitrogen) into the diamond structure during synthesis can increase the conductivity resulting in good materials for electrochemical applications; the most common of these is boron doped diamond (BDD) which is synthesized via plasma enhanced chemical vapour deposition using methane and a boron source. Boron acts as an electron acceptor imparting p-type semiconducting property and lowering the Fermi level. The boron doping level is typically high, often in the range of 10^{18}-10^{20} atoms/cm^3 [93-94]. n-type semiconducting properties can be obtained by using phosphorus (charge carrier activation energy 0.6 eV) [35-36], nitrogen (charge carrier activation energy 1.6 –1.7 eV) [95-96], or sulfur [97] as dopants. Co-doped diamond electrodes have also been produced, such as nitrogen-boron [98] or boron-sulfur [97] co-doped electrodes.

The application of diamond films as electrodes was first shown by Iwaki et al. in 1983 [99]. Pleskov et al. in 1987 published the first paper on diamond devoted to improving the technology for fabricating conducting thin films and the relationship between the semiconductor and structural properties of diamonds and their electrochemical characteristics [100]. Swain et al. in 1993 demonstrated that BDD electrodes have suitable properties for use in electroanalytical applications [92]. Later, Fujishima et al. in 1998, investigated polycrystalline diamond thin film as electrodes prepared via microwave plasma chemical vapor deposition (CVD) and showed that they have high conductivity ($\rho \approx 10^{-3}\ \Omega.\ \mathrm{cm}$) [100-101]. Because of their unique electrochemical properties BDD electrodes have found applications in multiple electroanalytical methods: cathodic stripping voltammetry (CSV), abrasive stripping voltammetry (AbSV), amperometric detection, anodic stripping voltammetry (ASV), and square wave voltammetry (SWV) [102-104]. Nitrogen doped diamond electrodes (NDD) have also shown high electrocatalytic activity and high selectivity in notoriously sluggish cathodic processes such as nitrobenzene reduction [95].

1.1.8 Amorphous carbon

a-C is comprised of both trigonally and tetrahedrally bonded carbon (sp^3/sp^2 mixture) and it does not possess a crystalline structure or long-range order. a-C can exhibit beneficial chemical and physical properties such as high chemical inertness, diamond-like properties, [105-109] favourable tribological proprieties [110-111], and a low frictional coefficient [112-113]. a-C can be doped with heteroatoms such as hydrogen, nitrogen and boron thereby making these materials extremely diverse in terms of structural, mechanical and electronic properties. Different methods have been used to deposit a-C films such as ion beam methods [114-116], magnetron sputtering [117-120], Chemical Vapour Deposition [121-123],and Pulsed Laser Deposition [124]. Depending on the deposition method the properties of amorphous carbon films can vary and that is why a-C finds uses in a wide range of applications, not only the typical applications as a barrier coating such as in wear resistant coatings, and corrosion resistant coatings, but also in optical applications such as photodiodes, light-emitting diodes, optical coatings and electroluminescent devices [125], as well as in applications requiring high biocompatibility such as orthopaedics and cardiovascular biodevices [126]. The family of amorphous carbon is schematically presented in Figure 1.3 [127], wherein the compositions of the various forms of amorphous carbon are displayed in a ternary phase diagram as first used by Jacob and Moller [128].

Table 1.1: Comparison of some main properties of some form of DLC with those of reference materials (diamond, graphite) **[127]**.

Materials	sp^3 (%)	H (%)	Bandgap (eV)	Hardness (GPa)	References
Diamond	100	0	5.5	100	[129]
Graphite	0	0	0		[130]
Glassy carbon	0	0	0.01		[131]
a-C	5-20	0	0.5		[132]
a-C:H	20-60	30-50	1.6-2.2	10-20	[133]
ta-C	80-88	0	2.5	80	[134, 135]
ta-C-H	70	30	2.0-2.5	50	[136]

Amorphous carbons with high sp^3-content (>80%) is termed Diamond Like Carbon (DLC) and possesses properties in common with diamond, such as wide band gap and lower conductivity than more graphitic films, mechanic hardness and chemical and electrochemical inertness; however the production cost of DLC is much lower than that of diamond.[134, 137-139] Nonetheless amorphous carbons can be prepared with low sp^3-content thus approaching the behaviour of graphitic materials. Typical properties of various forms of amorphous carbon are presented in table 1.1 [127]. Modified and doped DLC electrodes possess some attractive features such as a wide potential window, low background current, and strong anti-fouling capability [140]. DLC films have been used as electrode materials for electrochemical quartz crystal microbalance (EQCM) [141], optical transparent electrodes for spectroelectrochemistry [142], tip electrodes for SECM [143] and biosensing [144-145]. DLC films have been characterized as anode materials for Li–ion batteries and a high fraction of sp^2 bonding in the DLC films is preferred for high lithium storage capacity [146].

Amorphous carbons from highly reactive nanoacetylide precursors exhibit a high surface area associated with a mesoporous and microporous structure although the material can be prepared without an activation process [147]. Mesoporous carbon materials have attracted interest for use in numerous applications such as capacitors [148], absorbents, electrodes [149], and catalytic supports [150].

Films with high sp^2 content (>80%) are mechanically soft and display a lower band gap; these kinds of materials have been synthesized by our group and some of their electrochemical properties have been discussed in previous work [151-154]. This type of films is used in this thesis to investigate the role of nitrogenation on the capacitive properties of amorphous carbon electrodes which is explored in detail in chapter III.

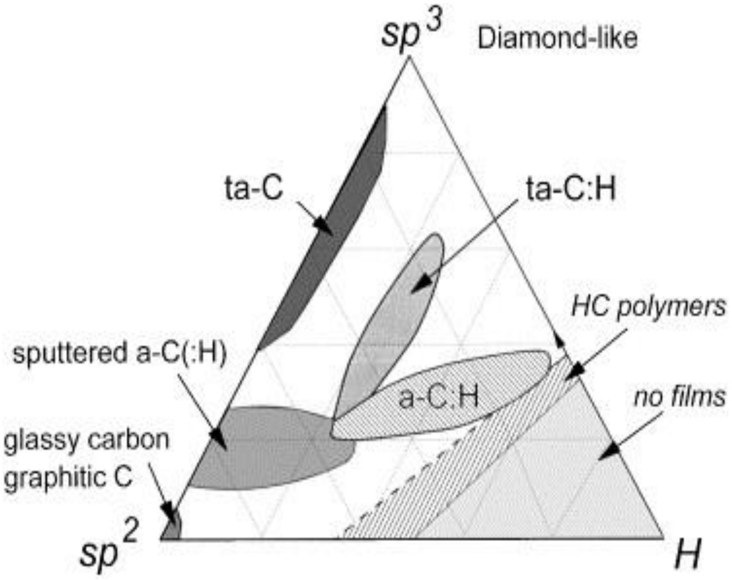

Figure 1.3: Ternary phase diagram of bonding in amorphous carbon-hydrogen alloys. Collected from ref 127. Copyright © 2002 Elsevier Science.

1.1.8.1 Nitrogen-Incorporated Amorphous Carbon (a-C:N)

Nitrogen doped carbon materials have received tremendous attention in the fields of electrocatalysis and energy storage due to the high ORR activity as well as low cost, good durability, and environmental friendliness [85, 155-156]. Pt-based materials are known to be the most active materials for catalysts the ORR reactions at the cathode of fuel cells. Due to high cost of Pt-based catalyst, their poor durability and slow electron-transfer kinetics, there have been significant efforts to reduce the use of Pt-based catalysts in electrochemical devices [157]. Development of non-precious metal-free catalysts which possess high activity and durability has been considered one of the most competitive fields in chemistry and materials science. Dai et al, firstly incorporated N into graphene for efficient metal free catalyst for the ORR in fuel cell [85]. N-doped carbon materials as ORR catalyst are further discussed in section 1.6.2. The modification of amorphous carbons via incorporation of heteroatoms such as nitrogen, phosphorus and boron has received much attention from various research groups. Beyond applications in electrocatalysis, nitrogen incorporation into carbons is motivated by the synthesis of super hard compound, e.g. C_3N_4 [158], and by the potential for achieving electronic doping for optoelectronic devices. Nitrogen is a good dopant as its radius is very close to that of carbon and being in group V it can in principle introduce donor levels in the carbon structure resulting in n-type doping; however, nitrogenation can also result in the creation of N-containing functional groups such as pyridinic, pyrrolic, amine, or nitrile groups. For example, nitrogen doped CNTs possess good electronic transport properties [159-160] and have several potential applications in energy, catalysis [161-162] and electroanalysis [160]. Different methods have been used to produce nitrogen incorporated a-C such as pulsed laser deposition (PLD) processes [163], CVD [164], or reactive sputtering [165-168].

Studies have found that incorporation of nitrogen changes several properties of amorphous carbon films. The electrical resistivity of a-C can be decreased by few orders of magnitude through nitrogen doping and nitrogen incorporation in a-C has been confirmed to behave as an n-type dopant because the fermi level shifts with increasing nitrogen concentration [169]. Nitrogen content in the material also influences the electrical properties as current-voltage (I-V) measurements show that current density and conductivity increase with N content in a-C films [170]. Nitrogen containing a-C as a catalyst has shown higher graphitic edge plane exposure such as a-C:N and higher ORR activity compared to undoped a-C [171-172]. Several studies found that a-C:N electrodes exhibit wider potential windows and low background current in aqueous systems [173-174], even exceeding those observed with BDD, reversible behaviour with outer-sphere redox couples, excellent analytical behaviour, higher catalytic activity for Cl_2/Cl^- than BDD [175]. XPS studies found that N-doped amorphous carbon has four different nitrogen sites such as graphitic nitrogen, pyrrolic nitrogen, pyridinic nitrogen and pyridine n-oxide type nitrogen [176]. Other types of N-sites such as amines and nitrile-like groups may be found via- XPS depending on the method of preparation of these materials [177]. Raman spectroscopy studies have found that N doping also increases graphitisation by promoting formation of sp^2 clusters [163]. These characteristics demonstrate the great promise of the a-C:N electrode for electroanalytical application [175].

1.2 The role of capacitive properties in electrode processes

When any electrode is immersed in an electrolyte solution, an interfacial region is formed between electrolyte and electrode. This region is called the double layer and the electrical properties of such a layer are important because they affect electrochemical measurements. If an electrical circuit is used to describe the current that flows at a particular working electrode under polarisation, the double layer can be viewed as a capacitor in this circuit. In order to obtain the desired potential at the working electrode the double layer first must be charged, and this charging current introduces a capacitive contribution to the total current passed at the electrode. Capacitive currents contain information about the double layer and its properties. The double layer structure and its capacity depend on several parameters such as: electrode material (metallic/semiconductive behaviour, electrode porosity, the presence of oxide or insulating layers), type of solvent, type of supporting electrolyte, total area, extent of specific adsorption of ions and molecules, and temperature [178]. In order to understand the structure of the double layer at the electrode/electrolyte interphase theoretical models of varying complexity have been discussed in the literature; these models are discussed in the following sections.

1.2.1 Helmholtz Model

The Helmholtz model was the first one proposed to describe the structure of the double layer at the electrode/electrolyte interface and it is inspired by the structure of a parallel plate capacitor. In a parallel plate capacitor two layers of charge of opposite sign are separated at a fixed distance (Figure 1.4a, aa) and the Helmholtz model assumes that electrons at a metal electrode and positive ions in solution behave in analogy to the charges in the two plates, forming two rigid charge layers of opposite charge at a fixed distance. The potential drop across the interface in this case is linear and the capacitance of the double layer per unit area is given by:

$$C=\frac{\varepsilon}{4\pi d} \qquad (1.1)$$

where ε is the permittivity of the medium between the plates and d is the distance between them.

Charge stored in an electrode per unit area upon a potential change from U_{PZC} (potential at the point of zero charge) to a given electrochemical double layer (EDL) potential is the integral capacitance of the electrode. At different applied potentials, the experimentally measured capacity is the differential capacitance of the electrode. [179] For this model differential and integral capacitances are equivalent and have a constant value.

1.2.2 Gouy and Chapman Model

Ions in the electric double layer are subjected to both electrical fields and thermal fluctuations and as a result the charge carriers of both electrode and electrolyte do not reside at rigid layers at a fixed distance from each other, as proposed in the Helmholtz model. The Gouy-Chapman model allows for the diffusion of ions in solution; the ions are distributed according to electrostatics and Boltzmann's statistics in a region near the electrode surface called diffuse double layer, or layer of Gouy-Chapman (figure 1.4b, bb). In this model, the diffuse charge at the electrode is given by:

$$q_D = (\frac{2kTn_O\varepsilon}{\pi})^{1/2} \sinh \frac{e_O V}{2kT} \qquad (1.2)$$

The differential capacitance is given by:

$$C = (\frac{n_0 \varepsilon e_0 2}{2\pi kT})^{1/2} \cosh \frac{e_0 V}{2kT} \qquad (1.3)$$

where n_0 is the number of ions of positive and negative charge per unit volume in the bulk of the electrolyte and V is the potential drop from the metal to the bulk of the electrolyte.

According to this model the double layer capacitance is maximum at V=0 and increases symmetrically to either side of V=0. This model has deficiencies in that the experimental capacity-potential relations do not behave in a symmetrical-parabolic manner, except at potentials close to the potential of zero charge of the metal. Ions cannot approach the surface at distances shorter than their radii. That is the reason why the double layer capacity rises at large potential relative to the point of zero charge. In this model, ion-ion interactions are neglected, however these might become important at high electrolyte concentrations; furthermore, the model assumes a constant dielectric constant in the region between the electrode and electrolyte [179].

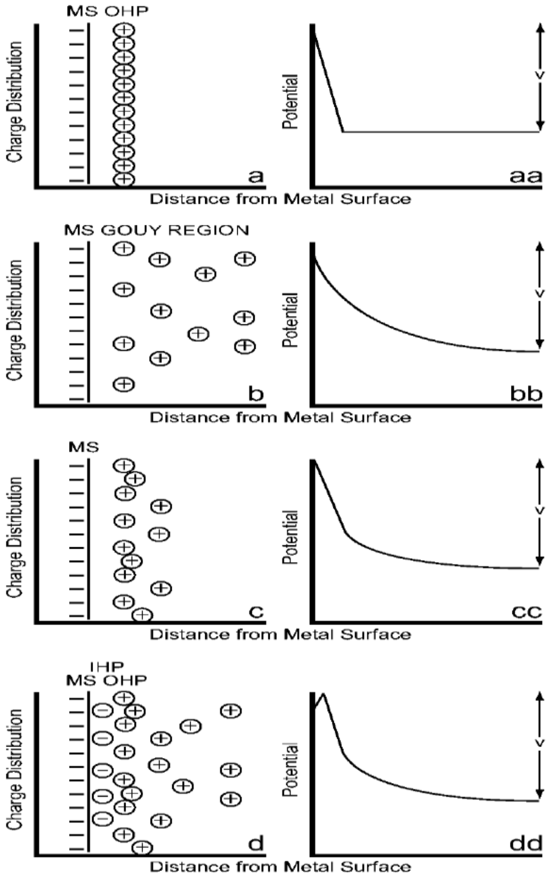

Figure 1.4: Different double layer models (a) and (aa) Helmhotz model; (b) and (bb) Gouy-Chapman model; (c) and (cc) Stern model, and (d) and (dd) Esin and Markov, Grahame, and Devanathan model [179]. Reproduced from reference 179.

1.2.3 Stern Model

The Stern model overcomes some of previous models' limitations. Firstly, in this model ions are considered to have a finite size and are located at a finite distance from the electrode, with the minimum distance usually taken to be their ionic radius. Secondly, the charge distribution in the electrolyte consists of two contributions: (a) ions as in the Helmholtz model, immobilized close to the electrode, and (b) ions as in the Gouy-Chapman model, distributed over a diffuse layer (figure 1.4c, cc). Thus, the total charge stored at the interface is given by:

$$q_M = q_H + q_G \qquad (1.4)$$

that is the sum of the Helmholtz fixed charge, q_H, and the Gouy-Chapman diffuse charge, q_G. It can be shown that the double layer capacitance across this electrode/electrolyte interface is given by these two contributions in series:

$$\frac{1}{C} = \frac{1}{C_H} + \frac{1}{C_G} \qquad (1.5)$$

where C_H and C_G stand for the contributions of the Helmholtz and Gouy-Chapman capacitances.

This model is very similar to Helmholtz's because most of the charge is concentrated at the Helmholtz layer. At low electrolyte concentrations $C_G > C_H$. whereas in concentrated electrolytes $C_H >> C_G$. Importantly, it means that when the diffuse layer capacitance escapes to infinity then the C_H becomes dominant and limits the total observed capacitance. This model is not applicable for electrolytes with specifically adsorbable anions and does not take into account the role of the solvent in ion solvation [179].

1.2.4 Esin and Markov, Grahame and Devanathan Model

This model was proposed by three groups of researchers and is represented in figure 1d, dd. The additional feature of the model is that it allows for ions to be dehydrated and specifically adsorbed at the electrode. Adsorption of ions occurs due to different types of interactions between the electrodes and ions such as electrostatic forces, image forces and dispersion forces. The specific adsorption (physical adsorption) of ions occurs when the image and dispersion forces are larger than the electronic or ion-ion repulsive force. However, stronger bonds can be formed by partial electron transfer between the ion and the electrode resulting in chemisorption [179]. An inner layer between the electrode surface and the Helmholtz layer further modifies the double layer. The inner layer is the locus of centers of desolvated ions strongly attached to the electrode. Devanathan derived the following relation for the total capacitance:

$$\frac{1}{C} = \frac{1}{C_{M-1}} + \left(\frac{1}{C_{M-2}} + \frac{1}{C_{2-b}}\right)\left(1 - \frac{dq1}{dq_M}\right) \qquad (1.6)$$

where C_{M-1} and C_{M-2} are the integral capacities of the interfaces between the electrode and the inner Helmholtz plane (IHP) and between the inner and outer Helmholtz planes (OHP), respectively; $C_{2-b}$is the differential capacity of the diffuse double layer, and $\frac{\mathrm{dq1}}{\mathrm{dq_M}}$ represents the rate of change of the specifically adsorbed charge with total charge q_M at the electrode.

Some important conclusions can be drawn from this equation. The capacity reaches a minimum at $\frac{\mathrm{dq1}}{\mathrm{dq_M}} = 0$ because the latter can have only positive values. At $\frac{\mathrm{dq1}}{\mathrm{dq_M}} = 1$ we obtain a high differential capacitance and the electrode becomes non-polarizable. The capacitance minimum is reached at the potential of zero charge.

1.3 Double layer properties of semiconducting electrode

Charged planes or space charge layers form at any interphase, including the solid /liquid interface when the electrons are transferred in or out of the semiconductor surface. The formation of these planes leads to electrical double layers consisting of layers of positive charge, layers of negative charge and regions of high electric field within the charged layers. Such double layers can dominate the electrical and chemical properties of the surface of semiconducting electrodes. There are three important double layers that appear at the electrode/electrolyte interface: first, the semiconductor space charge double layer; second, the Helmholtz double layer between the solid and the “outer Helmholtz plane”, i.e. the distance of closest approach of non-adsorbed ions to the surface; and third, the Gouy-Chapman double layer in the solution near the solid in which excess of ions exists. There are excess charge regions corresponding to these double layers. Firstly, the space charge region in the semiconducting electrode can be in the form of immobile charge impurities near the surface of the semiconductor or can be in the form of mobile electrons or holes in the conduction or valence bands of the semiconducting electrode. Secondly, the charged plane on the two sides of the Helmholtz region that form the Helmholtz double layer. One plane is at the solid surface and the charge is in the surface states or at the location of the adsorbed ions. The other plane is called the “outer Helmholtz plane” the position of closest approach of mobile ions. Thirdly, there is an extended region of excess space charge in the Gouy-Chapman region of the solution related to mobile ions. The amount of charge stored in the space charge region depends on several processes. These charged regions, together with the counter charge in the Helmholtz region form the Gouy double layer [126].

1.4 Contributions to the total double layer capacitance of carbon metallic and semiconductor electrodes

Carbon materials can display both metallic and semiconductive properties and the models described in the previous section can be used to interpret capacitive behaviour at carbon electrodes and to characterise carbon electronic properties. On a semiconducting electrode the capacity is a function of electrode potential. There are many elements in capacitive impedance associated with a semiconducting electrode and in this section these elements will be described in terms of equivalent circuits. The possibility of storing charge in space charge regions and Helmholtz planes is always related to electrical capacitance and each double layer has a capacitance associated with it. The capacitance C is defined by,

$$C=\frac{dQ}{dV} \qquad (1.7)$$

where dQ is the infinitesimal charge stored in the layer resulting from a dV differential voltage change across the double layer.

There are several contributions to the capacity at the semiconductor surface corresponding to various mechanisms by which charge is stored, such as across the Helmholtz double layer, across the semiconductor space charge region, in surface states and across an oxide/insulating film at the surface. Upon application of voltage change dV across the Helmholtz double layer, ions accumulate in or on the outer Helmholtz plane with a charge qdN_s/m^2 and counter charge appears on the solid of –qdNs, leading to a Helmholtz capacity:

$$C_H = \frac{dQ}{dV_H} \qquad (1.8)$$

If there is depletion layer at the semiconductor surface, the space charge capacity must be considered:

$$C_{sc}=\frac{dQ_{sc}}{dV_s} \qquad (1.9)$$

where V_s is the potential difference across the space-charge region and Q_s is the charge stored in the space charge region. The charge Q_s is not at the surface of the conducting layer, but instead spread out through the insulating (depletion) layer and principally the same charge stored at the surface of the two facing conducting regions.

Surface or defect states can also lead to an additional mechanism of charge storage and a corresponding capacitance C_{ss} . In a similar manner the surface state capacity is defined as:

$$C_{ss} =\frac{dQ_{SS}}{dV_S} \qquad (1.10)$$

Where Q_{ss} is the positive charge stored at surface/defect states. When V_s changes the occupancy of the surface state changes (figure 1.5). As V_s changes E_F moves relative to the surface states and this charge must be stored. When the voltage is restored to its initial value then the stored charge returns to the conduction band.

If there is an oxide layer at the surface of the electrode and this layer is reasonably insulating, a capacity called C_{ox} associated with the thickness of the oxide layer can be defined by the equation below:

$$d_Q = CdV = (\frac{k\varepsilon_0 A}{d})dV \qquad (1.11)$$

where A is the area and d the thickness of the oxide layer, k is the dielectric constant of the oxide and ε_0 the permittivity of free space.

The impedance measurement is associated with the combination of these three capacities C_H, C_{sc}, C_{ss} can be estimated with the help of figure 1.5 as described below. A change in the applied voltage ΔV is divided between ΔV_S and ΔV_H:

$$\Delta V = \Delta V_S + \Delta V_H \qquad (1.12)$$

By charge neutrality:

$$Q_{soln} = Q_{sc} + Q_{ss} \qquad (1.13)$$

ΔQ_{soln} is the charge stored from the external circuit upon an applied voltage change of Δ V, so that equation 1.7 becomes:

$$\frac{1}{C} = \frac{\Delta V}{\Delta Q} = \frac{\Delta V}{\Delta Q_{soln}} = \frac{\Delta V_S}{\Delta Q_{sc} + \Delta Q_{ss}} + \frac{\Delta V_H}{\Delta Q_{soln}} \qquad (1.14)$$

If we combine above equations (1.8), (1.9) and (1.10) we obtain:

$$\frac{1}{C} = \frac{1}{C_{sc}+C_{ss}} + \frac{1}{C_H} \qquad (1.15)$$

Here C_H acts as a capacitor in series with the parallel combination of C_{sc} and C_{ss} [126]

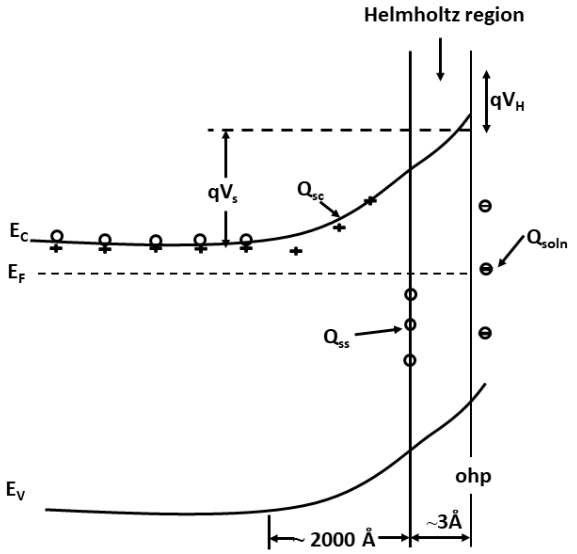

Figure 1.5: Schematic diagram of the energy gap model of the semiconductor surface showing the location of stored charge and voltage differences. E_c - bottom of the conduction band; E_V, - top of the valence band; EF - Fermi level; Q_{sc} -the positive charge in the space region; Q_{ss} -the positive charge on the surface states. Reproduced from reference 126.

1.5 Overview of carbon based materials in energy storage devices

With the rapid development of the world economy and the increasing demand for a transition to sustainable energy resources, energy storage has become one of the most important research topics worldwide and has gained an intensive attention from researchers and industrial developers. Over the past few decades a number of energy storage/conversion devices have been developed such as fuel cells, batteries, solar cells capacitors, super capacitors etc. Importantly, capacitors and batteries are necessary energy storage devices in modern society due to the tremendous growth and demand of portable electronic devices and hybrid electric vehicles (HEVs). Figure 1.6 shows a Ragone plot for various electrical energy storage devices where electrochemical capacitors (EC) having high specific power and short time constants, while on the other hand batteries have low specific power and long-time constants [180]. ECs are generally based on two types of capacitive behaviours associated with the double layer capacitance at electrode/electrolyte interfaces and another is with the pseudo-capacitance. There are three types of ECs depending on the electrode materials such as, electrical double layer capacitors (EDLCs), pseudocapacitors (PCs) and hybrid capacitors. Carbon electrodes are typical materials for the development of EDLCs with various forms of nanocarbons investigated due to their favourable features such as low weight, high conductivity, electrochemical stability, open ad controllable porosity, and relatively chemically inert. Porous carbon electrodes which have high specific area including activated carbon [181], carbon fibres [182], carbon nanotubes [183] and graphene [184] have been used for EDLC applications. Among them activated carbon is a widely used material for EDLC because of their high specific surface area and moderate cost. The double layer capacitance of activated carbons is in the range 100–120 F g^{-1} in organic electrolytes and 150–300 F g^{-1} in aqueous electrolytes [180].

The capacitance of pseudocapacitive electrodes offers high specific charge storage due to fast and highly reversible redox reactions but they often suffer from stability during cycling. Ruthenium oxide (RuO_2) [185], manganese oxide (MnO_x) [186], cobalt oxide (Co_3O_4) [187] and iron oxides (Fe_2O_3) [188] are commonly used electrode materials for pseudocapacitors.

Electrochemical batteries are considered as very important device for energy storage. It produces electricity from stored energy in the chemicals of the battery. There is an increasing demand of portable electronic devices which leads to the improvement of their performance and therefore, Li-ion batteries have gained considerable attention. The performance of the Li-ion batteries depends on the microstructure of the anode materials made of carbon and graphite. Graphite has remained the anode materials for batteries and cathode materials have been developed to further improve their performance. CNT based materials such as Fe_3O_4/CNTs nanocomposite [189], CNT/RuO_2 core-shell composite [190], CNT/amorphous $FePO_4$ [191] have shown excellent electrochemical performance as cathode material for Li-ion battery. In contrast to CNTs graphene are robust electrode material especially nitrogen and boron doped graphene are potential candidates for Li-ion battery (LIB) application [192]. Graphene based composite materials using tin oxide (SnO2), nickel oxide (NiO), and rGO acted as an anode materials has shown excellent performance for Li-ion battery application [193].

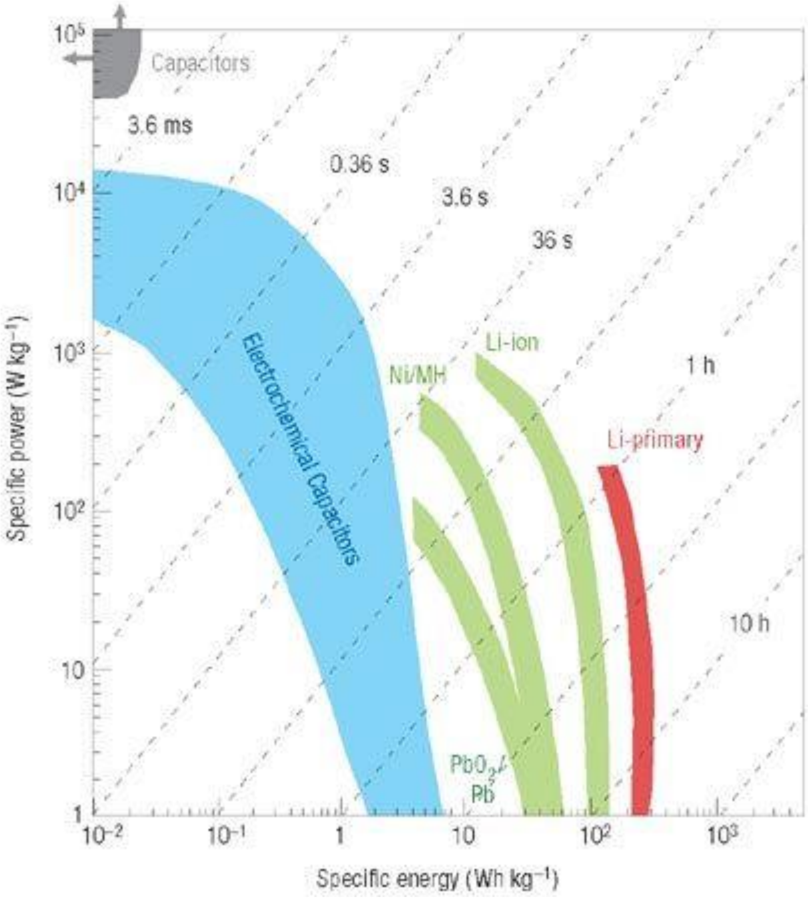

Figure 1.6: A Ragone plot for various electrical energy storage devices where it is showing the specific power against the specific energy. If an EC used in an electrical vehicle the specific energy shows how far one can go on a single charge and the specific power shows how fast one can go Times shown here are the time constant of the devices **180**. Taken from reference 180.Copyright © 2008, Springer Nature.

1.6 The oxygen reduction reaction

The oxygen reduction reaction (ORR) is a fundamental reaction for energy conversion due to its importance for the performance of fuel cells and metal-air batteries. This reaction can take place in either acid or alkaline solution and is a complex multistep process whose most desirable product for fuel cell applications is water/hydroxide according to the following net reactions:

$O_2 + 2H_2O + 4e^- \rightarrow 4OH^-$ E° = 1.229 V vs RHE

$O_2 + 4H^+ + 4e^- \rightarrow 2H_2O$ E° = 1.229 V vs RHE

However partial reduction of O_2 leading to formation of hydrogen peroxide/hydroperoxide anion is also possible according to the reactions:

$O_2 + H_2O + 2e^- \rightarrow HO_2^- + OH^-$ E° = 0.695 V vs. RHE

$O_2 + 2H^+ + 2e^- \rightarrow H_2O_2$ E° = 0.695 V vs. RHE

This H_2O_2/HO_2^- can be further reduced to two water molecules as follows:

$HO_2^- + H_2O + 2e^- \rightarrow 3OH^-$ E° = 1.763 V vs. RHE

$H_2O_2 + 2H^+ + 2e^- \rightarrow 2H_2O$ E° = 1.763 V vs. RHE

Full reduction requires that four electrons are transferred in sequence without release of H_2O_2 [194-196]; the complete 4e reduction by a catalyst surface is preferred due to the relatively high reactivity of hydrogen peroxide compared to water and its ability to corrode/degrade fuel cell components [197].

The full reduction process is favoured by adsorption of O_2 on the catalyst surface where 1st electron transfer and protonation can take place resulting in adsorbed *OOH; this can be followed by a 2nd electron transfer yielding H_2O_2/HO_2^- in acid/alkaline conditions. How the reaction proceeds depend on whether desorption of this intermediate occurs at a faster rate compared to subsequent electron transfer steps. In addition to an initial step involving chemisoroption of O_2 at the surface, it has also been proposed that an outer-sphere transfer mechanism is possible for the production of the superoxide anion/hydroperoxyl radical in the first step; this initial step has been proposed to play a more important role under alkaline conditions and for materials that display weaker interfacial interactions with O_2.

1.6.1 Carbon based ORR Catalysts

Large scale commercialization of FCs requires high cost materials and so far, precious group metals such Pt and other metals have proven to be the best catalysts for the hydrogen oxidation and the oxygen reduction in fuel cells. Pt is a scarce and expensive metal as shown in Figure 1.7. The cathode oxygen reduction reaction (ORR) is significantly more sluggish than the hydrogen oxidation reaction (HOR), therefore 80-85% of Pt is loaded in cathode of FCs in order to facilitate the ORR [198]. As the Pt based catalyst always suffers from limited long-term stability and in the case of methanol fuel cells Pt is also vulnerable to CO poisoning and poor tolerance to methanol it would therefore be desirable to develop non-precious metal-based catalysts (NPMC).

To replace Pt with NPMC in fuel cells it is necessary to provide requirements such as to provide power equivalent to that delivered with Pt electrocatalysts and to demonstrate a stability of at least 1000 h. Among the available NPMCs carbon-based catalysts are considered for investigation because of their high electrical conductivity, excellent stability and because the cost of these catalyst is low compare to other NPMCs [199-201]. Researchers have focused on several types of carbon-based catalysts in order to achieve NPMC with high activity which are the carbon catalysts with encapsulated nanoparticles, metal-free heteroatoms-doped carbons and metal/nitrogen-co-doped carbons. The actual active sites of catalyst have been investigated by using computational method as well as experimental measurements but remain under debate [202-205].

Carbon-based ORR catalysts can be divided into three types according to their composition such as 1) carbon catalysts with encapsulated nanoparticles (Fe, Fe_3C, Co) [206-207] ; 2) Metal (Fe, Co, Mn, Ni, Cu or Zn)/nitrogen-co-doped carbons [208-209]; and 3) Metal-free heteroatom (N, B, F, S, P)-doped carbons [210-211], all which remain under study by several research groups. In order to achieve high ORR activity for carbon based materials the most effective strategy will be modulation of electronic structure and geometric structure [212] although results on structure-activity descriptors for these materials are often contradictory and the design principles are hotly debated.

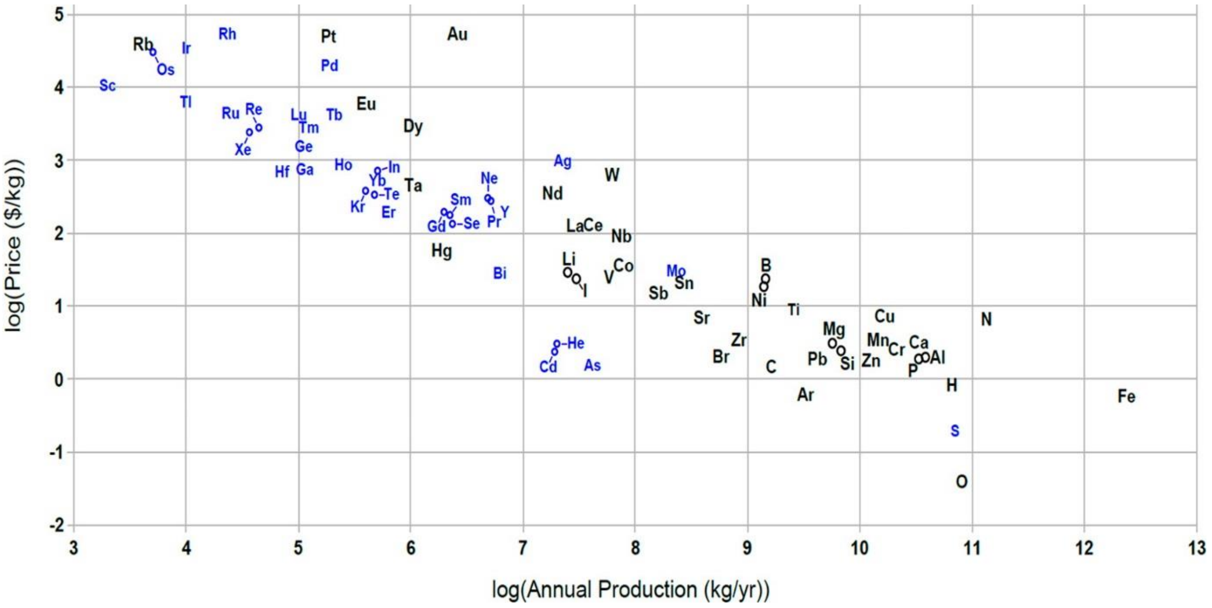

Figure 1.7: Price of the elements (in $/kg) versus their annual production (in kg/yr) **[213].** Reprinted with permission from ref 213. Copyright 2012 Royal Society of Chemistry.

1.6.2 Nitrogen Doped Carbon as ORR Catalysts

Metal free carbon based catalyst are alternatives to novel metals for oxygen reduction reaction due to low cost, abundant reserves and excellent resistance to carbon oxide and methanol [214]. Many heteroatom doped carbon materials have shown high activity towards ORR and among those nitrogen (N)-doped carbon materials are some of the most efficient metal-free catalysts [68, 215]. Nitrogen doped carbon materials can be synthesised by using different methods such as pyrolysis [216-217], carbonisation [218-219], chemical vapour deposition (CVD) [220] and other modified CVD methods [221]. Nitrogen can be doped into graphene sheets [222] and carbon nanostructures such as carbon nanotubes [223], carbon nanofibers [224], carbon nanocoils [225], carbon nanospheres [226] by in situ doping. Nitrogen doped carbon nanomaterials are the most commonly investigated for the ORR compare with other heteroatoms due to environmentally friendly and abundant of nitrogen resources. The differences of electronegativity between C (χ = 2.55) and N (χ = 3.06) facilitate the polarization of carbon matrix efficiently and the adsorption of oxygen on it [227]. Catalytic performance of the of N doped carbon nanomaterials also corelated with the type of N-sites such as graphitic N (400.9 eV), pyrrolic N (398.6 eV), and pyridinic N (397.9 eV) present in the electrocatalysts [228-229]. Zhenhai Xia et al. demonstrated that pyridinic N possess a lone electron pair which enhance electron donating capability and O-O bond break, and creation of water molecules [230]. Guo et al. [228] also demonstrated that the active sites in N doped carbon nanomaterials are located adjacent to pyridinic N. Some other research group considered graphitic N for the active site in N doped carbon nanomaterials because of coexistence of different N sites [231-232]. Types of N sites and the content of N in the electrocatalyst is also a controversial factor which affecting ORR performance where catalyst with higher N have low ORR activity [233]. Catalytic activity also depends on the structure of N doped carbon as well as morphology of the carbon nanomaterials which could control the activity and long-term stability of catalyst [234]. N doped metal free catalysts have improved tremendously the catalytic performance of the ORR, but its performance is still fall behind of commercial Pt. In order to improve the catalytic performance of N doped carbon nanomaterials towards efficient ORR, it is crucial to develop other strategies such as structure modification, introduction of defects into materials, coordination with other heteroatoms to further enhance the catalytic performance [227] In the future development of N-doped carbon-based nanomaterials should focus on design specific structure with high surface area, rich defects, optimal nitrogen content and abundant of macro and meso pores etc.

1.7 Aims of the Project

N doped amorphous carbon materials are used for vast range of applications from catalyst supports to electrodes, structural components and medical applications. There has been a significant amount of work done on the synthesis and characterisation of amorphous carbon by varying composition to achieve control over mechanical and electronic properties of these materials. How to control the interaction between their electronic properties and interfacial properties has not been fully elucidated. This work will address some of the gaps in the current literature, by synthesizing different N-doped amorphous carbon materials and characterizing those carbon materials by using XPS, Raman spectroscopy, ultraviolet photoelectron spectroscopy and electrochemical methods. It is known from the literature that N-doping increases charge carrier density and metallic character of a-C materials [127]. The aim of the thesis is to prepare different N doped a-C and corelate their electrochemical performance with structural, electronic and chemical properties.

In chapter III synthesis of a-C:N electrodes as well as the effects of different levels of nitrogen-incorporation on the properties of the a-C film is discussed. This included the investigation of the effects of gradual nitrogen incorporation into the graphitic scaffold and its effects on the electronic and capacitive properties. These electrochemical properties will be corelated with chemical, structural and valence electronic properties of a-C:N electrode.

Chapter IV explores the electrochemical capacitive properties of topographically smooth N doped and N free graphitized a-C. The effect of selective N-site incorporation could enhance the capacitive properties of a-C:N electrodes as a result of both surface chemical and electronic effects.

N incorporation into graphitised a-C using RF plasma system is presented in chapter V, where electrochemical capacitance study and oxygen reduction reaction (ORR) is discussed. These electrochemical properties are corelated to the chemical and structural properties of this materials. Finally results and conclusions of chapters III, IV and V are discussed along with possible future work.

1.8 References

1. Stephanie L.Candelariaa, Y., WeiZhouc,d, XiaolinLib, JieXiaob, Ji-Guang Zhangb, YongWangb, JunLiub,n, JinghongLic,d,nn, GuozhongCaoa Nanostructured carbon for energy storage and conversion. *Nano Energy* **2012,** *1* (2), 195–220.

2. Panagiotis Trogadas , T. F. F., Peter Strasser, Carbon as catalyst and support for electrochemical energy conversion. *CA R B O N* **2014,** *75* (4), 5-42.

3. Jiirgen 0. Besenhard, H. P. F., The electrochemistry of black carbons. *Angew. Chem. Int. Ed. Engl* **1983,** *22*, 950-975.

4. Elzbieta Frackowiak, F. B., Carbon materials for the electrochemical storage of energy in capacitors. *Carbon* **2001,** *39*, 937-950.

5. Wieckowski, A., *Interfacial Electrochemistry: Theory: Experiment, and Applications*. 1999; p 992.

6. HG, P. K., Processing of Graphene/CNT-Metal Powder. In *Powder Technology*, IntechOpen: 2018.

7. McCreery, R. L., *In Electroanalytical Chemistry*. Dekker: New York, 1991; Vol. 17.

8. Moore, A., In Chemistry and Physics of Carbon. Thrower, P. A., Ed. 1981; Vol. 17.

9. Matthews, M. J.; Pimenta, M. A.; Dresselhaus, G.; Dresselhaus, M. S.; Endo, M., Origin of dispersive effects of the Raman D band in carbon materials. *Physical Review B* **1999,** *59* (10), R6585-R6588.

10. Speck, J. S.; Steinbeck, J.; Dresselhaus, M. S., Microstructural studies of laser irradiated graphite surfaces. *Journal of Materials Research* **1990,** *5* (05), 980-988.

11. Al-Jishi, R.; Dresselhaus, G., Lattice-dynamical model for alkali-metal—graphite intercalation compounds. *Physical Review B* **1982,** *26* (8), 4523-4538.

12. McCreery, R. L., Advanced Carbon Electrode Materials for Molecular Electrochemistry. *Chem. Rev* **2008,** *108* (7), 2646-2687.

13. Xiong, D.; Li, X.; Shan, H.; Zhao, Y.; Dong, L.; Xu, H.; Zhang, X.; Li, D.; Sun, X., Oxygen-containing Functional Groups Enhancing Electrochemical Performance of Porous Reduced Graphene Oxide Cathode in Lithium Ion Batteries. *Electrochimica Acta* **2015,** *174*, 762-769.

14. Tojo, T.; Sakurai, K.; Muramatsu, H.; Hayashi, T.; Yang, K.-S.; Jung, Y. C.; Yang, C.-M.; Endo, M.; Kim, Y. A., Electrochemical role of oxygen containing functional groups on activated carbon electrode. *RSC Advances* **2014,** *4* (107), 62678-62683.

15. Kneten, K. R.; McCreery, R. L., Effects of redox system structure on electron-transfer kinetics at ordered graphite and glassy carbon electrodes. *Analytical Chemistry* **1992,** *64* (21), 2518-2524.

16. Jenkins;, G. M.; Kawamura;, K., *Polymeric Carbons ,Carbon Fibre, Glass and Char*. Cambridge University Press: England, 1976.

17. Gerischer, H.; McIntyre, R.; Scherson, D.; Storck, W., Density of the electronic states of graphite: derivation from differential capacitance measurements. *The Journal of Physical Chemistry* **1987,** *91* (7), 1930-1935.

18. McIntyre, R.; Scherson, D.; Storck, W.; Gerischer, H., Oxygen reduction at the basal plane of stress-annealed pyrolytic graphite in acetonitrile solutions. *Electrochimica Acta* **1987,** *32* (1), 51-53.

19. Smalley, R. E., Discovering the fullerenes. *Reviews of Modern Physics* **1997,** *69* (3), 723-730.

20. Ahmad, S., Carbon nanostructures fullerenes and carbon nanotubes. *IETE Technical Review* **1999,** *16* (3-4), 297-310.

21. Dresselhaus, M. S.; Dresselhaus, M. S.; Dresselhaus, G.; Dresselhaus, G.; Eklund, P. C.; Eklund, P. C., *Science of fullerenes and carbon nanotubes*. Academic Press: 1996.

22. Buseck, P. R.; Tsipursky, S. J.; Hettich, R., Fullerenes from the geological environment. *Science* **1992,** *257* (5067), 215-217.

23. Tohji, K.; Paul, A.; Moro, L.; Malhotra, R.; Lorents, D. C.; Ruoff, R. S., Selective and high-yield synthesis of higher fullerenes. *The Journal of Physical Chemistry* **1995,** *99* (50), 17785-17788.

24. Miller, N. C.; Cho, E.; Gysel, R.; Risko, C.; Coropceanu, V.; Miller, C. E.; Sweetnam, S.; Sellinger, A.; Heeney, M.; McCulloch, I.; Brédas, J.-L.; Toney, M. F.; McGehee, M. D.,Factors governing intercalation of fullerenes and other small molecules between the side chains of semiconducting polymers used in solar cells. *Advanced Energy Materials* **2012,** *2* (10), 1208-1217.

25. Diederich, F.; Whetten, R. L., Beyond C60: The higher fullerenes. *Accounts of Chemical Research* **1992,** *25* (3), 119-126.

26. Osterodt, J.; Zett, A.; Vögtle, F., Fullerenes by pyrolysis of hydrocarbons and synthesis of isomeric methanofullerenes. *Tetrahedron* **1996,** *52* (14), 4949-4962.

27. Donald, L. D. C., Deltahedral views of fullerene polymorphism. *Philosophical Transactions: Physical Sciences and Engineering* **1993,** *343* (1667), 133-144.

28. Bakry, R.; Vallant, R. M.; Najam-ul-Haq, M.; Rainer, M.; Szabo, Z.; Huck, C. W.; Bonn, G. K., Medicinal applications of fullerenes. *International journal of nanomedicine* **2007,** *2* (4), 639-649.

29. Xu, X.; Ray, R.; Gu, Y.; Ploehn, H. J.; Gearheart, L.; Raker, K.; Scrivens, W. A., Electrophoretic Analysis and Purification of Fluorescent Single-Walled Carbon Nanotube Fragments. *Journal of the American Chemical Society* **2004,** *126* (40), 12736-12737.

30. Chen, P.-C.; Chen, Y.-N.; Hsu, P.-C.; Shih, C.-C.; Chang, H.-T., Photoluminescent organosilane-functionalized carbon dots as temperature probes. *Chemical Communications* **2013,** *49* (16), 1639-1641.

31. Luo, P. G.; Sahu, S.; Yang, S.-T.; Sonkar, S. K.; Wang, J.; Wang, H.; LeCroy, G. E.; Cao, L.; Sun, Y.-P., Carbon “quantum” dots for optical bioimaging. *Journal of Materials Chemistry B* **2013,** *1* (16), 2116-2127.

32. Zhao, H. X.; Liu, L. Q.; Liu, Z. D.; Wang, Y.; Zhao, X. J.; Huang, C. Z., Highly selective detection of phosphate in very complicated matrixes with an off–on fluorescent probe of europium-adjusted carbon dots. *Chemical Communications* **2011,** *47* (9), 2604-2606.

33. Deng, Y.; Zhao, D.; Chen, X.; Wang, F.; Song, H.; Shen, D., Long lifetime pure organic phosphorescence based on water soluble carbon dots. *Chemical Communications* **2013,** *49* (51), 5751-5753.

34. Zhou, J.; Booker, C.; Li, R.; Zhou, X.; Sham, T.-K.; Sun, X.; Ding, Z., An electrochemical avenue to blue luminescent nanocrystals from multiwalled carbon nanotubes (MWCNTs). *Journal of the American Chemical Society* **2007,** *129* (4), 744-745.

35. Tian, L.; Ghosh, D.; Chen, W.; Pradhan, S.; Chang, X.; Chen, S., Nanosized carbon particles from natural gas soot. *Chemistry of Materials* **2009,** *21* (13), 2803-2809.

36. Zhu, H.; Wang, X.; Li, Y.; Wang, Z.; Yang, F.; Yang, X., Microwave synthesis of fluorescent carbon nanoparticles with electrochemiluminescence properties. *Chemical Communications* **2009,** (34), 5118-5120.

37. Wu, Z. L.; Gao, M. X.; Wang, T. T.; Wan, X. Y.; Zheng, L. L.; Huang, C. Z., A general quantitative pH sensor developed with dicyandiamide N-doped high quantum yield graphene quantum dots. *Nanoscale* **2014,** *6* (7), 3868-3874.

38. Lu, W.; Qin, X.; Liu, S.; Chang, G.; Zhang, Y.; Luo, Y.; Asiri, A. M.; Al-Youbi, A. O.; Sun, X., Economical, green synthesis of fluorescent carbon nanoparticles and their use as probes for sensitive and selective detection of mercury(ii) ions. *Analytical Chemistry* **2012,** *84* (12), 5351-5357.

39. Lai, C.-W.; Hsiao, Y.-H.; Peng, Y.-K.; Chou, P.-T., Facile synthesis of highly emissive carbon dots from pyrolysis of glycerol; gram scale production of carbon dots/mSiO2 for cell imaging and drug release. *Journal of Materials Chemistry* **2012,** *22* (29), 14403-14409.

40. Chowdhuri, A. R.; Singh, T.; Ghosh, S. K.; Sahu, S. K., Carbon dots embedded magnetic nanoparticles @chitosan @metal organic framework as a nanoprobe for ph sensitive targeted anticancer drug delivery. *ACS Applied Materials & Interfaces* **2016,** *8* (26), 16573-16583.

41. Kinoshita, K., *Carbon :* Electrochemical and physicochemical properties. Wiley: New York, 1988.

42. MATHER, P. J.; THOMAS, K. M., Carbon black/high density polyethylene conducting composite materials: Part II The relationship between the positive temperature coefficient and the volume resistivity. *Journal of Materials Science* **1997,** *32* (7), 1711-1715.

43. Chung, D. D. L., Electrical applications of carbon materials. *Journal of Materials Science* **2004,** *39* (8), 2645-2661.

44. Hindermann-Bischoff, M.; Ehrburger-Dolle, F., Electrical conductivity of carbon black–polyethylene composites: Experimental evidence of the change of cluster connectivity in the PTC effect. *Carbon* **2001,** *39* (3), 375-382.

45. Zhang, C.; Ma, C.-A.; Wang, P.; Sumita, M., Temperature dependence of electrical resistivity for carbon black filled ultra-high molecular weight polyethylene composites prepared by hot compaction. *Carbon* **2005,** *43* (12), 2544-2553.

46. Dowlapalli, M. R.; Atanassov, P.; Xie, J.; Rice, G., Electrochemical oxidation resistance of carbonaceous materials. *ECS Transactions* **2006,** *1* (8), 41-50.

47. González-García, P.; Centeno, T. A.; Urones-Garrote, E.; Ávila-Brande, D.; Otero-Díaz, L. C., Microstructure and surface properties of lignocellulosic-based activated carbons. *Applied Surface Science* **2013,** *265*, 731-737.

48. Simon, P.; Burke, A., Nanostructured carbons: double-layer capacitance and more. *The electrochemical society interface* **2008,** *17* (1), 38.

49. Dubey, R.; Guruviah, V., Review of carbon-based electrode materials for supercapacitor energy storage. *Ionics* **2019,** *25* (4), 1419-1445.

50. Wang, G.; Wang, H.; Lu, X.; Ling, Y.; Yu, M.; Zhai, T.; Tong, Y.; Li, Y., Solid-state supercapacitor based on activated carbon cloths exhibits excellent rate capability. *Advanced Materials* **2014,** *26* (17), 2676-2682.

51. Zhang, S.; Zheng, M.; Lin, Z.; Li, N.; Liu, Y.; Zhao, B.; Pang, H.; Cao, J.; He, P.; Shi, Y., Activated carbon with ultrahigh specific surface area synthesized from natural plant material for lithium–sulfur batteries. *Journal of Materials Chemistry A* **2014,** *2* (38), 15889-15896.

52. Endo, M.; Strano, M. S.; Ajayan, P. M., Potential applications of carbon nanotubes. in carbon nanotubes: advanced topics in the synthesis, structure, properties and applications, Jorio, A.; Dresselhaus, G.; Dresselhaus, M. S., Eds. Springer Berlin Heidelberg: Berlin, Heidelberg, 2008; pp 13-62.

53. Monthioux, M.; Kuznetsov, V. L., Who should be given the credit for the discovery of carbon nanotubes? *Carbon* **2006,** *44* (9), 1621-1623.

54. Qin, L.-C.; Zhao, X.; Hirahara, K.; Miyamoto, Y.; Ando, Y.; Iijima, S., The smallest carbon nanotube. *Nature* **2000,** *408*, 50.

55. Grobert, N., Carbon nanotubes – becoming clean. *Materials Today* **2007,** *10* (1), 28-35.

56. Iijima, S., Helical microtubules of graphitic carbon. *Nature* **1991,** *354* (6348), 56-58.

57. Iijima, S.; Ichihashi, T., Single-shell carbon nanotubes of 1-nm diameter. *Nature* **1993,** *363* (6430), 603-605.

58. Berber, S.; Kwon, Y.-K.; Tománek, D., Unusually high thermal conductivity of carbon nanotubes. *Physical Review Letters* **2000,** *84* (20), 4613-4616.

59. Georgakilas, V.; Perman, J. A.; Tucek, J.; Zboril, R., Broad family of carbon nanoallotropes: classification, chemistry, and applications of fullerenes, carbon dots, nanotubes, graphene, nanodiamonds, and combined superstructures. *Chemical Reviews* **2015,** *115* (11), 4744-4822.

60. Che, G.; Lakshmi, B. B.; Martin, C. R.; Fisher, E. R.; Ruoff, R. S., Chemical vapor deposition based synthesis of carbon nanotubes and nanofibers using a template method. *Chemistry of Materials* **1998,** *10* (1), 260-267.

61. Dumitrescu;, I.; Unwin;, P. R.; Macpherson, J. V., Electrochemistry at carbon nanotubes: perspective and issues. *Chemical Communications* **2009,** (45), 17.

62. Saito, R.; Fujita, M.; Dresselhaus, G.; Dresselhaus, M. S., Electronic structure of chiral graphene tubules. *Applied Physics Letters* **1992,** *60* (18), 2204-2206.

63. Wang, J., Carbon-nanotube based electrochemical biosensors: a review. *Electroanalysis* **2005,** *17* (1), 7-14.

64. Chou, A.; Böcking, T.; Singh, N. K.; Gooding, J. J., Demonstration of the importance of oxygenated species at the ends of carbon nanotubes for their favourable electrochemical properties. *Chemical Communications* **2005,** (7), 842-844.

65. Pumera, M.; míd, B.; etislav; Veltruská, K.; ina, Influence of nitric acid treatment of carbon nanotubes on their physico-chemical properties. *Journal of Nanoscience and Nanotechnology* **2009,** *9* (4), 2671-2676.

66. Pumera, M., The electrochemistry of carbon nanotubes: fundamentals and applications. *Chemistry – A European Journal* **2009,** *15* (20), 4970-4978.

67. Maldonado, S.; Stevenson, K. J., Direct preparation of carbon nanofiber electrodes via pyrolysis of iron(ii) phthalocyanine: electrocatalytic aspects for oxygen reduction. *The Journal of Physical Chemistry B* **2004,** *108* (31), 11375-11383.

68. Gong, K.; Du, F.; Xia, Z.; Durstock, M.; Dai, L., nitrogen-doped carbon nanotube arrays with high electrocatalytic activity for oxygen reduction. *Science* **2009,** *323* (5915), 760-764.

69. Inagaki, M.; Yang, Y.; Kang, F., Carbon nanofibers prepared via electrospinning. *Advanced Materials* **2012,** *24* (19), 2547-2566.

70. Maldonado, S.; Stevenson, K. J., Influence of nitrogen doping on oxygen reduction electrocatalysis at carbon nanofiber electrodes. *The Journal of Physical Chemistry B* **2005,** *109* (10), 4707-4716.

71. Allen, M. J.; Tung, V. C.; Kaner, R. B., Honeycomb carbon: a review of graphene. *Chemical Reviews* **2010,** *110* (1), 132-145.

72. Terrones, M.; Botello-Méndez, A. R.; Campos-Delgado, J.; López-Urías, F.; Vega-Cantú, Y. I.; Rodríguez-Macías, F. J.; Elías, A. L.; Muñoz-Sandoval, E.; Cano-Márquez, A. G.; Charlier, J.-C.; Terrones, H., Graphene and graphite nanoribbons: Morphology, properties, synthesis, defects and applications. *Nano Today* **2010,** *5* (4), 351-372.

73. Stankovich, S.; Dikin, D. A.; Dommett, G. H. B.; Kohlhaas, K. M.; Zimney, E. J.; Stach, E. A.; Piner, R. D.; Nguyen, S. T.; Ruoff, R. S., Graphene-based composite materials. *Nature* **2006,** *442*, 282.

74. Stankovich, S.; Dikin, D. A.; Piner, R. D.; Kohlhaas, K. A.; Kleinhammes, A.; Jia, Y.; Wu, Y.; Nguyen, S. T.; Ruoff, R. S., Synthesis of graphene-based nanosheets via chemical reduction of exfoliated graphite oxide. *Carbon* **2007,** *45* (7), 1558-1565.

75. Jung, I.; Dikin, D. A.; Piner, R. D.; Ruoff, R. S., Tunable electrical conductivity of individual graphene oxide sheets reduced at “low” temperatures. *Nano Letters* **2008,** *8* (12), 4283-4287.

76. Jeong, H.-K.; Lee, Y. P.; Lahaye, R. J. W. E.; Park, M.-H.; An, K. H.; Kim, I. J.; Yang, C.-W.; Park, C. Y.; Ruoff, R. S.; Lee, Y. H., Evidence of graphitic ab stacking order of graphite oxides. *Journal of the American Chemical Society* **2008,** *130* (4), 1362-1366.

77. Hummers, W. S.; Offeman, R. E., Preparation of graphitic oxide. *Journal of the American Chemical Society* **1958,** *80* (6), 1339-1339.

78. Sordan, R.; Traversi, F.; Russo, V., Logic gates with a single graphene transistor. *Applied Physics Letters* **2009,** *94* (7), 073305.

79. Meyer, J. C.; Girit, C. O.; Crommie, M. F.; Zettl, A., Imaging and dynamics of light atoms and molecules on graphene. *Nature* **2008,** *454*, 319.

80. Stoller, M. D.; Park, S.; Zhu, Y.; An, J.; Ruoff, R. S., Graphene-based ultracapacitors. *Nano Letters* **2008,** *8* (10), 3498-3502.

81. Zhang, L. L.; Zhou, R.; Zhao, X. S., Graphene-based materials as supercapacitor electrodes. *Journal of Materials Chemistry* **2010,** *20* (29), 5983-5992.

82. Huang, X.; Qi, X.; Boey, F.; Zhang, H., Graphene-based composites. *Chemical Society Reviews* **2012,** *41* (2), 666-686.

83. Liu, G.; Jin, W.; Xu, N., Graphene-based membranes. *Chemical Society Reviews* **2015,** *44* (15), 5016-5030.

84. Cho, E.-C.; Huang, J.-H.; Li, C.-P.; Chang-Jian, C.-W.; Lee, K.-C.; Hsiao, Y.-S.; Huang, J.-H., Graphene-based thermoplastic composites and their application for LED thermal management. *Carbon* **2016,** *102*, 66-73.

85. Qu, L.; Liu, Y.; Baek, J.-B.; Dai, L., Nitrogen-doped graphene as efficient metal-free electrocatalyst for oxygen reduction in fuel cells. *ACS Nano* **2010,** *4* (3), 1321-1326.

86. Xiang, Q.; Liu, Y.; Zou, X.; Hu, B.; Qiang, Y.; Yu, D.; Yin, W.; Chen, C., Hydrothermal synthesis of a new kind of n-doped graphene gel-like hybrid as an enhanced orr electrocatalyst. *ACS Applied Materials & Interfaces* **2018,** *10* (13), 10842-10850.

87. Gao, X.; Wang, L.; Ma, J.; Wang, Y.; Zhang, J., Facile preparation of nitrogen-doped graphene as an efficient oxygen reduction electrocatalyst. *Inorganic Chemistry Frontiers* **2017,** *4* (9), 1582-1590.

88. Wang, L.; Yin, F.; Yao, C., N-doped graphene as a bifunctional electrocatalyst for oxygen reduction and oxygen evolution reactions in an alkaline electrolyte. *International Journal of Hydrogen Energy* **2014,** *39* (28), 15913-15919.

89. Reddy, A. L. M.; Srivastava, A.; Gowda, S. R.; Gullapalli, H.; Dubey, M.; Ajayan, P. M., Synthesis of nitrogen-doped graphene films for lithium battery application. *ACS Nano* **2010,** *4* (11), 6337-6342.

90. Bachmann, P. K.; Messier, R., Advances in material sciences are paving the way for use of synthetic diamond. *Chem. Eng. News* **1989,** *67* (20), 24-37.

91. Ramesham, R.; Roppel, T.; Ellis, C.; Jaworske, D. A.; Baugh, W., Erratum: "Selective and low temperature synthesis of polycrystalline diamond" [J. Mater. Res. 6, 1278 (1991)]. *Journal of Materials Research* **2011,** *6* (9), 2013-2013.

92. Swain, G. M.; Ramesham, R., The electrochemical activity of boron-doped polycrystalline diamond thin film electrodes. *Analytical Chemistry* **1993,** *65* (4), 345-351.

93. Ken, O.; Hidetoshi, N.; Yukio, A.; Tateki, K.; Masamori, I.; Yoichi, H., Synthesis of Diamond Thin Films Having Semiconductive Properties. *Japanese Journal of Applied Physics* **1988,** *27* (2A), L173.

94. Holze , R., A.J. Bard, I. Rubinstein (eds): Electroanalytical chemistry, vol 22. *Journal of Solid State Electrochemistry* **2005,** *9* (4), 236-237.

95. Zhang, Q.; Liu, Y.; Chen, S.; Quan, X.; Yu, H., Nitrogen-doped diamond electrode shows high performance for electrochemical reduction of nitrobenzene. *Journal of Hazardous Materials* **2014,** *265*, 185-190.

96. Ristein, J.; Riedel, M.; Stammler, M.; Mantel, B. F.; Ley, L., Surface conductivity of nitrogen-doped diamond. *Diamond and Related Materials* **2002,** *11* (3), 359-364.

97. Eaton, S. C.; Anderson, A. B.; Angus, J. C.; Evstefeeva, Y. E.; Pleskov, Y. V., Co-Doping of Diamond with Boron and Sulfur. *Electrochemical and Solid-State Letters* **2002,** *5* (8), G65-G68.

98. Haenni, W.; Rychen, P.; Fryda, M.; Comninellis, C., Chapter 5 Industrial applications of diamond electrodes. In *Semiconductors and Semimetals*, Nebel, C. E.; Ristein, J., Eds. Elsevier: 2004; Vol. 77, pp 149-196.

99. Iwaki, M.; Sato, S.; Takahashi, K.; Sakairi, H., Electrical conductivity of nitrogen and argon implanted diamond. *Nuclear Instruments and Methods in Physics Research* **1983,** *209*, 1129-1133.

100. Pelskov, Y. V.; Sakharova, A. Y.; Krotova, M. D.; Bouilov, L. L.; Spitsyn, B. V., Photoelectrochemical properties of semiconductor diamond. *Journal of Electroanalytical Chemistry and Interfacial Electrochemistry* **1987,** *228* (1), 19-27.

101. Yano, T.; Tryk, D. A.; Hashimoto, K.; Fujishima, A., Electrochemical behavior of highly conductive boron - doped diamond electrodes for oxygen reduction in alkaline solution. *Journal of The Electrochemical Society* **1998,** *145* (6), 1870-1876.

102. Ivandini, T. A.; Sato, R.; Makide, Y.; Fujishima, A.; Einaga, Y., Pt-implanted boron-doped diamond electrodes and the application for electrochemical detection of hydrogen peroxide. *Diamond and Related Materials* **2005,** *14* (11-12), 2133-2138.

103. Siné, G.; Duo, I.; Roustom, B. E.; Fóti, G.; Comninellis, C., Deposition of clusters and nanoparticles onto boron-doped diamond electrodes for electrocatalysis. *Journal of Applied Electrochemistry* **2006,** *36* (8), 847-862.

104. Tsuyoshi, O.; Kazuki, A.; Chiaki, T.; Akira, F., Electrochemical reduction of ozone dissolved in perchloric acid solutions at boron-doped diamond electrodes. *Chemistry Letters* **2006,** *35* (9), 1018-1019.

105. Elinson, V. M.; Sleptsov, V. V.; Laymin, A. N.; Potraysay, V. V.; Kostuychenko, L. N.; Moussina, A. D., Barrier properties of carbon films deposited on polymer-based devices in aggressive environments. *Diamond and Related Materials* **1999,** *8* (12), 2103-2109.

106. Hao Wang, M.-R. S., Zhao-Yuan Ning, Chao Ye and He-Sun Zhu, Pulsed electrodeposition of diamond-like carbon films. *Journal of Materials Research* **1997,** *12*, 3102-3105.

107. Mehta, B. R.; Ogryzlo, E. A., Room-temperature deposition of diamond-like carbon films by the microwave plasma jet method. *Diamond and Related Materials* **1994,** *3* (1), 10-13.

108. Beghi, M. G.; Ferrari, A. C.; Teo, K. B. K.; Robertson, J.; Bottani, C. E.; Libassi, A.; Tanner, B. K., Bonding and mechanical properties of ultrathin diamond-like carbon films. *Applied Physics Letters* **2002,** *81* (20), 3804-3806.

109. Zhang, P.; Tay, B. K.; Sun, C. Q.; Lau, S. P., Microstructure and mechanical properties of nanocomposite amorphous carbon films. *Journal of Vacuum Science & Technology A* **2002,** *20* (4), 1390-1394.

110. Gangopadhyay, A., Mechanical and tribological properties of amorphous carbon films. *Tribology Letters* **1998,** *5* (1), 25-39.

111. Bhushan, B.; Kellock, A. J.; Cho, N.-H.; Ager, J. W., Characterization of chemical bonding and physical characteristics of diamond-like amorphous carbon and diamond films. *Journal of Materials Research* **1992,** *7* (02), 404-410.

112. Vojs, M.; Zdravecká, E.; Marton, M.; Boháč, P.; Franta, L.; Veselý, M., Properties of amorphous carbon layers for bio-tribological applications. *Microelectronics Journal* **2009,** *40* (3), 650-653.

113. Oliver, W. C.; Pharr, G. M., An improved technique for determining hardness and elastic modulus using load and displacement sensing indentation experiments. *Journal of Materials Research* **2011,** *7* (6), 1564-1583.

114. Kerwin, D. B.; Spain, I. L.; Robinson, R. S.; Daudin, B.; Dubus, M.; Fontenille, J., Properties of amorphous carbon films deposited by ion beam methods. *Thin Solid Films* **1987,** *148* (3), 311-321.

115. Schröer, A.; Ensinger, W.; Frech, G.; Wolf, G. K., The properties of amorphous carbon films obtained by ion-beam-assisted carbon evaporation. *Surface and Coatings Technology* **1991,** *47* (1), 418-425.

116. Marques, F. C.; Lacerda, R. G., Hardness and stress of amorphous carbon films deposited by glow discharge and ion beam assisting deposition. *Brazilian Journal of Physics* **2000,** *30*, 527-532.

117. Park, Y. S.; Myung, H. S.; Han, J. G.; Hong, B., Tribological properties of amorphous carbon thin films grown by magnetron sputtering method. *Surface and Coatings Technology* **2004,** *180–181*, 218-221.

118. Park, Y. S.; Hong, B., Characteristics of sputtered amorphous carbon films prepared by a closed-field unbalanced magnetron sputtering method. *Journal of Non-Crystalline Solids* **2008,** *354* (52–54), 5504-5508.

119. Wyon, C.; Gillet, R.; Lombard, L., Properties of amorphous carbon films produced by magnetron sputtering. *Thin Solid Films* **1984,** *122* (3), 203-216.

120. Javeed, S.; Yamin, S.; Janjua, S. A.; Yaqub, K.; Ashraf, A.; Zeeshan, S.; Mehmood, M.; Anwar-ul-Haq, M.; Ahmad, S., Amorphous carbon films in direct current magnetron sputtering from regenerative sooting discharge. *Vacuum* **2011,** *86* (2), 193-200.

121. Ma, B.; Yu, Q., Hot-filament chemical vapor deposition of amorphous carbon film on diamond grits and induction brazing of the diamond grits. *Applied Surface Science* **2012,** *258* (10), 4750-4755.

122. Nagasawa, H.; Kanezashi, M.; Yoshioka, T.; Tsuru, T., Plasma-enhanced chemical vapor deposition of amorphous carbon molecular sieve membranes for gas separation. *RSC Advances* **2016,** *6* (64), 59045-59049.

123. Hukka, T. I.; Zhang, J., Photoinduced chemical vapor deposition of amorphous carbon films from chloromethane using a vuv laser (157 nm). *The Journal of Physical Chemistry B* **2000,** *104* (30), 7115-7123.

124. Kim, D.-S.; Kang, T.-W., Deposition of amorphous carbon thin films by pulsed rf plasma CVD. *Journal Of Chemical Engineering Of Japan* **2005,** *38* (8), 593-599.

125. Cremona, M.; Reyes, R.; Achete, C. A.; Távora Britto, R.; Camargo Jr, S. S., Amorphous carbon nitride thin films as electron injection layer in organic LEDs. *Thin Solid Films* **2004,** *447–448*, 74-79.

126. Morrison, S. R., E*electrochemistry at semiconductor and oxidized metal electrodes*. 1 ed.; Plenum Press: New York, 1980.

127. Robertson, J., Diamond-like amorphous carbon. *Materials Science and Engineering: R: Reports* **2002,** *37* (4–6), 129-281.

128. Jacob, W.; Möller, W., On the structure of thin hydrocarbon films. *Applied Physics Letters* **1993,** *63* (13), 1771-1773.

129. J. E. Field (ed.). The properties of natural and synthetic diamond. Academic Press, London 1992. £ 90.00. ISBN 0-12-255352-7. *Crystal Research and Technology* **1993,** *28* (5), 602-602.

130. Cahn, R. W., Physics of graphite: B.T. Kelly (Applied Science Publishers, London, 1981) pp. 477. price: £48. *Journal of Nuclear Materials* **1983,** *114* (1), 116.

131. Robertson, J., Amorphous carbon. *Advances in Physics* **1986,** *35* (4), 317-374.

132. Pharr, G. M.; Callahan, D. L.; McAdams, S. D.; Tsui, T. Y.; Anders, S.; Anders, A.; III, J. W. A.; Brown, I. G.; Bhatia, C. S.; Silva, S. R. P.; Robertson, J., Hardness, elastic modulus, and structure of very hard carbon films produced by cathodic-arc deposition with substrate pulse biasing. *Applied Physics Letters* **1996,** *68* (6), 779-781.

133. Koidl, P.; Wild, C.; Dischler, B.; Wagner, J.; Ramsteiner, M., Plasma deposition, properties and structure of amorphous hydrogenated carbon films. *Materials Science Forum* **1991,** *52-53*, 41-70.

134. McKenzie, D. R., Tetrahedral bonding in amorphous carbon. *Reports on Progress in Physics* **1996,** *59* (12), 1611.

135. Fallon, P. J.; Veerasamy, V. S.; Davis, C. A.; Robertson, J.; Amaratunga, G. A.; Milne, W. I.; Koskinen, J., Properties of filtered-ion-beam-deposited diamondlike carbon as a function of ion energy. *Physical review. B, Condensed matter* **1993,** *48* (7), 4777-4782.

136. Weiler, M.; Sattel, S.; Jung, K.; Ehrhardt, H.; Veerasamy, V. S.; Robertson, J., Highly tetrahedral, diamond-like amorphous hydrogenated carbon prepared from a plasma beam source. *Applied Physics Letters* **1994,** *64* (21), 2797-2799.

137. Robertson, J., Hard amorphous (diamond-like) carbons. *Progress in Solid State Chemistry* **1991,** *21* (4), 199-333.

138. Robertson, J., Properties of diamond-like carbon. *Surface and Coatings Technology* **1992,** *50* (3), 185-203.

139. Lifshitz, Y., Hydrogen-free amorphous carbon films: Correlation between growth conditions and properties. *Diamond and Related Materials* **1996,** *5* (3-5), 388-400.

140. Zeng, A.; Neto, V. F.; Gracio, J. J.; Fan, Q. H., Diamond-like carbon (DLC) films as electrochemical electrodes. *Diamond and Related Materials* **2014,** *43*, 12-22.

141. Moon, J.-M.; Park, S.; Lee, Y.-K.; Sook Bang, G.; Hong, Y.-K.; Park, C.; Cheol Jeon, I., Diamond-like carbon electrodes in electrochemical microgravimetry. *Journal of Electroanalytical Chemistry* **1999,** *464* (2), 230-237.

142. Menegazzo, N.; Kahn, M.; Berghauser, R.; Waldhauser, W.; Mizaikoff, B., Nitrogen-doped diamond-like carbon as optically transparent electrode for infrared attenuated total reflection spectroelectrochemistry. *Analyst* **2011,** *136* (9), 1831-1839.

143. Tamiasso-Martinhon, P.; Cachet, H.; Deslouis, C.; Vivier, V., Amorphous carbon nitride a-CNx microelectrode: Fabrication and characterization. *Electrochemistry Communications* **2010,** *12* (8), 1074-1076.

144. Honda, K.; Yoshimatsu, M.; Kuriyama, K.; Kuwabara, R.; Naragino, H.; Yoshinaga, K.; Kondo, T.; Fujishima, A., Electrically-switchable, permselective membranes prepared from nano-structured N-doped DLC. *Diamond and Related Materials* **2011,** *20* (8), 1110-1120.

145. Kim, J.-I.; Bordeanu, A.; Pyun, J.-C., Diamond-like carbon (DLC) microelectrode for electrochemical ELISA. *Biosensors and Bioelectronics* **2009,** *24* (5), 1394-1398.

146. Lu, Z. G.; Chung, C. Y., Electrochemical characterization of diamond like carbon thin films. *Diamond and Related Materials* **2008,** *17* (11), 1871-1876.

147. Judai;, K.; Iguchi;, N.; Hatakeyama;, Y., Low-temperature production of genuinely amorphous carbon from highly reactive nanoacetylide precursors. *Journal of Chemistry* **2016,** *2016*, 6.

148. Numao, S.; Judai, K.; Nishijo, J.; Mizuuchi, K.; Nishi, N., Synthesis and characterization of mesoporous carbon nano-dendrites with graphitic ultra-thin walls and their application to supercapacitor electrodes. *Carbon* **2009,** *47* (1), 306-312.

149. Kavan, L., Electrochemical Carbon. *Chemical Reviews* **1997,** *97* (8), 3061-3082.

150. Judai, K.; Numao, S.; Nishijo, J.; Nishi, N., In situ preparation and catalytic activation of copper nanoparticles from acetylide molecules. *Journal of Molecular Catalysis A: Chemical* **2011,** *347* (1–2), 28-33.

151. Jayasundara, D. R.; Cullen, R. J.; Colavita, P. E., In situ and real time characterization of spontaneous grafting of aryldiazonium salts at carbon surfaces. *Chemistry of Materials* **2013,** *25* (7), 1144-1152.

152. Cullen, R. J.; Jayasundara, D. R.; Soldi, L.; Cheng, J. J.; Dufaure, G.; Colavita, P. E., Spontaneous grafting of nitrophenyl groups on amorphous carbon thin films: a structure–reactivity investigation. *Chemistry of Materials* **2012,** *24* (6), 1031-1040.

153. Murphy, D. M.; Cullen, R. J.; Jayasundara, D. R.; Doyle, R. L.; Lyons, M. E.; Colavita, P. E., Heterogeneous charge transfer at the amorphous carbon/solution interface: effect on the spontaneous attachment of aryldiazonium salts. *The Journal of Physical Chemistry C* **2013,** *117* (44), 22768-22777.

154. Murphy, D. M.; Cullen, R. J.; Jayasundara, D. R.; Scanlan, E. M.; Colavita, P. E., Study of the spontaneous attachment of polycyclic aryldiazonium salts onto amorphous carbon substrates. *RSC Advances* **2012,** *2* (16), 6527-6534.

155. Tang, Y.; Allen, B. L.; Kauffman, D. R.; Star, A., Electrocatalytic activity of nitrogen-doped carbon nanotube cups. *Journal of the American Chemical Society* **2009,** *131* (37), 13200-13201.

156. Liu, R.; Wu, D.; Feng, X.; Mullen, K., Nitrogen-doped ordered mesoporous graphitic arrays with high electrocatalytic activity for oxygen reduction. *Angew Chem Int Ed Engl* **2010,** *49* (14), 2565-9.

157. Lefèvre, M.; Proietti, E.; Jaouen, F.; Dodelet, J.-P., Iron-Based Catalysts with Improved Oxygen Reduction Activity in Polymer Electrolyte Fuel Cells. *Science* **2009,** *324* (5923), 71-74.

158. LIU, A. Y.; COHEN, M. L., Prediction of New Low Compressibility Solids. *Science* **1989,** *245* (4920), 841-842.

159. Latil, S.; Roche, S.; Mayou, D.; Charlier, J.-C., Mesoscopic Transport in Chemically Doped Carbon Nanotubes. *Physical Review Letters* **2004,** *92* (25), 256805.

160. Maiti, U. N.; Lee, W. J.; Lee, J. M.; Oh, Y.; Kim, J. Y.; Kim, J. E.; Shim, J.; Han, T. H.; Kim, S. O., Carbon: 25th Anniversary Article: Chemically Modified/Doped Carbon Nanotubes & Graphene for Optimized Nanostructures & Nanodevices (Adv. Mater. 1/2014). *Advanced Materials* **2014,** *26* (1), 2-2.

161. Sun, C.-L.; Pao, C.-W.; Tsai, H.-M.; Chiou, J.-W.; Ray, S. C.; Wang, H.-W.; Hayashi, M.; Chen, L.-C.; Lin, H.-J.; Lee, J.-F.; Chang, L.; Tsai, M.-H.; Chen, K.-H.; Pong,

W.-F., Atomistic nucleation sites of Pt nanoparticles on N-doped carbon nanotubes. *Nanoscale* **2013,** *5* (15), 6812-6818.

162. Lee, W. J.; Maiti, U. N.; Lee, J. M.; Lim, J.; Han, T. H.; Kim, S. O., Nitrogen-doped carbon nanotubes and graphene composite structures for energy and catalytic applications. *Chemical Communications* **2014,** *50* (52), 6818-6830.

163. Ray, S. C.; Mbiombi, W.; Papakonstantinou, P., Electrical and electronic properties of nitrogen doped amorphous carbon (a-CNx) thin films. *Current Applied Physics* **2014,** *14* (12), 1845-1848.

164. Zhou, K.; Ke, P.; Li, X.; Zou, Y.; Wang, A., Microstructure and electrochemical properties of nitrogen-doped DLC films deposited by PECVD technique. *Applied Surface Science* **2015,** *329*, 281-286.

165. Li, J. J.; Zheng, W. T.; Wu, H. H.; Sun, L.; Gu, G. G.; Bian, H. J.; Lu, X. Y.; Jin, Z. S., Compositional and structural modifications of amorphous carbon nitride films induced by thermal annealing. *Journal of Physics D: Applied Physics* **2003,** *36* (16), 2001.

166. Durand-Drouhin, O.; Benlahsen, M.; Clin, M.; Bouzerar, R., Deposition mechanism of sputtered amorphous carbon nitride thin film. *Applied Surface Science* **2004,** *223* (4), 269-274.

167. Jiang, L.; Fitzgerald, A. G.; Rose, M. J., The effect of postdeposition annealing on chemical bonding in amorphous carbon nitride films prepared by dc magnetron sputtering. *Applied Surface Science* **2001,** *181* (3–4), 331-338.

168. Oh, H.; Cho, K.; Kim, S., Effect of deposition pressure on the electrical properties of nitrogen-doped amorphous carbon films. *Journal of the Korean Physical Society* **2015,** *67* (4), 638-642.

169. Shi, X.; Fu, H.; Shi, J. R.; Cheah, L. K.; Tay, B. K.; Hui, P., Electronic transport properties of nitrogen doped amorphous carbon films deposited by the filtered cathodic vacuum arc technique. *Journal of Physics: Condensed Matter* **1998,** *10* (41), 9293.

170. Fadzilah, A. N.; Rusop, M. In effect of nitrogen doping on electrical properties of amorphous carbon thin film prepared by aerosol-assisted thermal CVD, Industrial Electronics and Applications (ISIEA), 2011 IEEE Symposium on, 25-28 Sept. 2011; 2011; pp 431-435.

171. Matter, P. H.; Zhang, L.; Ozkan, U. S., The role of nanostructure in nitrogen-containing carbon catalysts for the oxygen reduction reaction. *Journal of Catalysis* **2006,** *239* (1), 83-96.

172. Matter, P. H.; Wang, E.; Arias, M.; Biddinger, E. J.; Ozkan, U. S., Oxygen reduction reaction activity and surface properties of nanostructured nitrogen-containing carbon. *Journal of Molecular Catalysis A: Chemical* **2007,** *264* (1–2), 73-81.

173. Kamata, T.; Kato, D.; Hirono, S.; Niwa, O., Structure and electrochemical performance of nitrogen-doped carbon film formed by electron cyclotron resonance sputtering. *Anal Chem* **2013,** *85* (20), 9845-51.

174. Yang, X.; Haubold, L.; DeVivo, G.; Swain, G. M., Electroanalytical performance of nitrogen-containing tetrahedral amorphous carbon thin-film electrodes. *Anal Chem* **2012,** *84* (14), 6240-8.

175. Yoo;, K.; Miller;, B.; Kalish;, R.; Shi;, X., Electrodes of nitrogen - incorporated tetrahedral amorphous carbon a novel thin - film electrocatalytic material with diamond - like stability. *Electrochemical and Solid-State Letters* **1999,** *2* (5), 3.

176. Robertson, J.; Davis, C. A., Diamond Films '94Nitrogen doping of tetrahedral amorphous carbon. *Diamond and Related Materials* **1995,** *4* (4), 441-444.

177. Omer, A. M. M.; Rusop, M.; Adhikari, S.; Adhikary, S.; Uchida, H.; Umeno, M., Photovoltaic characteristics of nitrogen-doped amorphous carbon thin-films grown on quartz and flexible plastic substrates by microwave surface wave plasma CVD. *Diamond and Related Materials* **2005,** *14* (3), 1084-1088.

178. Scholz, F., *Electroanalytical methods :guide to experiments and applications*. Second, Revised and Extended ed.; Springer Heidelberg Dordrech: London New York, 2010.

179. Srinivasan, S., Fuel cells from fundamentals to applications. 2006.

180. Simon, P.; Gogotsi, Y., Materials for electrochemical capacitors. *Nature Materials* **2008,** *7*, 845.

181. Raymundo-Piñero, E.; Kierzek, K.; Machnikowski, J.; Béguin, F., Relationship between the nanoporous texture of activated carbons and their capacitance properties in different electrolytes. *Carbon* **2006,** *44* (12), 2498-2507.

182. Pan, Z. Z.; Nishihara, H.; Iwamura, S.; Sekiguchi, T.; Sato, A.; Isogai, A.; Kang, F.; Kyotani, T.; Yang, Q. H., Cellulose Nanofiber as a Distinct Structure-Directing Agent for Xylem-like Microhoneycomb Monoliths by Unidirectional Freeze-Drying. *ACS Nano* **2016,** *10* (12), 10689-10697.

183. Lee, G.; Lee, C.; Yoon, C.-M.; Kim, M.; Jang, J., High-Performance Three-Dimensional Mesoporous Graphene Electrode for Supercapacitors using Lyophilization and Plasma Reduction. *ACS Applied Materials & Interfaces* **2017,** *9* (6), 5222-5230.

184. Chen, Y.; Yan, Q.; Zhang, S.; Lu, L.; Xie, B.; Xie, T.; Zhang, Y.; Wu, Y.; Zhang, Y.; Liu, D., Buffering agents-assisted synthesis of nitrogen-doped graphene with oxygen-rich functional groups for enhanced electrochemical performance. *Journal of Power Sources* **2016,** *333*, 125-133.

185. Hu, C.-C.; Chang, K.-H.; Lin, M.-C.; Wu, Y.-T., Design and tailoring of the nanotubular arrayed architecture of hydrous Ruo_2 for next generation supercapacitors. *Nano Letters* **2006,** *6* (12), 2690-2695.

186. Chen, S.; Zhu, J.; Wang, X., From graphene to metal oxide nanolamellas: a phenomenon of morphology transmission. *ACS Nano* **2010,** *4* (10), 6212-8.

187. Rakhi, R. B.; Chen, W.; Cha, D.; Alshareef, H. N., Substrate dependent self-organization of mesoporous cobalt oxide nanowires with remarkable pseudocapacitance. *Nano Letters* **2012,** *12* (5), 2559-2567.

188. Wang, L.; Yu, J.; Dong, X.; Li, X.; Xie, Y.; Chen, S.; Li, P.; Hou, H.; Song, Y., Three-dimensional macroporous carbon/fe3o4-doped porous carbon nanorods for high-performance supercapacitor. *ACS Sustainable Chemistry & Engineering* **2016,** *4* (3), 1531-1537.

189. He, Y.; Huang, L.; Cai, J.-S.; Zheng, X.-M.; Sun, S.-G., Structure and electrochemical performance of nanostructured Fe3O4/carbon nanotube composites as anodes for lithium ion batteries. *Electrochimica Acta* **2010,** *55* (3), 1140-1144.

190. Jian, Z.; Liu, P.; Li, F.; He, P.; Guo, X.; Chen, M.; Zhou, H., Core–Shell-Structured CNT@RuO_2 Composite as a High-Performance Cathode Catalyst for Rechargeable Li–O2 Batteries. *Angewandte Chemie International Edition* **2014,** *53* (2), 442-446.

191. Kim, S.-W.; Ryu, J.; Park, C. B.; Kang, K., Carbon nanotube-amorphous FePO4 core-shell nanowires as cathode material for Li ion batteries. *Chemical communications (Cambridge, England)* **2010,** *46* (39), 7409-7411.

192. Wu, Z.-S.; Ren, W.; Xu, L.; Li, F.; Cheng, H.-M., Doped graphene sheets as anode materials with superhigh rate and large capacity for lithium ion batteries. *ACS Nano* **2011,** *5* (7), 5463-5471.

193. He, Y.; Li, A.; Dong, C.; Li, C.; Xu, L., Mesoporous tin-based oxide nanospheres/reduced graphene composites as advanced anodes for lithium-ion half/full cells and sodium-ion batteries. *Chemistry* **2017,** *23* (55), 13724-13733.

194. Schmidt, T. J.; Paulus, U. A.; Gasteiger, H. A.; Behm, R. J., The oxygen reduction reaction on a Pt/carbon fuel cell catalyst in the presence of chloride anions. *Journal of Electroanalytical Chemistry* **2001,** *508* (1), 41-47.

195. Hansen, H. A.; Viswanathan, V.; Nørskov, J. K., Unifying Kinetic and Thermodynamic Analysis of 2 e– and 4 e– Reduction of Oxygen on Metal Surfaces. *The Journal of Physical Chemistry C* **2014,** *118* (13), 6706-6718.

196. Stacy, J.; Regmi, Y. N.; Leonard, B.; Fan, M., The recent progress and future of oxygen reduction reaction catalysis: A review. *Renewable and Sustainable Energy Reviews* **2017,** *69*, 401-414.

197. Song, C.; Zhang, J., Electrocatalytic oxygen reduction reaction. in *pem fuel cell electrocatalysts and catalyst layers: Fundamentals and applications*, Zhang, J., Ed. Springer London: London, 2008; pp 89-134.

198. Wu, G.; Zelenay, P., Nanostructured nonprecious metal catalysts for oxygen reduction reaction. *Accounts of Chemical Research* **2013,** *46* (8), 1878-1889.

199. Xu, J.; Shi, L.; Liang, C.; Wu, H.; Lei, J.; Liu, D.; Qu, D.; Xie, Z.; Li, J.; Tang, H., Fe and N co-doped carbons derived from an ionic liquid as active bifunctional oxygen catalysts. *ChemElectroChem* **2017,** *4* (5), 1148-1153.

200. Wang, X.; Zhang, P.; Wang, W.; Lei, X.; Yang, H., Magnetic n-enriched fe3c/graphitic carbon instead of pt as an electrocatalyst for the oxygen reduction reaction. *Chemistry – A European Journal* **2016,** *22* (14), 4863-4869.

201. Lu, B.; Smart, T. J.; Qin, D.; Lu, J. E.; Wang, N.; Chen, L.; Peng, Y.; Ping, Y.; Chen, S., Nitrogen and iron-codoped carbon hollow nanotubules as high-performance catalysts toward oxygen reduction reaction: a combined experimental and theoretical study. *Chemistry of Materials* **2017,** *29* (13), 5617-5628.

202. Singh, D.; Mamtani, K.; Bruening, C. R.; Miller, J. T.; Ozkan, U. S., use of H_2S to probe the active sites in fenc catalysts for the oxygen reduction reaction (ORR) in acidic media. *ACS Catalysis* **2014,** *4* (10), 3454-3462.

203. Wu, K.-H.; Liu, Y.; Luo, J.; Wang, B.; Xu, J.; Pham-Huu, C.; Su, D., The coulombic nature of active nitrogen sites in n-doped nanodiamond revealed in situ by ionic surfactants. *ACS Catalysis* **2017,** *7* (5), 3295-3300.

204. Li, J.; Alsudairi, A.; Ma, Z.-F.; Mukerjee, S.; Jia, Q., Asymmetric volcano trend in oxygen reduction activity of pt and non-pt catalysts: in situ identification of the site-blocking effect. *Journal of the American Chemical Society* **2017,** *139* (4), 1384-1387.

205. Serov, A.; Artyushkova, K.; Niangar, E.; Wang, C.; Dale, N.; Jaouen, F.; Sougrati, M.-T.; Jia, Q.; Mukerjee, S.; Atanassov, P., Nano-structured non-platinum catalysts for automotive fuel cell application. *Nano Energy* **2015,** *16*, 293-300.

206. Jiang, W.-J.; Gu, L.; Li, L.; Zhang, Y.; Zhang, X.; Zhang, L.-J.; Wang, J.-Q.; Hu, J.-S.; Wei, Z.; Wan, L.-J., Understanding the high activity of fe–n–c electrocatalysts in

oxygen reduction: Fe/Fe_3C nanoparticles boost the activity of Fe–Nx. *Journal of the American Chemical Society* **2016,** *138* (10), 3570-3578.

207. Wang, Y.; Nie, Y.; Ding, W.; Chen, S. G.; Xiong, K.; Qi, X. Q.; Zhang, Y.; Wang, J.; Wei, Z. D., Unification of catalytic oxygen reduction and hydrogen evolution reactions: highly dispersive Co nanoparticles encapsulated inside Co and nitrogen co-doped carbon. *Chemical Communications* **2015,** *51* (43), 8942-8945.

208. Osmieri, L.; Monteverde Videla, A. H. A.; Ocón, P.; Specchia, S., Kinetics of oxygen electroreduction on Me–N–C (Me = Fe, Co, Cu) catalysts in acidic medium: insights on the effect of the transition metal. *The Journal of Physical Chemistry C* **2017,** *121* (33), 17796-17817.

209. Kattel, S.; Atanassov, P.; Kiefer, B., Density functional theory study of ni–nx/c electrocatalyst for oxygen reduction in alkaline and acidic media. *The Journal of Physical Chemistry C* **2012,** *116* (33), 17378-17383.

210. Liang, W.; Chen, J.; Liu, Y.; Chen, S., Density-functional-theory calculation analysis of active sites for four-electron reduction of O_2 on Fe/N-doped graphene. *ACS Catalysis* **2014,** *4* (11), 4170-4177.

211. Sharifi, T.; Hu, G.; Jia, X.; Wågberg, T., Formation of active sites for oxygen reduction reactions by transformation of nitrogen functionalities in nitrogen-doped carbon nanotubes. *ACS Nano* **2012,** *6* (10), 8904-8912.

212. Fu, X.; Zamani, P.; Choi, J.-Y.; Hassan, F. M.; Jiang, G.; Higgins, D. C.; Zhang, Y.; Hoque, M. A.; Chen, Z., In situ polymer graphenization ingrained with nanoporosity in a nitrogenous electrocatalyst boosting the performance of polymer-electrolyte-membrane fuel cells. *Advanced Materials* **2016,** *29* (7), 1604456.

213. Vesborg, P. C. K.; Jaramillo, T. F., Addressing the terawatt challenge: scalability in the supply of chemical elements for renewable energy. *RSC Advances* **2012,** *2* (21), 7933-7947.

214. Shao, M.; Chang, Q.; Dodelet, J.-P.; Chenitz, R., Recent advances in electrocatalysts for oxygen reduction reaction. *Chemical Reviews* **2016,** *116* (6), 3594-3657.

215. Zhang, J.; Zhao, Z.; Xia, Z.; Dai, L., A metal-free bifunctional electrocatalyst for oxygen reduction and oxygen evolution reactions. *Nat Nanotechnol* **2015,** *10* (5), 444-52.

216. Terrones, M.; Terrones, H.; Grobert, N.; Hsu, W. K.; Zhu, Y. Q.; Hare, J. P.; Kroto, H. W.; Walton, D. R. M.; Kohler-Redlich, P.; Rühle, M.; Zhang, J. P.; Cheetham, A. K., Efficient route to large arrays of CN_x nanofibers by pyrolysis of ferrocene/melamine mixtures. *Applied Physics Letters* **1999,** *75* (25), 3932-3934.

217. Liu, G.; Li, X.; Ganesan, P.; Popov, B. N., Studies of oxygen reduction reaction active sites and stability of nitrogen-modified carbon composite catalysts for PEM fuel cells. *Electrochimica Acta* **2010,** *55* (8), 2853-2858.

218. Ozaki, J.-i.; Tanifuji, S.-i.; Furuichi, A.; Yabutsuka, K., Enhancement of oxygen reduction activity of nanoshell carbons by introducing nitrogen atoms from metal phthalocyanines. *Electrochimica Acta* **2010,** *55* (6), 1864-1871.

219. Lefèvre, M.; Dodelet, J.-P., Fe-based catalysts for the reduction of oxygen in polymer electrolyte membrane fuel cell conditions: determination of the amount of peroxide released during electroreduction and its influence on the stability of the catalysts. *Electrochimica Acta* **2003,** *48* (19), 2749-2760.

220. Li, H.; Liu, H.; Jong, Z.; Qu, W.; Geng, D.; Sun, X.; Wang, H., Nitrogen-doped carbon nanotubes with high activity for oxygen reduction in alkaline media. *International Journal of Hydrogen Energy* **2011,** *36* (3), 2258-2265.

221. Liu, J.; Webster, S.; Carroll, D. L., Highly aligned coiled nitrogen-doped carbon nanotubes synthesized by injection-assisted chemical vapor deposition. *Applied Physics Letters* **2006,** *88* (21), 213119.

222. Chen, W.; Kim, J.; Sun, S.; Chen, S., Electrocatalytic reduction of oxygen by fept alloy nanoparticles. *The Journal of Physical Chemistry C* **2008,** *112* (10), 3891-3898.

223. Kim, T.-Y.; Lee, K.-R.; Eun, K. Y.; Oh, K.-H., Carbon nanotube growth enhanced by nitrogen incorporation. *Chemical Physics Letters* **2003,** *372* (3), 603-607.

224. Shalagina, A. E.; Ismagilov, Z. R.; Podyacheva, O. Y.; Kvon, R. I.; Ushakov, V. A., Synthesis of nitrogen-containing carbon nanofibers by catalytic decomposition of ethylene/ammonia mixture. *Carbon* **2007,** *45* (9), 1808-1820.

225. Jafri, R. I.; Rajalakshmi, N.; Ramaprabhu, S., Nitrogen-doped multi-walled carbon nanocoils as catalyst support for oxygen reduction reaction in proton exchange membrane fuel cell. *Journal of Power Sources* **2010,** *195* (24), 8080-8083.

226. Ozaki, J.-i.; Kimura, N.; Anahara, T.; Oya, A., Preparation and oxygen reduction activity of BN-doped carbons. *Carbon* **2007,** *45* (9), 1847-1853.

227. Wu, Z.; Song, M.; Wang, J.; Liu, X., Recent progress in nitrogen-doped metal-free electrocatalysts for oxygen reduction reaction. *Catalysts* **2018,** *8* (5), 196.

228. Guo, D.; Shibuya, R.; Akiba, C.; Saji, S.; Kondo, T.; Nakamura, J., Active sites of nitrogen-doped carbon materials for oxygen reduction reaction clarified using model catalysts. *Science* **2016,** *351* (6271), 361.

229. Wu, Z.; Wang, J.; Han, L.; Lin, R.; Liu, H.; Xin, H. L.; Wang, D., Supramolecular gel-assisted synthesis of double shelled Co@CoO@N–C/C nanoparticles with synergistic electrocatalytic activity for the oxygen reduction reaction. *Nanoscale* **2016,** *8* (8), 4681-4687.

230. Zhang, L.; Xia, Z., Mechanisms of oxygen reduction reaction on nitrogen-doped graphene for fuel cells. *The Journal of Physical Chemistry C* **2011,** *115* (22), 11170-11176.

231. Yang, H. B.; Miao, J.; Hung, S. F.; Chen, J.; Tao, H. B.; Wang, X.; Zhang, L.; Chen, R.; Gao, J.; Chen, H. M.; Dai, L.; Liu, B., Identification of catalytic sites for oxygen reduction and oxygen evolution in N-doped graphene materials: Development of highly efficient metal-free bifunctional electrocatalyst. *Science advances* **2016,** *2* (4), e1501122.

232. Wu, Z.; Song, M.; Wang, J.; Liu, X., Supramolecular gel assisted synthesis of Co2P nanosheets as an efficient and stable catalyst for oxygen reduction reaction. *New Journal of Chemistry* **2018,** *42* (11), 8800-8804.

233. Higgins, D.; Chen, Z.; Chen, Z., Nitrogen doped carbon nanotubes synthesized from aliphatic diamines for oxygen reduction reaction. *Electrochimica Acta* **2011,** *56* (3), 1570-1575.

234. Shamsunnahar, S. M.; Nagai, M., Nitrogen doping of ash-free coal and effect of ash components on properties and oxygen reduction reaction in fuel cell. *Fuel* **2014,** *126*, 134-142.

Chapter 2

Experimental Methods

This chapter introduces the theory behind the main experimental methods employed throughout this thesis. The magnetron sputtering system is used to synthesis amorphous carbon and nitrogenated amorphous carbon films is described along with a brief discussion of the deposition conditions. RF plasma system used to perform N incorporation into graphitised amorphous carbon. Here these materials characterisation techniques applied throughout the work are described are X-ray photoelectron spectroscopy, Ultraviolet photoelectron spectroscopy and Raman spectroscopy. The apparatus used in the electrochemical characterisation is also described together with voltametries and impedance techniques. Capacitance of the materials was determined using impedance method.

2 Experimental Section

2.1 Chemicals and Materials

Potassium chloride (Bioxtra, >99.0%), hydrogen peroxide (>30% w/v), Tetrabutylammonium hexafluorophosphate (≥99.0%), Acetonitrile (anhydrous, 99.8%), Sulfuric Acid (95 – 97%) and methanol (semiconductor grade) were purchased from Sigma Aldrich. Glassy Carbon discs (Sigradur® 0.25 ± 0.05 mm) were obtained from HTW. Alumina slurries (1 µm, 0.3 µm and 0.05 µm) were purchased from Buehler.

2.2 Preparation of Substrates

B-Doped Silicon wafers were used as substrate for deposition of a-C and a-C:N films for XPS and Raman. Substrates were cleaned with Piranha solution (3:1 H_2SO_4: H_2O_2) rinsed with Millipore water and dried under Ar.

Glassy Carbon (GC) disks were prepared by 4 steps polishing procedure. First, the discs were polished with sand paper and alumina slurry of 1 µm grade. Secondly, the disks were polished with nylon paper and alumina slurry of 0.3 µm; thirdly, 0.3 µm slurry and micro-cloth were used to polish the disks. Finally, the disks were polished with 0.05 µm slurry and micro-cloth before depositing a-C or a-C:N on them. 10 min of sonication of polished disk with Millipore water was done between each step of polish and after the final step. The clean disks were mounted in a Teflon® holder and placed in the vacuum chamber.

2.3 Deposition of a-C and a-C:N

2.3.1 Sputtering Method

Sputtering is a process where atoms are ejected from a solid target material due to bombardment of the target by energetic particles. Ions of inert gases such as Ar or Xe, are accelerated in a plasma and directed towards the sputtering target. This accelerated ion can then be displaced through direct collisions or a ‘collision cascade’ resulting in emission of atoms. Figure 2.1 shows the process of ion bombardment on the target surface. This sputtering method is used to deposit thin films on a substrate.

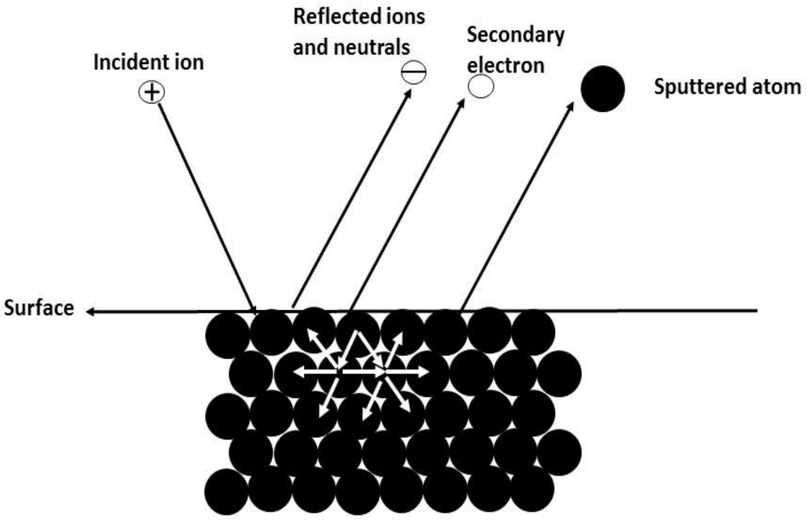

Figure 2.1: Interaction of an incident ion with surface and associated process may happen due to ion interaction with the material surface are secondary electron emission, reflection of the incident particles.

There are different sputtering techniques used to deposit thin films such as Ion Beam Sputtering (IBD) [1-2], Ion Beam Assisted Deposition (IBAD) [3-5], Gas Flow Sputtering (GFS) and Magnetron Sputtering. Ion Beam Sputtering is also called Ion Beam Deposition (IBD); this process is used to deposit thin films using an ion source to sputter a target material onto a substrate to create either a metallic or a dielectric film. The advantage of this techniques is the independent control over kinetic energy and current density of ions and no need for substrate heating. Ion beam assisted deposition (IBAD) is a process usually combines sputtering with the ion implantation concurrent ion beam bombardment, produce a coating with less built-in strain and highly intermixed interface. This technique is desirable where metal oxides and metal nitride films are needed to grow. Sputtering by IBAD is more energetic and highly directional. Gas flow sputtering is a special physical vapour deposition (PVD) method that utilizes a hollow cathode with a flow of gas (usually Argon) going through it. If pressure P and characterization length L of the hollow cathode obeys the condition $0.5 \text{ Pa. m} < P L < 5.0 \text{ Pa. m}$, where Pa is the unit of pressure and m is the unit of length, an enhanced plasma density can be established in a hollow cathode. One of the main advantages of this technique is that it lowers the kinetic energy of the depositing atom and decreases damage to the growing film.

In this work magnetron sputtering was used to deposit thin films. Magnetron sputtering was used to deposit amorphous carbon (a-C) films of thickness ranging between 80 and 100 nm onto substrates prepared as above. In this deposition method a target (cathode) is bombarded by energetic ions generated in a plasma situated in proximity of the target. This cathode generally a solid material source, commonly referred as a 'target', with energetic ions. This method involves the generation of an Ar plasma that is created and supported by a high voltage DC source. The sputtered atoms generate a condensable vapour which forms a thin layer of target material on the desired substrate [6]. A graphite target was used to deposit carbon materials [7], while Si wafers and glassy carbon disks were used as substrates.

Deposition of amorphous carbon (a-C) was carried out using a DC magnetron sputtering chamber (Torr International Inc.,USA) at base pressure $\leq 2 \times 10^{-6}$ mbar and a deposition pressure of 7×10^{-3} mbar using Ar (25 sccm) as previously described[8]. The deposition time was kept constant at 40 min. In order to deposit a-C:N films an N_2/Ar gas mixer consisting of mass flow controllers (Brooks Inc.) and a control unit (Brooks Instrument LLC,USA) was used. The N_2 concentration ranged from 2-10% percent set at 50 sccm for all a-C:N depositions. A picture of inner of the sputtering system used is presented in figure 2.The setup is equipped with two deposition guns. The carbon source for both a-C and a-C:N was a graphite target (99.999%, Lesker). In order to avoid cross contamination of the undoped films with residual nitrogen, two separate targets were used. Nitrogenated films are referred here as a-C:N-X (X=0,2,5,10) where X is the percentage flux of N_2 in the vacuum chamber.

Selected a-C:N samples were also annealed to modify the composition of the film. The sputtered samples were placed on a clean alumina crucible and the crucible was placed inside a quartz tube in a furnace. The samples were annealed at 900 ^{0}C for 1 h under nitrogen gas flow.

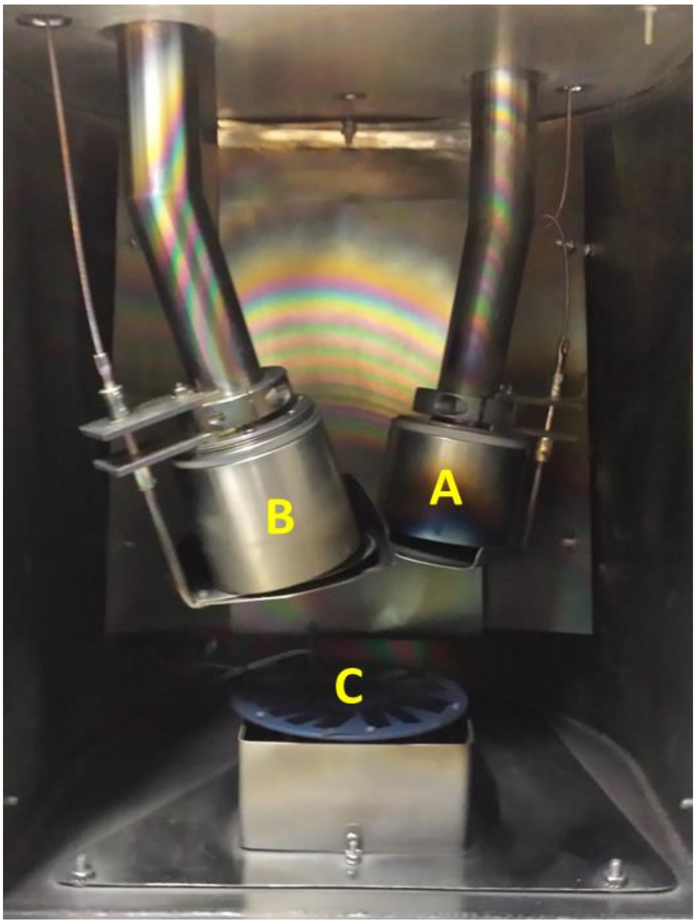

Figure 2.2: Magnetron sputtering chamber used in our lab in order to sputter amorphous carbon, titanium and N doped amorphous carbon. The plasma is generated at the two sputtering guns with the graphite (A) and titanium (B) targets, located above the rotating stage (C), where samples are placed.

2.3.2 Surface Nitrogenation by RF plasma generator

Radio frequency generated plasmas are a type of plasma used in industry for different applications such as etching, materials processing and sputtering applications [9-11]. Radio frequency plasma can be produced by applying an ac voltage at radio frequency to appropriate gases at low pressures. This type of plasma is preferred in industry because they can be operated at low pressure and they are also more efficient at sustaining the discharge than dc plasmas [11]. Inductive coupling in combination with the RF input allows to create the plasma without introducing the electrodes into the chamber thus achieving high purity conditions. Plasmas are used in industry frequently for etching and deposition purposes. The use of an ac discharge means that the substrate continuously charges and discharges to its surface can be changed by varying the driving frequency and the applied potential. A schematic diagram of plasma chamber used in our lab is presented in figure 2.3. RF plasma chamber equipped with RF power (500 W, 13.56 MHz) and roller inductor antenna tuner (1.5 KW). This chamber is connected with rotary pump which can maintain the base pressure of 10-18 mTorr inside of the chamber. N_2/Ar gas lines are also connected to this chamber using bulb and mass flow controller (Brooks Inc.) with a control unit (Brooks Instrument LLC, USA). A coil is placed on the outside middle of the chamber and a plasma switch is connected with it. RF power is kept as low as 10 W to avoid sample damage and inductor tuner was used to adjust RF plasma power as to keep the same applied power. a-C a900 carbon films were deposited via DC-magnetron sputtering (Torr International) and followed by a thermal annealing treatment. In order to perform nitrogen incorporation into a-C a900, the samples are placed on sample plate of the chamber and the bulb of the chamber is being closed. The rotary pump is turned on and within few min base pressure of the chamber is reached. Nitrogen flow was started, initially it was set at 5 ml/min and eventually it was increases up to 20 ml/min. Plasma exposer time was maintained depending on the samples and three different exposer time reported in this thesis such as 5 min, 10 min and 20 min.

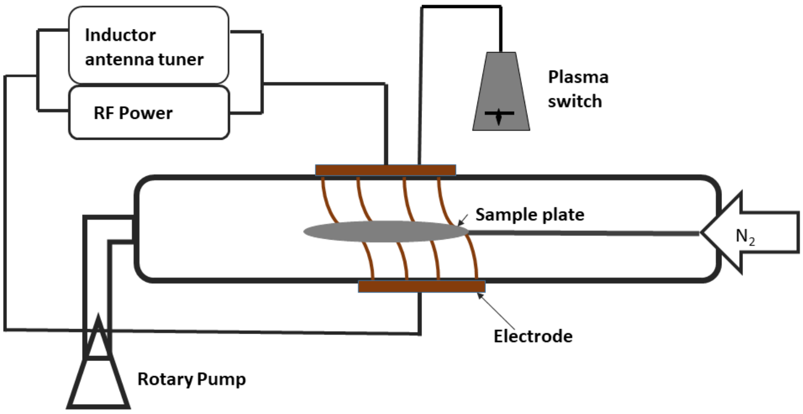

Figure 2.3: A schematic diagram of RF plasma chamber used in our lab to do plasma treatment on carbon-based electrodes.

2.4 Surface characterization

2.4.1 X-ray Photoelectron Spectroscopy

X-ray photoelectron spectroscopy (XPS) is a photoemission spectroscopic technique to analyse the chemical composition of material surfaces. It is accomplished by irradiating a sample with monoenergetic soft x-rays and analyzing the energy of the detected electrons.

X-rays of Mg Kα (1253.6 eV) or Al Kα (1486.6 eV) are usually used. $K\alpha_{1,2}$ lines are convoyed by 'satellite' lines due to similar transitions and Bremsstrahlung spectrum are formed due to the primary electron's energy. When higher resolution is needed, a monochromatic X-ray source is used to remove 'satellite' lines and Bremsstrahlung. Monochromatic x-ray sources are based on Al Kα x-rays (1486.6 eV) [12]. These photons have limited penetrating power in a solid on the order of 1-10 µm. These photons interact with atoms in the surface region , causing electron to be emitted by photoelectric effect. The emitted electrons have measured kinetic energy given below,

$$E = h\nu - BE - \phi \qquad (2.1)$$

Where hυ is the energy of the incident photon, BE is the binding energy of the atomic orbital from which the electron originates and ϕ the work function of the spectrometer. A schematic energy level diagram for a conductive sample in contact with an electron spectrometer is shown in Figure 2.4. The work function is the energy barrier that must be overcome to bring an electron from the Fermi level into vacuum, right outside the surface. The binding energy is the energy difference between the core electronic level and the Fermi level [12].

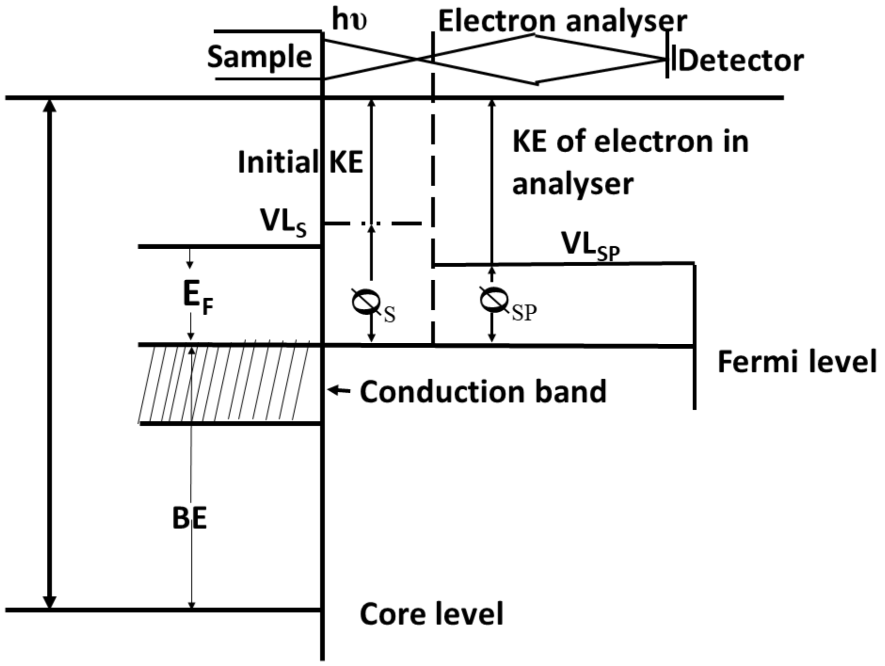

Figure 2.4: Schematic energy level diagram for a conducting (metallic) sample in electrical equilibrium with the spectrometer, where E_F is the Fermi energy and VL is the vacuum level. The work function (ϕ) and the Fermi energy are not identical because the work function includes not only a bulk term, but also a surface term [12].

XPS can be used to identify and determine the concentration of the elements in the surface by the determination of the BE of core level electrons and spectral profile which can give the composition and the element concentration at the sample surface. Changes in the elements BE's are correlated to chemical information of the materials surface. These differences in BE's are called chemical shift which can be used to identify the chemical state of the materials being analysed. In addition to this photoelectric process, Auger electrons may be emitted because of relaxation of the excited ions remaining after photoemission and occurs roughly 10^{-14} s after the photoelectric event.

In this thesis, results obtained from two different XPS instruments are presented. In chapter III a monochromatized XPS instrument was used for the determination of *sp*^{2} and *sp*^{3} content in a-C films and annealed a-C (chapter IV). In these cases, XPS characterization was performed on an ultrahigh vacuum system (Omicron) at $1 \times 10{-}10$ mbar base pressure equipped with a monochromatized Al Kα source (1486.6 eV) and a multichannel array detector. Spectra were recorded with an analyzer resolution of 0.5 eV at 45 ° take off angle.

In the case of a-C:N films, XPS characterization was performed on a VG Scientific ESCAlab Mk II system under ultra-high vacuum conditions (<2 × 10-8 mbar), using Al Ka X-rays (1486.6 eV). and the binding energy scale was referenced to the C 1s core-level at 284.4 eV. An analyser pass energy of 200 eV and 20 eV were used for survey spectra and individual core-level spectra. The area sampled was approximately 1 cm in diameter. a-C:N films in chapter III, IV and V VG Scientific ESCAlab Mk II system is used. Selected XPS measurements were carried out by Dr. Serban Stamatin of the Colavita group; data were analysed by the author using CasaXPS software.

The spectra obtained from XPS was deconvoluted using CasaXPS software. Firstly, survey of each spectrum was considered to calculate elemental composition. The entire survey spectra were calibrated based on C 1s at 284.8 eV. Secondly, spectra of each element deconvoluted using Gaussian-Lorentzian GL 30 (70% Gaussian & 30% Lorentzian) with Shirley baseline background subtraction, which is one of the most commonly used line shape. The proper line shape should be selected based on the symmetry and geometry of the peak. In order to extract chemical states of an element in an XPS spectra, there are exact binding energies in data base. Extracted parameters are used to analyzed the surface chemistry of these materials.

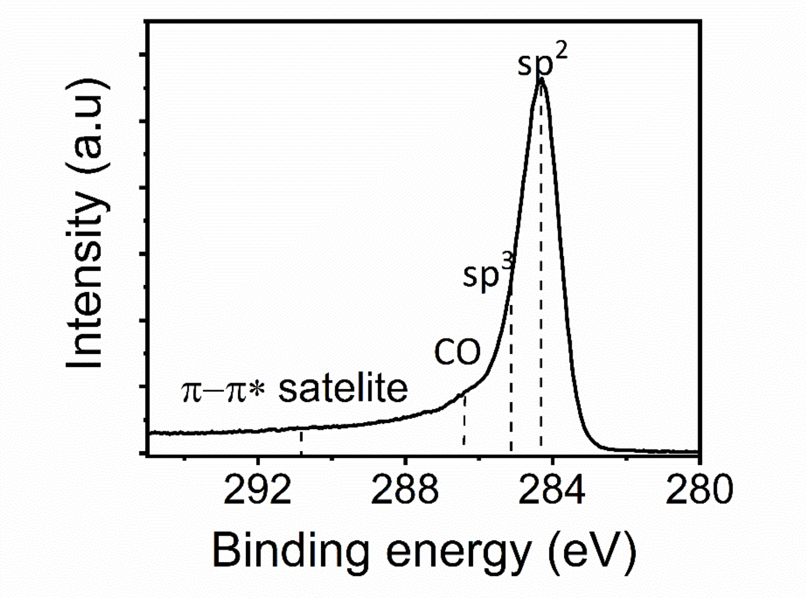

Figure 2.5: XPS spectrum of C 1s envelope for an amorphous carbon material.

A typical XPS spectrum of C 1s envelope for an amorphous carbon material is presented in figure 2.5. The C1s envelope contain number of different contributions such as sp^2 and sp^3 centres lies between 284-286 eV. The peaks above the binding energy of 286 eV typically assigned as C-O,C=O components such as hydroxyl and ether moieties [13-16]. The broad peak closes the binding energy of 291 eV are commonly referred as a π-π* satellite or a 'shake-up' feature.

2.4.2 Raman spectroscopy

Raman spectroscopy is a non-destructive tool for structural characterization of carbon films [17]. Raman scattering is based on inelastic scattering of incident radiation through its interaction with vibrational modes of molecules or solids. Raman spectroscopy uses inelastically scattered light from a monochromatic light source (usually a laser) incident onto a sample to extract information. When a laser is incident on a sample it scatters elastically (Rayleigh scattering) after interaction with the sample but a small fraction interacts with molecular vibrational modes of the sample and is inelastically scattered (Stokes or anti-Stokes scattering). This scattered light is shifted in frequency from the incident light and this shift is referred to as Raman shift. A Raman spectrum is a plot of the intensity of the shifted light vs frequency. A schematic diagram of a Raman apparatus is presented in figure 2.6 and it consists of three main components. First, an excitation source which excites the sample. Second, there is an illumination system and in our case a microscope in back scattering configuration was used. Third, a spectrometer is used to collect the Raman spectrum and is equipped with an edge filter to attenuate the Rayleigh scattered laser line.

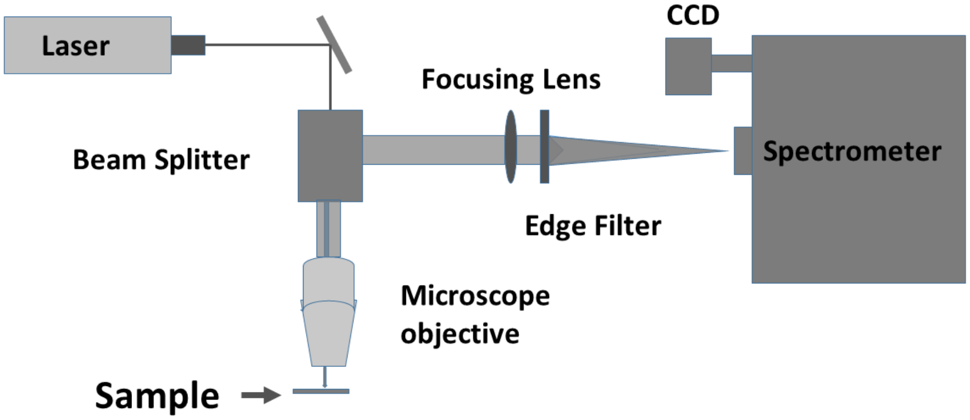

Figure 2.6: A schematic diagram of Raman apparatus.

Each band in a Raman spectrum corresponds to a particular molecular vibration induced by incident light. Under illumination, a photon excites a molecule from the ground state to a virtual electronic state, the molecule can emit a photon and relax to the ground electronic state but reaching a different vibrational state from the initial one. The difference between the absorbed and emitted photon energy is called Raman shift. Not all modes are Raman active and a change of polarizability must be needed with respect to vibrational coordinates for a mode to be Raman active. A transition is allowed if the symmetry of the wave function in the virtual state and transition moment operator is same, otherwise the transition moment integral will be zero.

Raman scattering from carbons is always a resonant process that is the energy of the incident radiation is nearly in resonance with the difference between the ground state and a real electronic state therefore Raman scattering from carbons is typically intense. Raman spectra of a-C show two sharp modes, the G peak around 1580–1600 cm^{-1} due to the bond stretching of sp^2 atoms in both rings and chains and D peak around 1350 cm-^{1} due to the breathing modes of sp^2 atoms in rings. G and D peaks usually assigned to zone center phonons of E2g symmetry and K-point phonons of A1g symmetry. The T peak can be seen for UV excitation due to the C-C sp3 vibrations and appears only in UV excitation [18]. Raman spectrum of amorphous carbon materials in the region 900-1900 cm^{-1} is presented in figure 2.7

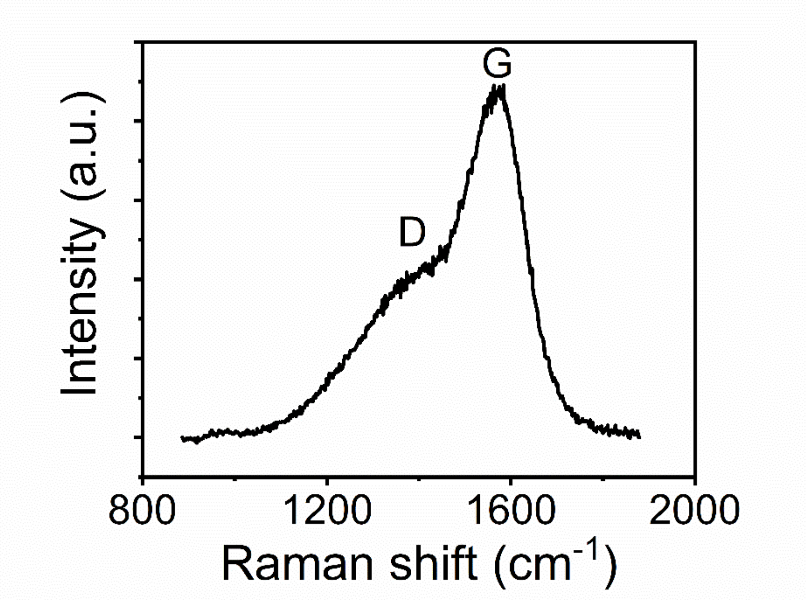

Figure 2.7: Raman spectrum of an amorphous carbon material in the region 1800-1000 cm^{-1}. The dashed lines illustrate the G and D peaks associated with different stretching and breathing modes of sp^2 atoms.

Several peak fitting system used in the literature including use of Gaussian/Lorentzian functions [19-20], Breit-Wigner-Fano (BWF) and Lorentzian functions [18, 21] and all Gaussian functions in the spectral region of 1100-1880 cm^{-1}. In order to analyse Raman spectra quantitively, the Raman spectra can be fitted with different peak fitting functions of Gaussian, Lorentzian and BWF etc. These spectra can be fitted with any of these functions or a mix of these functions. The Gaussian function is described by the following expression,

$$I_G(\omega)=I_{G0}\times e^{-(\frac{\omega-\omega_0}{\Gamma})^2} \qquad (2.2)$$

Where I_G is the peak intensity as a function of frequency (ω), I_{G0} is the maximum peak amplitude, ω_0 is the peak position, Γ is the FWHM [22].

Lorentzian function: $$I_L=\frac{I_{L0}}{1+(\frac{\omega-\omega_0}{\Gamma})^2} \qquad (2.3)$$

Where IL is the peak intensity as a function of frequency (ω), IL0 is the maximum peak amplitude, ω_0 is the peak position, is the FWHM.

BWF function: Ferrari and Robertson suggested fitting method other than two-Gaussian or two Lorentzian is the combined function from one single BWF G peak and one single Lorentzian D peak.[23] BWF function is described by,

$$I_{BWF}(\omega)=\frac{I_{BWF0(1+(\omega-\omega_0)/Q\Gamma)2}}{I_{(1+((\omega-\omega_0)/Q\Gamma)2}} \qquad (2.4)$$

Where I_{BWF} is the peak intensity as a function of frequency (ω), I_{BWF0} is the maximum peak amplitude, ω_0 is the peak position, Γ is the FWHM, Q is the BWF coupling coefficient of the Raman spectrum.

In this thesis Raman spectra were collected on Renishaw 1000 micro Raman equipped with a CCD camera and a Leica microscope using the 488 nm line of argon laser line and 633 nm line of a HeNe laser. The spectra were collected with scan times of 40 s, 1 accumulation, and a power of 25 mW (10% of the laser power). All the measurements were taken carefully to avoid burning of the sample, however in some cases this was unavoidable. The spectra were normalised with respect to the G peak height to facilitate comparison and analysed using commercial software (WiRe 3.2).

2.4.3 Ultraviolet photoelectron spectroscopy (UPS)

Ultraviolet photoelectron spectroscopy (UPS) is known as valence photoelectron spectroscopy used to probe the valence electrons. Photoelectron are produced by valence photoionization measurement of kinetic energy of spectra of photoelectrons emitted by molecules which absorbed ultraviolet photons to determine molecular orbital energies in the valence region. The main aim of the UPS experiments is to gain information about the distribution of electrons in the valence or conduction band region of the materials. These electrons are responsible for the chemical, magnetic, optical and mechanical properties of each material [24].

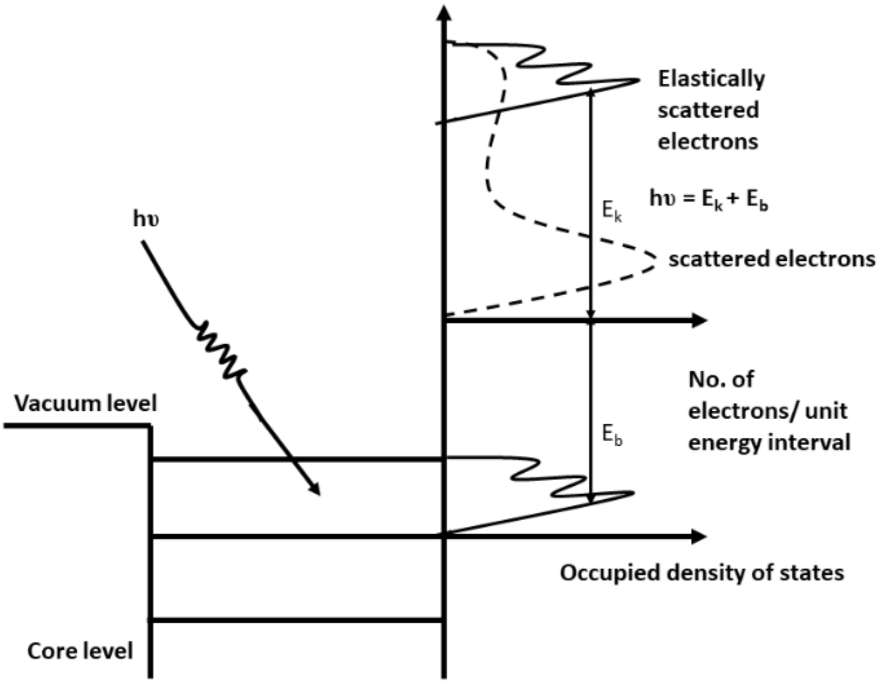

Figure 2.8: Schematic diagram of the photoexcitation of electrons from a valence band due to monochromatic photons of energy hυ [24].

Compared with Auger electron spectroscopy (AES) or X-ray photoelectron spectroscopy (XPS), ultraviolet photoelectron spectroscopy (UPS) is not generally considered to be an analytic technique for the surface characterization of materials. It is an extremely surface sensitive technique where small amount of contaminant can completely change the signal from a given surface. The main strength of this technique is its robust ability to explore the electronic structure of valence band/conduction region of the various types of solid materials [24]. Sometime this technique is added as an option to other surface science instrumentation of XPS/AES equipment as per manufacturers of these equipment. UPS depends on the photoelectric effects where a beam of monochromatic photons is used to eject electrons from the valence or conduction band region of a material. A hollow cathode discharge lamp which running in an inert gas is used as photon source for UPS. There are several resonance lines being of them most common lines are as He 1 at 21.21 eV and Ne 1 at 16.86 eV. Band width ranges of this valence/conduction band materials is 5-10 eV which enough to explore the entire band structure region of most materials. The photoemitted electrons have energies less than 17 eV using He 1 which consists of two main groups [24].

The first group of electrons excited within few atomic layers and escape into vacuum with no inelastic collisions. The energy and the direction of emission of such electrons are associate to their binding energy within the solid and their momentum related to their original states. This binding energy E_b of such electrons are simply associated with their observed kinetic energy E_k according to Einstein formula, as indicated in figure 2.8

$$h\nu = E_k + E_b \qquad (2.5)$$

Second group of electrons observed in UPS spectra consist of such electrons which have either made one or more inelastic collisions or secondary electrons which have gained enough energy to escape from such collisions. These electrons constitute a largely featureless low energy peak in all UPS spectra with a shape of similar like a Maxwellian distribution [24].

In this thesis UPS measurements of N free a-C and a-C:N films (chapter III and IV) were performed in an Omicron system at 1×10^{-10} mbar base pressure, using monochromatic Al Kα source (1486.6 eV) and equipped a multichannel array detector. Spectra were collected using He 1 excitation source (21.22 eV) at 90° take-off, with 0.02 eV analyser resolution. Negative bias were applied to the sample (0-12 V) to measure the high binding energy edge of the photoelectron spectrum; spectra were then corrected to account for bias and referenced to the Fermi energy measured on a Ag surface in contact with the carbon [25]. Work function (ϕ) values were calculated using the intercept at the binding energy axis of linear fits of the cut-off edge, as $\phi = 21.22 - \text{intercept}$.

2.5 Electrochemical method of characterisation

Electrochemical measurements were carried out in this thesis was on a Metrohm Autolab AUT50324 potentiostat with a Frequency Response Analyser (FRA) module. All electrochemical characterisation presented in this thesis using a 3-electrode setup consists of a working electrode (WE), counter electrode (CE) and reference electrode (RE) illustrated in figure 2.9. Reference electrode was chosen depending on the experiment and electrolyte used as Ag/AgCl was used in the case of aqueous electrolyte while Ag/Ag+ was used in the case organic electrolyte. All WEs in this work prepared by using glassy carbon (GC) disks (Sigradur, grade K radius 0.25 ± 0.05 cm). These disks either used directly as working electrode or used as substrate for the deposition of amorphous carbon and N-doped amorphous carbon thin film electrodes via magnetron sputtering. Polishing /pre-treatment was performed on these disks as described in following chapters prior to electrochemical measurements and deposition on it.

The reference electrode allows us to control of the potential of a working electrode. The standard hydrogen electrode plays the role of a basic reference element in most electrochemical devices, however practically it is difficult to handle. Therefore, secondary reference electrodes are preferred in most of the experiments [26]. In this work Ag/AgCl RE was used when KCl was used as aqueous electrolyte. An Ag/AgCl RE can be easily prepared using an anodised piece of silver wire immersed in a saturated salt solution of KCl. A porous frit was used to separate the RE internal solution from the working solution. In order to avoid the mobilities of the ions on both sides of the frit and liquid junction potentials across the frit a similar electrolyte is used in the working solution as well as in the RE compartment. Electrochemical measurements in organic electrolyte of 0.1 M $TBAPF_6$/ acetonitrile was used in this work where Ag/Ag^+ as reference electrode was used. The Ag/Ag^+ reference electrode is prepared by placing a clean silver wire into an electrolyte containing silver. The electrolyte in the reference compartment is the same as the solution electrolyte. 0.01 M $AgNO_3$ was dissolve in the reference compartment electrolyte which provide Ag^+ ion. A graphite rod was used as a CE for all electrochemical experiments.

Electrochemical methods used in this work are cyclic voltammetry (CV), Electrochemical Impedance Spectroscopy (EIS), Rotating Disk Electrode (RDE) and Rotating Ring Disk Electrode (RRDE).These characterisation methods are discussed below,

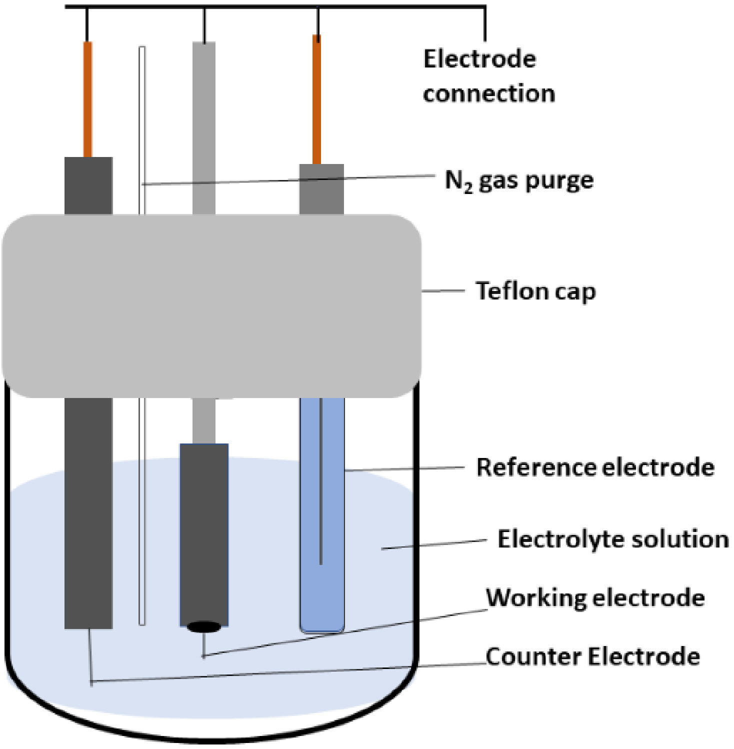

Figure 2.9: Schematic representation of an electrochemical cell for electrochemical experiments carried out in this thesis.

2.5.1 Cyclic Voltammetry (CV)

Cyclic voltammetry (CV) is a type of potentiodynamic electrochemical tool for studying electrochemical reactions, for obtaining good estimates of formal reduction potentials, formation constants, reaction mechanisms and diffusion coefficients. A typical CV experiment using three electrodes (working electrode, reference electrode and counter electrode) involves applying a varying potential at the working electrode and reference electrode while measuring the current passing through the working and the counter electrodes. The rate of voltage change over time during each cyclic phase is called scan rate. The response of the electrochemical system highly depends on the analyte being used and on the properties of the working electrode during the experiments. A typical CV plot figure 2.10 shows some important pieces of information obtained from a CV experiment such as the cathodic peak height (I_{pc}), the anodic peak height (I_{pa}), the cathodic peak potential (E_{pc}) and the anodic peak potential (E_{pa}). A single CV is useful for determining whether the species is electro active or not. A conclusion that can be drawn about a redox couple from this CV is that if $I_{pc}= I_{pa}$ and Δ E ~ 60 mV $s^{-1}$the system is reversible (*i.e.*, follows the Nernst equation) and from this number of electrons transferred during the oxidation/reduction can be determined.

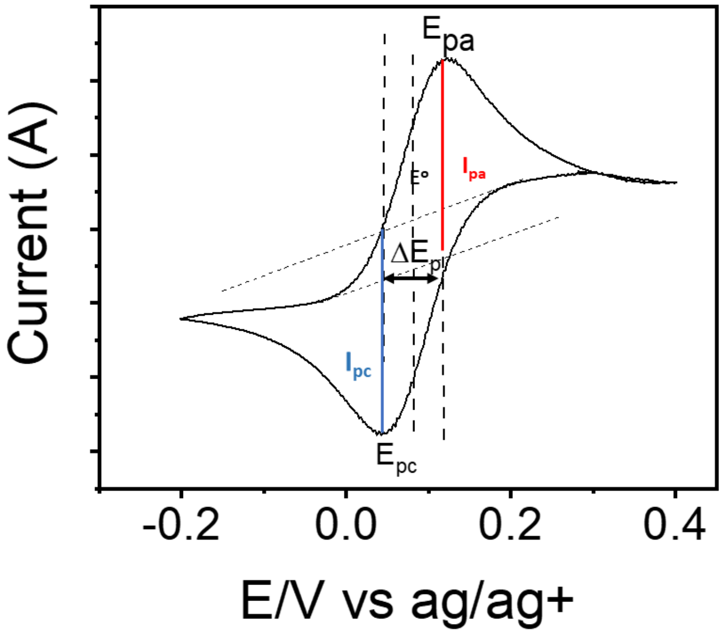

Figure 2.10: Typical cyclic voltammogram for reversible redox process showing Nernstian behaviour. Parameters are as follows, the peak-to-peak separation ΔEp and the peak currents I_{pa} and I_{pc} are anodic and cathodic peak current.

Multiple CV experiments allow to see chemical changes with time and to observe reaction products formed at the surface of an electrode. In a typical CV, the diffusion coefficient of a species can be determined by varying the scan rate. For a reversible system with a redox species in solution, the peak height will increase linearly with the square root of the scan rate. The deviation from reversible behaviour in CV is due to coupled chemical reactions. In this case the system could be irreversible or quasi-reversible depending on the extent of deviation from the reversible case. Typical CV experiments are also widely used for studying electrode processes of Capacitive current. When there is no redox couple present in the electrolyte a typical CV curve does not show any redox peak and only double layer capacitive process is present. Figure 2.11 shows a typical CV where no redox peak is present. The specific capacitance can be calculated from the CV curve. In this work a similar type of CV experiment was performed to confirm that there is no redox process present, and that only capacitive contributions are present within the potential window.

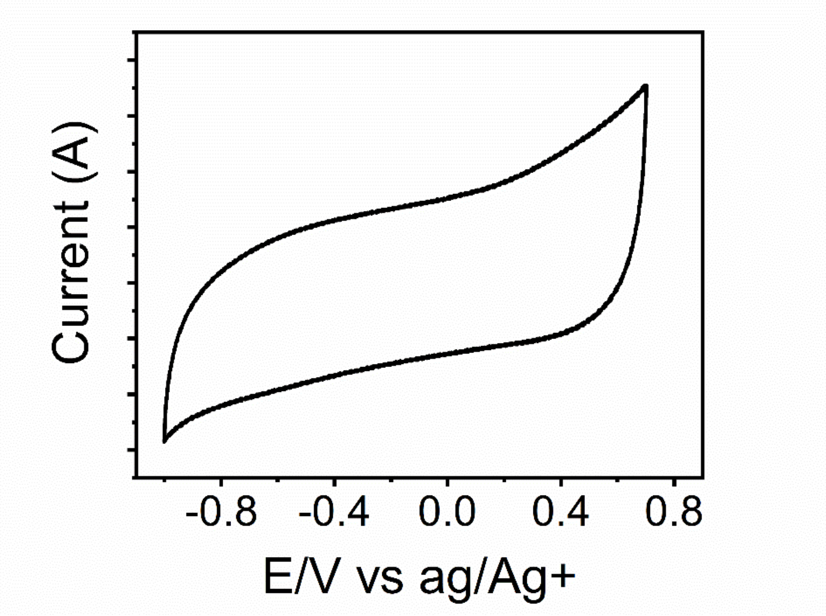

Figure 2.11: Typical cyclic voltammogram where no redox process present.

2.5.2 Rotating Disk Electrode (RDE) and Rotating Ring Disk Electrode (RRDE)

Voltammetry at the rotating disk electrode (RDE) is a widely used method for the study of various solid electrode systems with constant thickness, minimum double layer charging effect and a mass transfer process whose theoretical basis is well investigated and the equations are related to experimental electrocatalytic parameters [27]. The RDE is constructed from a disk of electrode material (glassy carbon) which is affixed to a cylindrical holder made of PTFE. The electrode is attached to a motor and rotated at a certain frequency, f = ω/2π, where ω is the angular velocity (s^{-1}). During the rotation of the electrode in an electrolyte, mass transfer of reactants and products is by convective-diffusional mechanisms [27]. Some important equations are used to extract electrocatalytic oxygen reduction reaction relevant parameters from RDE experiments.

The Levich equation related to the limiting current density j_L to the square root of the angular velocity, ω in a reversible system,

$$j_L = 0.201nFD^{2/3}v^{-1/6}C\omega^{1/2} \qquad (2.6)$$

n is the number of electrons transferred ; F is Faraday's constant; D is the diffusion coefficient of the analyte, v is the kinematic viscosity and C is the concentration of the analyte in bulk solution.

Similar to the Levich equation is the Koutecky-Levich equation which was developed to accommodate quasi-reversible systems controlled by mass-transfer and kinetic limitations. Current density j_c measured at the electrode is represented by,

$$\frac{1}{\mathrm{jc}} = \frac{1}{\mathrm{nFkC}} + \frac{1}{0.201\mathrm{nFD}^{2/3}\mathrm{v}^{-1/6}\mathrm{C}\omega^{1/2}} \qquad (2.7)$$

Here k is the heterogeneous reaction rate constant with unit of cm s^{-1}. From the equation, a plot of $1/j_c$ vs $1/\omega^{1/2}$ should be a straight-line which slope is used to calculate the number of electrons involved in the reduction of oxygen reduction reaction.

The rotating ring disk electrode (RRDE) setup is little more complex than the RDE. The RRDE is RDE with a ring electrode around the disk, separated by an insulating non-catalytic material. Typical advantages of RRDE experiments is to study the ORR and detect peroxide production at the ring electrode. During the RRDE experiment setting the ring at certain voltage enough to oxidize the peroxide. The RRDE is very useful for investigation of major mechanism during oxygen reduction. Number of electrons (n) transfer for RRDE experiment,

$$\mathrm{n} = \frac{4\mathrm{I_D}}{\mathrm{I_D} + \frac{\mathrm{I_R}}{\mathrm{N}}} \qquad (2.8)$$

Where n is the average number of electrons transferred, I_D is the disk current, I_R the ring current generated because of the oxidation of hydrogen peroxide and N is the collection efficiency which is determine experimentally and specified by the manufacturer.

The mole fraction of peroxide production at the disk can be calculated from the equation,

$$X_{H2O2} = \frac{\frac{2I_R}{N}}{\mathrm{I_D} + \frac{\mathrm{I_R}}{\mathrm{N}}} \qquad (2.9)$$

X_{H2O2} is the mole fraction of peroxide which determine the catalytic efficiency in terms of how much of ORR proceed with a full 4 e^- reduction of O_2 to H_2O. RRDE studies of the ORR on N-doped carbon materials are presented in chapter V of this thesis.

2.5.3 Electrochemical Impedance Spectroscopy (EIS)

In this thesis, electrochemical impedance spectroscopy (EIS) was used to analyse the capacitance of a-C and a-C:N films deposited on GC discs. EIS is a powerful method of characterizing electrical properties of a variety of different materials and their interfaces with conducting electrodes. It is also used to investigate the dynamics of the mobile charge in the bulk or interfaces between solid or liquid materials which may be ionic, semiconducting, mixed ionic -electronic and even insulators [28]. EIS is applied to the determination of the double-layer capacitance [29-31], characterization of electrode processes [32] and complex interfaces [33]. A fixed potential is first applied to the WE and enough time is allowed to reach equilibrium at the electrode. The FRA module generates a sine wave with a user-defined frequency and a small voltage amplitude, typically 5-10 mV. The AC response current components are analysed by the FRA channels and the transfer function. The complex impedance Z is calculated and the module and phase angle shift or the real and imaginary components of the total impedance are calculated. The total impedance, Z is given by (Figure 2.12),

$$Z(\omega) = Z' + jZ'' \qquad (2.10)$$

Where Z' and Z'' are the real and imaginary components of the impedance, respectively.

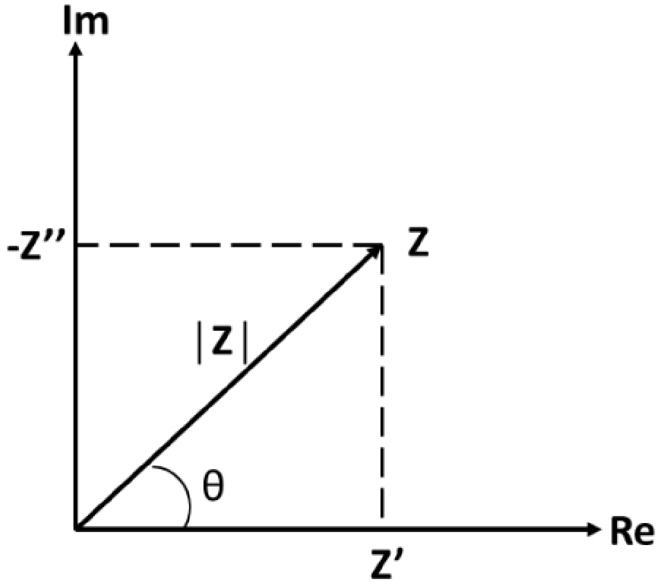

Figure 2.12: The impedance Z plotted as a planar vector using rectangular and polar coordinates.

From figure 2.12 two rectangular coordinate values are

$$\mathrm{Re}(Z) = Z' = |Z| \cos\theta \qquad (2.11)$$

$$\text{and } \mathrm{Im}(Z) = -Z'' = |Z| \sin\theta \qquad (2.12)$$

The phase angle is,

$$\phi = \tan^{-1}(Z''/Z') \qquad (2.13)$$

Z is in general frequency-dependent and EIS spectra show values of Z as a function of V or ω. Impedance by definition is a complex quantity. The impedance of resistor is Z_R=R which does not have an imaginary part and the phase angle is zero at all frequencies. The impedance of a capacitor is instead a complex quantity as expressed below:

$$Z_C = \frac{1}{i\omega C} = \frac{1}{i2\pi fC} \qquad (2.14)$$

Where the **c**apacitance C is measured in farads (F).For any given capacitance, the impedance decreases with increasing frequency and at any given frequency the impedance decreases with the value of the capacitance C. The impedance is imaginary, and it has -90^0 phase angle. Therefore, the real part of a generic impedance Z is represented by a resistance R and the imaginary part of an impedance is referred to as a capacitance C. The variation of the impedance with frequency is often of interest and displayed in a different way. In a bode plot , log|Z| and phase ϕ are both plotted against log *f*. An alternative representation, a Nyquist plot, displays Z_{Im} vs. Z_{Re} for different values of frequency [34]. The typical Nyquist plots for the series RC circuit and parallel RC circuit are shown in figure 2.13. The drawback of Nyquist plot is that they do not provide frequency information directly. In this thesis capacitance was calculated from imaginary part of the Nyquist plot at a certain frequency by using equation 2.14.

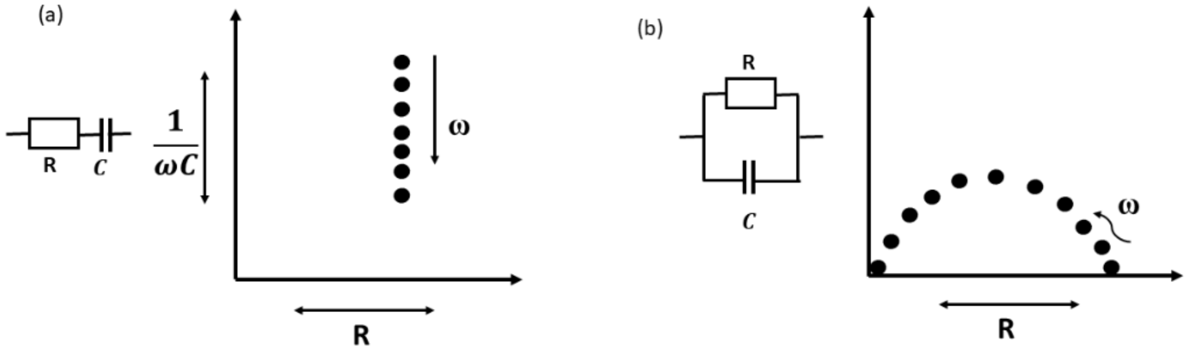

Complex plane Impedance spectrum- series resistance, capacitance

Complex plane Impedance spectrum- parallel resistance, capacitance

Figure 2.13: The schematic Nyquist plot of series and parallel resistance and capacitance. Reproduced from reference 34.

2.6 References

1. Ali, M. Y.; Hung, W.; Yongqi, F., A review of focused ion beam sputtering. *International Journal of Precision Engineering and Manufacturing* **2010,** *11* (1), 157-170.

2. Sadki, E. S.; Ooi, S.; Hirata, K., Focused-ion-beam-induced deposition of superconducting nanowires. *Applied Physics Letters* **2004,** *85* (25), 6206-6208.

3. Mattox, D. M., Chapter 9 - Ion plating and ion beam-assisted deposition. In *Handbook of Physical Vapor Deposition (PVD) Processing (Second Edition)*, Mattox, D. M., Ed. William Andrew Publishing: Boston, 2010; pp 301-331.

4. Takahashi, Y.; Ishii, H.; Tanabe, Y.; Watanabe, S.; Pang, Q.; Li, S.; Inoue, K., auger analysis of (al, ti)n/si interface synthesized by ion beam assisted deposition and optimization of film formation factors. In *Novel Materials Processing by Advanced Electromagnetic Energy Sources*, Miyake, S., Ed. Elsevier Science Ltd: Oxford, 2005; pp 423-426.

5. Dorozhkin, S. V., 7 - Surface modification of magnesium and its biodegradable alloys by calcium orthophosphate coatings to improve corrosion resistance and biocompatibility. In *Surface Modification of Magnesium and its Alloys for Biomedical Applications*, Narayanan, T. S. N. S.; Park, I.-S.; Lee, M.-H., Eds. Woodhead Publishing: 2015; pp 151-191.

6. Mahan, J. E., *Physical Vapor Deposition of Thin Films*. Wiley: 2000.

7. Robertson, J., Diamond-like amorphous carbon. *Materials Science and Engineering: R: Reports* **2002,** *37* (4–6), 129-281.

8. Cullen, R. J.; Jayasundara, D. R.; Soldi, L.; Cheng, J. J.; Dufaure, G.; Colavita, P. E., Spontaneous grafting of nitrophenyl groups on amorphous carbon thin films: a structure–reactivity investigation. *Chemistry of Materials* **2012,** *24* (6), 1031-1040.

9. Coburn, J. W., Surface processing with partially ionized plasmas. *IEEE Transactions on Plasma Science* **1991,** *19* (6), 1048-1062.

10. Graves, D. B., Plasma processing. *IEEE Transactions on Plasma Science* **1994,** *22* (1), 31-42.

11. Chapman, B. N., *Glow discharge processes : sputtering and plasma etching*. Wiley: New York, 1980.

12. Handbook of X-ray and ultraviolet photoelectron spectroscopy. Herausgegeben von D. Briggs; Heyden & Son LTD, 1977, 400 Seiten, DM 192,—. *Physik in unserer Zeit* **1979,** *10* (1), 30-30.

13. Gelius, U.; Hedén, P. F.; Hedman, J.; Lindberg, B. J.; Manne, R.; Nordberg, R.; Nordling, C.; Siegbahn, K., Molecular Spectroscopy by Means of ESCA III.Carbon compounds. *Physica Scripta* **1970,** *2* (1-2), 70-80.

14. Proctor, A.; Sherwood, P. M. A., X-ray photoelectron spectroscopic studies of carbon fibre surfaces—II: The effect of electrochemical treatment. *Carbon* **1983,** *21* (1), 53-59.

15. Yumitori, S., Correlation of C1s chemical state intensities with the O1s intensity in the XPS analysis of anodically oxidized glass-like carbon samples. *Journal of Materials Science* **2000,** *35* (1), 139-146.

16. Yang, D.; Velamakanni, A.; Bozoklu, G.; Park, S.; Stoller, M.; Piner, R. D.; Stankovich, S.; Jung, I.; Field, D. A.; Ventrice, C. A.; Ruoff, R. S., Chemical analysis of graphene oxide films after heat and chemical treatments by X-ray photoelectron and Micro-Raman spectroscopy. *Carbon* **2009,** *47* (1), 145-152.

17. Ferrari, A. C.; Robertson, J., Raman spectroscopy of amorphous, nanostructured, diamond–like carbon, and nanodiamond. *Philosophical Transactions of the Royal Society of London A: Mathematical, Physical and Engineering Sciences* **2004,** *362* (1824), 2477-2512.

18. Ferrari, A. C.; Robertson, J., Interpretation of Raman spectra of disordered and amorphous carbon. *Physical Review B* **2000,** *61* (20), 14095-14107.

19. Tay, B. K.; Shi, X.; Tan, H. S.; Yang, H. S.; Sun, Z., Raman studies of tetrahedral amorphous carbon films deposited by filtered cathodic vacuum arc. *Surface and Coatings Technology* **1998,** *105* (1–2), 155-158.

20. Shi, J. R.; Shi, X.; Sun, Z.; Lau, S. P.; Tay, B. K.; Tan, H. S., Resonant Raman studies of tetrahedral amorphous carbon films. *Diamond and Related Materials* **2001,** *10* (1), 76-81.

21. Ferrari, A. C.; Rodil, S. E.; Robertson, J., Interpretation of infrared and Raman spectra of amorphous carbon nitrides. *Physical Review B* **2003,** *67* (15), 155306.

22. Tai, F. C.; Lee, S. C.; Chen, J.; Wei, C.; Chang, S. H., Multipeak fitting analysis of Raman spectra on DLCH film. *Journal of Raman Spectroscopy* **2009,** *40* (8), 1055-1059.

23. Prawer, S.; Nugent, K. W.; Lifshitz, Y.; Lempert, G. D.; Grossman, E.; Kulik, J.; Avigal, I.; Kalish, R., Systematic variation of the Raman spectra of DLC films as a function of sp2:sp3 composition. *Diamond and Related Materials* **1996,** *5* (3), 433-438.

24. Leckey, R., Ultraviolet photoelectron spectroscopy of solids. In *Surface Analysis Methods in Materials Science*, O'Connor, D. J.; Sexton, B. A.; Smart, R. S. C., Eds. Springer Berlin Heidelberg: Berlin, Heidelberg, 1992; pp 291-300.

25. Colavita, P. E.; Sun, B.; Tse, K.-Y.; Hamers, R. J., Photochemical grafting of n-alkenes onto carbon surfaces: the role of photoelectron ejection. *Journal of the American Chemical Society* **2007,** *129* (44), 13554-13565.

26. Kahlert, H., Reference Electrodes. in electroanalytical methods: guide to experiments and applications, Scholz, F., Ed. Springer Berlin Heidelberg: Berlin, Heidelberg, 2002; pp 261-278.

27. Town, J. L.; MacLaren, F.; Dewald, H. D., Rotating disk voltammetry experiment. *Journal of Chemical Education* **1991,** *68* (4), 352.

28. Evgenij Barsoukov , J. R. M., *Impedance Spectroscopy: Theory, Experiment, and Applications*. 2005; p 616.

29. Grahame, D. C., The electrical double layer and the theory of electrocapillarity. *Chemical Reviews* **1947,** *41* (3), 441-501.

30. Parsons, R., *Modern Aspects of Electrochemistry*. 1954; Vol. 1.

31. Delahay, P., Double layer and electrode kinetics. Wiley-Inter science: New York, 1965.

32. Jüttner, K., Electrochemical impedance spectroscopy (EIS) of corrosion processes on inhomogeneous surfaces. *Electrochimica Acta* **1990,** *35* (10), 1501-1508.

33. Park, J.-S.; Choi, J.-H.; Woo, J.-J.; Moon, S.-H., An electrical impedance spectroscopic (EIS) study on transport characteristics of ion-exchange membrane systems. *Journal of Colloid and Interface Science* **2006,** *300* (2), 655-662.

34. Bard, A. J., *Electrochemical methods : fundamentals and applications / Allen J. Bard, Larry R. Faulkner*. Wiley: New York, 1980.

Chapter 3

Capacitive Storage at Nitrogenated Amorphous Carbon

The effect of nitrogen incorporation on the capacitive properties of amorphous carbon (a-C) thin-film electrodes is reported. A combination of structural characterisation methods, surface analysis and electrochemical analysis is performed in order to study the bulk electronic, structural, valences electronic properties, chemical composition and capacitance of the film.

The data presented in this chapter are part of the following publications:

1. Hoque, M. K.; Behan, J. A.; Stamatin, S. N.; Ciapetti, G.; Zen, F.; Esteban-Tejeda, L.; Colavita, P. E. ***RSC Adv.***, 2019,**9**, 4063-4071.
2. Behan, J. A.; Stamatin, S. N.; Hoque, M. K.; Ciapetti, G.; Zen, F.; Esteban-Tejeda, L.; Colavita, P. E. *The Journal of Physical Chemistry C* **2017,** ***121*****,** 12, 6596-6604.

Co-author contributions to this chapter are as follows: F.Z, and S.N. contributed several of the XPS and UPS measurements.

3.1 Introduction

As fossil fuel reserves diminish, there is an increasing demand on energy resources and growing environmental concerns. The development of clean and sustainable energy conversion and energy storage systems with low cost and high efficiency such as batteries, fuel cells and electrochemical capacitors has received much attention over the past few decades [1]. Carbon materials and nanomaterials play an important role in electrochemical energy conversion technologies. Carbon is ubiquitous as an electrode material and its electronic and capacitive properties and its surface chemistry are suitable for electrode materials for several applications such as fuel cells, capacitive storage devices and batteries. Carbon materials are also indispensable in electroanalysis Carbon electrodes have been used in a range of disciplines by materials chemists, engineers and physicists as well as those involved in more traditional (academic and technological) aspects of electrochemistry [2]. Highly graphitic forms of carbon such as carbon blacks and graphitic powders are used for energy application due to their low cost, good conductivity and reasonable resistance to corrosion. Development of porous carbon structure based materials using various synthetic methods has attracted tremendous interest in fuel cell electrocatalysis and energy-storage fields such as electrochemical capacitors and supercapacitors due to their high surface areas and high density of reactive edge sites [3-4].

Some of the best performing carbons for electrochemical capacitive storage consist of carbon materials with no long-range order or low crystallinity [5]. Porous activated carbon with high surface areas and porosities display excellent capacitive properties that can be comparable with more costly ordered carbon structure based materials such as graphene or carbon nanotubes [6]. These low costs activated carbon materials are synthesized through an activation process by creating a 3D porous network in the bulk. Their 3D structure contains a network of mainly sp^2 and some sp^3 bonded atoms. However, the presence of disorder can also lead to limited conductivity. The capacitive performance of these materials has been greatly improved during the past years. There is a great interest in understanding the interplay between interfacial capacitance, surface functionalities and bulk electronic properties in amorphous carbon materials [5-7].

The incorporation of nitrogen functional sites has emerged as one of the important tools to modulate both electronic and interfacial chemistry of carbon electrodes. Nitrogenation has complex and multifaceted effects on the physico-chemical properties of carbons such as change in metallic/semiconducting character [8], surface free energy and wettability [9-10], type of reactive sites and Lewis acid/base behaviour [11-12]. In recent decades the incorporation of nitrogen into carbon scaffolds has been investigated by several research groups [13-15]. There has been growing interest in understanding the effects of N-doping on the properties of carbon materials for electroanalytical applications [14, 16-17], as well as promising metal-free electrocatalytic performance in ORR[14, 18]. The effect of nitrogenation on the electrochemical double-layer and redox-capacitance of carbons and nanocarbons has therefore also received considerable attention with the objective of designing improved energy storage devices [19-20]. For instance, the effect of nitrogenation on the capacitance of carbon nanomaterials with crystalline structure such as graphene [21-22] or carbon nanotube [23- 24] or graphite [25] have been studied by several research groups. Recent work from our group has studied the effects of heteroatom N incorporation on the kinetics of interfacial charge-transfer at nitrogenated amorphous carbon (a-C:N) electrodes where the electrochemical redox response is correlated to the bulk electronic properties or dominated by surface effects [26].

In this chapter a detailed study of the effect of nitrogen incorporation on the capacitive properties of amorphous carbon (a-C) thin-film electrodes as a result of both surface chemical and electronic effects is presented. Nitrogenated carbon (a-C:N) thin film electrodes were synthesized with varying nitrogen content prepared via DC magnetron sputtering and the materials were characterized using X-ray photoelectron spectroscopy (XPS), ultraviolet photoelectron spectroscopy (UPS), Raman spectroscopy, cyclic voltammetry (CV), and electrochemical impedance spectroscopy (EIS). XPS, Raman and UPS were performed in order to study the bulk electronic, structural, valences electronic properties and chemical composition of the films. EIS measurement was carried out in both aqueous and organic media in order to distinguish electronic and pseudocapacitive contributions to the overall response.

It is shown that N doping can be achieved even with low level N_2 additions to the reactive gases during carbon deposition. High levels of N incorporation contribute mostly to the formation of functional groups and the disruption of the carbon scaffold with resulting loss of metallic character. Results in aqueous electrolyte show that a-C:N materials possess a very significant amount of higher capacitance compared with a-C due to porosity and pseudo capacitive contributions from N containing functional groups present in the surface of a-C:N electrode where results in organic electrolyte shows that the overall capacitance is mostly dominated by the double layer capacitance.

3.2. Materials and methods

3.2.1 Chemicals and Materials

Tetrabutylammonium hexafluorophosphate (TBAPF$_6$) (≥99.0%, electrochemical analysis), acetonitrile (MeCN, 99.8%, anhydrous), potassium chloride (Bioxtra, >99.0%), sulfuric acid (95 - 97%), hydrogen peroxide (>30% w/v), lithium chloride (>99%) were purchased from Sigma Aldrich. Glassy carbon (GC) discs (HTW Sigradur® radius 2.5mm) and B-doped Si wafers (MicroChemicals; resistivity 5 – 10 Ω-cm) were used as substrates for carbon deposition.

3.2.2 Substrate Preparation

GC disks were polished with finer grades of alumina slurry (Buehler). GC disks were first polished using 1200 grit sandpaper and 1 µm slurry. After rinsing with plenty of Millipore water the disks were sonicated for 20 min in Millipore water, polished on nylon paper (Buehler) using 1 µm slurry, sonicated for 20 min in Millipore water, then polished on nylon paper using 0.3 µm slurry and sonicated for 20 min in Millipore water; disks were subsequently polished to a mirror finish using 0.3 and 0.05 µm slurries on MicroCloths® pads (Buehler) and sonicated for 20 min in Millipore water between each steps. Clean disks were mounted in a custom-made Teflon® holder and placed in the vacuum chamber for deposition of thin film carbon electrodes on their surfaces. Si wafers were cleaned with piranha solution (3:1 H_2SO_4:H_2O_2; *CAUTION piranha solutions are explosive in contact with organics*), rinsed with plenty of Millipore water and dried with Ar prior to deposition.

3.2.3 Deposition of carbon electrode materials

Amorphous carbon films were deposited via DC-magnetron sputtering (Torr International) from a graphite target (99.999%) at base pressures <2 x10^{-6} mbar, deposition pressures 2-7 x10^{-3} mbar and total gas flow of 50 mL min^{-1}, following previously reported protocols [27, 28]. Nitrogenated a-C films (a-C:N) were synthesised by using N_2/Ar gas at flow ratios of 2%, 5% and 10% while keeping deposition time constant at 40 min, whereas non-nitrogenated amorphous carbon (a-C) was obtained by carrying out the deposition using 100% Ar during deposition. Nitrogen percentages were obtained by introducing a nitrogen (N4.5, BOC) and argon (N4.8, BOC) gas mixture into the sputtering chamber using two mass flow controllers

(Brooks Instruments).Total gas flow rate for all a-C:N electrode was kept at 50 ml min^{-1}. Deposited films are topographically smooth and in the thickness range 70-120 nm [28].

3.3 Characterization

In the case of a-C films, X-ray photoelectron spectroscopy (XPS) characterization was performed at 1×10^{-10} mbar base pressure in an ultrahigh vacuum system (Omicron), using monochromatic Al Kα source (1486.6 eV) and equipped a multichannel array detector. XPS spectra were collected at 45° take-off angle and 0.5 eV resolution. In the case of a-C:N films XPS characterization was performed on a VG Scientific ESCAlab Mk II system ($<2 \times 10^{-8}$ mbar), using Al Kα X-rays (1486.6 eV); core-level spectra were collected with analyzer pass energy of 20 eV and survey spectra were collected with analyzer pass energy of 200 eV. In order to do charge compensation an electron flood gun and the binding energy scale was referenced to the C 1s core-level at 284.8 eV. Peaks were fitted with Voigt functions after Shirley background subtraction using commercial software (CasaXPS); at.% composition was obtained from peak area ratios after correction by Scofield relative sensitivity factors (C = 1.0, N = 1.8, O = 2.93).

Ultraviolet photoelectron spectroscopy (UPS) measurements of a-C and a-C:N films were performed in an Omicron system at 1×10^{-10} mbar base pressure, using monochromatic Al Kα source (1486.6 eV) and equipped a multichannel array detector. UPS spectra were collected using He (I) excitation source (21.22 eV) at 90° take-off, with 0.02 eV analyser resolution. Negative bias were applied to the sample (0-12 V) to measure the high binding energy edge of the photoelectron spectrum; spectra were then corrected to account for bias and referenced to the Fermi energy measured on a Ag surface in contact with the carbon [29]. Work function (ϕ) values were calculated using the intercept at the binding energy axis of linear fits of the cut-off edge, as $\phi = 21.22 -$ intercept.

Raman spectra were measured in backscattering configuration using a Renishaw 1000 micro-Raman system equipped with an Ar$^+$ laser for 488 nm excitation and a HeNe laser for 633 nm excitation. The incident beam was focused by a Leica microscope with a 50× magnification objective and short-focus working distance; incident power was kept <2 mW to avoid sample damage. Spectra were baseline corrected using commercial software prior to analysis (Wire 3.2).

Electrochemical measurements were carried using a three-electrode cell controlled by a potentiostat with a graphite rod as counter electrode and Ag/AgCl (sat.) and Ag/Ag^+ reference electrodes (IJCambria) for characterisation in aqueous and organic electrolyte, respectively. A Teflon static disk holder (Pine Instruments) enclosing a GC disk coated with the sputtered carbon film was used as a working electrode; all contacts were confirmed to be ohmic with <8 Ω resistance. Cyclic voltammetry (CV) was carried out in aqueous 0.1 M KCl solutions and in 0.1 M $TBAPF_6$ solutions in MeCN, at 25 °C, 50 mV s^{-1} and using iR compensation. Electrochemical impedance spectroscopy (EIS) was carried out over the range of 0.1-100 kHz using a 10 mV AC amplitude. Spectra were collected at either open circuit potential (OCP) or at varying DC offsets in 0.2 V steps as indicated in the text; 300 s equilibration time was allowed between each potential step. The specific capacitance was obtained via normalisation by the geometric area of the electrodes; this was determined in aqueous solution via a Randles-Sevcik plot [28,30], and in 0.1 M $TBAPF_6$/MeCN via capacitance measurements on a reference GC disk of known area to account for any capillary wetting within the Teflon shielding in MeCN [31].

3.4. Results and discussion

3.4.1 Chemical Composition of a-C and a-C:N Films

Nitrogen-free and nitrogenated carbon electrodes were prepared in the form of thin films via magnetron sputtering and characterised as described in previous work from our group [28]. In order to deposit nitrogenated carbon film introduction of N_2 in the gas flow at varying % flow ratios of 2%, 5% and 10% results in electrode materials referred to as a-C:N-2%, a-C:N-5% and a-C:N-10% , respectively. The chemical composition of a-C and a-C:N films were examined using XPS measurements. Survey scans of all the films show characteristic C 1s, O 1s and N 1s peaks at 284, 532 and 400 eV, respectively (Figure 3.1). a-C was prepared without N_2 in the gas flow exclusively Ar in the deposition gas, as confirmed by the absence of N 1s peaks in the survey spectra.

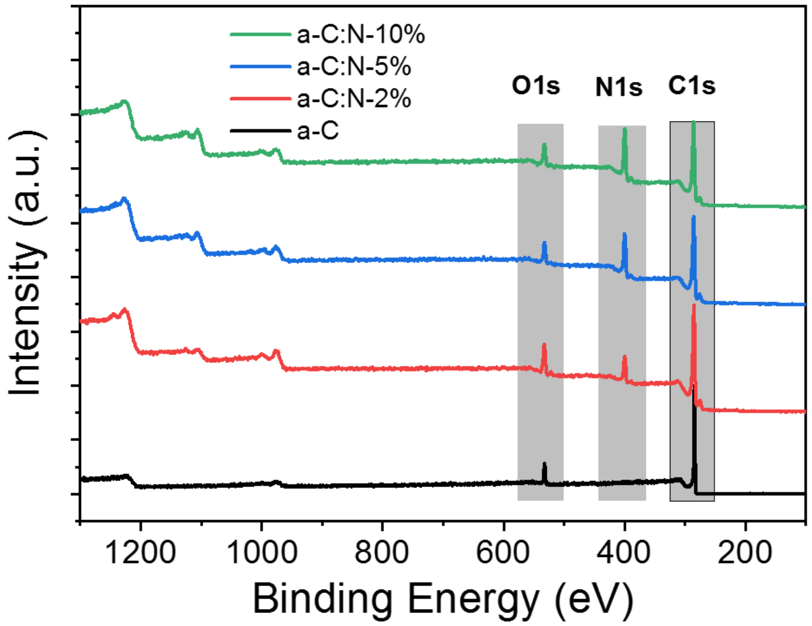

Figure 3.1: XPS spectra of survey scans of a-C and a-C:N-2-10% films.

Figures 3.2 a-c show the N 1s spectra of a-C:N-2%, 5% and 10%, respectively. The broad peak envelope results from the total contribution of multiple N-sites. Atomic surface concentrations were obtained from a deconvolution of the N 1s peak into five contributions corresponding to pyridinic (398.6 eV), pyrrolic (400.2 eV), graphitic-center (401.1 eV), graphitic-valley (402.1 eV) and N-oxides (403.5 eV) [32-33]. Figure 3.2 d shows N/C % as a function of N_2 % in the chamber where N/C % increases with the increment of N_2 % in the deposition chamber. Pyridinic-N and pyrrolic-N sites were found to dominate the N 1s spectra as N/C % of them is high among the N-sites.

XPS and Tauc gap results are presented in Table 3.1 where the nitrogen content in the carbon scaffold increases with increasing N_2 flow% in the chamber. The increase of Tauc gap values indicate an increase in semiconducting character. All a-C:N films have been shown to possess a mixture of N-sites such as pyridinic-N, pyrrolic-N, graphitic-N and N-oxides and they were found to be smooth and conformal to the substrate surface [28].

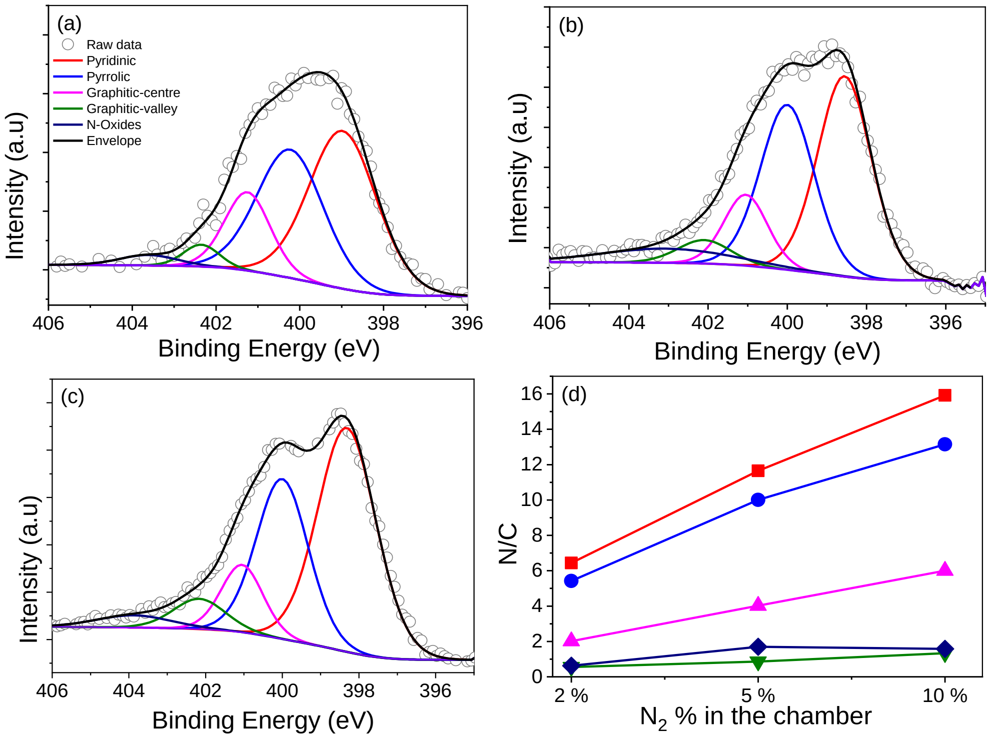

Figure 3.2: XPS N1 spectra of (a) a-C:N-2% (b) a-C:N-5% (c) a-C:N-10%. (d) Total N/C as a function of N_2 % present during deposition.

3.4.2 Structural Characterization of a-C and a-C:N electrodes using Raman spectroscopy

Raman spectroscopy is a popular and non-destructive tool which is commonly used to characterise the structural properties of amorphous carbons [34-36]. Figure 3.3 shows baseline-corrected Raman spectra in the 900-1900 cm^{-1} range of a-C and a-C:N electrodes deposited on silicon wafers, obtained using 488 nm excitation. Spectra display two broad peaks characteristic of amorphous carbon materials, assigned to the G and D bands at approximately 1580 cm^{-1} and 1380 cm^{-1}, respectively. The G band is associated with an optically allowed E_{2g} mode of sp^2 centres, while the D band is associated with a disorder-allowed A_{1g} mode of six-membered carbon rings in graphite [36-39]. Although it is not possible to exclude contributions from C-N and N-N modes in the same spectral region, Raman spectra of a-C:N materials is typically interpreted without an attempt to discriminate contributions from heterocyclic structures to these two main vibrational modes in the carbon matrix [38].

The spectral profile changes significantly after the introduction of N_2 in the deposition gas, as the D band increases in intensity relative to the G peak, suggesting a significant restructuring of the carbon matrix due to nitrogen incorporation. All Spectra were deconvoluted using two Gaussian peaks [40-42] and presented in figure 3.4. Figure 3.4 a-d displays deconvoluted a-C, a-C:N-2-10% spectra using two Gaussian peak fitting method and all the spectra were normalised prior to fitting. The main peak parameters were used to generate the data in Figures 3.5a-d. Peak heights from best fits were used to calculate the I_D/I_G ratio of each spectrum, which is diagnostic for amorphous carbon materials [34, 37-38, 43-44]. Figure 3.5a shows the change in I_D/I_G vs. N_2%-content in the deposition. Upon introduction of 2% N_2 the relative height of the D band increases when compared with the nitrogen-free a-C material, which indicates an increase in the concentration of six-membered rings within the amorphous carbon scaffold [38]. The I_D/I_G ratio is known to increase as the average graphitic cluster size L_a increases in amorphous carbons, as discussed by Ferrari and Robertson [37]; therefore, the increase of I_D/I_G for a-C:N-2% relative to a-C confirms the important effect of nitrogenation on the clustering of sp^2 centres. However, higher concentrations of N_2 (>25% N/C at.%) result in a decrease of the I_D/I_G value, suggesting that at high concentrations, the dominant effect of these heteroatoms is that of disrupting the graphitic network in a-C:N, leading to greater defect density. This is supported by an analysis of the full width half maximum (FWHM) of the G band shown on Figure 3.5b; this FWHM is diagnostic of the distribution of bond angles at excited sp^2 centres and therefore tracks the local carbon disorder [38]. It is evident from the figure that a slight increase in FWHM is observed for a-C:N-2% and -5% relative to a-C, whereas a-C:N-10% shows a major increase in FWHM that indicates a broad distribution of bonding geometries for sp^2 centres.

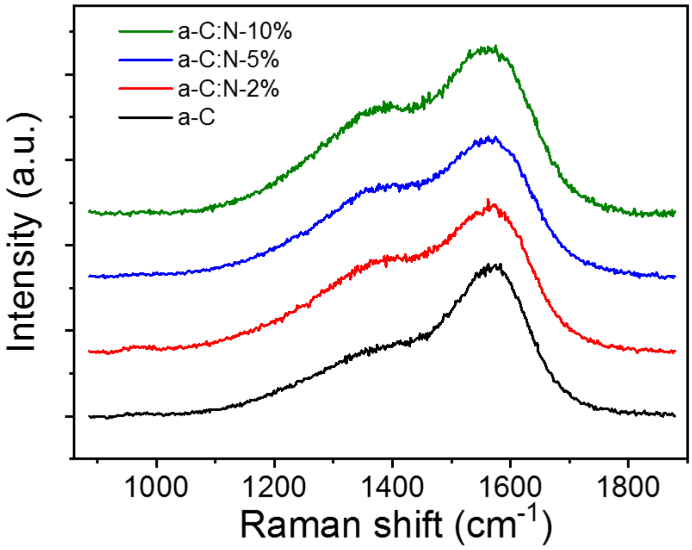

Figure 3.3: Raman spectra of amorphous carbon electrodes prepared with varying N_2% content in the deposition gas mixture; excitation 488 nm. Spectra are normalised relative to the G band intensity.

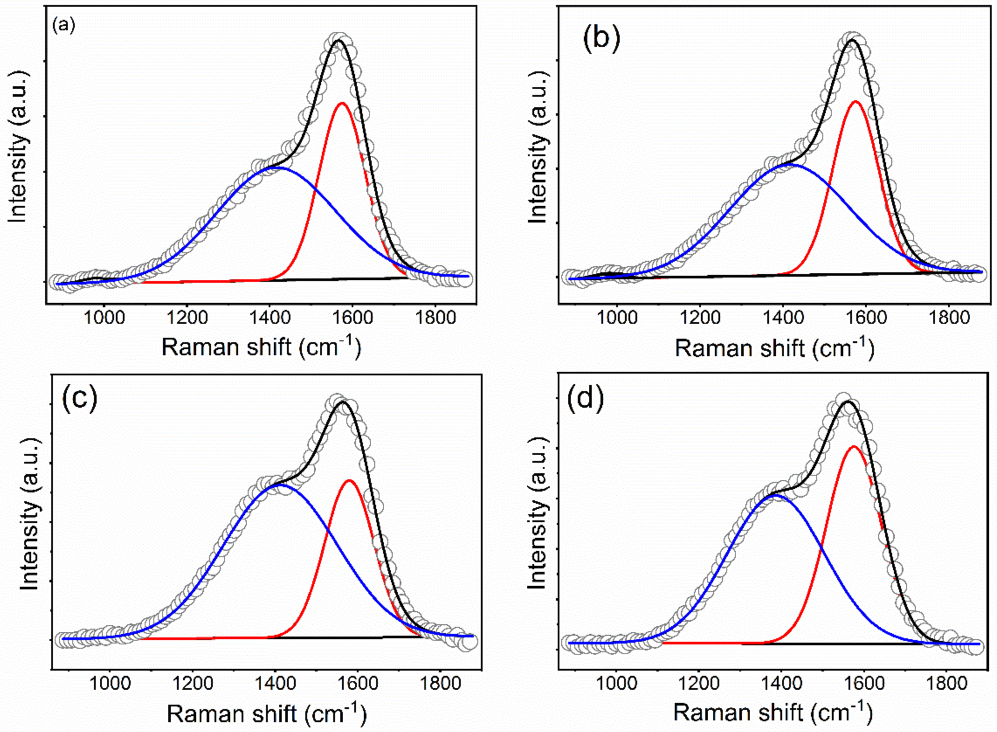

Figure 3.4: Raman spectra and peak deconvolution of (a) a-C, (b) a-C:N-2%, (c) a-C:N-5% and (d) a-C:N-10%; excitation 488 nm. Spectra are normalised relative to the G band intensity.

The trends observed are in good agreement with those reported by Ferrari et al. for amorphous carbon films with increasing nitrogen content deposited using a variety of methods. Figure 3.5c-d shows change in d peak position and FWHM of d peak vs. N_2%-content in the deposition. No significant change in d peak position and FWHM of d peak was observed upon nitrogen incorporation whereas further nitrogen incorporation in a-C:N-10% a major decrease in D peak position and FWHM indicating a greater disorder. Raman results for nitrogenated a-C:N films are generally more complex to interpret than for nitrogen-free a-C, due to the non-uniqueness of sp^3-centre content and sp^2 structuring that results from nitrogen incorporation [38]. However, the dispersion of the G peak position is unequivocally associated with disordering as a result of nitrogenation; for this purpose, Raman spectra obtained at 633 nm excitation were also analysed to obtain the values of G-peak dispersion summarised in Figure 3.61b. G peak dispersion falls sharply upon incorporation of nitrogen indicating an ordering effect resulting from nitrogenation [37]. However, further nitrogen incorporation in a-C:N-10% does not result in greater ordering and a slight increase in dispersion is registered, in agreement with trends in Figures 3.4a-b. In summary, analysis of Raman spectra indicates that a-C:N-2% and a-C:N-5% possess a more graphitic structure than nitrogen-free a-C; this is in agreement with previous determinations of Tauc gaps, which indicate an increase in metallic character for these two materials vs. a-C.

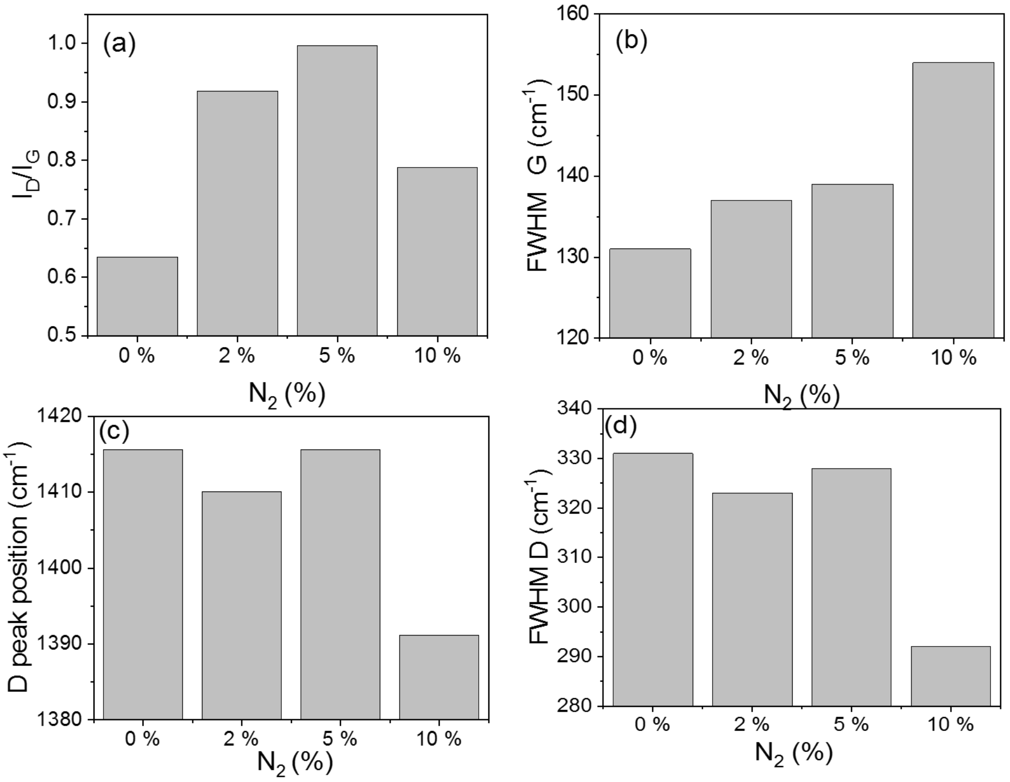

Figure 3.5: (a) Variation of D to G peak height ratio (ID / IG), (b) FWHM G peak (c) D peak position and (d) FWHM of D peak vs. N_2% content in the deposition gas.

Further incorporation of nitrogen to form a-C:N-10% however results in carbon materials that are significantly more defective, and that likely possess smaller graphitic cluster sizes. This confirms that using the range 0-10% N_2 concentration in our deposition system it is possible to explore both the ordering and the defect-inducing effects of nitrogen incorporation on the electrochemical performance of non-crystalline carbon electrodes.

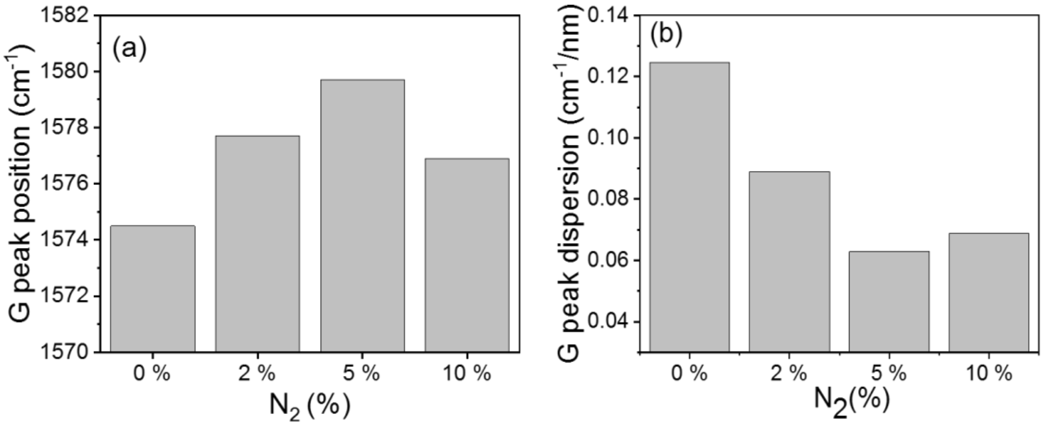

Figure 3.6: (a) G peaks position and (b) G peak dispersion vs. N_2% content in the deposition gas (bottom axis).

Table 3.1. Summary of properties of sputtered a-C:N electrodes used in our studies

Sample	N_2 %	N at.%[a]	N/C at.%[a]	Tauc gap[a]	Φ (eV)[b]
a-C	0%	n/a	n/a	0.66 ± 0.01	4.69±0.03
a-C:N-2%	2%	8.3	15	0.25 ± 0.07	4.94±0.02
a-C:N-5%	5%	15.6	28	0.19 ± 0.09	4.82±0.01
a-C:N-10%	10%	19.5	35	0.7 ± 0.1	4.84±0.02

a - values of N at%. And Tauc gap determined via XPS and ellipsometry, respectively, from [28, 45]. *b* – obtained from UPS in this work.

3.4.3 Valence Electronic Properties of a-C and a-C:N electrodes

UV photoelectron spectroscopy (UPS) was used to study the valence electronic properties of a-C and a-C:N electrodes. The UPS spectra in the high-binding and low-binding energy regions is presented in Figure 3.7a and 3.7b, respectively. The high binding energy edge was used to calculate work function values (ϕ), which are summarised in Table 3.1. The work function of a-C at 4.69 eV is in good agreement with previous reports on magnetron sputtered carbon [29, 46] and close to values quoted for graphitic nitrogen-free materials such as graphite (4.4 eV) [47-48] and glassy carbon (4.6 eV) [48]. Incorporation of nitrogen results in an increase of work function values which fall in the range 4.82-4.94 eV; these values are above those of a-C but below those reported for O-terminated sputtered carbons (5.1 eV) [49]. The observed increase of ϕ upon N-modification is in agreement with experimental results by Wiggins-Camacho and Stevenson [24] obtained from nitrogenated and N-free carbon nanotubes. Nitrogen incorporation can result in both an increase [24, 50] or a decrease [51-52] in the work function of carbons arising from changes to semiconducting properties (e.g. n-type doping) and from the creation of surface functional groups. The observed increase suggests the presence of C—N terminations that add a positive contribution from surface dipoles to the work function [29, 50], as observed for O-containing groups [49, 51, 53] and as argued in the case of N-modified carbon nanotubes in [24]. No clear trend could be identified over the 2-10% deposition range, however it is possible that reorganisation of the carbon scaffold, e.g. due to defect creation [24] or to clustering of sp^2 centres [38], might further contribute to the net change in ϕ, thus resulting in a non-linear trend vs. N-content.

Figure 3.7b shows details of the photoemission intensity of a-C:N samples and that of N-free a-C near E_F. The intensity changes suggest that incorporation of nitrogen results in a slight increase in occupied states near the E_F for a-C:N-2% (N/C = 15 at.%) and to a larger extent for a-C:N-5% (N/C = 28 at.%); further incorporation in a-C:N-10% (N/C = 35 at.%) appears to result in a decrease in occupied states. These observations are consistent with metallic/semiconducting character inferred from Tauc gap values (Table 1). Interestingly, the photoemission near E_F is maximised for a-C:N-5% which is also the sample that appears to be richest in graphitic clusters based on Raman results.

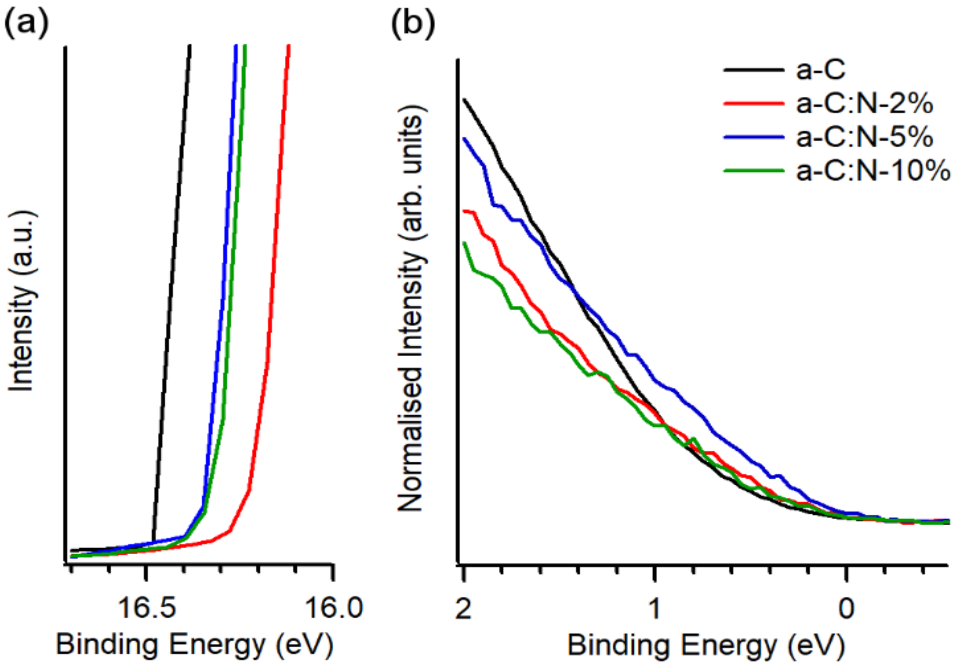

Figure 3.7: UPS of a-C and a-C:N electrodes. (a) High binding energy cut-off obtained at 10 V bias, showing the change in work function due to nitrogen incorporation. (b) Low binding energy region of N-free a-C and a-C:N materials showing photoemission near E_F; spectra are shown normalised by the total photoemission intensity. (adapted from reference 54). [54]

3.4.4 Electrochemical Characterization in aqueous electrolyte (0.1 M KCl)

In order to study electrochemical capacitance responses cyclic voltammetry (CV) and electrochemical impedance spectroscopy (EIS) was carried out using a three-electrode system. Figure 3.8 shows typical cyclic voltammograms (CVs) of a-C and a-C:N electrodes over the -0.3 – 0.7 V potential window at 50 mV s^{-1} in 0.1 M KCl. The CV response of a polished GC substrate disk is also included for comparison. The curves display the characteristic shape of a capacitive response, with all capacitive currents being larger than that of the GC substrate disk. Capacitance of a-C:N electrodes increases with progressively higher current upon incorporation of Nitrogen into carbon scaffold.

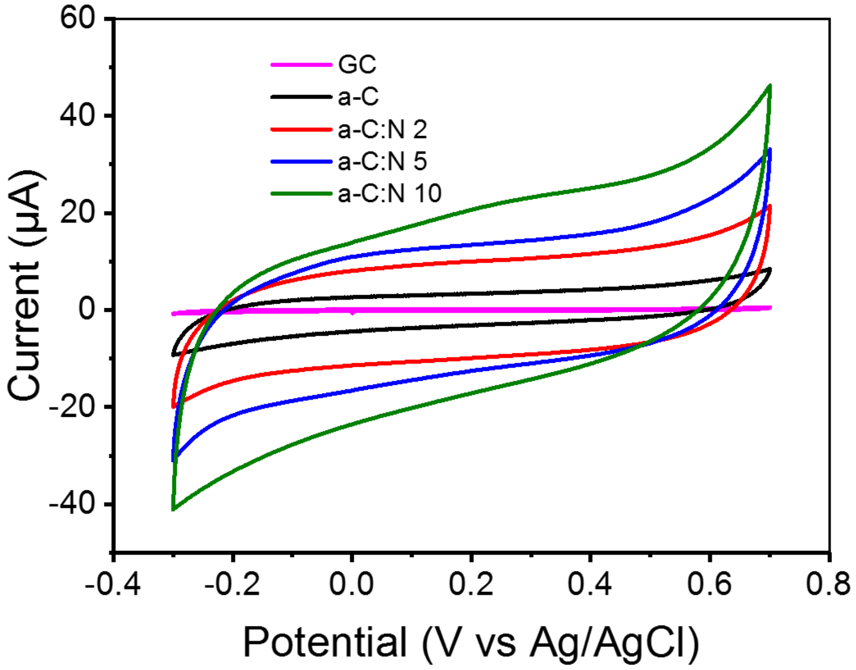

Figure 3.8: Cyclic votammograms of GC,a-C, a-C:N-2%-10% in Ar-saturated 0.1 M KCl at 50 mV s^{-1}. (Adapted from reference 54)

In order to compare electrochemical capacitance responses of a-C:N electrodes EIS was carried out over the 0.1-10^5 Hz range in the same solution. Bode plots of absolute impedance (|Z|) and phase angle for nitrogen-free a-C electrodes and GC electrode obtained at OCP (0-0.05 V vs. Ag/AgCl) are shown in Figure 3.9a and 3.9b respectively. Results for the GC substrate are in good agreement with those reported for planar GC electrodes under similar conditions [55]. The GC electrode yields a response characteristic of an equivalent series RC circuit, thus consistent with a double layer capacitance (C_{dl}) contribution with close to ideal behaviour. At 0.1 Hz the phase angle is approximately -83°, slightly below the ideal capacitor value of -90°, while at high frequency the response is resistive (Phase ≈ 0°) with |Z| determined by the solution resistance (R_s). a-C electrodes display a lower impedance at low frequency compared to that of GC and a phase angle of -77°, indicating a mainly capacitive response; however, the appearance of an additional time constant evident from the phase plot at high frequency (~600 Hz) suggests the presence of at least two distinct capacitive contributions. Figures 3.9c and 3.9d show Bode plots obtained for a-C:N-2%-10% electrodes. The curves indicate that nitrogenation results in a further reduction in |Z| and greater deviations from ideal capacitive behaviour, while at high frequency the plots show evidence of additional capacitive contributions to the overall response.

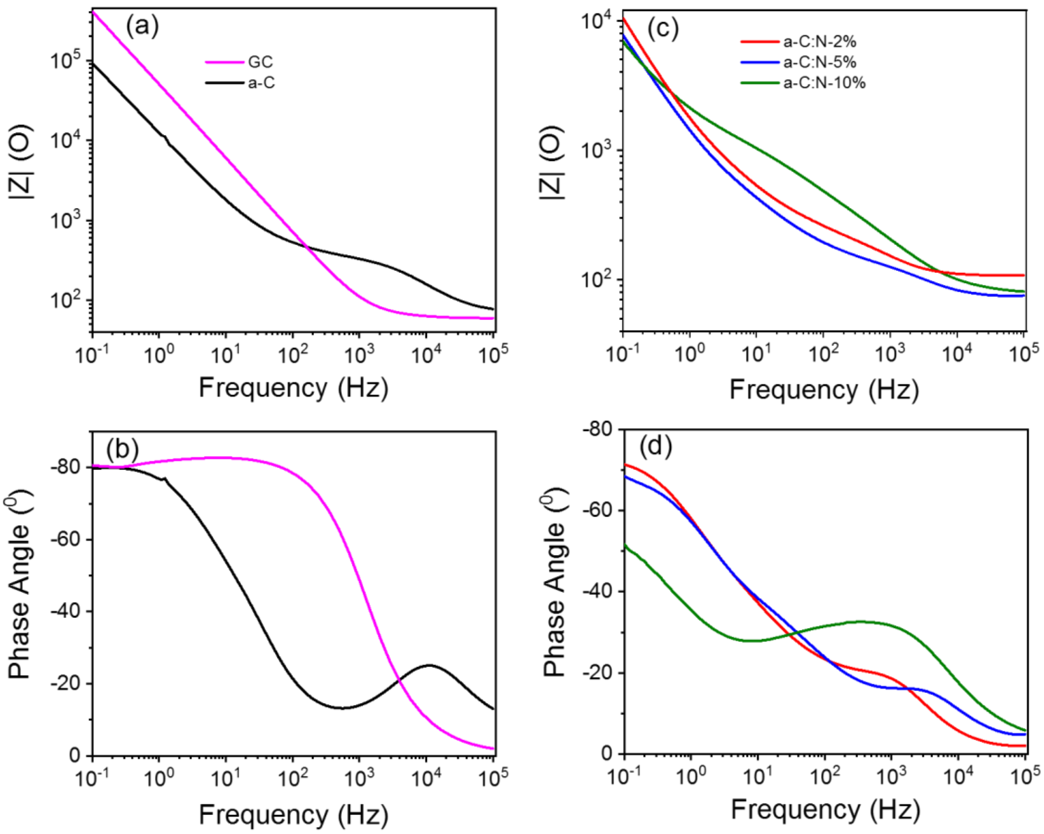

Figure 3.9. Bode plots of impedance module |Z| and phase angle of (a-b) nitrogen-free GC and a-C electrodes and (c-d) of nitrogenated a-C:N-2%, a-C:N-5% and a-C:N-10%. EIS spectra obtained in 0.1 M KCl at open circuit potential (OCP, 0.01-0.05 V vs. Ag/AgCl). (Adapted from reference 54).

The effective or equivalent series capacitive contribution to EIS spectra was calculated as a function of frequency *f* from the imaginary part of the complex impedance Z_{im} according to:

$$C = -(2\pi f Z_{im})^{-1} \qquad (3.1)$$

Figure 3.10 shows a plot of the specific capacitance extracted over the 0.1-500 Hz range at OCP. The capacitance for the GC electrode was found to be 16 μF cm^{-2} at 1 Hz, in good agreement with reference values of C_{dl} in aqueous KCl [30], while the capacitance for nitrogen-free a-C is 4.4 times larger at *ca.* 70 μF cm^{-2}. A very significant increase in capacitance is observed for a-C:N materials which yielded values in the mF cm^{-2} range. In the case of a-C:N samples there is also clear evidence of frequency dispersion, which is related to disorder and inhomogeneity in electrode surfaces [56-57], and this is seen to be particularly pronounced for a-C:N-10%.

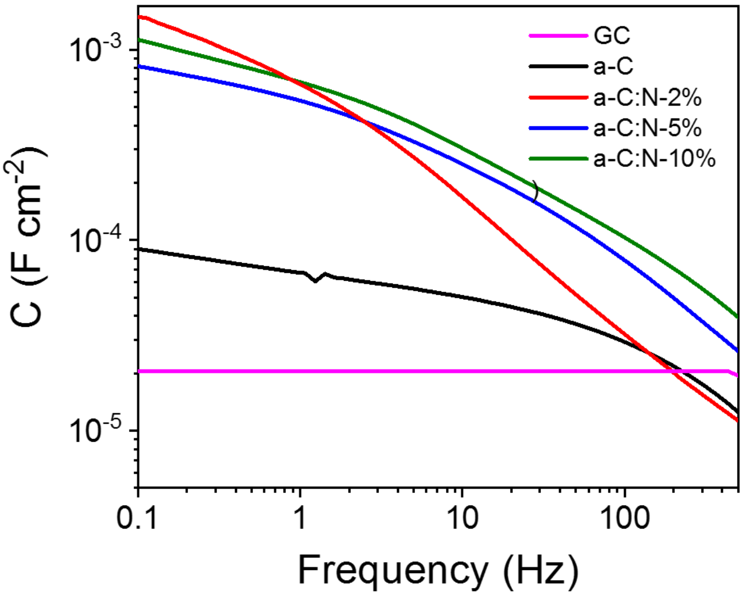

Figure 3.10. Equivalent series capacitance at OCP in 0.1 M KCl.

Figure 3.11 shows the change in the series equivalent capacitance at 1 Hz as a function of the DC offset over the range -0.4 – 0.8 V vs. Ag/AgCl in 0.1 M KCl. The nitrogen-free a-C electrode shows a shallow minimum in the capacitance that suggests a potential of zero charge (pzc) of 45 µF cm^{-2} at ca. 0.2 V. Nitrogenation leads to a considerable increase in the area-normalised capacitance. There is no detectable shift in the potential at the minimum capacitance for a-C:N-2% (*ca.* 0.5 mF cm^{-2}) and 5% (*ca.* 0.7 mF cm^{-2}), however, a significant positive shift is observed for a-C:N-10%, whose minimum (*ca.* 0.3 mF cm^{-2}) falls in the range 0.4-0.6 V. As the equivalent capacitance was calculated from the imaginary part of the Nyquist plot obtained at different applied potential, Nyquist plot of EIS spectra obtained at 0 V, 0.2 V and 0.4 V are presented in figure 3.12 a-b and 3.13 respectively. High frequency region of Nyquist plot is shown in inset. It is seen from Nyquist plot that real and imaginary impedance dropped enormously upon nitrogen incorporation which corresponds to the capacitance changes in Figure 3.11.

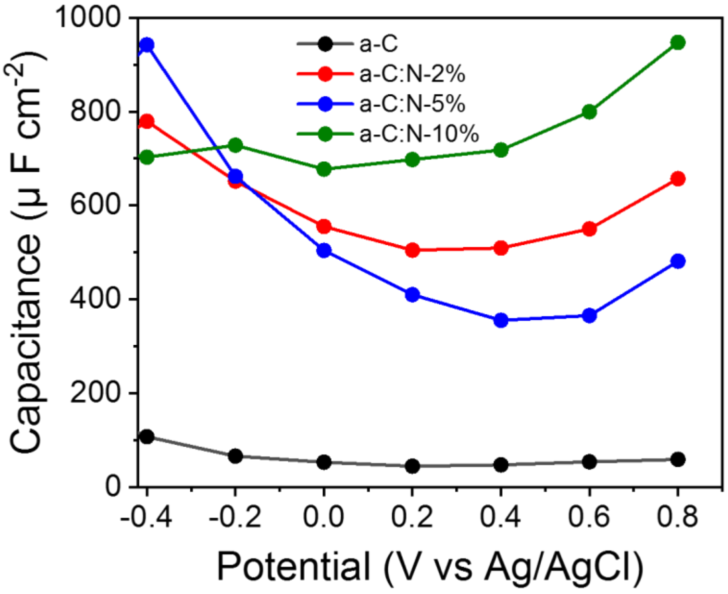

Figure 3.11. Equivalent series capacitance as a function of potential in 0.1 M KCl calculated at 1 Hz. (Adapted from reference 54)

The capacitance values of nitrogenated a-C:N electrodes in Figure 3.11 are large compared to those typical of planar carbon electrodes (1-70 µF cm^{-2} [30, 58-59]). This indicates that a-C:N materials possess intra-film capacitance due to porosity and/or pseudo-capacitive contributions. The presence of both such contributions is reasonable as a result of nitrogen incorporation. Previous work had shown that these a-C:N films are topographically smooth and featureless, however they might still allow for the presence of small cavities or "fissures" accessible to the electrolyte [60].

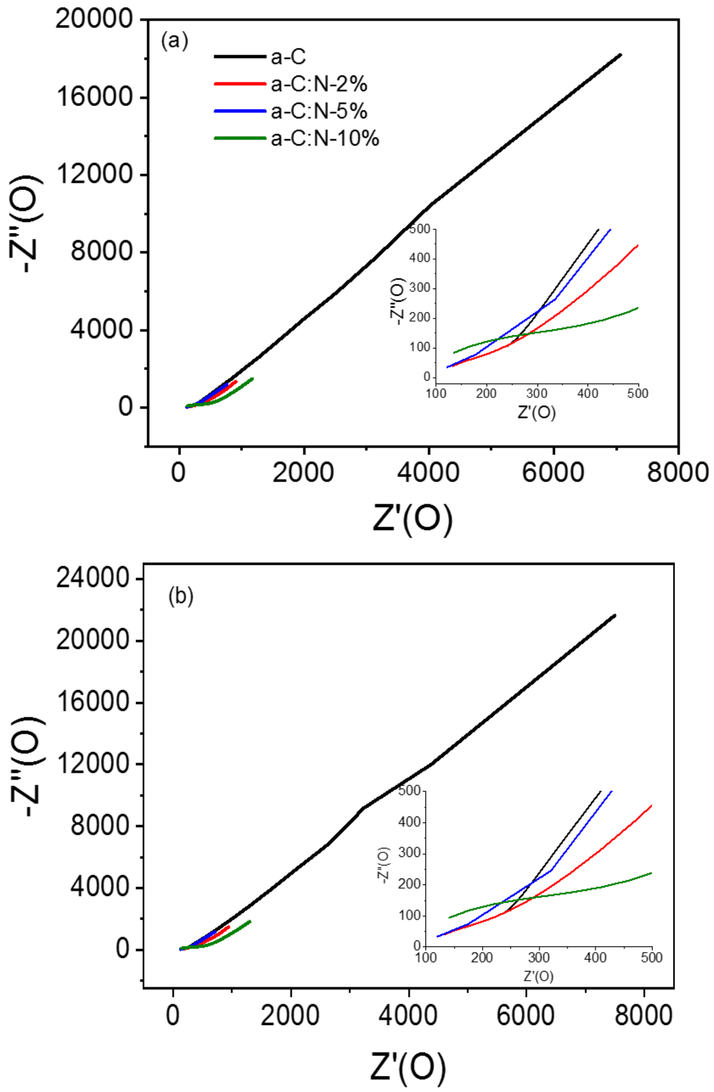

Figure 3.12: Nyquist plots of EIS spectra of a-C, a-C:N-2%, a-C:N-5%, a-C:N-10% in aqueous 0.1 M KCl at (a) 0.0 V, (b) 0.2 V. The inset shows the magnified portion of the Nyquist plots near the origin.

As the capacitive response at low frequency results from probing by the AC signal deep into any pores present in the material [61-63], the large values observed could arise from intra-film porosity in all three a-C:N electrodes. This appears possible when considering the structurally disruptive effect of nitrogenation at high concentrations on the graphitic matrix [28, 38].

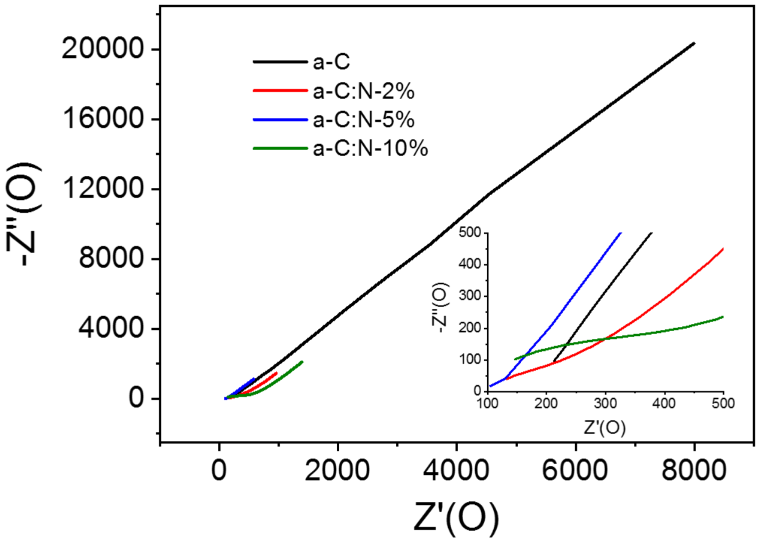

Figure 3.13: Nyquist plots of EIS spectra of a-C, a-C:N-2%, a-C:N-5%, a-C:N-10% in aqueous 0.1 M KCl at 0.4 V. The inset shows the magnified portion of the Nyquist plots near the origin.

Beyond the development of a pore structure, nitrogenation can also introduce local surface states due to structural disorder in the carbon scaffold which are known to result in increased capacitance at low frequency [60]. Finally, the presence of N-containing functional groups at the a-C:N surface in a protic solvent can promote specific adsorption [64] and redox reactions at these sites (e.g. amine/hydroxylamine, amine/immine or pyridine/pyridone) [65-67], thus introducing a pseudo-capacitive contribution in parallel to that of the double layer capacitance.

3.4.5 Electrochemical Characterization in organic electrolyte (0.1 M TBAPF6/acetonitrile)

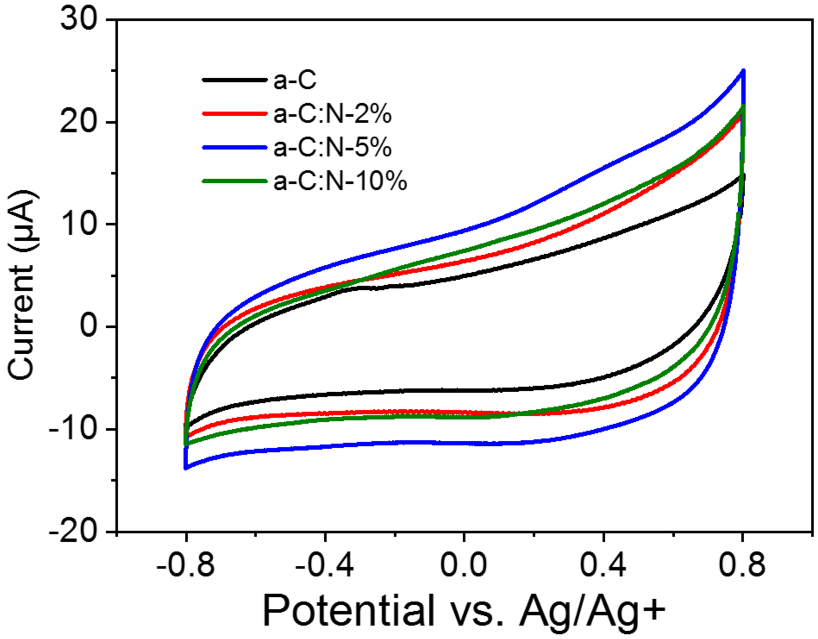

Figure 3.14: Cyclic votammograms of GC, a-C, a-C:N-2%-10% in Ar-saturated 0.1 M $TBAPF_6$ /acetonitrile at 50 mV s^{-1}.

To further study the effect of nitrogenation on the capacitive properties, electrochemical characterization was performed in organic electrolyte of 0.1 M $TBAPF_6$/acetonitrile. Figure 3.14 shows typical cyclic voltammograms (CVs) of a-C and a-C:N electrodes over the -0.3 – 0.7 V potential window at 50 mV s^{-1} in 0.1 M $TBAPF_6$/ acetonitrile. The curves display the characteristic shape of a capacitive response, with all capacitive currents of a-C:N electrode being larger than that of the a-C electrode. There is no faradic peak present within the potential window indicates no faradic contribution from electrolyte. Capacitance of a-C:N electrodes increases with progressively higher current upon incorporation of Nitrogen into carbon scaffold. Capacitance current of a-C:N-5% is among the highest compare with other a-C:N electrodes. CVs of a-C and a-C:N electrodes from -0.3 V to 0.2 V at different scan rates are displayed in figure 3.15.

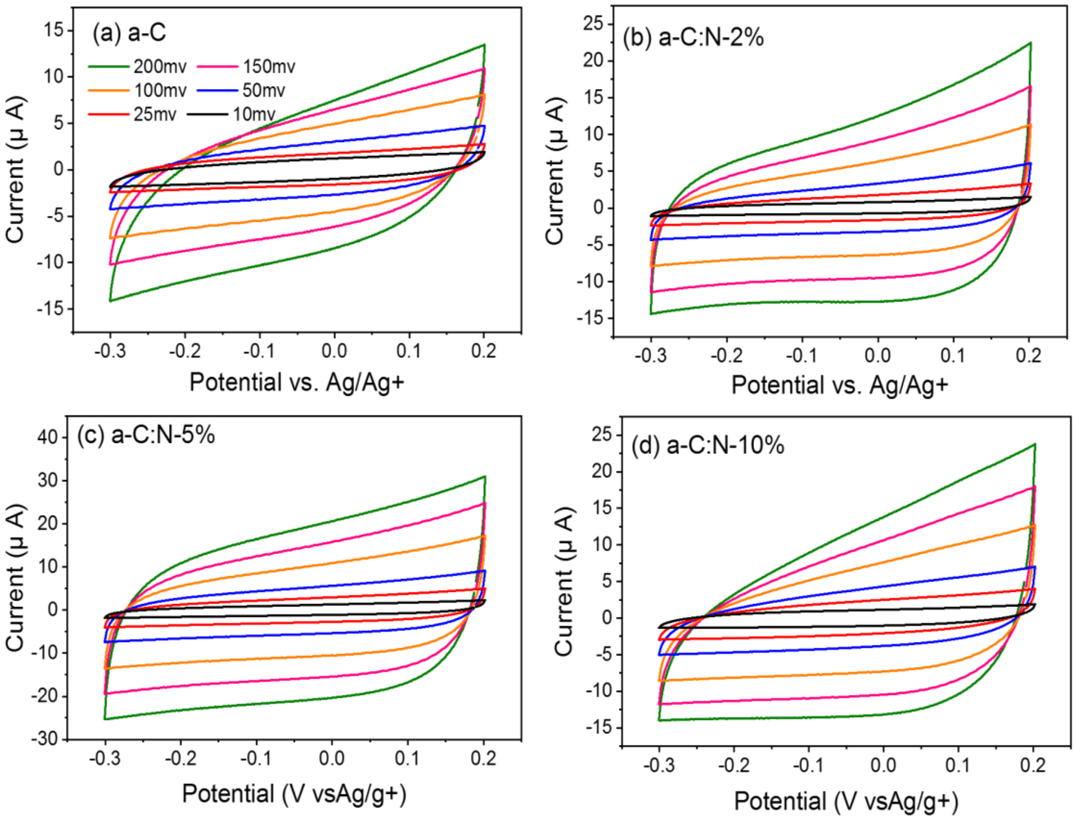

Figure 3.15: Cyclic voltammograms of a-C:N-2%, a-C:N-5% and a-C:N-10% electrode in 0.1 M $TBAPF_6$/acetonitrile at varying scan rates. No Faradaic peaks are visible in the potential window used for our experiments.

With the aim of investigating the effects of nitrogenation on the capacitive properties, while minimising complications arising from pseudo-capacitive effects, EIS studies were carried out in organic aprotic solvent using a 1:1 electrolyte with large ionic radii [24, 68, 69]. Bode plots of absolute impedance (|Z|) and phase angle for nitrogen-free a-C electrodes and GC electrode obtained at OCP (0 V-0.2 V vs. Ag/Ag+) are shown in figure 3.16a and 3.16b respectively. The GC electrode yields a response characteristic of an equivalent series RC circuit, thus consistent with a double layer capacitance (C_{dl}) contribution with close to ideal behaviour. The phase angle is approximately -80° at 20Hz and it decreases to -72° at 0.1 Hz. Impedance of a-C electrode display a low impedance at low frequency compare to that of GC and phase angle of -62° at 0.1 HZ. Figures 3.16c and 3.16d show Bode plots obtained for a-C:N-2%-10% electrodes. The curves indicate that nitrogen incorporation results in a further reduction in |Z| and greater deviations from ideal capacitive behaviour, while at high frequency the plots show evidence of additional capacitive contributions to the overall response.

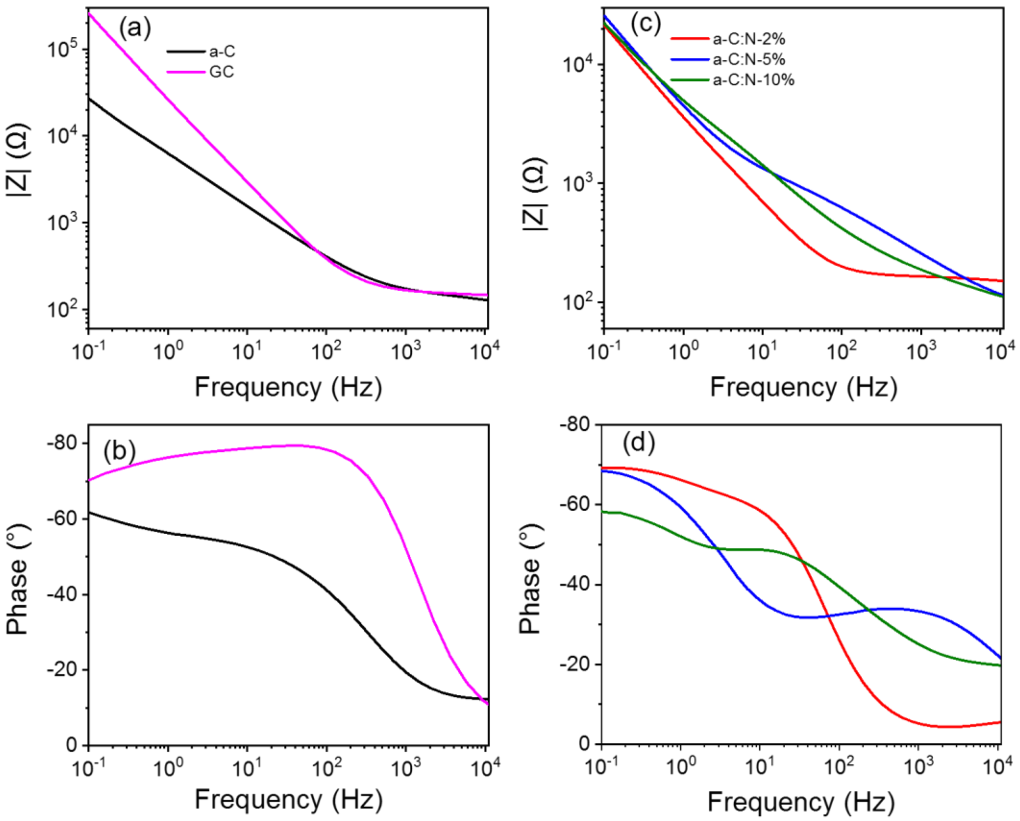

Figure 3.16: Bode plots of impedance module |Z| and phase angle of (a-b) nitrogen-free GC and a-C electrodes and (c-d) of nitrogenated a-C:N-2%, a-C:N-5% and a-C:N-10%. EIS spectra obtained in 0.1 M $TBAPF_6$/acetonitrile at open circuit potential (OCP, 0.01-0.05 V vs. Ag/Ag+). (Adapted from reference 54)

Figure 3.17 shows the series equivalent capacitance at 1 Hz as a function of potential over the range -0.6 – 0.8 V vs. Ag^+/Ag in 0.1 M $TBAPF_6$ in acetonitrile for a-C and a-C:N electrodes. The capacitance curve of the a-C electrode is asymmetric with a capacitance at pzc of 73 µF cm^{-2} at 0 V vs Ag^+/Ag. This value is 3.5 times larger than that of a GC electrode disk measured under identical conditions. The C_{aC}/C_{GC} ratio is very close to that observed in aqueous electrolyte, therefore indicating that the larger capacitance of a-C electrodes relative to GC is mostly due to microroughness effects. Remarkably, while the capacitances at the potential of zero charge for a-C:N in KCl are 5-10 times larger than that of a-C, the difference is instead small in $TBAPF_6$ solutions. The capacitances at pzc are remarkably close to each other and to the a-C value, being in a ratio $C_{aCN10} : C_{aC} : C_{aCN5} : C_{aCN2} = 1 : 1.1 : 1.4 : 1.4$. This strongly suggests that the large differences observed between a-C:N and a-C in KCl arise from pseudo-capacitive effects brought about by the presence of surface N-sites. Although it is not possible to exclude that intra-film porosity also contributes to the values in Figure 3.10, protonation and faradaic activity of N-sites can be identified as the dominant contribution to the capacitive response of a-C:N electrodes in aqueous KCl.

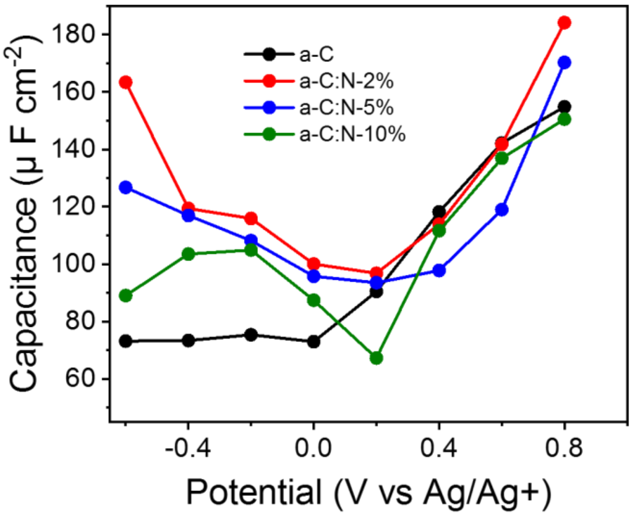

Figure 3.17. Equivalent series capacitance as a function of potential in 0.1 M TBAPF$_6$/acetonitrile calculated at 1 Hz. (Adapted from reference 54)

The capacitance in TBAPF$_6$/acetonitrile on the other hand is dominated by the double layer (C_{DL}); furthermore, use of a high electrolyte concentration also ensures that the series contribution to the double layer capacitance arising from the diffuse layer (C_{diff}) can be neglected. Under such conditions the observed capacitance is modulated by the electronic properties of a-C/a-C:N materials and by any differences in microroughness among the electrodes, thus enabling an analysis of the effects of nitrogen incorporation beyond those of surface chemical reactivity. The asymmetry in the a-C curve is consistent with an accumulation region at potentials anodic to 0 V vs Ag$^+$/Ag, which agrees with previous reports of p-type behaviour in nitrogen-free sputtered a-C [29, 70]. All of the plots for a-C:N materials display relatively symmetric minima at 0.2 V vs. Ag$^+$/Ag, thus indicating that nitrogen incorporation into a-C results in an increase in the pzc [71]. The shift in pzc relative to a-C is in good agreement with UPS data, which show that nitrogenation of a-C results in work function increases of 0.1-0.2 eV (Table 1). The minimum capacitance of a-C:N-10% is the lowest among a-C:N materials, while a-C:N-2% and a-C:N-5% display the largest ones; assuming that the microroughness factor remains constant across all sputtered electrodes, this finding is consistent with a-C:N-10% having the largest Tauc gap (Table 1) and greatest semiconducting character. The largest carrier density is achieved instead at low N/C contents. As the origin of capacitance calculation is from the imaginary part of the Nyquist plot obtained at different applied potential, Nyquist plots of EIS spectra obtained at 0 V, 0.2 V and -0.2 V are presented in figure 3.18 a-c respectively corresponding to the capacitance minima of a-C and a-C:N electrodes. Nyquist plots display low impedance for a-C:N electrodes compared to a-C electrodes, in good agreement with equivalent series capacitances obtained at different applied potentials.

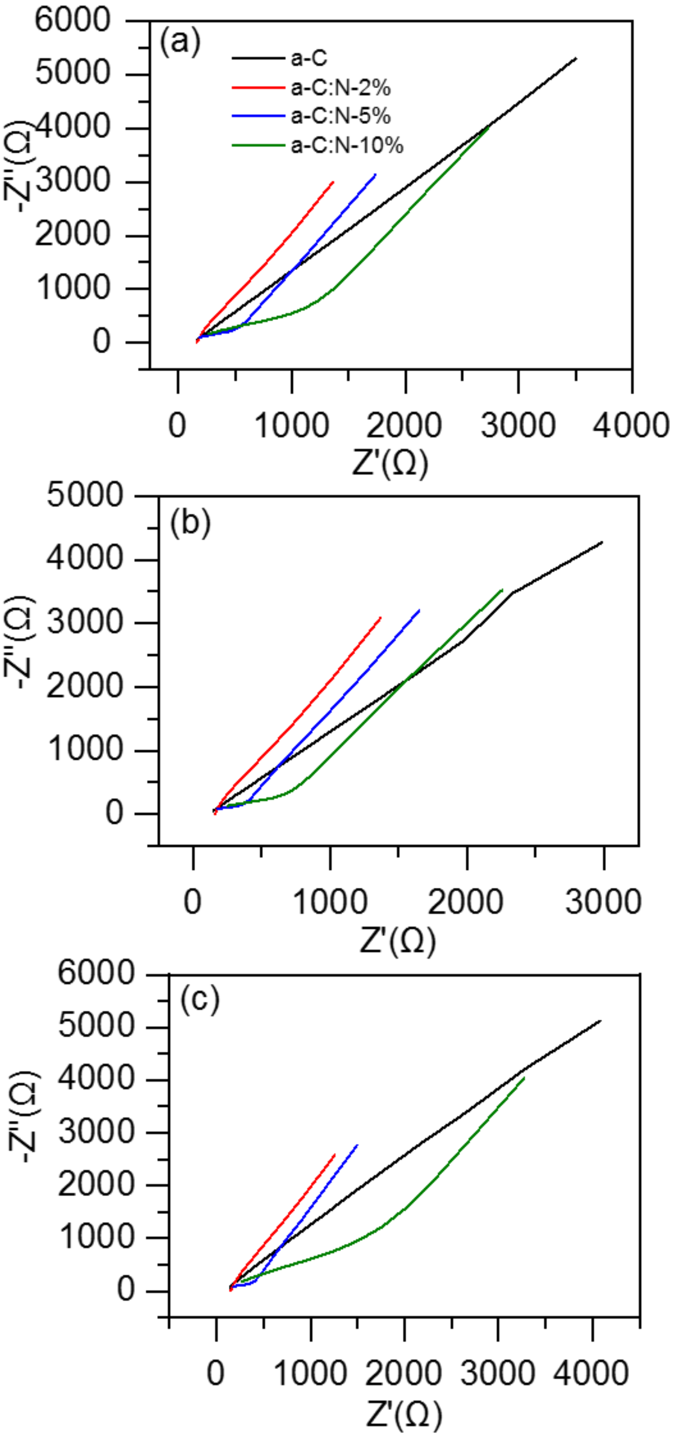

Figure 3.18: Nyquist plots of EIS spectra of a-C, a-C:N-2%, a-C:N-5%, a-C:N-10% in 0.1 M $TBAPF_6$/acetonitrile at (a) 0.0 V, (b) 0.2 V and (c) -0.2V.

In the absence of an experimental determination of the microroughness factor for each electrode, it is not possible to obtain estimates of the density of states from values of C_{pzc}, as previously done by other groups in the case of nanocarbon electrodes [24, 68]. However, it is interesting to note that C_{pzc} values are strongly correlated to the resistance to charge transfer (R_{ct}) obtained in our previous work with the same electrode materials using $Ru(NH_3)_6^{+2/+3}$ [28] an outer-sphere redox couple, as shown in Table 3.2. The highest R_{ct} values correspond to the lowest C_{pzc} values obtained from EIS and CV; as the R_{ct} is strongly dependent on the density of states near the Fermi energy this observation confirms that the trends observed in Figure 3.17 are controlled by the space-charge properties of a-C/a-C:N electrodes (albeit for small differences in microroughness). C_{pzc} values obtained from CV calculated using J_i/V formula where J_i is current density at applied potential and V is scan rate. C_{pzc} values obtained from CV is higher than that was obtained from EIS measurement as it depends on scan rates. On the basis of the asymmetry observed in the curves, it is therefore possible to conclude that N-free a-C materials start as p-doped in character; a small amount of nitrogen incorporation as in a-C:N-2% has a drastic effect in reducing the p-character, as expected from the role of group V atoms as n-type donors. This is evident from the greater symmetry in the C vs E curve and the increase in its C_{pzc} value, which are also consistent with the graphitizing effect of nitrogen incorporation observed from Raman. Further nitrogen incorporation, beyond ~15 at.% results in no apparent further increases in n-type character in the materials. This is likely due to rapid saturation of sites in the carbon matrix suitable for N-doping (graphitic-N); further increase in N/C at.% involve the creation of functional groups that instead contribute to pseudocapacitance in aqueous solutions.

Table 3.2. Capacitance at potential of zero charge (C_{pzc}) and comparison with resistance to charge transfer (Rct) reported in [28] for $Ru(NH_3)_6^{+2/+3}$.

Sample	**C_{pzc} ($\mu F\ cm^{-2}$) From EIS**	**R_{ct} (Ω) [28]**	**C_{pzc} ($\mu F\ cm^{-2}$) From CV**
a-C	73	256	89
a-C:N-2%	97	46	126
a-C:N-5%	94	21	118
a-C:N-10%	67	197	106

3.5. Conclusion

In this chapter a-C and N incorporated a-C in the form of thin films were prepared via magnetron sputtering and were characterised those using X-ray photoelectron spectroscopy (XPS), ultraviolet photoelectron spectroscopy (UPS), Raman spectroscopy, cyclic voltammetry (CV), and electrochemical impedance spectroscopy (EIS). XPS results show that all a-C:N materials possess a mixture of pyridinic-N, pyrrolic-N and graphitic-N and N oxides. Capacitance studies in aqueous KCl shows that a-C:N materials possess a significantly higher (5-10 times) capacitance compare to a-C due to porosity /pseudo capacitive contributions which is supported by observed trends in the work function for each surface. The capacitance of a-C:N-5 is higher than other a-C:N materials which is also correlated to I_D/I_G and Tauc gap, E_T. In order to avoid pseudo-capacitive effects from N containing functional group EIS studies carried out in organic electrolyte (0,1M $TMAPF_6$/acetonitrile) and results show that capacitance at pzc are remarkably close to each other which implies the capacitance in 0,1M $TBAPF_6$/ acetonitrile is dominated by the double layer capacitance. a-C:N 10 possesses the lowest capacitance minima among all a-C:N materials in 0,1M $TBAPF_6$/ acetonitrile which is consistent with it having the largest Tauc gap and greatest semiconducting character of the materials studied. The results presented herein demonstrate that low N incorporation reduce the p-type character of a-C and further incorporation increases the n -type character in the materials.

In the following chapter, the electrochemical capacitance response of the modified a-C and a-C:N materials will be studied. These materials will be prepared via post deposition treatments of the sputtered films such as thermal annealing and RF plasma treatment as described in Chapters V and VI.

3.6.References

1. Dunn, B.; Kamath, H.; Tarascon, J.-M., Electrical Energy Storage for the Grid: A Battery of Choices. **2011,** *334* (6058), 928-935.

2. Dyatkin, B.; Ash, P. A.; Sharma, S., Highlights from Faraday Discussion 172: Carbon in Electrochemistry, Sheffield, UK, July 2014. *Chemical Communications* **2015,** *51* (12), 2199-2207.

3. Qie, L.; Chen, W.; Xu, H.; Xiong, X.; Jiang, Y.; Zou, F.; Hu, X.; Xin, Y.; Zhang, Z.; Huang, Y., Synthesis of functionalized 3D hierarchical porous carbon for high-performance supercapacitors. *Energy & Environmental Science* **2013,** *6* (8), 2497-2504.

4. Kim, Y. J.; Yang, C.-M.; Park, K. C.; Kaneko, K.; Kim, Y. A.; Noguchi, M.; Fujino, T.; Oyama, S.; Endo, M., Edge-Enriched, Porous Carbon-Based, High Energy Density Supercapacitors for Hybrid Electric Vehicles. **2012,** *5* (3), 535-541.

5. Simon, P.; Gogotsi, Y., Capacitive Energy Storage in Nanostructured Carbon–Electrolyte Systems. *Accounts of Chemical Research* **2013,** *46* (5), 1094-1103.

6. Wei, L.; Sevilla, M.; Fuertes, A. B.; Mokaya, R.; Yushin, G., Hydrothermal Carbonization of Abundant Renewable Natural Organic Chemicals for High-Performance Supercapacitor Electrodes. *Advanced Energy Materials* **2011,** *1* (3), 356-361.

7. Moussa, G.; Hajjar-Garreau, S.; Taberna, P.-L.; Simon, P.; Matei Ghimbeu, C., Eco-Friendly Synthesis of Nitrogen-Doped Mesoporous Carbon for Supercapacitor Application. *C* **2018,** *4* (2), 20.

8. Robertson, J., Diamond-like amorphous carbon. *Materials Science and Engineering: R: Reports* **2002,** *37* (4–6), 129-281.

9. Serp, P.; Figueiredo, J. L., *Carbon Materials for Catalysis*. John Wiley & Sons: Hoboken, New Jersey, 2009.

10. Silva, S. R. P., *Properties of amorphous carbon*. 1st ed.; INSPEC, Inc. The Institution of Electrical Engineers: London, 2003.

11. Guo, D.; Shibuya, R.; Akiba, C.; Saji, S.; Kondo, T.; Nakamura, J., Active sites of nitrogen-doped carbon materials for oxygen reduction reaction clarified using model catalysts. *Science* **2016,** *351* (6271), 361.

12. Shao, Y.; Sui, J.; Yin, G.; Gao, Y., Nitrogen-doped carbon nanostructures and their composites as catalytic materials for proton exchange membrane fuel cell. *Applied Catalysis B: Environmental* **2008,** *79* (1), 89-99.

13. Robertson, J.; Davis, C. A., Nitrogen doping of tetrahedral amorphous carbon. *Diamond and Related Materials* **1995,** *4* (4), 441-444.

14. Yoo;, K.; Miller;, B.; Kalish;, R.; Shi;, X., Electrodes of Nitrogen-Incorporated Tetrahedral Amorphous Carbon A Novel Thin-Film Electrocatalytic Material with Diamond-like Stability. *Electrochemical and Solid-State Letters* **1999,** *2* (5), 3.

15. Zhang, J.; Xia, Z.; Dai, L., Carbon-based electrocatalysts for advanced energy conversion and storage. **2015,** *1* (7), e1500564.

16. Kamata, T.; Kato, D.; Hirono, S.; Niwa, O., Structure and electrochemical performance of nitrogen-doped carbon film formed by electron cyclotron resonance sputtering. *Anal Chem* **2013,** *85* (20), 9845-51.

17. Yang, X.; Haubold, L.; DeVivo, G.; Swain, G. M., Electroanalytical performance of nitrogen-containing tetrahedral amorphous carbon thin-film electrodes. *Anal Chem* **2012,** *84* (14), 6240-8.

18. Perini, L.; Durante, C.; Favaro, M.; Agnoli, S.; Granozzi, G.; Gennaro, A., Electrocatalysis at palladium nanoparticles: Effect of the support nitrogen doping on the catalytic activation of carbonhalogen bond. *Applied Catalysis B: Environmental* **2014,** *144*, 300-307.

19. Stephanie L.Candelariaa, Y., WeiZhouc,d, XiaolinLib, JieXiaob, Ji-Guang Zhangb, YongWangb, JunLiub,n, JinghongLic,d,nn, GuozhongCaoa Nanostructured carbon for energy storage and conversion. *Nano Energy* **2012,** *1* (2), 195–220.

20. Deng, Y.; Xie, Y.; Zou, K.; Ji, X., Review on recent advances in nitrogen-doped carbons: preparations and applications in supercapacitors. *Journal of Materials Chemistry A* **2016,** *4* (4), 1144-1173.

21. Zhan, C.; Zhang, Y.; Cummings, P. T.; Jiang, D.-e., Enhancing graphene capacitance by nitrogen: effects of doping configuration and concentration. *Physical Chemistry Chemical Physics* **2016,** *18* (6), 4668-4674.

22. Kumar, M. P.; Kesavan, T.; Kalita, G.; Ragupathy, P.; Narayanan, T. N.; Pattanayak, D. K., On the large capacitance of nitrogen doped graphene derived by a facile route. *RSC Advances* **2014,** *4* (73), 38689-38697.

23. Latil, S.; Roche, S.; Mayou, D.; Charlier, J.-C., Mesoscopic Transport in Chemically Doped Carbon Nanotubes. *Physical Review Letters* **2004,** *92* (25), 256805.

24. Wiggins-Camacho, J. D.; Stevenson, K. J., Effect of Nitrogen Concentration on Capacitance, Density of States, Electronic Conductivity, and Morphology of N-Doped Carbon Nanotube Electrodes. *The Journal of Physical Chemistry C* **2009,** *113* (44), 19082-19090.

25. Zhou, Y.; Holme, T.; Berry, J.; Ohno, T. R.; Ginley, D.; O'Hayre, R., Dopant-Induced Electronic Structure Modification of HOPG Surfaces: Implications for High Activity Fuel Cell Catalysts. *The Journal of Physical Chemistry C* **2010,** *114* (1), 506-515.

26. Behan, J. A.; Stamatin, S. N.; Hoque, M. K.; Ciapetti, G.; Zen, F.; Esteban-Tejeda, L.; Colavita, P. E., Combined Optoelectronic and Electrochemical Study of Nitrogenated Carbon Electrodes. *The Journal of Physical Chemistry C* **2017**.

27. Cullen, R. J.; Jayasundara, D. R.; Soldi, L.; Cheng, J. J.; Dufaure, G.; Colavita, P. E., Spontaneous Grafting of Nitrophenyl Groups on Amorphous Carbon Thin Films: A Structure–Reactivity Investigation. *Chemistry of Materials* **2012,** *24* (6), 1031-1040.

28. Behan, J. A.; Stamatin, S. N.; Hoque, M. K.; Ciapetti, G.; Zen, F.; Esteban-Tejeda, L.; Colavita, P. E., Combined Optoelectronic and Electrochemical Study of Nitrogenated Carbon Electrodes. *The Journal of Physical Chemistry C* **2017,** *121* (12), 6596-6604.

29. Colavita, P. E.; Sun, B.; Tse, K.-Y.; Hamers, R. J., Photochemical Grafting of n-Alkenes onto Carbon Surfaces: the Role of Photoelectron Ejection. *Journal of the American Chemical Society* **2007,** *129* (44), 13554-13565.

30. Kissinger, P.; Heineman, W. R., *Laboratory Techniques in Electroanalytical Chemistry, Second Edition, Revised and Expanded*. Taylor & Francis: 1996.

31. De Levie, R., Capillary response at a dropping mercury electrode. *Journal of Electroanalytical Chemistry (1959)* **1965,** *9* (2), 117-127.

32. Sharifi, T.; Hu, G.; Jia, X.; Wågberg, T., Formation of Active Sites for Oxygen Reduction Reactions by Transformation of Nitrogen Functionalities in Nitrogen-Doped Carbon Nanotubes. *ACS Nano* **2012,** *6* (10), 8904-8912.

33. Rodil, S. E.; Morrison, N. A.; Robertson, J.; Milne, W. I., Nitrogen Incorporation into Tetrahedral Hydrogenated Amorphous Carbon. **1999,** *174* (1), 25-37.

34. Chu, P. K.; Li, L., Characterization of amorphous and nanocrystalline carbon films. *Materials Chemistry and Physics* **2006,** *96* (2-3), 253-277.

35. Ferrari, A. C.; Robertson, J., Raman spectroscopy of amorphous, nanostructured, diamond–like carbon, and nanodiamond. *Philosophical Transactions of the Royal Society of London A: Mathematical, Physical and Engineering Sciences* **2004,** *362* (1824), 2477-2512.

36. Ferrari, A. C.; Rodil, S. E.; Robertson, J., Resonant Raman spectra of amorphous carbon nitrides: the G peak dispersion. *Diamond and Related Materials* **2003,** *12* (3–7), 905-910.

37. Ferrari, A. C.; Robertson, J., Interpretation of Raman spectra of disordered and amorphous carbon. *Physical Review B* **2000,** *61* (20), 14095-14107.

38. Ferrari, A. C.; Rodil, S. E.; Robertson, J., Interpretation of infrared and Raman spectra of amorphous carbon nitrides. *Physical Review B* **2003,** *67* (15), 155306.

39. Gilkes, K. W. R.; Prawer, S.; Nugent, K. W.; Robertson, J.; Sands, H. S.; Lifshitz, Y.; Shi, X., Direct quantitative detection of the sp3 bonding in diamond-like carbon films using ultraviolet and visible Raman spectroscopy. *Journal of Applied Physics* **2000,** *87* (10), 7283-7289.

40. Nathan, M. I.; Jr, J. E. S.; Tu, K. N., Raman spectra of glassy carbon. *Journal of Applied Physics* **1974,** *45* (5), 2370-2370.

41. Robertson, J., Properties of diamond-like carbon. *Surface and Coatings Technology* **1992,** *50* (3), 185-203.

42. Tai, F. C.; Lee, S. C.; Chen, J.; Wei, C.; Chang, S. H., Multipeak fitting analysis of Raman spectra on DLCH film. *Journal of Raman Spectroscopy* **2009,** *40* (8), 1055-1059.

43. Tamor, M. A.; Vassell, W. C., Raman ‘‘fingerprinting’’ of amorphous carbon films. *Journal of Applied Physics* **1994,** *76* (6), 3823-3830.

44. Yoshikawa, M.; Katagiri, G.; Ishida, H.; Ishitani, A.; Akamatsu, T., Raman spectra of diamondlike amorphous carbon films. *Journal of Applied Physics* **1988,** *64* (11), 6464-6468.

45. Zen, F.; Karanikolas, V. D.; Behan, J. A.; Andersson, J.; Ciapetti, G.; Bradley, A. L.; Colavita, P. E., Nanoplasmonic Sensing at the Carbon-Bio Interface: Study of Protein Adsorption at Graphitic and Hydrogenated Carbon Surfaces. *Langmuir* **2017,** *33* (17), 4198-4206.

46. Murphy, D. M.; Cullen, R. J.; Jayasundara, D. R.; Doyle, R. L.; Lyons, M. E. G.; Colavita, P. E., Heterogeneous Charge Transfer at the Amorphous Carbon/Solution Interface: Effect on the Spontaneous Attachment of Aryldiazonium Salts. *The Journal of Physical Chemistry C* **2013,** *117* (44), 22768-22777.

47. Chen, E. C. M.; Chen, E. S. D., Theoretical Basis of the Experimental Tools. In *The Electron Capture Detector and the Study of Reactions with Thermal Electrons*, John Wiley & Sons, Inc.: 2004; pp 47-74.

48. Lipkin, H. J., Beta-Ray Spectra. *Physical Review* **1949,** *76* (4), 567-567.

49. Colavita, P. E.; Sun, B.; Wang, X.; Hamers, R. J., Influence of Surface Termination and Electronic Structure on the Photochemical Grafting of Alkenes to Carbon Surfaces. *The Journal of Physical Chemistry C* **2009,** *113* (4), 1526-1535.

50. Kaukonen, M.; Nieminen, R. M.; Pöykkö, S.; Seitsonen, A. P., Nitrogen Doping of Amorphous Carbon Surfaces. *Physical Review Letters* **1999,** *83* (25), 5346-5349.

51. Yang, N.; Yang, D.; Chen, L.; Liu, D.; Cai, M.; Fan, X., Design and adjustment of the graphene work function via size, modification, defects, and doping: a first-principle theory study. *Nanoscale Research Letters* **2017,** *12* (1), 642.

52. Xu, J.; Mei, J.; Huang, X. H.; Li, X.; Li, Z.; Li, W.; Chen, K., Effect of nitrogen surface doping on the work function and field emission of hydrogenated amorphous carbon films. *Applied Physics A* **2005,** *80* (1), 123-126.

53. Ago, H.; Kugler, T.; Cacialli, F.; Salaneck, W. R.; Shaffer, M. S. P.; Windle, A. H.; Friend, R. H., Work Functions and Surface Functional Groups of Multiwall Carbon Nanotubes. *The Journal of Physical Chemistry B* **1999,** *103* (38), 8116-8121.

54. Hoque, M. K.; Behan, J. A.; Stamatin, Serban N.; Zen, F.; Perova, T. S.; Colavita, P. E., Capacitive storage at nitrogen doped amorphous carbon electrodes: structural and chemical effects of nitrogen incorporation. *RSC Advances* **2019,** *9* (7), 4063-4071.

55. Metz, K. M.; Colavita, P. E.; Tse, K.-Y.; Hamers, R. J., Nanotextured gold coatings on carbon nanofiber scaffolds as ultrahigh surface-area electrodes. *Journal of Power Sources* **2012,** *198*, 393-401.

56. Pajkossy, T., Impedance of rough capacitive electrodes. *Journal of Electroanalytical Chemistry* **1994,** *364* (1), 111-125.

57. Kerner, Z.; Pajkossy, T., On the origin of capacitance dispersion of rough electrodes. *Electrochimica Acta* **2000,** *46* (2), 207-211.

58. Fagan, D. T.; Hu, I. F.; Kuwana, T., Vacuum heat-treatment for activation of glassy carbon electrodes. *Analytical Chemistry* **1985,** *57* (14), 2759-2763.

59. Ranganathan, S.; Kuo, T.-C.; McCreery, R. L., Facile Preparation of Active Glassy Carbon Electrodes with Activated Carbon and Organic Solvents. *Analytical Chemistry* **1999,** *71* (16), 3574-3580.

60. Randin, J.-P.; Yeager, E., Differential capacitance study on the edge orientation of pyrolytic graphite and glassy carbon electrodes. *Journal of Electroanalytical Chemistry and Interfacial Electrochemistry* **1975,** *58* (2), 313-322.

61. Fletcher, S.; Black, V. J.; Kirkpatrick, I., A universal equivalent circuit for carbon-based supercapacitors. *Journal of Solid State Electrochemistry* **2014,** *18* (5), 1377-1387.

62. Yoo, H. D.; Jang, J. H.; Ryu, J. H.; Park, Y.; Oh, S. M., Impedance analysis of porous carbon electrodes to predict rate capability of electric double-layer capacitors. *Journal of Power Sources* **2014,** *267*, 411-420.

63. Lufrano, F.; Staiti, P., Conductivity and Capacitance Properties of a Supercapacitor Based on Nafion Electrolyte in a Nonaqueous System. *Electrochemical and Solid-State Letters* **2004,** *7* (11), A447-A450.

64. Jeong, H. M.; Lee, J. W.; Shin, W. H.; Choi, Y. J.; Shin, H. J.; Kang, J. K.; Choi, J. W., Nitrogen-Doped Graphene for High-Performance Ultracapacitors and the Importance of Nitrogen-Doped Sites at Basal Planes. *Nano Letters* **2011,** *11* (6), 2472-2477.

65. Kim, J.-I.; Park, S.-J., Effect of nitrogen-containing groups on enhanced capacitive behaviors of multi-walled carbon nanotubes. *Journal of Solid State Chemistry* **2011,** *184* (8), 2184-2189.

66. Béguin, F.; Szostak, K.; Lota, G.; Frackowiak, E., A Self-Supporting Electrode for Supercapacitors Prepared by One-Step Pyrolysis of Carbon Nanotube/Polyacrylonitrile Blends. *Advanced Materials* **2005,** *17* (19), 2380-2384.

67. Candelaria, S. L.; Shao, Y.; Zhou, W.; Li, X.; Xiao, J.; Zhang, J.-G.; Wang, Y.; Liu, J.; Li, J.; Cao, G., Nanostructured carbon for energy storage and conversion. *Nano Energy* **2012,** *1* (2), 195-220.

68. Gerischer, H.; McIntyre, R.; Scherson, D.; Storck, W., Density of the electronic states of graphite: derivation from differential capacitance measurements. *The Journal of Physical Chemistry* **1987,** *91* (7), 1930-1935.

69. Hahn, M.; Baertschi, M.; Barbieri, O.; Sauter, J.-C.; Kötz, R.; Gallay, R., Interfacial Capacitance and Electronic Conductance of Activated Carbon Double-Layer Electrodes. *Electrochemical and Solid-State Letters* **2004,** *7* (2), A33-A36.

70. Hastas, N. A.; Dimitriadis, C. A.; Panayiotatos, Y.; Tassis, D. H.; Patsalas, P.; Logothetidis, S., Noise characterization of sputtered amorphous carbon films. *Journal of Applied Physics* **2000,** *88* (9), 5482-5484.

71. Trasatti, S.; Parsons, R., Interphases in systems of conducting phases (Recommendations 1985). In *Pure and Applied Chemistry*, 1986; Vol. 58, p 437.

Chapter IV

Electrochemical Capacitance Study on Graphitised N doped carbon

In this chapter, the capacitive properties of nitrogenated graphitised amorphous carbon are reported. Nitrogenated materials are prepared by dc magnetron sputtering and thermal annealing. A combination of structural characterisation methods, surface analysis and electrochemical methods are performed in order to study the bulk electronic, structural, valence electronic properties, chemical composition and capacitance of the film

Co-author contributions to this chapter are as follows: James Behan, and Serban Stamatin have contributed several of the XPS and UPS measurements. All data were analysed by the author.

4.1 Introduction

Carbon materials play an important role in energy storage technology applications. To meet the global challenges caused by an increase in global energy demand of an ever-increasing population and the associated environmental consequence, very innovative, efficient and sustainable solutions must be found. In order to meet those demands the development of novel, high performance and sustainable materials is extremely important [1]. Carbon is the most abundant element in the earth and carbon-based systems are increasingly performing a major role in various applications such as energy storage devices, electrocatalysis, photocatalysis, heterogeneous catalysis, fuel cells etc. For example, graphite material is used as an anode material in batteries, carbon black is used as an electrocatalytic support material in fuel cells and activated carbon is used as an active material for supercapacitors. There are several reasons for choosing these carbon materials: they are cheaper, abundant, environmentally friendly and they possess unique properties, e.g. morphology, electrical, optical and mechanical, allowing prominent enhancing of energy-conversion and storage performances [2].

The best performing materials for capacitive energy storage devices are ordered carbon materials such as carbon nanotubes or graphene [2-3], activated carbon and carbon black [4], etc. Performance of amorphous carbon seems to be less efficient, compared with ordered materials e.g. graphene and carbon nanotubes in energy storage applications [5-6]. Nitrogen doping is an effective method for further improving the chemical and physical properties of carbon materials to enhance energy storage capabilities or electrocatalytic ability [7]. Nitrogen has been successfully incorporated into several carbon based materials such as graphene [8-10], carbon nanotubes [11-14] and amorphous carbon [15-18]. Nitrogen doping can be substitutionally incorporated into the carbon structure and is called graphitic-N site [19] and/or in other chemical forms such as pyridinic-N and pyrrolic-N sites. In Chapter III we have shown that N incorporation not only introduces different N sites but also creates vacancies, defects and edge sites [20]. Capacitance studies on these materials were performed in aqueous KCl and organic electrolyte (TBAPF$_6$/acetonitrile) and we have shown that low N incorporation reduces the p-type character of a-C and further incorporation increases the n-type character in the materials. Capacitance studies of a-C:N electrodes in aqueous electrolyte have shown mostly pseudo-capacitive contributions, which is supported by the work function, which in organic electrolytes is dominated by the double layer capacitance.

This chapter focuses on the capacitive properties of topographically smooth graphitized a-C with and without incorporated nitrogen. Incorporating graphitised a-C with N complexes and multifaceted effects on physic chemical properties of a-C such as to reduce the electrical resistivity, defect density of these films, minimize the compressive stress and optical bandgap, etc. [21-22]. The effect of nitrogen incorporation into carbon materials on the electrochemical double-layer and redox-capacitance of carbon has received considerable attention in order to design materials for energy storage devices[23-24]. The effect of nitrogenation on the capacitive properties of ordered carbon nanomaterials such as graphite [25] and carbon nanotubes [14, 26] has been studied by various groups.

Recent work from our group has also studied dopamine (DA) adsorption on N-doped graphitised a-C system examining the effect of carbon nanostructuring and organization on the adsorption and redox response of DA [27]. Herein we study the effect of N-site incorporation into smooth graphitized a-C and how this enhances the capacitive properties of a-C:N electrodes as a result of both surface chemical and electronic effects. These a-C:N electrodes were prepared by thermal annealing of sputtered N-doped amorphous carbon films and they were characterized using X-ray photoelectron spectroscopy (XPS), ultraviolet photoelectron spectroscopy (UPS), Raman spectroscopy, cyclic voltammetry (CV), and electrochemical impedance spectroscopy (EIS). Our results indicate that graphitized a-C:N based carbon structures possess higher metallic character and capacitance if compared with graphitized a-C electrode.

4.2 Materials and methods

4.2.1 Chemicals and Materials

Tetrabutylammonium hexafluorophosphate (TBAPF$_6$) (≥99.0%, electrochemical analysis), Acetonitrile (MeCN) (99.8%, anhydrous), Sulfuric Acid (95 – 97%), Hydrogen Peroxide (>30% w/v), were purchased from Sigma Aldrich.

Glassy carbon (GC) discs (HTW Sigradur® radius 2.5mm) were polished with finer grades of alumina slurry (Buehler) consisting multiple steps have discussed in previous chapter. Clean disks were mounted in a custom-made Teflon® holder and placed in the vacuum chamber for deposition.

B-Doped Silicon wafers (MicroChemicals; resistivity 5 – 10 Ω-cm) were used as substrates for amorphous carbon film and nitrogenated amorphous carbon film deposition. The substrates were cleaned with piranha solution (3:1 H_2SO_4:H_2O_2) and rinsed with plenty of Millipore water and dried with argon gas before being placed in the vacuum chamber for deposition.

4.2.3 Synthesis of electrodes

Amorphous carbon films and nitrogenated amorphous carbon films were synthesized via DC-magnetron sputtering (Torr International) from a carbon target (Lesker, 99.999%) at base pressures of <2 x10^{-6} mbar and deposition pressures of 2-7 x10^{-3} mbar and a total gas flow of 50 mL min^{-1}.

Nitrogenated amorphous carbon film were prepared by using nitrogen (N4.5, BOC) and argon (N4.8, BOC) gas mixtures which were adjusted by two mass flow controllers and a mass flow control unit (Brooks Instruments). Deposition time was kept constant at 40 min for all samples. Films were deposited on glassy carbon disks (5 mm in diameter, HTW) for electrochemical characterization and on p-type Si wafers (MicroChemicals GmbH) for all other characterization. Deposited films were annealed at 900º C for 1hr under N_2 gas flow by using an electric furnace. Non-nitrogenated annealed films will be denoted as anC in this work and annealed N-doped films, denoted as anC:N, where the films prepared using 2% N_2 gas in a total flux of 50 sccm Ar/N_2 during the deposition later annealed at 900º C for 1 hr under N_2 gas flow will be named as anC:N 1 and 10% N_2 gas annealed film will be denoted as anC:N 2.

4.3 Characterization

In the case of graphitised a-C films, X-ray photoelectron spectroscopy (XPS) characterization was performed at 1 × 10^{-10} mbar base pressure in an ultrahigh vacuum system (Omicron), using monochromatic Al Kα source (1486.6 eV) and equipped with a multichannel array detector. XPS spectra were collected at a 45° take-off angle and a 0.5 eV resolution. In the case of annealed a-C:N films XPS characterization was performed on a VG Scientific ESCAlab Mk II system (<2 ×10^{-8} mbar), using Al Kα X-rays (1486.6 eV); core-level spectra were collected with an analyzer pass energy of 20 eV and survey spectra were collected with an analyzer pass energy of 200 eV. In order to do charge compensation an electron flood gun and the binding energy scale was referenced to the C 1s core-level at

284.8 eV. Peaks were fitted with Voigt functions after Shirley background subtraction using commercial software (CasaXPS); at.% composition was obtained from peak area ratios after correction by Scofield relative sensitivity factors (C = 1.0, N = 1.8, O = 2.93).

Ultraviolet photoelectron spectroscopy (UPS) measurements of films were performed in an Omicron system with a multichannel array detector, at 1×10^{-10} mbar base pressure. UPS spectra were collected using an excitation source He (I) line at a takeoff angle of 90°, with an analyser resolution of 0.02 eV. A negative bias was applied to the sample in order to measure the high binding energy edge of the photoelectron spectrum. UPS spectra were corrected for bias and referenced to the Fermi energy.

Raman spectra of amorphous carbon and nitrogenated amorphous carbon were measured with a room temperature backscattering configuration using a Renishaw 1000 micro-Raman system equipped with an Ar^+ laser providing 488 nm excitation and a HeNe laser providing 633nm excitation. In order to avoid damage and overheating to the samples, the power was kept to 1-2mW. The laser spot was focused on the sample surface by using a Leica microscope with a 50X magnification objective with a short-focus working distance.

Electrochemical measurements were carried using an Autolab PGSTAT30 potentiostat interfaced with both Autolab FRA. Electrochemical measurements were carried out in an organic electrolyte of 0.1M $TBAPF_6$/MeCN. Cyclic voltammograms (CVs) were obtained at 25 °C at a scan rate of 50 mV/s with iR compensation. EIS spectra were obtained at open circuit potential (OCP) as well as at different applied potentials at 0.2V step from -0.8V to +0.8V vs. Ag/Ag+ in the frequency range from 100 kHz to 0.1 Hz using an ac amplitude of 10 mV with 300s equilibration time allowed between each step by following the method of Hahn et al.[28] EIS spectra were fitted with equivalent model using commercial software (Z-View) and double layer capacitance was extracted from this model as well as from the imaginary part of the impedance (Z^{im}) according to $C = -1/(2\pi f Z^{im})$ [28]. The geometric area of each disc was determined using callipers and verified via cyclic voltammetry experiments at various scan rates using the Randles−Sevcik equation.

4.4 Results and discussion

4.4.1 Chemical composition of anC and anC:N electrodes using XPS

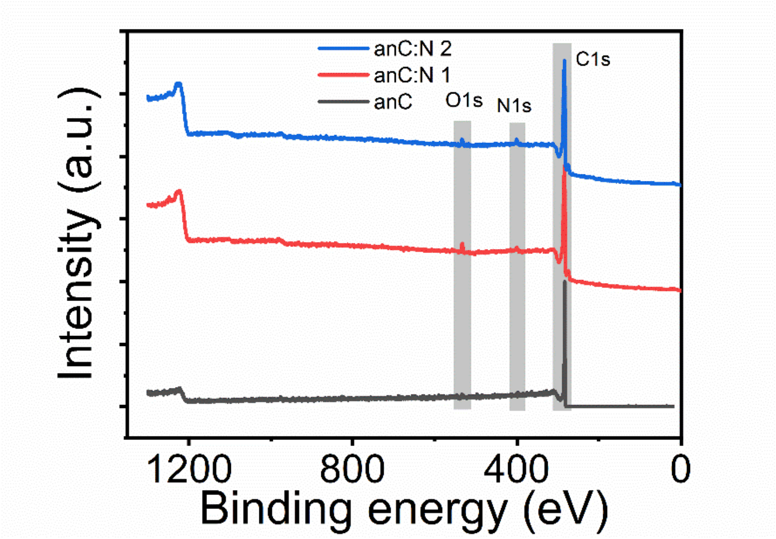

Figure 4.1: Survey scans of anC, anC:N 1, anC:N 2 electrodes.

Nitrogen-doped amorphous carbon thin film electrodes were prepared via dc magnetron sputtering and characterised as described in chapter III of this thesis. N_2/Ar mixture was used to deposit carbon thin films and the nitrogen content of the films was varied by changing the proportion of N_2 gas flow ratios of 2% and 10% into the chamber. These sputtered films with and without nitrogen were further annealed at 900 °C for 1 h under nitrogen [27]. Nitrogen-free annealed carbon is referred to as anC and annealed 2% and 10 % are referred to as anC:N 1 and anC:N 2 respectively, which originate from precursors with the lower and higher N-contents, respectively. Figure 4.1 displays survey scans for all films showing the characteristic C 1s, O 1s and N 1s peaks at 284, 532 and 400 eV respectively. anC doesn’t contain any nitrogen, as confirmed by the absence of N 1s peaks in the survey spectra. Table 4.1 summarises the XPS results of all the electrodes. All a-C:N surfaces were found to possess a mixture of pyridinic-N and graphitic-N. The oxygen content of the anC and anC:N films was reported to be 1-2 % and similar for both anC:N 1 and anC:N2 surfaces. Nitrogenation of the carbon scaffold has the effect of increasing the full-width at half maximum (FWHM) of the C 1s (Table 4.1) in anC:N samples [29].

Table 4.1. Summary of the properties of sputtered a-C:N electrodes used in our studies.

Sample	FWHM of C 1s	O/C %	N/C %	N_P/C %	N_G/C %	N_G %	N_P %	Φ (eV)^b
anC	1.00 ± 0.05	1	n/a					4.46
anC:N1	1.8	2	2.4	0.4	2.0	83	17	4.40
anC:N2	1.9	2.4	2.7	0.3	2.4	87	13	4.14

Figure 4.2a-c displays deconvoluted high resolution scans of the C 1s region for anC, anC:N 1 and anC:N 2, respectively. The asymmetric envelopes with maxima in the range 284-285 eV indicates that these carbon materials are mostly sp^2 bonded carbon, as expected for graphitized carbon surfaces. The contributions at *ca.* 284.4 eV and 285.5 eV present in all deconvolutions are assigned to sp^2 and sp^3 carbon centres, respectively [30]. Nitrogen incorporated materials (anC:N) have higher FWHM of C 1s compared with anC due to an increased degree of disorder in the carbon sp^2-network and the presence of C-N functional groups.

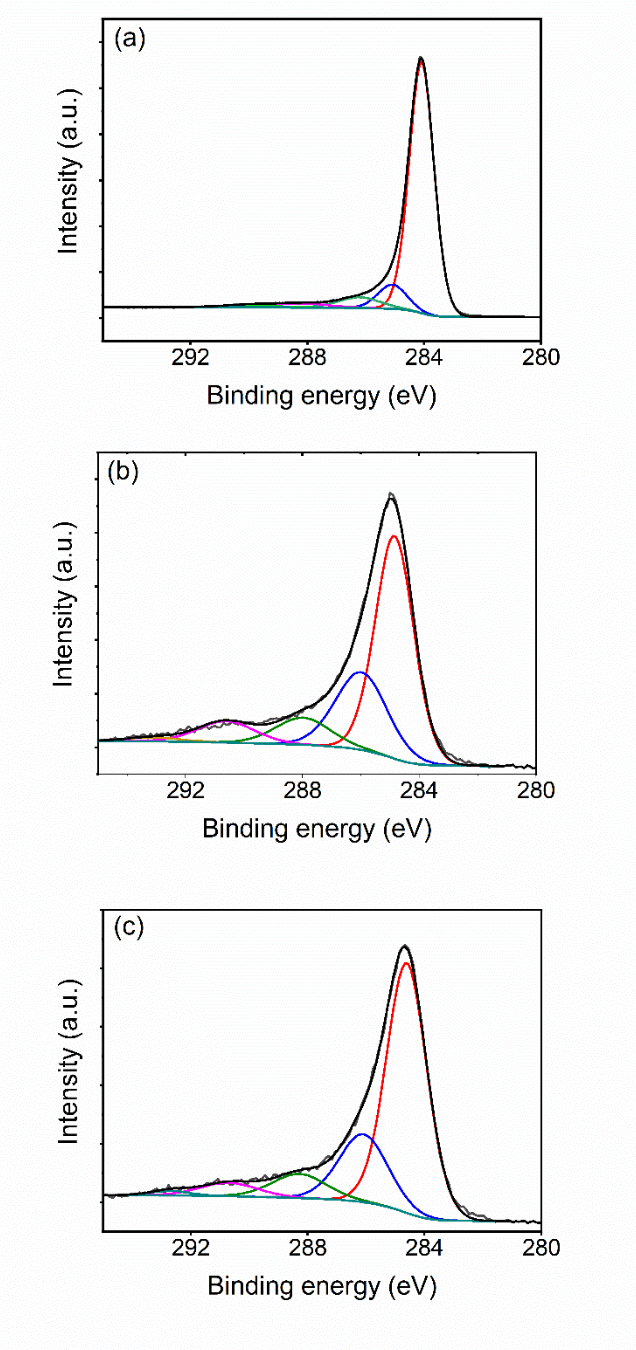

Figure 4.2: Deconvoluted C 1s envelopes of a) anC, b) anC:N 1, and c) anC:N 2.

The area ratios A_{O1s}/A_{C1s} and A_{N1s}/A_{C1s} were used to quantify the nitrogen and oxygen content of each film and the ratios were also corrected by sensitivity factors (O = 2.93, N = 1.8, C = 1). The resulting O/C and N/C at. % values are reported in Table 4.1. O/C % of *ca* 3 % is observed for all films due to the effect of air exposure [31].

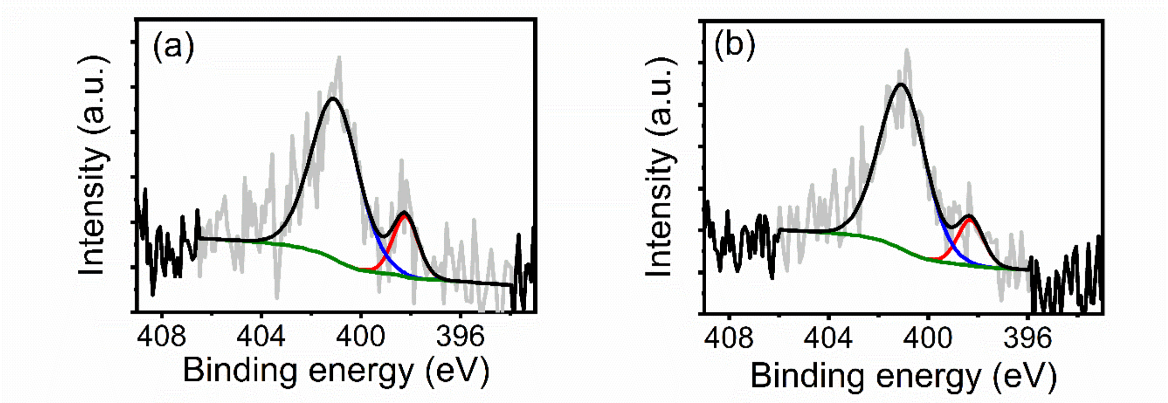

Figure 4.3: a-b) N 1s spectra of anC:N 1, anC:N 2 respectively.

Deconvoluted N 1s spectra for the anC:N 1 and anC:N 2 electrode surfaces are shown in Figure 4.3a and b, respectively. Best fittings of the N 1s spectra of anC:N films were obtained by using two components; the dominant contribution to the envelope at *ca.* 401 eV is associated with graphitic-N, while a smaller shoulder in the envelope at *ca.* 398 eV is assigned to pyridinic-N [32-33]. The ratio of Np/C % and N_G/C % is 0.3 % and 2.4 % for anC:N2 and 0.4 and 2.0 for anC:N1 respectively, indicating that both systems possess similar N-site distribution.

In summary, XPS characterization of anC and anC:N films indicates that sputtered carbon deposition followed by thermal annealing at 900 °C results in N-free and N-incorporated graphitised carbon thin films, respectively. anC:N films possess comparable levels of oxygen and similar N-site distribution.

4.2.2 Structural Characterization of electrodes using Raman spectroscopy

Raman spectroscopy was used to characterize the organisation of the carbon scaffold of the graphitised electrode materials.[34-36] Raman spectroscopy measurements were carried out at two different excitation wavelengths of 488 nm and 633nm. Figure 4.4a shows baseline-corrected Raman spectra in the 900-1900 cm^{-1} range of anC and anC:N electrodes deposited on silicon wafers, obtained using 488 nm excitation. All the spectra presented here in figure 4.4a and 4.4b were normalised based on the G peak height. All the spectra show two basic features of amorphous carbon assigned to the G and D bands at approximately 1580 cm^{-1} and 1380 cm^{-1}, respectively. The G peak is associated with the bond stretching of all pairs of sp^2 atoms in both rings and chains and the D peak is associated to the breathing modes of sp^2 atoms in rings.[29, 36-37] Figure 4.4b shows Raman spectra for a-C:N 10 and anC:N 2 samples, which are diagnostic of changes observed for all amorphous carbon films. From figure 4.4b, it can be seen that the G-band is shifted to higher frequencies by 15 cm^{-1} after annealing at 900 °C, while simultaneously its linewidth decreases.

Several fitting methods were used in the literature in order to extract structural parameters of amorphous carbons in the spectral ranges from 900 – 1900 cm^{-1} , including use of Gaussian/Lorentzian functions,[38-39] Lorentzian functions and Breit-Wigner-Fano (BWF) [29, 37, 40] and all Gaussian functions. The structural parameters were obtained from these anC and anC:N samples by using a three-peak Gaussian deconvolution where peaks 1 and 2 assigned as G and D, and the 3rd peak centred close to 1510 cm^{-1} is assigned as the A peak which is associated to the C-C vibration in an amorphous network, composed of an atomically mixed structure of three- and fourfold-coordinated carbon [41-42]. A small peak at 960 cm^{-1} observed in some spectra is associated with the Si substrate. Deconvoluted spectra of anC and anC:N were fitted with three Gaussian functions as shown figure 4.5a-c, where red, green and blue peaks are assigned to D band, G band and A band, respectively.

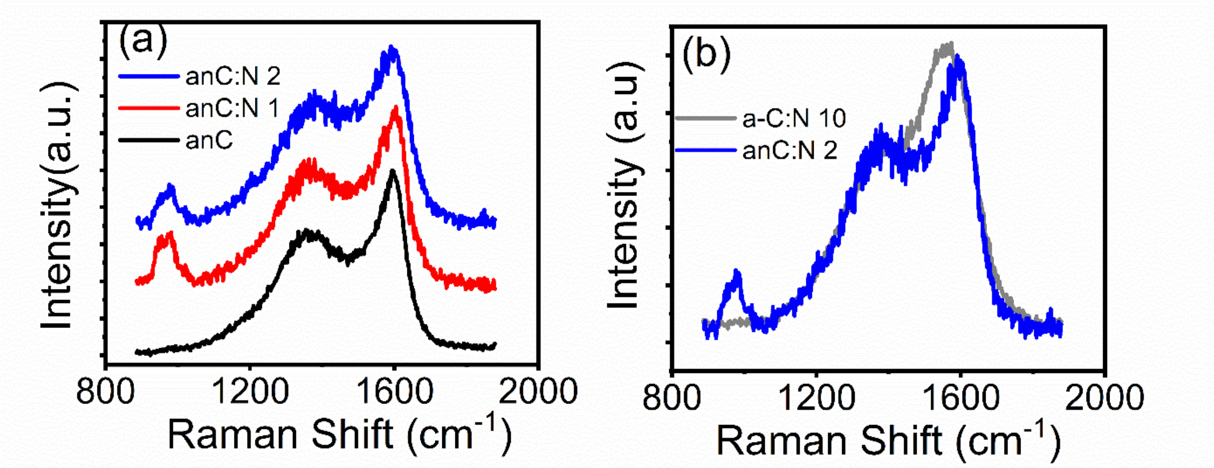

Figure 4.4: Raman spectra of (a) samples with anC, anC:N1, and anC:N 2. Spectra of (b) annealed and non-annealed a-C:N-10% carbon films further named as anC:N2 and a-C:N 10. All the spectra were background subtracted and normalised based on G peak height.

Parameters obtained from these deconvoluted spectra are shown in figure 4.6. Based on fitting results and obtained spectral parameters I_D/I_G ration, I_A/I_G ratio, FWHM of G and G peak dispersion, it is clear that there are remarkable differences in the structure of the carbon matrix among the examined samples. Based on the G peak position, anC and all anC:N samples are best described according to Ferrari and Robertson's three stage model,[29, 35, 43] as nanocrystalline graphite (nc-G). Figures 4.6a and 4.6b show the changes in I_D/I_G ratio and I_A/I_G ratios of nitrogen-free anC and anC:N, which are diagnostic of the degree of order/disorder. The I_D/I_G and I_A/I_G ratios of anC and anC:N 1 samples were found to be similar, however anC:N 2 has the highest I_D/I_G, which suggests that this sample has the smallest average crystallite size in its graphitic clusters. anC:N 2 also displays the lowest I_A/I_G ratio which indicates that its graphitic clusters are more closely packed than in anC:N 1 or anC, thus reducing the proportion of amorphous C—C regions in the carbon scaffold. Figure 4.6c and 4.6d show changes in FWHM of the G peak and dispersion of G peak for nitrogen-free anC and anC:N. The FWHM is diagnostic of the distribution of bond angles at excited sp^2 centres and therefore tracks the local carbon disorder.[29] FWHM is higher for anC:N 2 compared to anC:N 1 and non-modified carbon which indicates a broad distribution of bonding geometries for sp^2 centres. The dispersion of the G peak positions is associated with disordering as a result of nitrogenation. For this purpose, Raman spectra obtained at 633 nm excitation were also analysed to obtain the values. G-peak dispersion rises sharply for anC:N samples which indicates an disorder into the sp^2 sites resulting from nitrogenation [36]. Figure 4.7 displays the peak position of D and G bands as a function of anC:N. The G peak increases sharply with N content leading to graphitisation. D peak position of anC and anC:N 1 is similar and anC:N 2 is higher which indicate indicating the higher disorder in anC:N 2 compare with anC and anC:N 1 [44]. The increase in disorder in anC:N 2 a be explained on the basis of differences in the organization of the carbon scaffold rather than on the basis of N_G and N_P concentration changes.

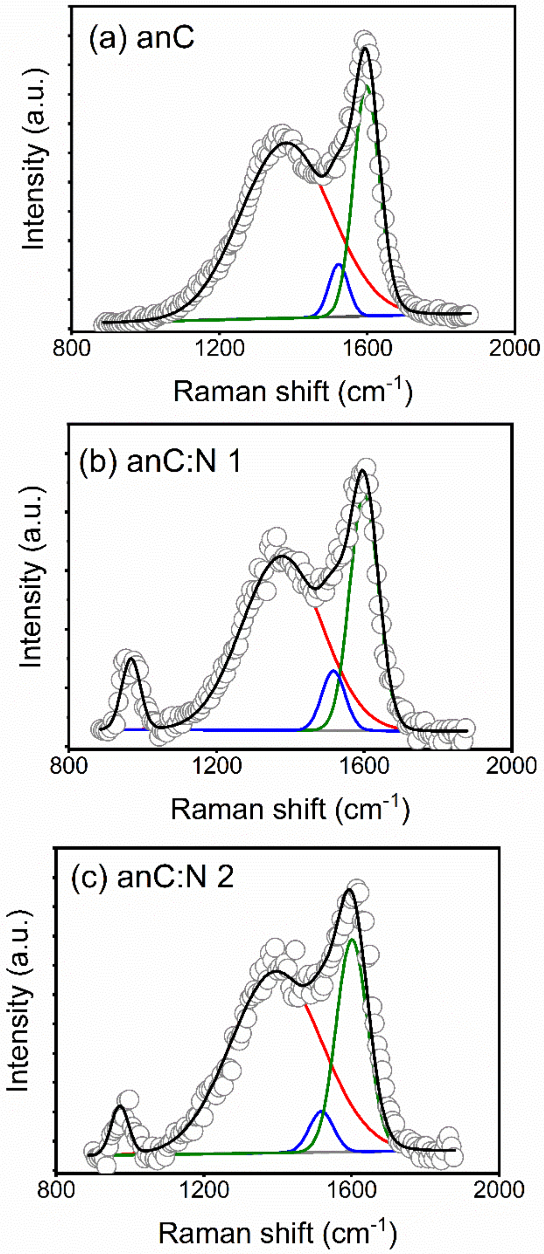

Figure 4.5: Raman spectra and peak deconvolution of (a) anC, (b) anC:N 1 and (c) a-C:N 2 ; excitation 488 nm. Spectra are normalised relative to the G band intensity.

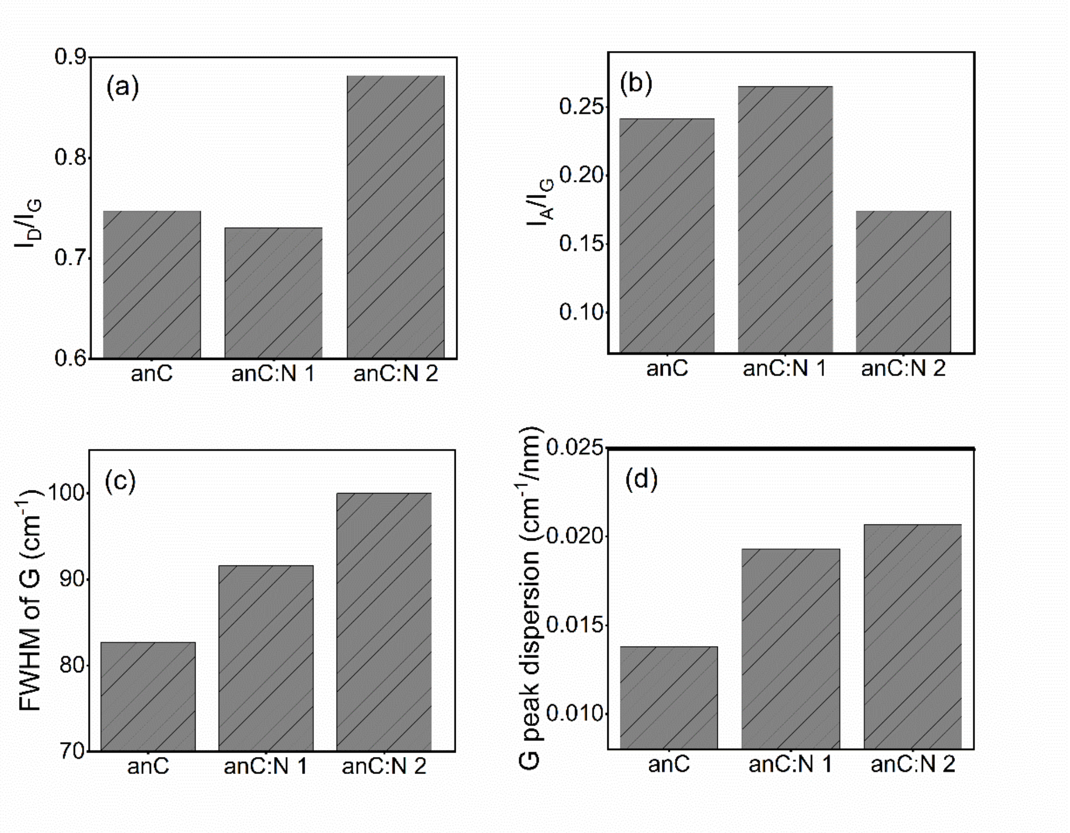

Figure 4.6: (a).Variation of D to G peak height ratio (ID / IG), (b) variation of A to G peak height ratio (c) FWHM of G peaks and (d) G peak dispersion vs. annealed a-C:N .

Raman spectra obtained using a 633 nm excitation laser in the range of 900-1900 cm^{-1} for anC and anC:N electrodes are also presented in figure 4.8; all spectra presented are normalised by the G peak height to facilitate comparison. Structural parameters obtained by using a three-peak Gaussian deconvolution were summarised in table 4.2. An increase in the I_D/I_G ratio of anC:N compared to anC was observed which is in good agreement with Ferrari et al.[34] FWHM of G peak for anC:N increases relative to N-free anC and anC:N 2 has the highest FWHM indicating the greatest disorder.

Overall Raman results indicate that there are significant differences in the organization of the carbon matrix among the three anC and anC:N electrodes, although differences in overall N concentration in anC:N electrodes are very small.

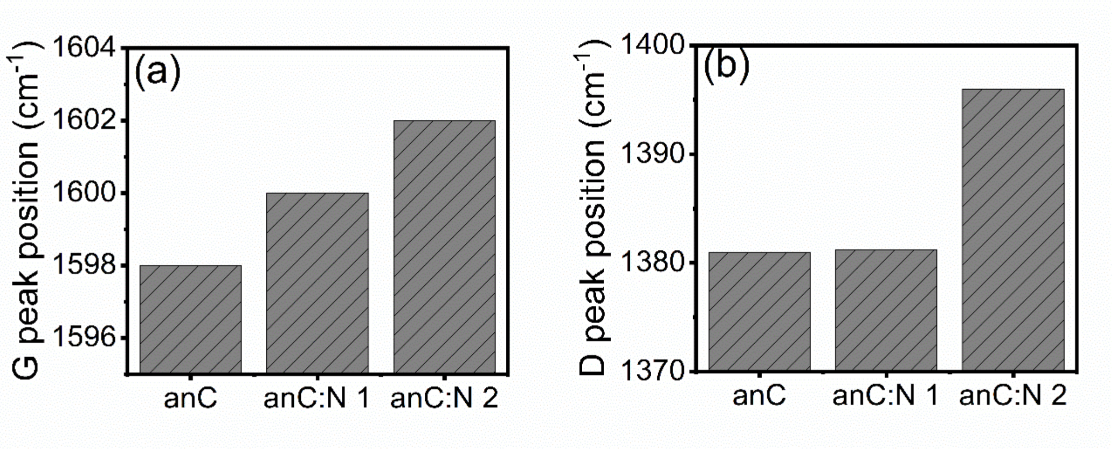

Figure 4.7: a) G peak position b) D peak position vs annealed a-C:N.

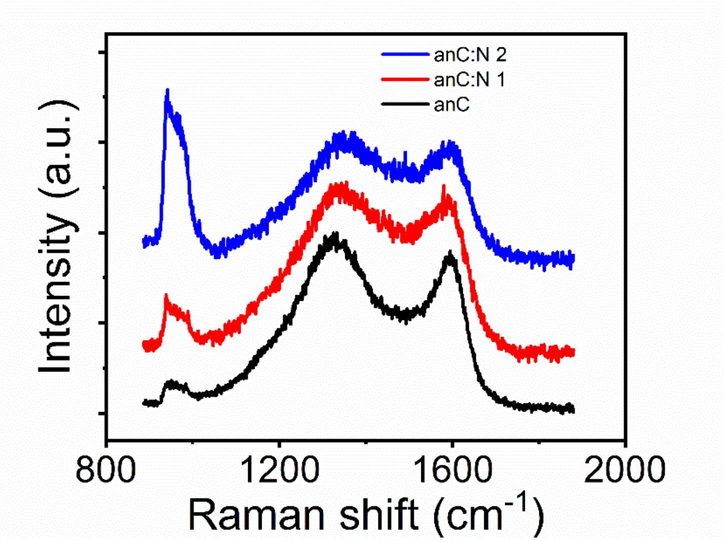

Figure 4.8: Raman spectra of (a) samples with anC, anC:N1, and anC:N 2 at 633 excitation. All spectra were background subtracted and normalised based on G peak height.

Table 4.2: Raman Spectral Parameters for anC and anC:N Carbon Materials at 633 excitation.

Samples	D peak Position	FWHM of D	G peak Position	FWHM of G	ID/IG	IA/IG
anC	**1331**	**263**	**1596**	**87**	**1.15**	**0.39**
anC:N 1	**1353**	**297**	**1597**	**96**	**1.22**	**0.3**
anC:N 2	**1356**	**253**	**1599**	**97**	**1.18**	**0.36**

4.4.3 Valence Electronic Properties of anC and anC:N electrodes

UV photoelectron spectroscopy (UPS) was used to investigate the valence electronic properties of anC:N electrodes. Figure 4.9 show the UPS spectra in the secondary edge or high-binding energy region. The high binding energy edge was used to calculate work function values (ϕ), which are summarised in Table 4.1. The work function of non-nitrogenated annealed amorphous carbon anC was found to be 4.46 eV, which is very close to the values quoted for graphitic nitrogen-free materials such as graphite (4.4 eV) [45-46]. Incorporation of nitrogen results in a decrease in work function values which fall in the range 4.39-4.15 eV. The observed decrease of ϕ upon N-modification is in agreement with experimental results by Seiji Obata, and Koichiro Saik obtained from nitrogenated graphene [47]. Nitrogen incorporation can result in both an increase [14, 48] or a decrease [49-50] in the work function of carbons arising from changes to semiconducting properties . Work function of anC:N 1 (4.4 eV) is very close to anC and these observations are consistent with Raman data where anC and anC:N shows similar structure. anC:N 2 possess lowest work function of 4.14 eV as greatest disorder observed in Raman characterization.

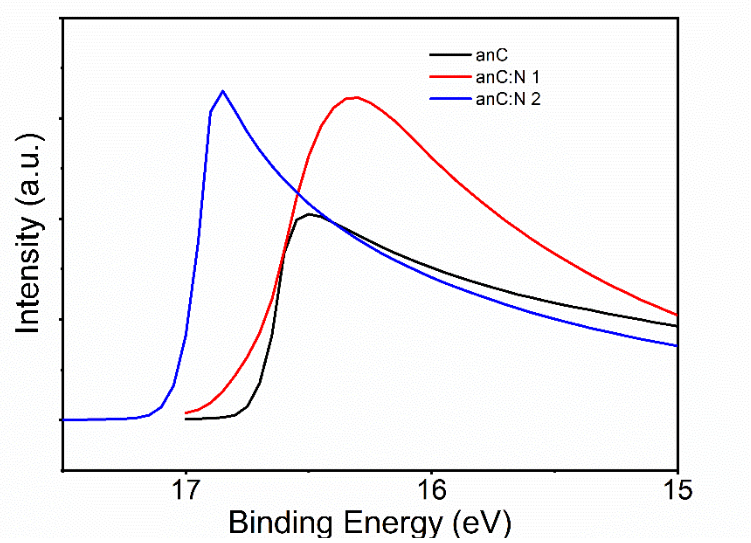

Figure 4.9: Ultraviolet photoemission spectroscopy (UPS) spectra of anC and anC:N electrodes secondary edge region. Spectra are shown normalised by the total photoemission intensity.

4.4.4 Capacitance study in organic electrolyte

Electrochemical characterisation via cyclic voltammetry (CV) and electrochemical impedance spectroscopy (EIS) was carried out using a three-electrode system. Typical cyclic voltammograms (CVs) of anC and anC:N electrodes over a -0.3 – 0.7 V potential window at

50 mV s^{-1} in 0.1 M TBAPF$_6$/acetonitrile are shown in Figure 4.10. The curves show the characteristic shape of a capacitive response; no significant differences in capacitive current responses were observed among anC and anC:N 1-2 electrodes.

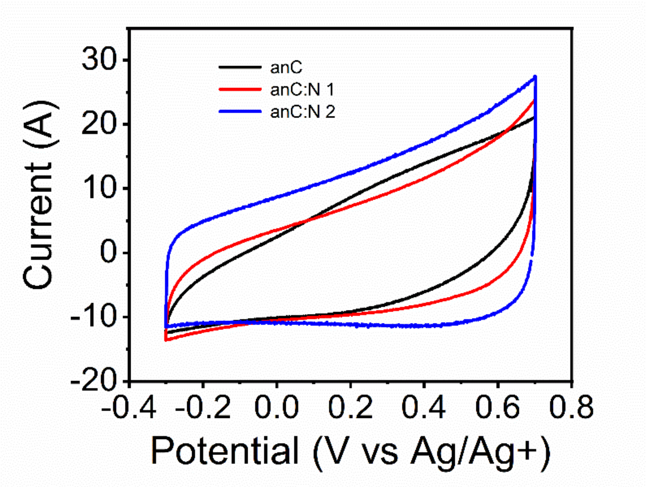

Figure 4.10: Cyclic votammograms of anC, anC:N 1 and anC:N 2 in Ar-saturated 0.1 M TBAPF$_6$ /acetonitrile at 50 mV s^{-1}.

A study of the electrochemical response was carried out using EIS over the 0.1-10^4 Hz range in 0.1 M TBAPF$_6$ /Acetonitrile electrolyte. Figures 4.11a and 4.11b show Bode plots of absolute impedance (|Z|) and phase angle obtained at OCP (-0.3 V-0.15V vs. Ag/Ag+), respectively, for nitrogen-free anC electrodes and for nitrogen doped anC:N electrodes. anC electrodes display higher impedance at low frequency compared to that of anC:N electrodes at 0.1Hz frequency. The curves indicate that nitrogenation results in a further reduction in |Z|. The phase angle suggests a capacitive response with deviations from ideal behaviour as suggested from phase angles at 0.1 Hz of *ca.* -70 °; the deviations are less pronounced from nitrogenated anC:N 1 and 2, given more negative values of -81 ° and -82 °, respectively.

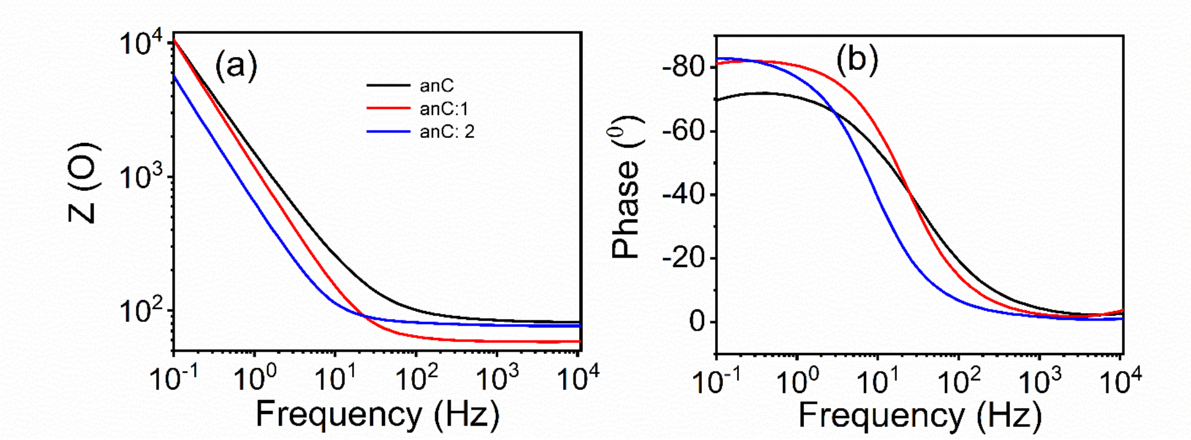

Figure 4.11: Bode plots of impedance module |Z| (a) and phase angle (b) of anC, anC:N1, and anC:N 2. EIS spectra obtained in 0.1 M TBAPF$_6$ /acetonitrile at open circuit potential (OCP, -0.3-0.15 V vs. Ag/Ag+).

The effective or equivalent series capacitive contribution to EIS spectra was calculated as a function of frequency from the imaginary part of the complex impedance Z_{im} by using equation 3.1. Figure 4.12 shows a plot of the specific capacitance extracted over the 0.5-100 Hz range at OCP. The capacitance is normalized by geometric area of the disk. This figure shows that capacitance increases with an increase in N content over the frequency range 0.5-100 Hz which yielded values in the mF cm^{-2} range. A very significant increase in capacitance is observed for anC:N 2 electrodes compared with anC:N 1 and non nitrogenated anC electrodes. The appearance of frequency dependent capacitance dispersion is clearly observed in figure 4.12 and this occurred due to surface roughness and defects on the electrode surface [51-52]. An additional contribution to the total capacitance likely arises from the difficulty in sealing a well defined geometric area using a Teflon shroud in organic solvent, as discussed in chapter 3.

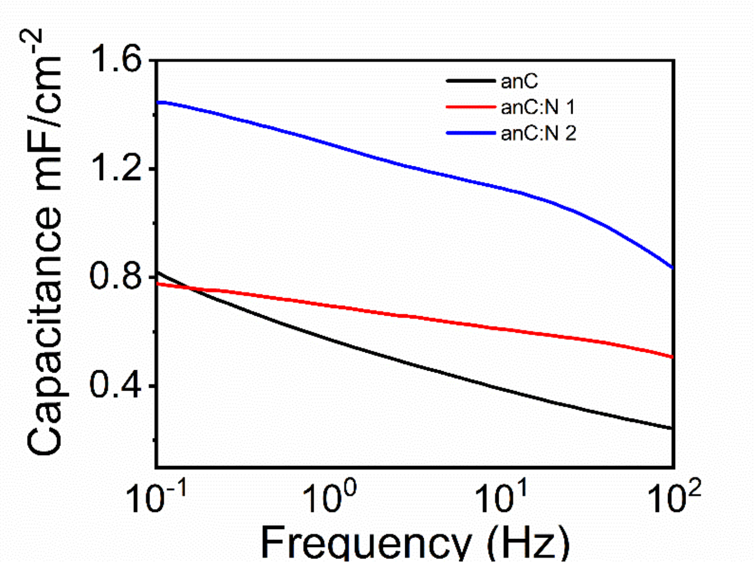

Figure 4.12: Equivalent series capacitance at OCP in 0.1 M TBAPF$_6$ /acetonitrile.

The capacitance is extracted from the imaginary part of the Nyquist plot obtained at different applied potential. Therefore, Nyquist plots of EIS spectra at 0 V, 0.4 V and -0.4 V are presented in figure 4.13 a-c respectively, corresponding to the capacitance minima of anC and anC:N electrodes. Nyquist plots display low impedance for anC:N electrodes compared to anC electrodes, in good agreement with equivalent series capacitance obtained at different applied potentials.

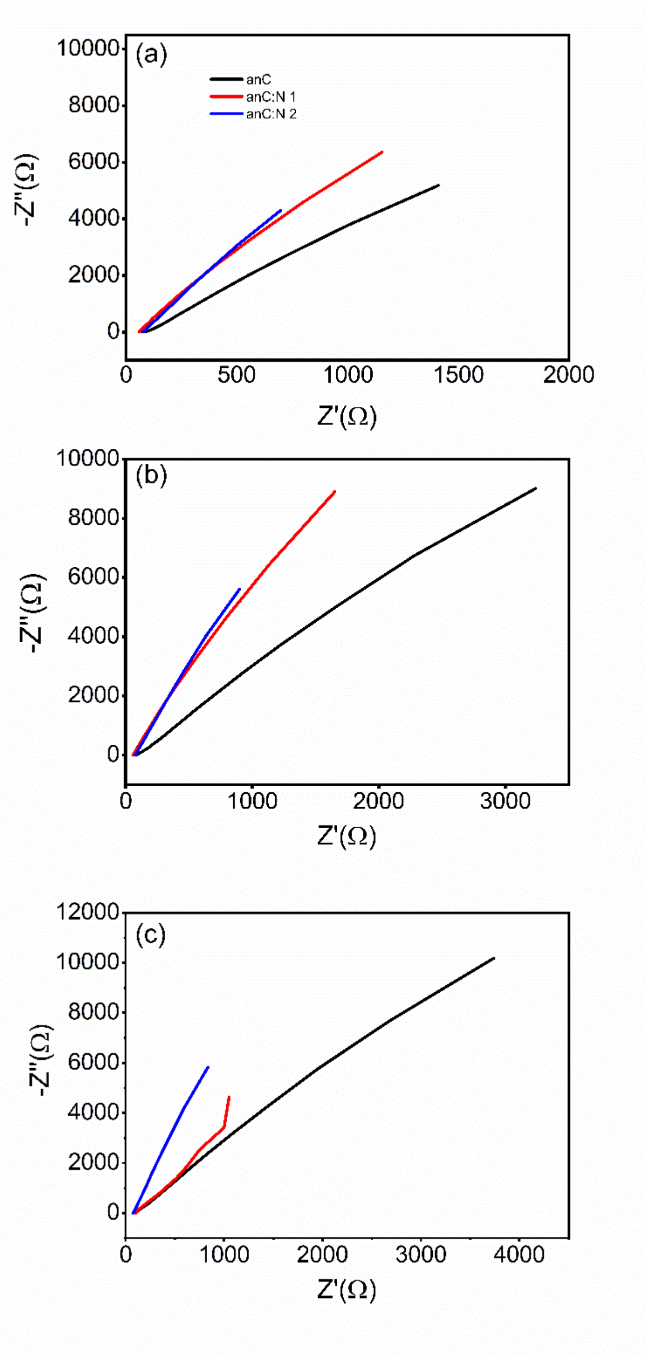

Figure 4.13: Nyquist plots of EIS spectra of anC, anC:N 1, anC:N 2, in organic 0.1 M $TBAPF_6$/acetonitrile at (a) 0.4 V, (b) 0 V and (c) -0.4 V respectively.

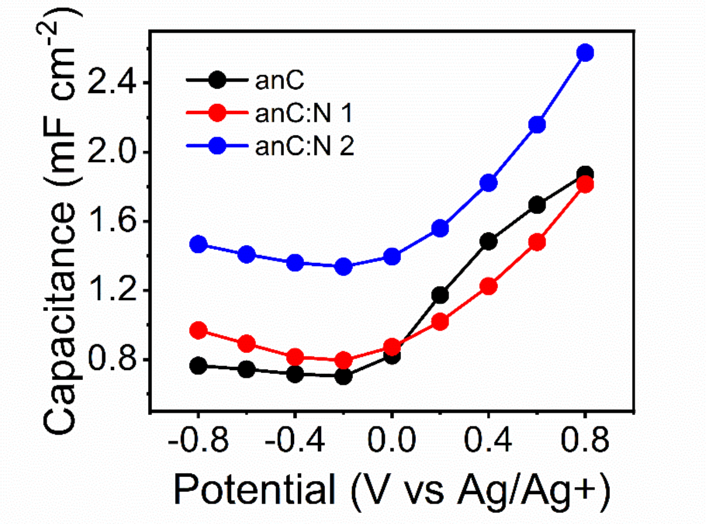

Figure 4.14: Equivalent series capacitance as a function of potential in 0.1 M $TBAPF_6$/acetonitrile.

Figure 4.15: Equivalent circuit model where R_S is solution resistance and C_{Dl} is the double layer capacitance.

Figure 4.14 shows the change in the series equivalent capacitance as a function of the DC offset over the range -0.8 – 0.8 V vs. Ag/Ag+ in 0.1 M $TBAPF_6$/acetonitrile. Capacitance obtained in $TBAPF_6$/acetonitrile is dominated by the double layer (C_{DL}). The capacitance was extracted from EIS spectra obtained at different potentials by using an equivalent circuit model (figure 4.15). The nitrogen-free anC electrode shows minima in the capacitance that suggest a potential of zero charge (pzc) of 0.7 mF cm^{-2} at ca. -0.2 V. Nitrogenation leads to a considerable increase in the area-normalised capacitance. There is no detectable shift in the potential at the minimum capacitance for anC:N 1 (ca. 0.8 mF cm^{-2}) and anC:N2 (ca. 1.3 mF cm^{-2}). This figure shows that, as predicted, the capacitance increases with an increase in the N content of the film. Asymmetry in the non-nitrogenated anC curve agrees with previous reports of p-type behaviour in nitrogen-free sputtered a-C [53]. Small amounts of nitrogen content as in anC:N 1 have a drastic effect in reducing the p-character. The minimum capacitance of anC:N 2 is highest among anC:N electrodes. In order to find the minimum , we have measured EIS at two frequencies such as 0.5 Hz and 10 Hz over the potential range of -0.8 V to 0.8 V with a 0.05 V of potential step. The effective or equivalent series capacitive contribution to EIS spectra at 0.5 Hz and 10 Hz frequency were calculated from the imaginary part of the complex impedance Zim according to equation 3.1. are plotted in figure 4.16.

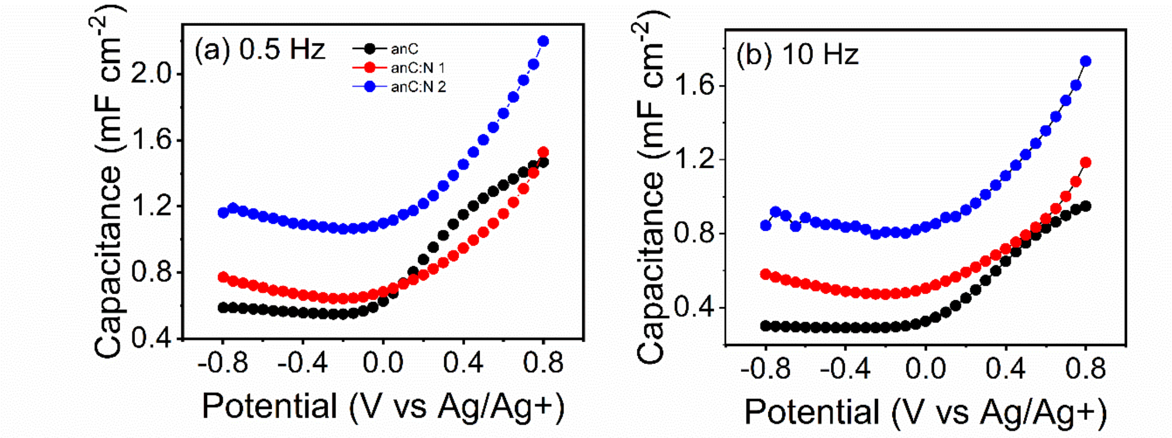

Figure 4.16: Equivalent series capacitance as a function of potential in 0.1 M TBAPF$_6$/acetonitrile at (a) 10 Hz and (b) 0,5 HZ frequency.

In figure 4.16a the capacitance curve of anC electrode is asymmetric with a capacitance at pzc of 0.55 mF cm^{-2} at -0.25 V vs Ag$^+$/Ag which is high compared with the literature value of carbon based electrodes varying from 5 to 50 µFcm^{-2} depending on carbon structure, i.e., basal, edge sites as well as its electronic properties [54-55]. This yielded a roughness factor of *ca.* 10-15 for this electrode. The capacitances at pzc are remarkably close to each other and to the anC value, being in a ratio C_{anC} : $C_{anC:N\ 1}$: $C_{anC:N\ 2}$ = 1 : 1.1 : 1.9. Although N-site concentrations for all anC:N electrodes have no major differences, increases in capacitance values are due to re-organisation of the carbon scaffold and greater disorder in the carbon structure [56]. All anC:N materials display semi-symmetry in capacitance plots obtained at different applied potentials and capacitive behaviour characteristing of p-type doped materials, perhaps suggesting that the effect of vacancies and unsaturations is dominant over any n-type doping effects arising from the present of N_G-sites.

Further, equivalent series capacitance at 10 Hz as a function of the DC offset over the range -0.8 – 0.8 V vs. Ag/Ag+ in 0.1 M TBAPF$_6$/ acetonitrile is presented in figure 4.16b . A similar trend in change of capacitances is observed with higher capacitance for anC:N 2 than anC:N 1 and anC respectively, and a characteristic asymmetry in the capacitance curve of anC is observed which is typical of p-type semiconducting behaviour [57].The anC:N electrodes display semi-symmetry in capacitance obtained at different applied potentials. The capacitances at pzc of anC of *ca.* 0.29 mF cm^{-2} at -0.4 V show there were considerable increases in capacitances upon nitrogen incorporation which is also consistent with Raman data where the structure of anC:N electrodes are similar in their organization of the carbon scaffold and their degree of graphitization while anC:N2 displays the most disordered carbon structure and smallest crystalline size compare with anC electrode. There is a potential shift at the minimum capacitances for anC:N 1 (*ca.* 0.47 mF cm^{-2}) and anC:N 2 (*ca.* 0.8 mF cm^{-2}) whose minima fall in the range -0.4 -0.25 V. There is clear evidence of capacitance dispersion at different frequencies in a-C:N electrodes, which is due to disorder and inhomogeneity in the electrode surface [51-52].

In summary, capacitance studies in organic electrolyte of 0.1 M TBAPF$_6$/ acetonitrile indicate that small N-site concentration in graphitised a-C significantly increases the capacitance as well as reduces the p-type behaviour of N free anC electrodes. There is a potential shift in the negative direction in the minimum capacitances upon nitrogen incorporation, which is in good agreement with UPS studies on these materials.

4.5 Conclusion

This chapter has successfully demonstrated the synthesis of N-free and N-doped graphitized carbon materials and characterisation of their surface chemistry and carbon nanostructure, by using spectroscopic techniques such as XPS and Raman spectroscopy. The electrochemical characterisation was carried out using CV and EIS techniques. These materials were synthesized using a combination of magnetron sputtering and thermal annealing at 900 °C for 1 hr under an inert atmosphere. XPS results show that anC:N electrodes possess identical N/C % with a mixture of pyridinic-N and graphitic-N where graphitic-N dominates. Raman studies shows that a significant difference in the organization of the carbon matrix between anC and anC:N electrodes, which is in good agreement with the XPS results of FWHM of the C 1s envelope. anC:N 2 possesses a smaller average crystallite size for the more closely packed graphitic clusters and a lower proportion of amorphous C-C regions in the carbon scaffolds. UPS studies suggest that small amounts of nitrogen incorporation decrease the work function of carbon, arising from changes in semiconducting properties. Capacitance studies were successfully performed in an organic electrolyte of 0.1 M TBAPF$_6$/ acetonitrile. The results suggest that electrochemical capacitance significantly increases relative to the N free graphitised anC electrode. In organic electrolytes the overall capacitance is dominated by the double layer capacitance and an increase in the capacitance is due to re-organisation of the carbon matrix and greater disorder in the carbon structure upon N incorporation. anC:N 2 possesses the highest capacitance among the electrodes. In the following chapter, oxygen reduction reaction in alkaline media and the electrochemical capacitance responses of the RF plasma treated graphitised a-C materials will be studied.

4.6 References

1. Zhang, Q.; Uchaker, E.; Candelaria, S. L.; Cao, G., Nanomaterials for energy conversion and storage. *Chem Soc Rev* **2013,** *42* (7), 3127-71.

2. Su, D. S.; Centi, G., A perspective on carbon materials for future energy application. *Journal of Energy Chemistry* **2013,** *22* (2), 151-173.

3. Zhao, X.; Sánchez, B. M.; Dobson, P. J.; Grant, P. S., The role of nanomaterials in redox-based supercapacitors for next generation energy storage devices. *Nanoscale* **2011,** *3* (3), 839-855.

4. Paul, R.; Chen, X.; Dai, L., Carbon-based supercapacitors for efficient energy storage. *National Science Review* **2017,** *4* (3), 453-489.

5. Pandolfo, A. G.; Hollenkamp, A. F., Carbon properties and their role in supercapacitors. *Journal of Power Sources* **2006,** *157* (1), 11-27.

6. Huang, Y.; Liang, J.; Chen, Y., An overview of the applications of graphene-based materials in supercapacitors. **2012,** *8* (12), 1805-1834.

7. Wu, J.; Pan, Z.; Zhang, Y.; Wang, B.; Peng, H., The recent progress of nitrogen-doped carbon nanomaterials for electrochemical batteries. *Journal of Materials Chemistry A* **2018,** *6* (27), 12932-12944.

8. Xu, H.; Ma, L.; Jin, Z., Nitrogen-doped graphene: Synthesis, characterizations and energy applications. *Journal of Energy Chemistry* **2018,** *27* (1), 146-160.

9. Wang, H.; Maiyalagan, T.; Wang, X., Review on recent progress in nitrogen-doped graphene: synthesis, characterization, and its potential applications. *ACS Catalysis* **2012,** *2* (5), 781-794.

10. Shao, Y.; Zhang, S.; Engelhard, M. H.; Li, G.; Shao, G.; Wang, Y.; Liu, J.; Aksay, I. A.; Lin, Y., Nitrogen-doped graphene and its electrochemical applications. *Journal of Materials Chemistry* **2010,** *20* (35), 7491-7496.

11. Gong, K.; Du, F.; Xia, Z.; Durstock, M.; Dai, L., Nitrogen-doped carbon nanotube arrays with high electrocatalytic activity for oxygen reduction. *Science* **2009,** *323* (5915), 760-764.

12. Maldonado, S.; Morin, S.; Stevenson, K. J., Structure, composition, and chemical reactivity of carbon nanotubes by selective nitrogen doping. *Carbon* **2006,** *44* (8), 1429-1437.

13. Lee, W. J.; Maiti, U. N.; Lee, J. M.; Lim, J.; Han, T. H.; Kim, S. O., Nitrogen-doped carbon nanotubes and graphene composite structures for energy and catalytic applications. *Chemical Communications* **2014,** *50* (52), 6818-6830.

14. Wiggins-Camacho, J. D.; Stevenson, K. J., Effect of nitrogen concentration on capacitance, density of states, electronic conductivity, and morphology of n-doped carbon nanotube electrodes. *The Journal of Physical Chemistry C* **2009,** *113* (44), 19082-19090.

15. Veerasamy, V. S.; Amaratunga, G. A. J.; Davis, C. A.; Timbs, A. E.; Milne, W. I.; McKenzie, D. R., N-type doping of highly tetrahedral diamond-like amorphous carbon. *Journal of Physics: Condensed Matter* **1993,** *5* (13), L169-L174.

16. Kaufman, J. H.; Metin, S.; Saperstein, D. D., Symmetry breaking in nitrogen-doped amorphous carbon: Infrared observation of the Raman-active G and D bands. *Physical Review B* **1989,** *39* (18), 13053-13060.

17. Hoque, M. K.; Behan, J. A.; Stamatin, Serban N.; Zen, F.; Perova, T. S.; Colavita, P. E., Capacitive storage at nitrogen doped amorphous carbon electrodes: structural and chemical effects of nitrogen incorporation. *RSC Advances* **2019,** *9* (7), 4063-4071.

18. Tali, S. A. S.; Soleimani-Amiri, S.; Sanaee, Z.; Mohajerzadeh, S., Nitrogen-doped amorphous carbon-silicon core-shell structures for high-power supercapacitor electrodes. *Scientific Reports* **2017,** *7*, 42425.

19. Robertson, J.; Davis, C. A., Nitrogen doping of tetrahedral amorphous carbon. *Diamond and Related Materials* **1995,** *4* (4), 441-444.

20. Kleinsorge, B.; Ferrari, A. C.; Robertson, J.; Milne, W. I.; Waidmann, S.; Hearne, S., Bonding regimes of nitrogen in amorphous carbon. *Diamond and Related Materials* **2000,** *9* (3), 643-648.

21. Khun, N. W.; Liu, E., Effect of substrate temperature on corrosion performance of nitrogen doped amorphous carbon thin films in NaCl solution. *Thin Solid Films* **2009,** *517* (17), 4762-4766.

22. Aryal, H. R.; Adhikari, S.; Kalita, G.; Ghimire, D. C.; Uchida, H.; Hideo, S.; Umeno, M. In Some aspects of nitrogen doped amorphous carbon thin films, 2008 33rd IEEE Photovoltaic Specialists Conference, 11-16 May 2008; 2008; pp 1-4.

23. Candelaria, S. L.; Shao, Y.; Zhou, W.; Li, X.; Xiao, J.; Zhang, J.-G.; Wang, Y.; Liu, J.; Li, J.; Cao, G., Nanostructured carbon for energy storage and conversion. *Nano Energy* **2012,** *1* (2), 195-220.

24. Deng, Y.; Xie, Y.; Zou, K.; Ji, X., Review on recent advances in nitrogen-doped carbons: preparations and applications in supercapacitors. *Journal of Materials Chemistry A* **2016,** *4* (4), 1144-1173.

25. Zhou, Y.; Holme, T.; Berry, J.; Ohno, T. R.; Ginley, D.; O'Hayre, R., Dopant-Induced Electronic Structure Modification of HOPG Surfaces: Implications for High Activity Fuel Cell Catalysts. *The Journal of Physical Chemistry C* **2010,** *114* (1), 506-515.

26. Kim, K.-S.; Park, S.-J., Synthesis and high electrochemical capacitance of N-doped microporous carbon/carbon nanotubes for supercapacitor. *Journal of Electroanalytical Chemistry* **2012,** *673*, 58-64.

27. Behan, J. A.; Hoque, M. K.; Stamatin, S. N.; Perova, T. S.; Vilella-Arribas, L.; García-Melchor, M.; Colavita, P. E., Experimental and computational study of dopamine as an electrochemical probe of the surface nanostructure of graphitized n-doped carbon. *The Journal of Physical Chemistry C* **2018,** *122* (36), 20763-20773.

28. Hahn, M.; Baertschi, M.; Barbieri, O.; Sauter, J. C.; Kötz, R.; Gallay, R., Interfacial Capacitance and Electronic Conductance of Activated Carbon Double-Layer Electrodes. *Electrochemical and Solid-State Letters* **2004,** *7* (2), A33.

29. Ferrari, A. C.; Rodil, S. E.; Robertson, J., Interpretation of infrared and Raman spectra of amorphous carbon nitrides. *Physical Review B* **2003,** *67* (15), 155306.

30. Díaz, J.; Paolicelli, G.; Ferrer, S.; Comin, F., Separation of the ${\mathit{sp}}^{3}$ and ${\mathit{sp}}^{2}$ components in the C1s photoemission spectra of amorphous carbon films. *Physical Review B* **1996,** *54* (11), 8064-8069.

31. Hellgren, N.; Haasch, R. T.; Schmidt, S.; Hultman, L.; Petrov, I., Interpretation of X-ray photoelectron spectra of carbon-nitride thin films: New insights from in situ XPS. *Carbon* **2016,** *108*, 242-252.

32. Qu, L.; Liu, Y.; Baek, J.-B.; Dai, L., Nitrogen-Doped Graphene as Efficient Metal-Free Electrocatalyst for Oxygen Reduction in Fuel Cells. *ACS Nano* **2010,** *4* (3), 1321-1326.

33. Titantah, J. T.; Lamoen, D., Carbon and nitrogen 1s energy levels in amorphous carbon nitride systems: XPS interpretation using first-principles. *Diamond and Related Materials* **2007,** *16* (3), 581-588.

34. Chu, P. K.; Li, L., Characterization of amorphous and nanocrystalline carbon films. *Materials Chemistry and Physics* **2006,** *96* (2-3), 253-277.

35. Ferrari, A. C.; Robertson, J., Raman spectroscopy of amorphous, nanostructured, diamond–like carbon, and nanodiamond. *Philosophical Transactions of the Royal Society of London A: Mathematical, Physical and Engineering Sciences* **2004,** *362* (1824), 2477-2512.

36. Ferrari, A. C.; Rodil, S. E.; Robertson, J., Resonant Raman spectra of amorphous carbon nitrides: the G peak dispersion. *Diamond and Related Materials* **2003,** *12* (3–7), 905-910.

37. Ferrari, A. C.; Robertson, J., Interpretation of Raman spectra of disordered and amorphous carbon. *Physical Review B* **2000,** *61* (20), 14095-14107.

38. Tay, B. K.; Shi, X.; Tan, H. S.; Yang, H. S.; Sun, Z., Raman studies of tetrahedral amorphous carbon films deposited by filtered cathodic vacuum arc. *Surface and Coatings Technology* **1998,** *105* (1–2), 155-158.

39. Shi, J. R.; Shi, X.; Sun, Z.; Lau, S. P.; Tay, B. K.; Tan, H. S., Resonant Raman studies of tetrahedral amorphous carbon films. *Diamond and Related Materials* **2001,** *10* (1), 76-81.

40. Gilkes, K. W. R.; Prawer, S.; Nugent, K. W.; Robertson, J.; Sands, H. S.; Lifshitz, Y.; Shi, X., Direct quantitative detection of the sp3 bonding in diamond-like carbon films using ultraviolet and visible Raman spectroscopy. *Journal of Applied Physics* **2000,** *87* (10), 7283-7289.

41. Laidani, N.; Guzman, L.; Miotello, A.; Brusa, R. S.; Karwasz, G. P.; Zecca, A.; Bottani, C.; Perrière, J., Nitrogen effects on the microstructural evolution of carbon films under thermal annealing. *Nuclear Instruments and Methods in Physics Research Section B: Beam Interactions with Materials and Atoms* **1997,** *122* (3), 553-558.

42. Nemanich, R. J.; Glass, J. T.; Lucovsky, G.; Shroder, R. E., Raman scattering characterization of carbon bonding in diamond and diamondlike thin films. *Journal of Vacuum Science & Technology A* **1988,** *6* (3), 1783-1787.

43. Ferrari, A. C.; Robertson, J., Resonant Raman spectroscopy of disordered, amorphous, and diamondlike carbon. *Physical Review B* **2001,** *64* (7).

44. Martins Ferreira, E. H.; Moutinho, M. V. O.; Stavale, F.; Lucchese, M. M.; Capaz, R. B.; Achete, C. A.; Jorio, A., Evolution of the Raman spectra from single-, few-, and many-layer graphene with increasing disorder. *Physical Review B* **2010,** *82* (12), 125429.

45. Chen, E. C. M.; Chen, E. S. D., Theoretical basis of the experimental tools. in *the electron capture detector and the study of reactions with thermal electrons*, John Wiley & Sons, Inc.: 2004; pp 47-74.

46. Lipkin, H. J., Beta-Ray Spectra. *Physical Review* **1949,** *76* (4), 567-567.

47. Akada, K.; Terasawa, T.-o.; Imamura, G.; Obata, S.; Saiki, K., Control of work function of graphene by plasma assisted nitrogen doping. *Applied Physics Letters* **2014,** *104* (13), 131602.

48. Kaukonen, M.; Nieminen, R. M.; Pöykkö, S.; Seitsonen, A. P., Nitrogen doping of amorphous carbon surfaces. *Physical Review Letters* **1999,** *83* (25), 5346-5349.

49. Yang, N.; Yang, D.; Chen, L.; Liu, D.; Cai, M.; Fan, X., Design and adjustment of the graphene work function via size, modification, defects, and doping: a first-principle theory study. *Nanoscale Research Letters* **2017,** *12* (1), 642.

50. Xu, J.; Mei, J.; Huang, X. H.; Li, X.; Li, Z.; Li, W.; Chen, K., Effect of nitrogen surface doping on the work function and field emission of hydrogenated amorphous carbon films. *Applied Physics A* **2005,** *80* (1), 123-126.

51. Kerner, Z.; Pajkossy, T., On the origin of capacitance dispersion of rough electrodes. *Electrochimica Acta* **2000,** *46* (2), 207-211.

52. Pajkossy, T., Impedance of rough capacitive electrodes. *Journal of Electroanalytical Chemistry* **1994,** *364* (1), 111-125.

53. Colavita, P. E.; Sun, B.; Tse, K.-Y.; Hamers, R. J., Photochemical grafting of n-alkenes onto carbon surfaces: the role of photoelectron ejection. *Journal of the American Chemical Society* **2007,** *129* (44), 13554-13565.

54. Vlad, A.; Balducci, A., Porous materials get energized. *Nature Materials* **2017,** *16*, 161.

55. Fic, K.; Platek, A.; Piwek, J.; Frackowiak, E., Sustainable materials for electrochemical capacitors. *Materials Today* **2018,** *21* (4), 437-454.

56. Dyatkin, B.; Gogotsi, Y., Effects of structural disorder and surface chemistry on electric conductivity and capacitance of porous carbon electrodes. *Faraday Discussions* **2014,** *172* (0), 139-162.

57. Memming, R., Semiconductor Electrochemistry, Weinheim: Wiley–VCH, 2001 %J Russian Journal of Electrochemistry. **2003,** *39* (9), 1011-1012.

Chapter 5

RF plasma N-Doped Amorphous Carbon

In this chapter, electrochemical capacitance study of N doped amorphous carbon in organic electrolyte (0.1 M TBAPF$_6$/MeCN) is discussed. Further, performance of these materials in the Oxygen reduction reaction under alkaline condition (0.1 M KOH) is studies. Nitrogenated materials were prepared using a radiofrequency chamber and a combination of XPS and Raman spectroscopy was used to correlate the electrochemical performance of these materials with electronic and structural properties.

5.1. Introduction

Carbon materials have been widely explored as electrode materials for the fabrication of electrochemical capacitors, batteries and fuel cells [1-3]. Nitrogen doping is an effective route to improving electrochemical properties of carbon-based materials. Nitrogen doped carbon materials have become important in the area of metal-free electrocatalysts for fuel cell applications [4-7] and for supercapacitor applications [8-11]. Nitrogen incorporation has been performed in different types of carbon materials such as carbon nanotubes [6, 12-13], graphene [14-15], amorphous carbon [16-17] and graphite [18].The motivation for choice of carbon materials for energy applications are their availability at typically low cost and large scale, coupled to unique properties such as potential for complex morphology and their high conductivity [19].

Nitrogen doping into carbon materials chemically and structurally changes the carbon scaffold. Several N sites such as pyridinic, pyrrolic, graphitic and N oxides are found on the surface of nitrogenated carbons. Nitrogen doping into the carbon matrix introduces vacancies, edge sites and defects that may have significant impact on electrochemical performance in materials for supercapacitors, electrochemical capacitors and ORR catalysts [20].

Activated carbon materials are often considered as the Electrical Double Layer *Capacitor* (EDLC), supercapacitor electrode materials, because of high surface area, good electrical properties, moderate cost, and controllable pore size [8]. Ordered materials CNTs have attracted supercapacitor electrode applications due to their superior electrical properties, pore size and good mechanical and thermal stability [21-23]. Templated porous carbon with well controlled narrow pore size distributions, ordered pore structures, large specific surface areas are promising candidates for supercapacitor electrode materials and high performance EDLC electrodes [24-25]. In order to enhance the efficiency and performance of these materials for energy storage applications there is interest in understanding the effects on their properties resulting from incorporation of heteroatoms such as nitrogen, phosphorous and boron. Previous chapters discussed the effect of bulk N doping on the capacitive properties of amorphous carbon. This chapter focuses on structure activity studies of RF plasma enhanced N-doped annealed amorphous carbon electrodes for electrochemical capacitance studies in organic electrolyte and the result of these modifications on the performance in the oxygen reduction reaction (ORR) in alkaline electrolyte. Annealed a-C was surface-doped with nitrogen via RF plasma under nitrogen gas flow; this methodology has been previously explored in the literature for the nitrogenation of materials such as graphene [26-27], diamond like carbon [28-29], a-C [30]. Capacitive properties of the amorphous graphitized electrode materials will be determined by using cyclic voltammetry (CV) and electrochemical impedance spectroscopy (EIS) techniques in organic electrolyte to avoid pseudo capacitive contribution. In order to understand catalytic activity of these electrode materials the oxygen reduction reaction (ORR) study was carried out on these electrodes under alkaline condition.

5.2. Materials and methods

5.2.1 Chemicals and Materials

Tetrabutylammonium hexafluorophosphate (TBAPF$_6$) (≥99.0%, electrochemical analysis), acetonitrile (MeCN, 99.8%, anhydrous), sulfuric acid (95 - 97%), hydrogen peroxide (>30% w/v), Potassium hydroxide (KOH, semiconductor grade pellets, 99.99%, SigmaAldrich) were purchased from Sigma Aldrich. Glassy carbon (GC) discs (HTW Sigradur® radius 2.5 mm) and B-doped Si wafers (MicroChemicals; resistivity 5 – 10 Ω-cm) were used as substrates for carbon deposition.

5.2.2 Substrate Preparation

GC disks were polished with progressively finer grades of alumina slurry (Buehler). The GC disk was first polished using 1200 grit sandpaper. After rinsing with plenty of Millipore water the disks were sonicated for 20 min in Millipore water. polished on nylon paper (Buehler) using 1 μm slurry, sonicated for 20 min in Millipore water, then polished on nylon paper using 0.3 μm slurry and sonicated for 20 min in Millipore water; disks were subsequently polished to a mirror finish using 0.3 and 0.05 μm slurries on MicroCloths® pads (Buehler) and sonicated for 20 min in Millipore water between each step. Clean disks were mounted in a custom-made Teflon® holder and placed in the vacuum chamber for deposition of thin film carbon electrodes on their surfaces. B-doped Si wafers were prepared according to the same protocol described in Chapter III prior to deposition.

5.2.3 Deposition of carbon electrode materials

a-C a900 carbon films were prepared by first depositing a precursor a-C film via DC-magnetron sputtering (Torr International) followed by a thermal annealing treatment. The films were deposited via DC-magnetron sputtering from a graphite target (99.999%) at base pressures <2 x10^{-6} mbar, deposition pressures 2-7 x10^{-3} mbar and total gas flow of 50 mL min^{-1}, following previously reported protocols [31-32]. Deposited films are topographically smooth and in the thickness range 70-120 nm [32]. After deposition, the resulting films were transported directly to a tube furnace and annealed under N_2 atmosphere for 1 h at 900 °C. To incorporate N into a-C 900 electrodes, RF nitrogen plasma exposure was performed in vacuum chamber with a base pressure of 10-18 mTorr, equipped with an induction coil connected to an RF generator (500 W, 13.56 MHz) through a matching network (MFC tuner). The flow rate of N_2 gas through the generator was regulated at 20 ml min^{-1} and the chamber pressure during the nitridation process was maintained at 118 mTorr. The nitrogen flow rate was controlled using mass flow controllers (Brooks Instruments). The plasma exposure time was set at 0, 5, 10 and 20 min resulting in samples here onwards referred to as a-C a900, a-C:N a900-pl-5, a-C:N a900-pl-10 and a-C:N a900-pl-20, respectively.

5.3 Characterization

XPS characterization was performed on a VG Scientific ESCAlab Mk II system (<2 $\times 10^{-8}$ mbar), using Al Kα X-rays (1486.6 eV); core-level spectra were collected with analyzer pass energy of 20 eV and survey spectra were collected with analyser pass energy of 200 eV; the binding energy scale was referenced to the C 1s core-level at 284.8 eV. Peaks were fitted with Voigt functions after Shirley background subtraction using commercial software (CasaXPS); at.% composition was obtained from peak area ratios after correction by Scofield relative sensitivity factors (C = 1.0, N = 1.8, O = 2.93).

Raman spectra were measured in backscattering configuration using a Renishaw 1000 micro-Raman system equipped with an Ar^+ laser for 488 nm excitation. The incident beam was focused by a Leica microscope with a 50× magnification objective and short-focus working distance; incident power was kept <2 mW to avoid sample damage. Spectra were baseline corrected using commercial software prior to analysis (Wire 3.2).

In order to study capacitance of plasma-exposed electrodes, electrochemical measurements were carried using a three-electrode cell controlled by a potentiostat with a graphite rod as counter electrode and Ag/Ag^+ reference electrodes (IJCambria) for characterisation in organic electrolyte. The Ag/Ag^+ reference 1.0 mM $AgNO_3$ in 0.1 M $TBAPF_6$ in acetonitrile yielded $E^{0\prime}$ = 0.080 V for 0.001 M Fc/Fc^+ in the same electrolyte, thus placing the Ag/Ag^+ potential at 0.320 V *vs.* SHE [33]. A Teflon static disk holder (Pine Instruments) enclosing a GC disk coated with Nitrogen plasma exposed the sputtered carbon film was used as a working electrode; all contacts were confirmed to be ohmic with <8 Ω resistance. Cyclic voltammetry (CV) was carried out in 0.1 M $TBAPF_6$ solutions in MeCN, at 25 °C, 50 mV s^{-1} and using IR compensation. Electrochemical impedance spectroscopy (EIS) was carried out over the range of 0.1-100 kHz using a 10 mV AC amplitude. Spectra were collected at either open circuit potential (OCP) or at varying DC offsets in 0.2 V or 0.05 V steps as indicated in the text; 300 s equilibration time was allowed between each potential step. The specific capacitance was obtained via normalisation by the geometric area of the electrodes.

In order to perform oxygen reduction reactions on these electrodes, electrochemical measurements were carried out using a Metrohm Autolab AUT50324 potentiostat using a 3-electrode setup thermostated at 25 °C. A Hydroflex hydrogen electrode (Gaskatel) graphite rod (GoodFellow) and GC disk coated with Nitrogen plasma exposed the sputtered carbon film were used as reference, counter and working electrodes respectively. The electrochemical cell (Pine Instruments) was cleaned using Piranha solution (3:1 H_2SO_4:H_2O_2 **CAUTION:** Piranha solution is a strong oxidant followed by rinsing several times with Millipore water. The cell was rinsed with the electrolyte (0.1 M KOH) used in the experiment. Prior to start experiment, working electrodes were cleaned via potential cycling from 0.05 to 1.1 V vs. RHE in Ar-saturated 0.1 M KOH (20 cycles). CVs were obtained in a potential window of 0.05-1 V vs RHE. All the CVs were taken with iR compensation using commercial software (NOVA) with the uncompensated solution resistance determined prior to each experiment using EIS.

The rotating ring-disk electrode experiments (RRDE, pine instrument) were carried out using Pine RRDE tip coupled with Metrohm Autolab AUT50324 potentiostat. ORR polarization curves were obtained in O_2-saturated 0.1 M KOH electrolyte over the potential window of 0.05–1.0 V range at 50 mV s−1 and at 400, 900 and 1600 rpm. CVs were also collected in Ar-saturated 0.1 M KOH under similar experimental conditions. Faradic current densities were obtained by subtracting the capacitive current obtained in Ar-saturated electrolyte from that obtained in O_2-saturated electrolyte under identical experimental conditions. For the calculation of the turnover frequency (TOF) was determined by integrating the area under the oxidation sweep of the relevant voltammogram in 0.1 M KOH and the TOF was calculated at a potential of 0.3 V as TOF = $J_i/4Q$. In this expression, J_i is the current density at potential 0.3 V, Q is the charge associated with the redox processes occurring on the electrode.

5.4. Results and Discussion

5.4.1 Chemical composition of a-C:N electrodes using XPS

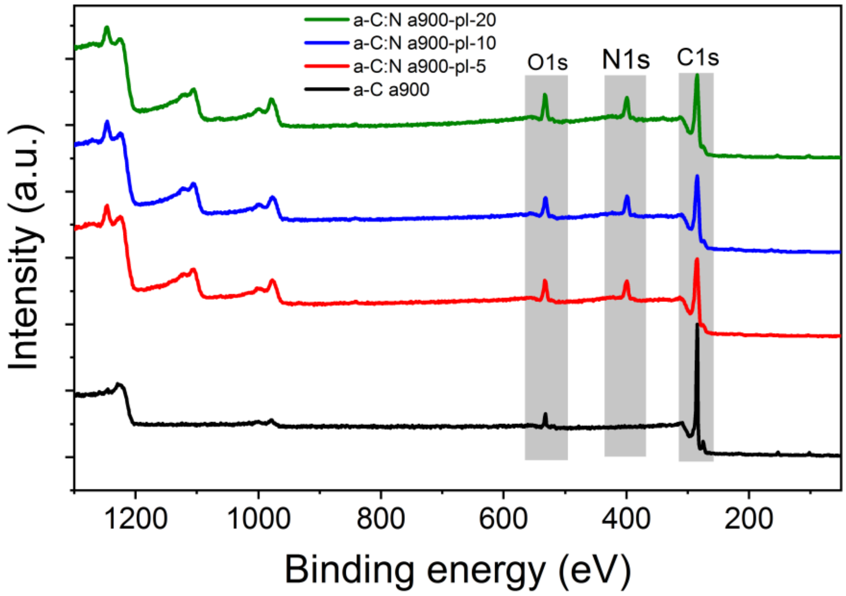

Figure 5.1: Survey scans of a-C a900, a-C:N a900-pl-5, a-C:N a900-pl-10 and a-C:N a900-pl-20 electrodes.

Nitrogen free carbon electrodes were prepared in the form of thin films via magnetron sputtering and characterised as described in previous work from our group [32]. Deposited films were annealed under N_2 atmosphere for 1 h at 900 °C by using electric tube furnace. In order incorporate N into graphitised a-C, the annealed films were placed into an RF plasma chamber under N_2 flow of 20 ml min^{-1} which was controlled by mass flow controller. Three different plasma exposure times were investigated: 5 min, 10 min and 20 min. Figure 5.1 shows survey scans of the N-free graphitized electrode and of the three samples obtained after plasma exposure. The spectra show characteristic features of C 1s, O 1s and N 1s peaks at 284, 532 and 400 eV, respectively. No other peaks are observed in the spectra thus confirming that all samples are metal-free. a-C a900 prepared via annealing in the absence of plasma exposure shows no evidence of N-content in its structure, as confirmed by an absence of N 1s peaks in the survey.

Figure 5.2 displays deconvoluted high resolution scans of the C 1s region of all samples examined. The asymmetric envelope indicates that these carbon materials are mostly sp^2 bonded carbon, as expected for graphitized carbon surfaces. The peak position at *ca.* 284.4 eV and *ca.* 285.5 eV present in all deconvolutions are typically assigned to sp^2- and sp^3-centers in the carbon scaffold, respectively [34]. Nitrogen incorporation into graphitised a-C through RF plasma exposer has the effect of increasing the full-width at half maximum (FWHM) of the C 1s envelope due to an increased degree of disorder in the carbon sp^2-network and due to the introduction of C-N and C-O functionalities as discussed below in greater detail [35].

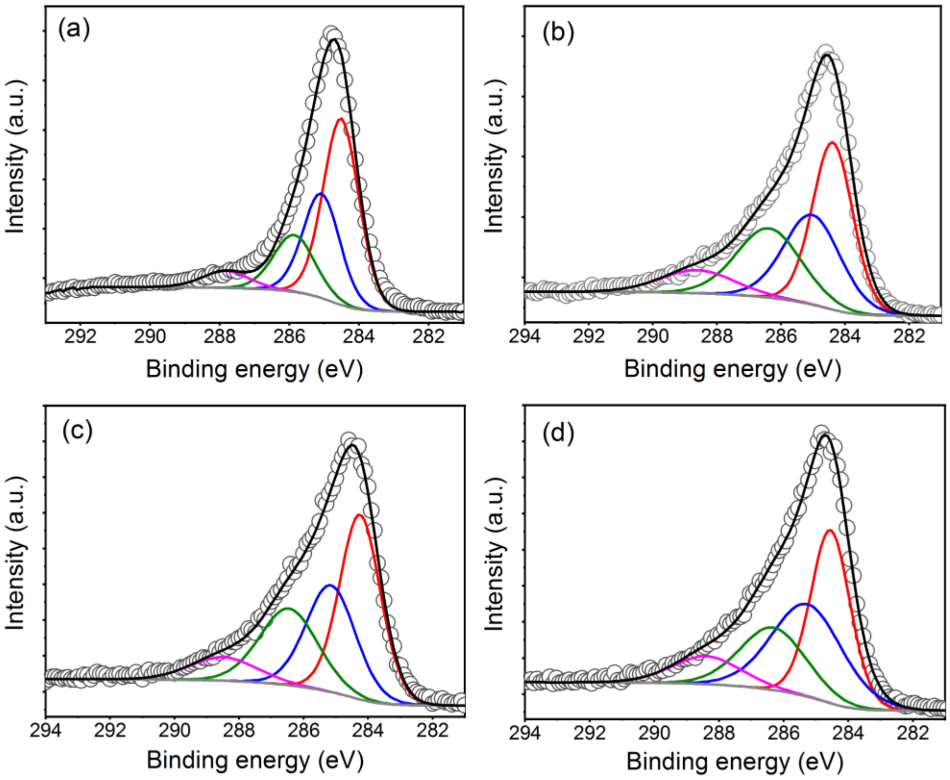

Figure 5.2: Deconvoluted C 1s envelopes of a) a-C a900, b) a-C:N a900-pl-5, c) a-C:N a900-pl-10 and d) a-C:N a900-pl-20.

Table 5.1: C 1s FWHM, and chemical composition of a-C a900 and nitrogenated a-C a900 materials obtained from XPS deconvolutions.

Sample	C1s FWHM	O/C %	N/C %	At. N%
a-C a900	1.57	5.3	-	-
a-C:N a900-pl-5	2.25	11	16	8.9
a-C:N a900-pl-10	2.42	11	17	9.4
a-C:N a900-pl-20	2.37	14	17	9.4

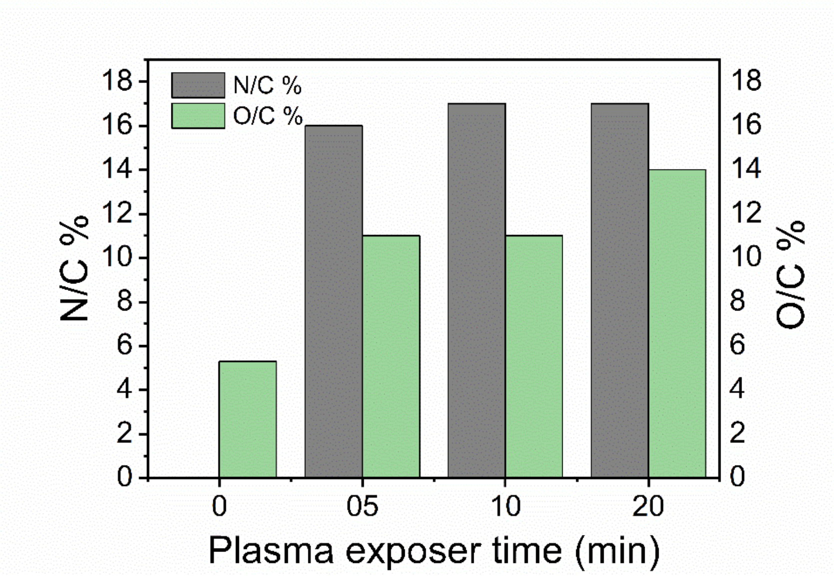

Figure 5.3: N/C % and O/C % of a-C:N electrodes versus plasma exposer time.

It is complex to quantify the sp^3/sp^2 ratio of C 1s for nitrogenated carbon as the region above the 285.5 eV has contributions from N-bonded sp^3 and sp^2 carbon atoms [36]. The peaks at binding energies above 286 eV are assigned to C- O or C= O in the case of a-C a900 however in the case of Nitrogenated a-C a900 it is difficult to deconvolute C-O and C-N contributions due to spectral overlap [37]. The area ratios A_{O1s}/A_{C1s} and A_{N1s}/A_{C1s} corrected by the sensitivity factors (RSF, O = 2.93, N = 1.8, C = 1) were used to quantify the nitrogen and oxygen content of the films. Table 5.1 shows a summary of the elemental composition of the films; Figure 5.3 also summarises these results in a bar chart plot. The O/C% and N/C% were found to increase after plasma treatment relative to the graphitised a-C a900 sample. Slight differences were observed in the N/C % and O/C % across the a-C:N electrodes. The N/C % was found to level off at *ca.* 17% after 10 min exposure (*ca*. 9% N at.%) , thus suggesting that nitrogenation of graphitised a-C via plasma reaches a self-limiting concentration under the investigated experimental conditions. The O/C% content is slightly higher for the sample treated for 20 min.

Deconvoluted N 1s spectra for the a-C:N a900-pl-5, a-C:N a900-pl-10 and a-C:N a900-pl-20 surfaces are shown in Figure 5.3 a-c, respectively. The broad peak envelope suggests that multiple types of N-sites are present at the carbon surface. The N 1s peak was fitted with five different contributions corresponding to pyridinic (398.6 eV), pyrrolic (400.2 eV), graphitic-center (401.1 eV), graphitic-valley (402.1 eV) and N-oxides (403.5 eV)[38-39] .Pyridinic-N and pyrrolic-N sites were found to dominate the N 1s spectra while comparatively smaller contributions were attributed to graphitic-N and N-oxide sites. Overall, the XPS data indicate that plasma exposure of graphitised a-C introduces a distribution of different N-sites that do not however change significantly with increasing exposure time.

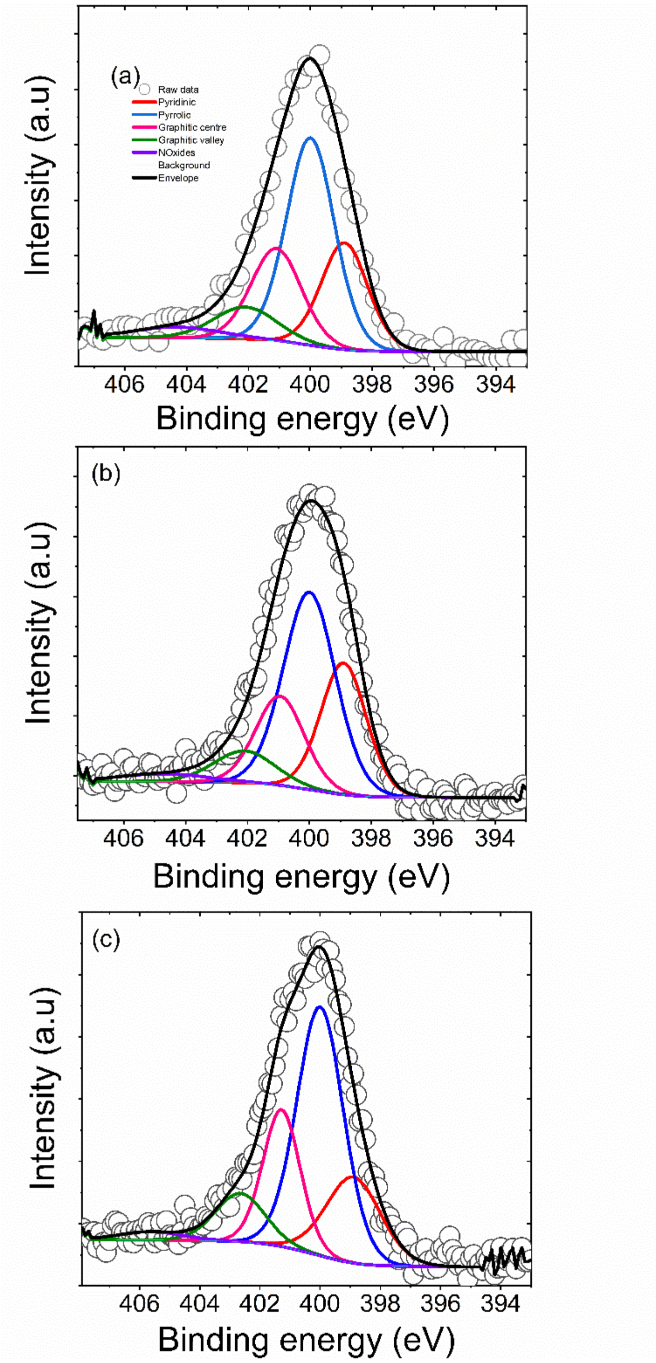

Figure 5.4: a-c) N 1s spectra of a900-pl-5, a900-pl-10 and a900-pl-20 respectively.

5.4.2 Structural characterisation of a-C:N electrodes using Raman spectroscopy

Structural properties of a-C a900 and a-C:N a900-pl-5-20 materials were investigated by using Raman spectroscopy at an excitation wavelength of 488 nm. Figure 5.5 shows baseline-corrected Raman spectra in the 900-1900 cm^{-1} range of a-C a900 and a-C:N a900-

pl-5-20 materials deposited on silicon wafers. All the spectra were normalised relative to the G band intensity. Spectra of show two characteristic peaks assigned to the G and D bands at approximately 1580 cm^{-1} and 1380 cm^{-1}, respectively for visible excitation. The G peak is associated to the bond stretching of all pairs of sp^2 atoms in both rings and chains, while the D peak is associated to the breathing modes of sp^2 atoms in rings [35, 40-41].

In order to estimate spectral parameters of G and D peaks all the spectra were deconvoluted with three Gaussian functions and all the spectra were normalised prior to fitting. Deconvoluted spectra of a-C:N a900-pl-5, a-C:N a900-pl-10 and a-C:N a900-pl-20 materials were presented in figure 5.6. Several fittings methods of the Raman spectra have been discussed in the literature including use of Gaussian/Lorentzian functions (Voigt functions) [42-43], Breit-Wigner-Fano (BWF) and Lorentzian functions [41, 44] and all Gaussian functions. The spectrum in Figure 5.5 were fitted with three Gaussian functions~~.~~

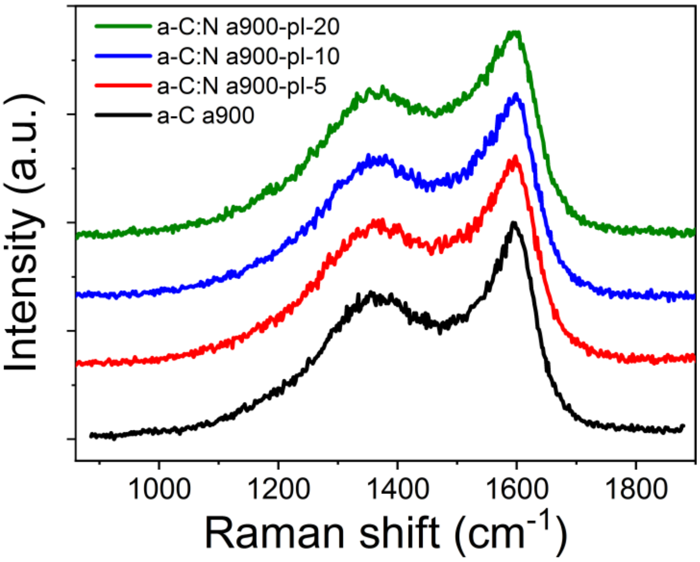

Figure 5.5: Raman spectra of amorphous carbon electrodes prepared with varying N2% content in the deposition gas mixture; excitation 488 nm. Spectra are normalised relative to the G band intensity.

Two Gaussian peaks were assigned to G and D bands described above with a third peak centred close to 1510 cm^{-1} commonly referred to as the A peak. The A peak is attributed to C-C vibrations in the amorphous network consisting of an atomically mixed structure of sp^2 and sp^3 hybridised carbon atoms located between graphitic clusters [45-46]. A summary of Raman spectral parameters obtained from deconvoluted spectra are presented in figures 5.7 and 5.8. Figure 5.7a displays the peak height ratio of D to G (I_D/I_G); the increase in I_D/I_G with plasma treatment time suggests an increase in the disorder in the carbon scaffolds where a-C:N a900-pl-20 has highest I_D/I_G of 0.88 implying a smaller average cluster size. This sample also displays the highest I_A/I_G ratio of 0.25 (figure 5.7b) thus suggesting that disordered/amorphous regions are more abundant in the sample that underwent longest plasma exposure. These findings therefore support a progressive increase in scaffold disorder resulting from plasma treatment, likely due to an increase in sp^2/sp^3 mixed regions at the expense of extended graphitic clusters.

Further evidence of progressive increase in defects and amorphous content emerges from an analysis of the FWHM of the G and D peaks, in figures 5.7b and 5.7c. The FWHM are diagnostic of the distribution of bond angles at excited sp^2-centres and a measure of disorder [47]. A slight increase in FWHM of D and G increases with plasma exposer time (upon nitrogen incorporation) indicates a broad distribution of bonding geometries for sp^2 centre.

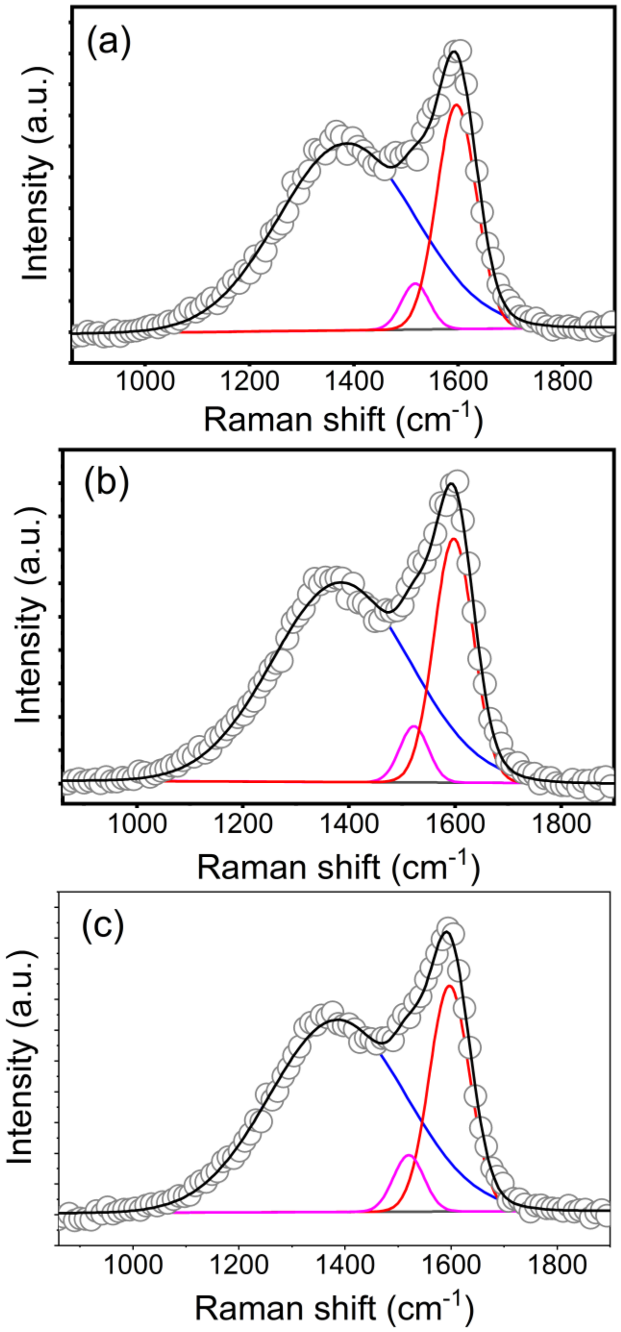

Figure 5.6: Raman spectra and peak deconvolution of (a) a-C:N a900-pl-5, (b) a-C:N a900-pl-10 and (c) a-C:N a900-pl-20 ; excitation 488 nm. Spectra are normalised relative to the G band intensity.

A remarkable increase is observed in FWHM of the D peak, relative to a-C a900, in a-C:N a900-pl-5; this indicates that even 5 min of plasma exposure have a transformative effect in the defect density of the graphitized a-C materials.

Figure 5.8 displays peak position of D and G bands as a function of plasma exposure time. The G peak position properties of these electrodes are similar to that of nanocrystalline graphite (nc-G) on the basis of three stage model of Ferrari and Robertson [35,41]. No significant change of G peak position was observed for a-C a900 and a-C:N a900 electrodes as they possess similar graphitic structure, on the other hand D peak position increases with plasma exposure time thus indicating the presence of disorder in the structure [48].

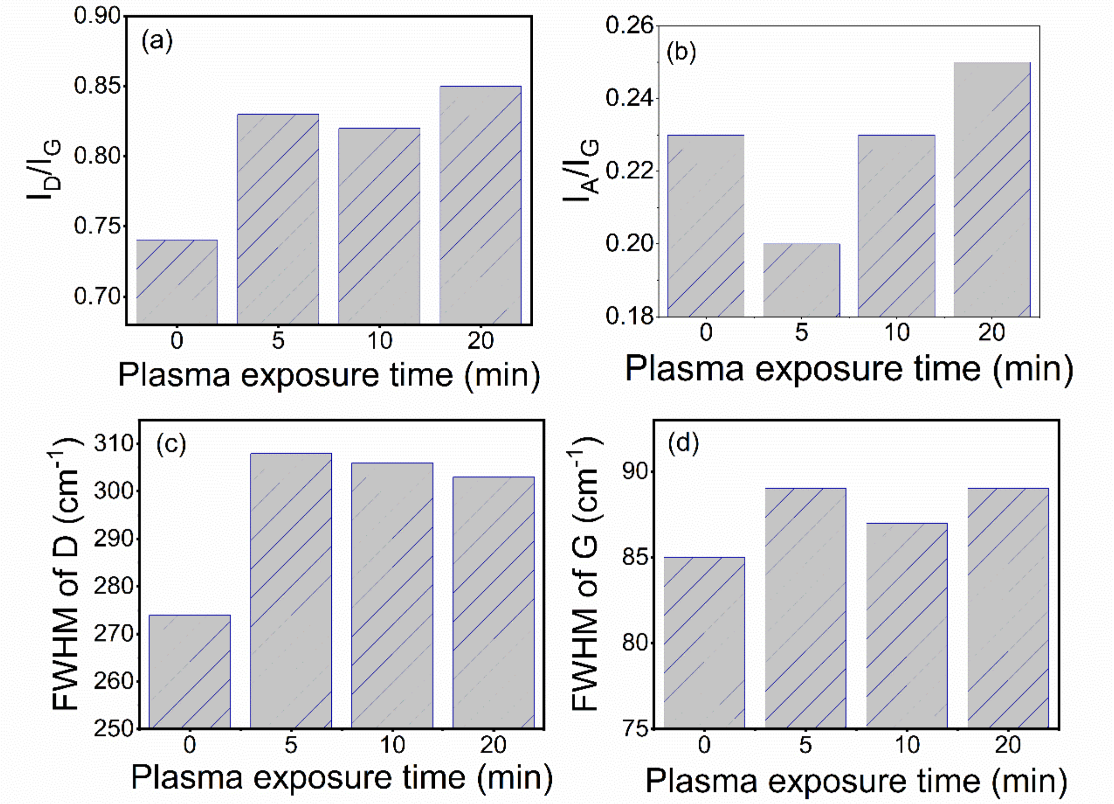

Figure 5.7: (a) Variation of D to G peak height ratio (ID / IG), (b) FWHM G peak (c) FWHM of D peak and (d) Variation of A to G peak height ratio vs Plasma exposer time.

In summary, Raman spectroscopy indicates that metal free a-C:N a900-Pl carbon electrodes prepared through RF plasma treatment display increased disorder and/or defect density in the carbon scaffold as a result of plasma exposure. Despite the three plasma-treated samples displaying similar N-site concentrations, as evidenced by XPS, the degree of disorder appears to increase progressively in the order a-C:N a900-pl-5 < pl-10 < pl-20.

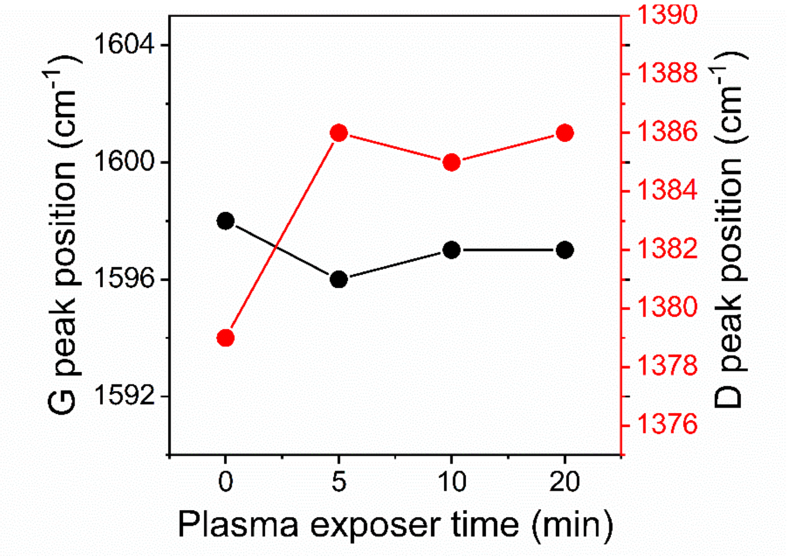

Figure 5.8: D peak position and G peak position as function of Plasma exposer time.

5.4.3 Capacitance study in Organic electrolyte

Electrochemical characterisation via CV and EIS was carried out on a-C:N electrodes to understand how the electrochemical capacitance properties are affected by the plasma nitrogenation process. Organic electrolyte 0.1 M $TBAPF_6$ in acetonitrile was chosen for electrochemical capacitance measurements to minimize the pseudocapacitance contribution from functional groups on the carbon surface [49-50] as previously discussed in chapter III.

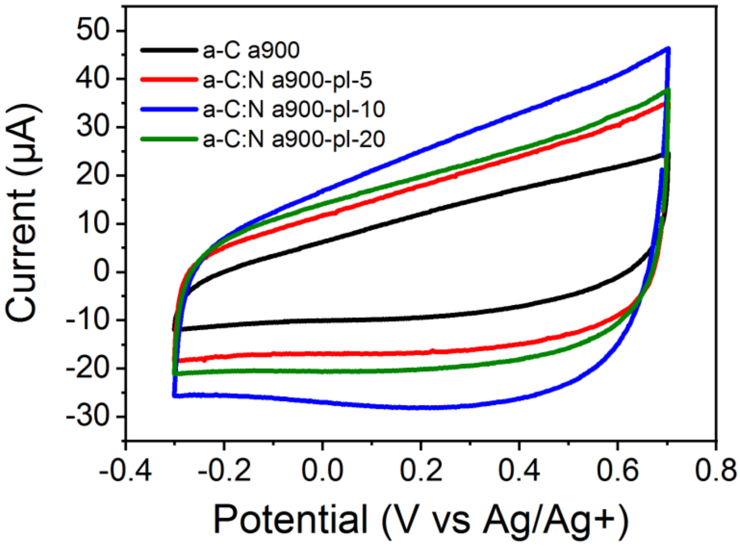

Figure 5.9: Cyclic votammograms of a-C a900, a-C:N a900-pl-5, a-C:N a900-pl-10 and a-C:N a900-pl-20 in Ar-saturated 0.1 M $TBAPF_6$ /acetonitrile at 50 mV s^{-1}. No Faradaic peaks are visible in the potential window used for our experiments.

In order to study electrochemical capacitance responses, cyclic voltammetry (CV) and electrochemical impedance spectroscopy (EIS) were carried out using a three-electrode system. Figure 5.9 shows typical cyclic voltammograms (CVs) of a-C a900 and a-C:N a900-pl-5-20 electrodes over the -0.3 – 0.7 V potential window at 50 mV s^{-1} in 0.1 M TBAPF6/acetonitrile. The curves display the characteristic shape of a capacitive response while no faradic peaks are visible in the potential window used for this experiment. The capacitive currents of a-C:N electrodes were found to be larger than that of the a-C a900 electrode, while the capacitive current of a-C:N a900-pl-10 was found to be the highest among all a-C:N electrodes despite all having similar N-site concentration.

Figures 5.10 a-c display CVs of a-C a900, a-C:N a900-pl-5 and a-C:N a900-pl-10 electrodes over the -0.3 – 0.7 V potential window at different scan rates ranging from 200 mV/s to 10 mVs^{-1} in 0.1 M TBAPF6/acetonitrile. The capacitive current responses increase with scan rates for all the electrodes, while the rectangular shape of the CVs suggest near-ideal capacitive behaviour over the potential window.

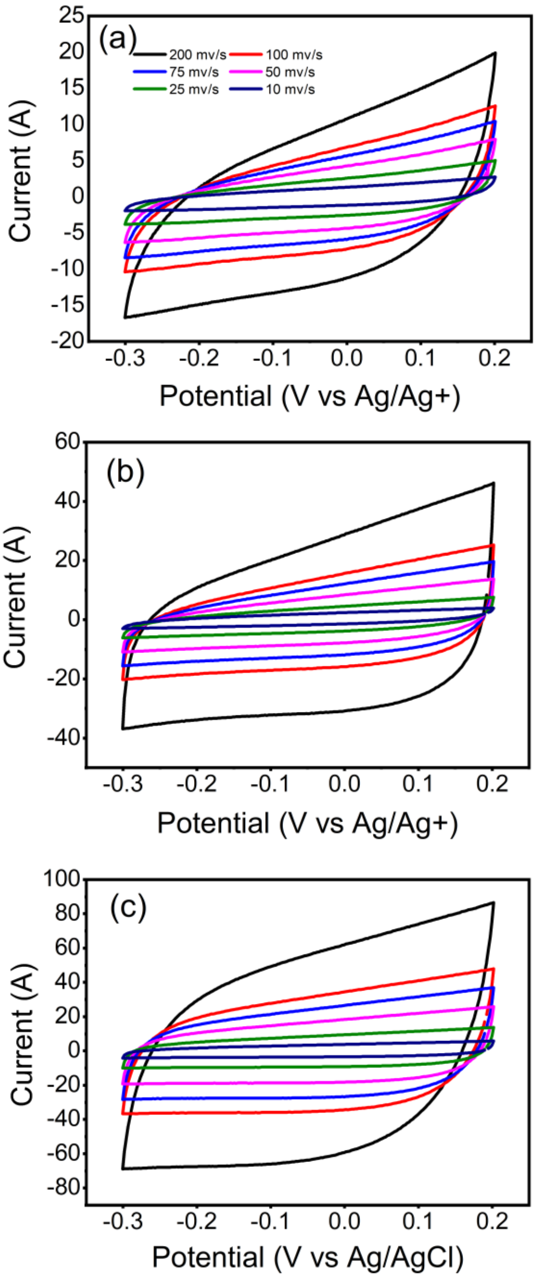

Figure 5.10: Cyclic voltammograms of a-C a900, a-C:N a900-pl-5, a-C:N a900-pl-10 and a-C:N a900-pl-20 at varying scan rates(from 200-10 mV s^{-1}). No Faradaic peaks are visible in the potential window used for our experiments.

The plot of positive current at the centre of the voltammograms of -0.05 V versus scan rates is presented in figure 5.11, where the current can be observed to vary approximately linearly with the rate. The slope of a-C:N electrodes is higher than that of non nitrogenated a-C a900 electrode thus suggesting that the capacitance increases upon exposure to the plasma treatment; notably, this happens despite the electrodes displaying very similar N/C% content, as discussed in the previous sections.

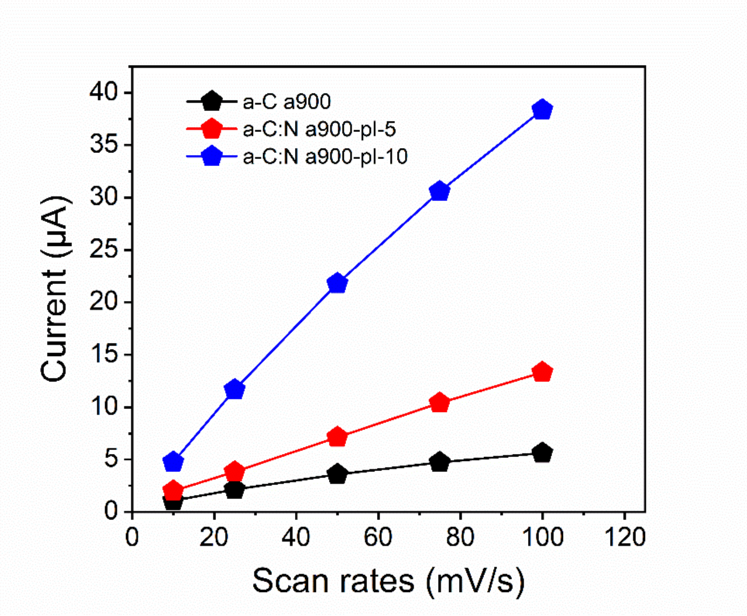

Figure 5.11: The dependence of current on the scan rates taken in 0.1 M $TBAPF_6$ /acetonitrile at 25°C. The current was obtained at -0.05 V from the anodic scans of the cyclic voltammograms taken at different scan rates.

EIS was carried out over the frequency range of 0.1-10^4 Hz in 0.1 M $TBAPF_6$ /acetonitrile in order to investigate electrochemical capacitance responses. Figures 5.12 a-b display Bode plots of absolute impedance (|Z|) and phase angle for nitrogen-free a-C a900 electrodes and nitrogenated a-C:N a900-pl-5-20 electrodes obtained at OCP (-0.28 -0.05 V vs. Ag/Ag+). At 0.1 Hz the absolute impedance (|Z|) of a-C a900 was 10537 Ω; this value decreases upon nitrogen incorporation (figure 5.12a) to 7421 Ω, 5154 Ω and 5411 Ω for a-C:N a900-pl-5, a-C:N a900-pl-10 and a-C:N a900-pl-20, respectively. The phase behaviour of a-C a900 shows a typical capacitive response with deviations from ideality indicated by a phase angle at 0.1 Hz of *ca.* -70°. Upon 5 min of plasma exposure, the phase preserves its capacitive characteristics with an improvement in phase angle to -75 °. Significant and progressive deviations from ideality are observed for exposures of 10 and 20 min thus indicating that, despite the absence of changes in the N/C% content, prolonged exposure to the plasma introduces further changes in the carbon nanostructure, albeit it without introducing further chemical changes in the carbon surface.

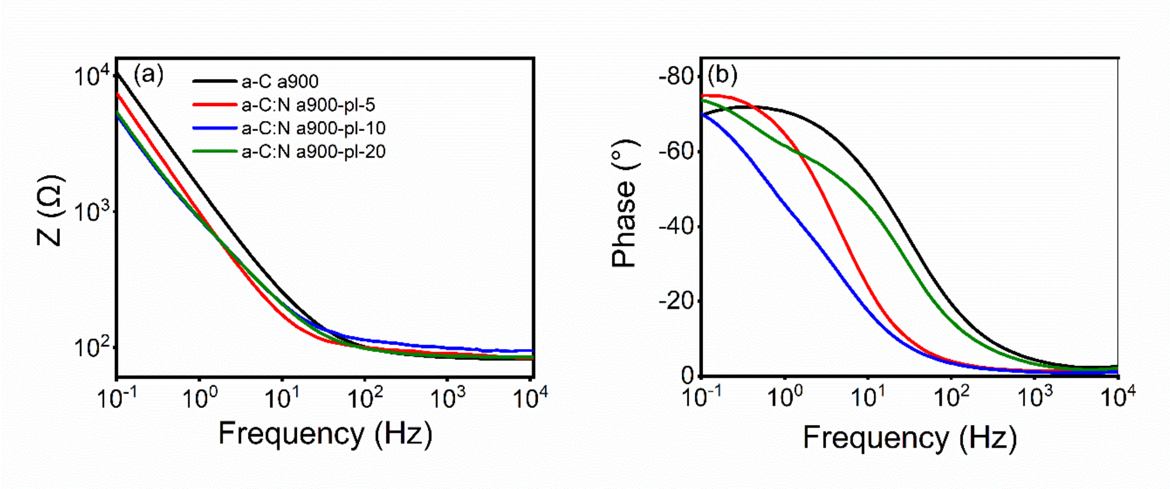

Figure 5.12: Bode plots of impedance module |Z| and phase angle of (a-b) nitrogen free a-C a900 and of nitrogenated a-C:N a900-pl-5, a-C:N a900-pl-10 and a-C:N a900-pl-20. EIS spectra obtained in 0.1 M $TBAPF_6$/acetonitrile at open circuit potential (OCP, -0.28-0.1 V vs. Ag/Ag+).

Nyquist plots of EIS spectra obtained at open circuit potential (OCP, -0.28-0.1 V vs. Ag/Ag+) are presented in figure 5.13. The real and imaginary parts of the impedance show a considerable decrease in value upon plasma exposure, which correlates with the change in capacitance observed for the a-C:N electrodes in the CVs. The impedance of a-C a900 is high compared with a-C:N electrodes and follows the trend as a-C a900 > a-C:N a900-pl-5 > a-C:N a900-pl-20 > a-C:N a900-pl-10.

The effective or equivalent series capacitive contribution to EIS spectra was calculated from the imaginary part of the complex impedance Z_{im} according to equation 3.1. Figure 5.14a shows the change in the series equivalent capacitance at 0.1 Hz as a function of the DC offset over the range -0.8 – 0.8 V vs. Ag/Ag+ in 0.1 M $TBAPF_6$/ acetonitrile. The capacitance curve of a-C a900 electrode is asymmetric with a capacitance at pzc of 0.76 mF cm^{-2} at -0.2 V vs Ag^+/Ag; this value is high compared with literature values of carbon based electrodes, which range from 5 to 70 μF cm^{-2} depending on the carbon structure, i.e., basal, edge sites as well as its electronic properties [51-52]. This suggests a microroughness factor of *ca.* 10-20 for annealed N-free a-C a900 electrodes. Remarkably, while the capacitances at the potential of zero charge for a-C:N a900-pl-5 in are 1.5-2.5 times larger than that of a-C a900 electrode. The capacitances at pzc are remarkably close to each other and to the a-C a900 value, being in a ratio $C_{\text{a-C a900}} : C_{\text{a-C:N a900-pl-5}} : C_{\text{a-C:N a900-pl-20}} : C_{\text{a-C:N a900-pl-10}} = 1 : 1.5 : 2 : 2.3$. Although N-site concentration of all a-C:N electrodes have no major differences, increases in capacitance values for higher plasma exposure time due to creation of microroughness among the electrodes during plasma treatment are observed [53].

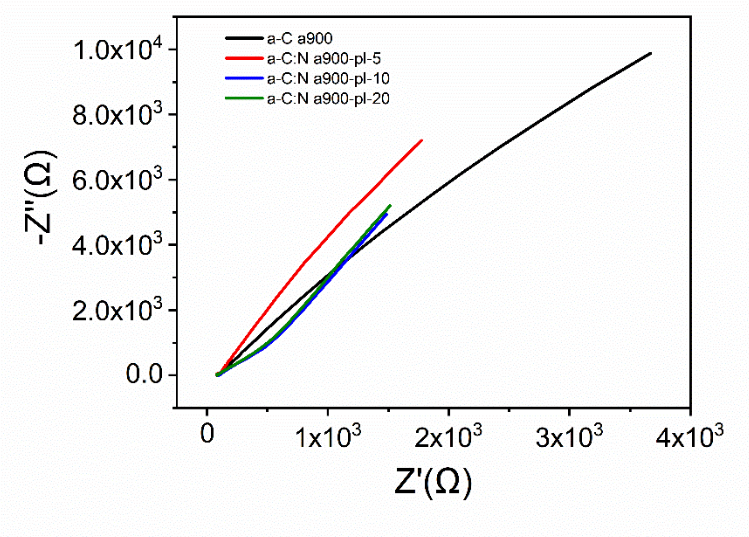

Figure 5.13: Nyquist plots of EIS spectra of a-C a900, a-C:N a900-pl-5, a-C:N a900-pl-10 and a-C:N a900-pl-20 in non-aqueous 0.1 M TBAPF$_6$/acetonitrile at open circuit potential (OCP, -0.28-0.1 V vs. Ag/Ag+).

Minimum capacitance of a-C a900 at potentials of -0.2 V vs Ag$^+$/Ag characteristic asymmetry curve which agrees with previous reports of p-type behaviour in nitrogen-free sputtered a-C [54]. All the a-C:N plots display capacitance minima at potentials of -0.35 V vs Ag$^+$/Ag thus indicating that nitrogen incorporation into a-C a900 results a decrease in the pzc [55] . The minimum capacitance of a-C:N a900-pl-10 is the highest among a-C:N materials, while a900-pl-5 and a-C:N a900-pl-20 also display higher minimum capacitance compare with a-C a900. All a-C:N materials display asymmetry in the capacitance vs. potential plots that suggests a p-type character also for N-modified materials. This is somewhat surprising as nitrogenation of carbons is typically thought to result in n-type character. Therefore, it suggests that other effects of plasma exposure beyond electronic doping, such as amorphization and O-site introduction might dominate the overall capacitive behaviour at the interface.

Further, the equivalent series capacitance at 0.5 Hz as a function of the DC offset over the range -0.8 – 0.8 V vs. Ag/Ag+ in 0.1 M TBAPF$_6$/acetonitrile is presented in figure 5.14b. Similar trends in capacitances are observed with higher values for a-C:N a900-pl-10 followed by a-C:N a900-pl-20, a-C:N a900-pl-5, and a-C a900; the asymmetry in the capacitance curve observed also indicates p-type semiconducting behaviour at this higher frequency [56].

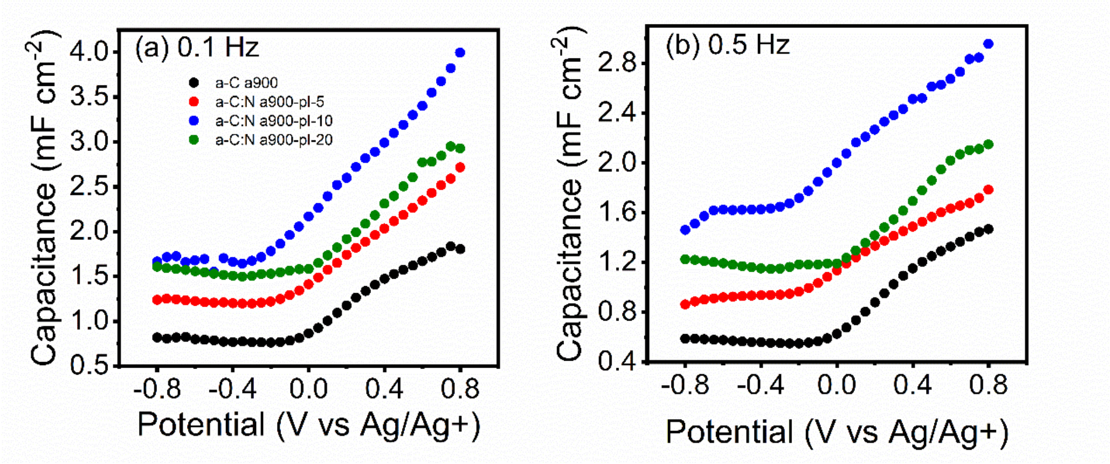

Figure 5.14: Equivalent series capacitance of a-C a900, a-C:N a900-pl-5, a-C:N a900-pl-10 and a-C:N a900-pl-20 as a function of potential in 0.1 MTBAPF$_6$ /acetonitrile calculated at (a) 0.1 Hz and (b) 0.5Hz.

The capacitances at pzc at 0.5 Hz of a-C a900 was found to be *ca.* 0.55 mF cm^{-2} at -0.25 V. Shifts in the capacitance at the minimum are observed for a-C:N a900-pl-5 (*ca.* 0.5 mF cm^{-2}) , 10 (*ca*. 1.46 mF cm^{-2}) and 20 (*ca*. 1.14 mF cm^{-2}). Figure 5.15 displays equivalent series capacitance at intermediate frequency of 10 Hz as a function of the DC offset over the range -0.8 – 0.8 V vs. Ag/Ag+ in 0.1 M TBAPF$_6$/ acetonitrile. Minimum capacitance of a-C a900 *ca.* 0.29 mF cm^{-2} at -0.35 V. On the other hand, minimum capacitance of a-C:N electrodes falls in the range of -0.8-0.35 V. There is a clear evidence of capacitance dispersion at different frequencies was observed in a-C:N electrodes which is due to disorder and inhomogeneity in electrode surface [57-58].

Summary of capacitance study in organic solvent of 0.1 M TBAPF$_6$/ acetonitrile indicate that nitrogenation of graphitic a-C through RF N$_2$ plasma exposer introduce different N-sites and defect into carbon scaffolds. Results show that nitrogen incorporation significantly increases the capacitance in organic media relative to the N-free a-C a900 materials.

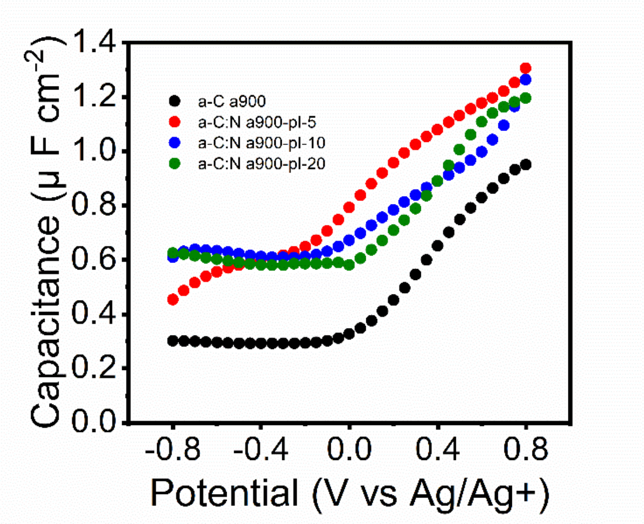

Figure 5.15: Equivalent series capacitance of a-C a900, a-C:N a900-pl-5, a-C:N a900-pl-10 and a-C:N a900-pl-20 as a function of potential in 0.1 M $TBAPF_6$/acetonitrile calculated at 10 Hz.

5.4.4 ORR Performance of N-doped Carbon Electrodes in Alkaline Medium

The electrocatalytic activity of RF plasma treated N-doped graphitised a-C carbon materials in O_2-saturated 0.1 M KOH was evaluated via cyclic voltammetry (CV) experiments using a rotating and rotating ring disk electrode (RDE and RRDE) methods at a scan rate of 50 mV s^{-1} and rotation rates of 2500, 1600, 900 and 400 rpm. In order to evaluate background current contributions of these electrodes, CVs were also carried out in N_2-saturated KOH; the background capacitive contributions were subtracted from the CVs in O_2-saturated KOH. Figure 5.16a displays CVs of the a-C a900 electrode at 1600 rpm in O_2-saturated and N_2-saturated 0.1 M KOH, while the CV corrected by the background capacitive contribution is shown in Figure 5.16b. The onset potential (E_{ON}) of this electrode, defined at current density of 0.1 mA cm^{-2}, was found to be 0.64 V vs RHE (Table 5.2).

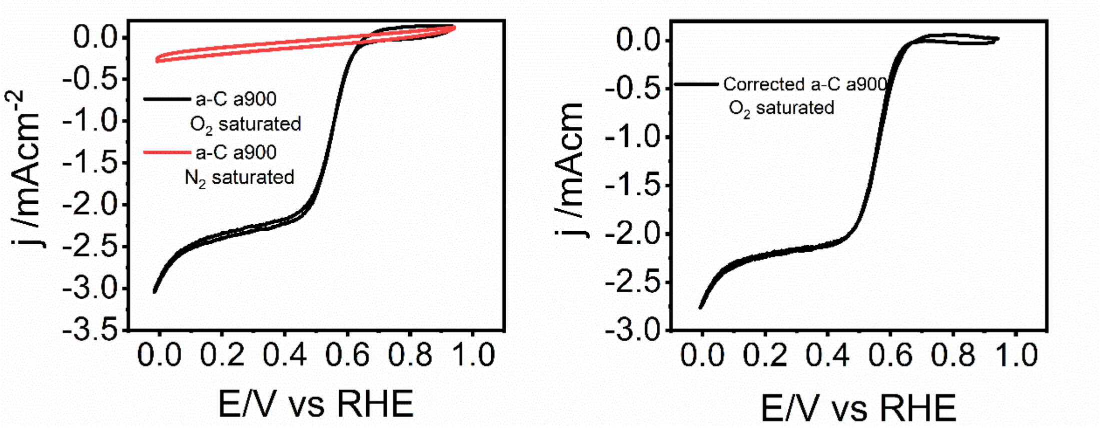

Figure 5.16: a) CV of an a-C a900 electrode in a solution of 0.1 M KOH obtained at a scan rate of 50 mVs^{-1} and a rotation speed of 1600 rpm. The inset plot shows the onset region close to 0.65 V vs RHE. b) background-corrected CV of the a-C a900 electrode.

ORR polarization curves of nitrogen-free a-C a900 and plasma treated a-C:N materials in O_2-saturated 0.1 M KOH at 50 mV s^{-1} as a function of rotation rate are presented in Figure 5.17a-d. Figure 5.18a and b display a comparison of the ORR polarization curves of a-C a900 and a-C:N a900-pl-5-20 in O_2-saturated KOH after background subtraction at 1600 rpm, with Figure 5.18b showing details of the onset potential region. It is apparent that plasma treatment enhances the ORR activity of a-C:N electrodes compared with the nitrogen-free precursor material. There is a clear improvement in the onset potential values with increasing plasma treatment times (Table 5.2). No significant improvement in the current densities in the mass-transport limited region were observed in the case of a-C:N a900-pl-5 and a-C:N a900-pl-10 compared with nitrogen free carbon electrodes [5], while a-C:N a900-pl-20 displays slightly higher current densities compared with other a-C:N materials. Interestingly, while the mass-transport limited region of the nitrogen-free sample is nearly flat as expected for an ideal RDE response, plasma treatment results in an ill-defined plateau region. This behaviour has previously been attributed to heterogeneity/disorder in electrocatalyst materials and the presence of a distribution of active sites, in good agreement with trends in structural disorder evidenced via Raman spectroscopy.

Oxygen reduction in alkaline media is a complex process where reduction of O_2 can proceed to hydroxide through transfer of a total of 4e$^-$, or be limited to the formation of peroxide via a 2e$^-$ pathway. If the peroxide is retained at the surface to be subsequently reduced by an additional 2e- then hydroxide is the final product. However, if the reduction stops at the peroxide product formation, this can be detected via RRDE measurements. RRDE studies were carried out to quantify the relative amount 2e$^-$ and 4e$^-$ reduction in alkaline media.

Figure 5.19 shows plots of the ring current (I_R) and disk current (I_D) of a-C a900 and a-C:N a900-pl-5-20 electrodes. The onset of all ring currents coincides with the onsets at the disk, thus indicating that the ring current results from products of reduction at the disk. The a-C a900 electrode displays the highest ring current compared with a-C:N electrodes; while among a-C:N materials the lowest I_R values are observed for after 5 min plasma treatment.

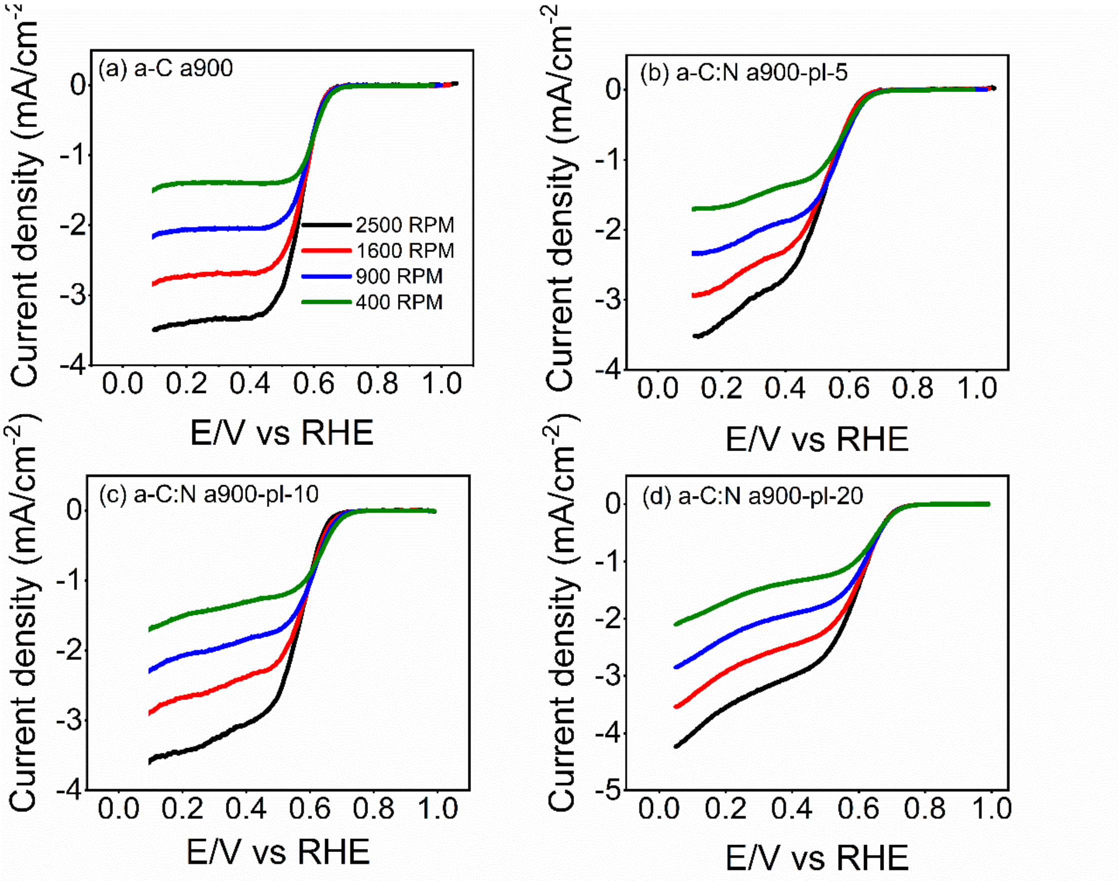

Figure 5.17: ORR polarization curves of a) a-C a900, b) a-C:N a900-pl-5, c) a-C:N a900-pl-10 and d) a-C:N a900-pl-20 in 0.1 M KOH at 50 mV s^{-1} at varying rotation rates of 2500, 1600, 900, 400 rpm respectively. All CVs were background subtracted.

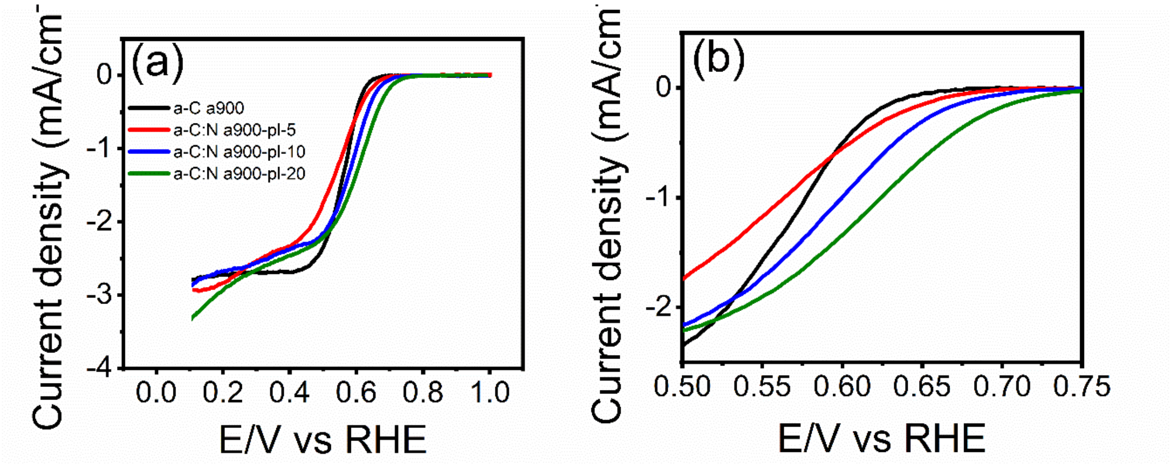

Figure 5.18: (a) ORR polarization curves of a-C a900, a-C:N a900-pl-5-20 in O_2 saturated KOH after background subtraction at rotation rates of 1600 rpm.(b) the onset region of all the electrodes.

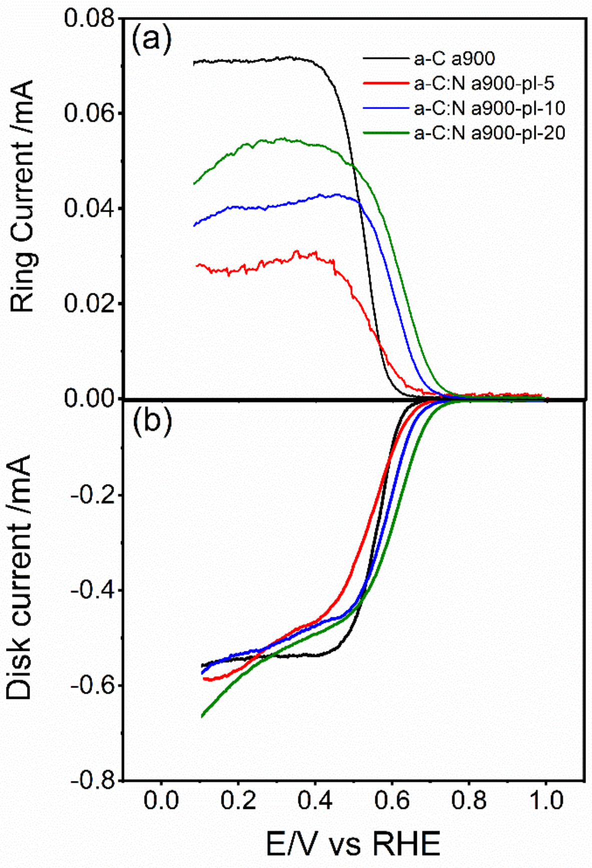

Figure 5.19: RRDE Studies of a-C a900, a-C:N a900-pl-5-20 electrodes in O2 saturated 0.1 M KOH electrolyte. a) Ring current b) Disk current.

H_2O_2 yields were calculated using equation 5.1:

$$H_2O_2\% = 100 \times 2\left(\frac{\frac{I_R}{N}}{I_D+\frac{I_R}{N}}\right) \tag{5.1}$$

where *N* is the collection efficiency which was set at 0.26 is the manufacturer value. Using the values of I_R and I_D in the plateau region of the ring current (0.3 V vs RHE), the peroxide yield was found to be 34% for a-C:N a900-pl-5, 43% for a-C:N a900-pl-10, 56% for a-C:N a900-pl-20 and 73% for a-C a900 (Table 5.2). Figure 5.20 shows the equivalent number of electrons involved in the reduction pathway as a function of potential at 1600 RPM and 2500 RPM*,* calculated according to equation 5.2

$$\mathrm{n} = \frac{4\mathrm{I_D}}{\mathrm{I_D}+\frac{\mathrm{I_R}}{\mathrm{N}}} \tag{5.2}$$

Where n is the average number of electrons transferred

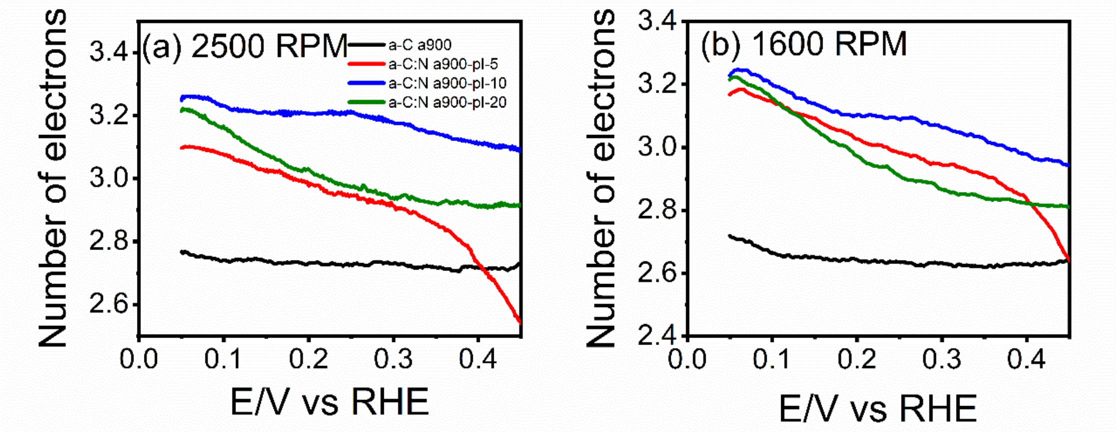

Figure 5.20: Number of electron reduction of a-C a900, a-C:N a900-pl-5-20 electrodes O_2 saturated 0.1 M KOH electrolyte as a function of voltage are references relative to RHE at a) 2500 RPM and b) 1600 RPM.

The average number of electrons transferred was found to be in the range 2.7-3.3, with the highest value observed for the sample plasma treated for 10 min. Values of *n* between 2 and 4 indicate that the reduction proceeds via mixed $2e^-/4e^-$ pathways which occur simultaneously at the electrode surface. Among the a-C:N electrodes, the a-C:N a900-pl-5 is more selective towards the complete reduction of O_2 to hydroxide, despite the onset potential being more positive than that of the a-C:N a900-pl-20 electrode.

The TOF of ORR catalyst provide a matrix of materials ability to produce active sites per unit time. The TOF values obtained for these electrodes are presented in table 5.2. Larger the TOF values the better the catalyst for ORR.

Table 5.2: Summary of ORR performance on a-C a900, a-C:N a900-pl-5-20 electrodes. All voltages are references relative to RHE.

Samples	E_{ON} / V @ 0.1 mA cm^{-2}	n @ 0.3 V	H_2O_2 % @ 0.3 V	TOF @ 0.3V
a-C a900	0.64	2.7	73	0.39
a-C:N a900-pl-5	0.67	3.0	34	0.36
a-C:N a900-pl-10	0.69	3.1	43	0.95
a-C:N a900-pl-20	0.72	2.9	56	0.62

5.5. Conclusions

In summary, we have demonstrated a rapid and controllable approach, based on RF nitrogen plasma processing of annealed amorphous carbon solid thin film, to synthesize a-C:N electrodes. a-C:N materials were characterised using X-ray photoelectron spectroscopy (XPS), Raman spectroscopy, cyclic voltammetry (CV), electrochemical impedance spectroscopy (EIS), rotating disk electrode (RDE) and rotating ring disk electrode (RRDE) methods. XPS results show that a-C:N electrodes display a range of N-containing species, including pyridinic-N, pyrrolic-N, graphitic-N and N oxides. Neither the total N/C content nor the distribution of N-sites was observed to vary with plasma exposure time, thus suggesting that the chemical composition of the carbon surface reaches steady state within *ca.* 5 min of exposure. The evolution of the Raman spectral profile of these a-C:N electrodes however suggests a significant restructuring of the carbon scaffold with progressive exposure to the plasma treatment, resulting in increased disorder and amorphisation.

Capacitance studies in organic media show that plasma treatment significantly increases the capacitance relative to the nitrogen-free a-C a900 surfaces. This is likely due to structural disorder given the observed changes in the Raman spectra outlined above. The RF plasma treatment significantly enhances the capacitive performance of a-C a900, thus opening a new route for the development of metal-free cost-effective and high-performance electrode materials for energy storage applications. ORR studies in alkaline media demonstrate that the ORR activity is enhanced by plasma treatment. This is observed in both an anodic shift of the onset potential and a reduction of H_2O_2 yields. Interestingly, despite the onset improving progressively with plasma treatment time, the best selectivity towards the full 4e$^-$ reduction of O_2 to hydroxide is observed for samples treated for only 5 min. This suggests that the optimised chemistry for enhancing 4e$^-$

selectivity is rapidly obtained via the rapid chemical changes under N_2 plasma. It appears likely that the improvement in onset potential is mainly a result of increased microroughness or porosity in the samples that arises from the restructuring and amorphization effects of the plasma treatment.

5.5. References

1. Gür, T. M., Critical review of carbon conversion in “carbon fuel cells”. *Chemical Reviews* **2013,** *113* (8), 6179-6206.

2. Marom, R.; Amalraj, S. F.; Leifer, N.; Jacob, D.; Aurbach, D., A review of advanced and practical lithium battery materials. *Journal of Materials Chemistry* **2011,** *21* (27), 9938-9954.

3. Inagaki, M.; Konno, H.; Tanaike, O., Carbon materials for electrochemical capacitors. *Journal of Power Sources* **2010,** *195* (24), 7880-7903.

4. Wong, W. Y.; Daud, W. R. W.; Mohamad, A. B.; Kadhum, A. A. H.; Loh, K. S.; Majlan, E. H., Recent progress in nitrogen-doped carbon and its composites as electrocatalysts for fuel cell applications. *International Journal of Hydrogen Energy* **2013,** *38* (22), 9370-9386.

5. Shui, J.; Wang, M.; Du, F.; Dai, L., N-doped carbon nanomaterials are durable catalysts for oxygen reduction reaction in acidic fuel cells. *Science Advances* **2015,** *1* (1), e1400129.

6. Tang, Y.; Allen, B. L.; Kauffman, D. R.; Star, A., Electrocatalytic activity of nitrogen-doped carbon nanotube cups. *Journal of the American Chemical Society* **2009,** *131* (37), 13200-13201.

7. Gong, Y.; Li, M.; Wang, Y., Carbon nitride in energy conversion and storage: recent advances and future prospects. *ChemSusChem* **2015,** *8* (6), 931-946.

8. Deng, Y.; Xie, Y.; Zou, K.; Ji, X., Review on recent advances in nitrogen-doped carbons: preparations and applications in supercapacitors. *Journal of Materials Chemistry A* **2016,** *4* (4), 1144-1173.

9. Yang, M.; Zhou, Z., Recent breakthroughs in supercapacitors boosted by nitrogen-rich porous carbon materials. *Advanced Science* **2017,** *4* (8), 1600408.

10. Hou, J.; Cao, C.; Idrees, F.; Ma, X., Hierarchical porous nitrogen-doped carbon nanosheets derived from silk for ultrahigh-capacity battery anodes and supercapacitors. *ACS Nano* **2015,** *9* (3), 2556-2564.

11. Long, C.; Qi, D.; Wei, T.; Yan, J.; Jiang, L.; Fan, Z., Nitrogen-doped carbon networks for high energy density supercapacitors derived from polyaniline coated bacterial cellulose. *Advanced Functional Materials* **2014,** *24* (25), 3953-3961.

12. Gong, K.; Du, F.; Xia, Z.; Durstock, M.; Dai, L., Nitrogen-doped carbon nanotube arrays with high electrocatalytic activity for oxygen reduction. **2009,** *323* (5915), 760-764.

13. Czerw, R.; Terrones, M.; Charlier, J. C.; Blase, X.; Foley, B.; Kamalakaran, R.; Grobert, N.; Terrones, H.; Tekleab, D.; Ajayan, P. M.; Blau, W.; Rühle, M.; Carroll, D. L., Identification of electron donor states in n-doped carbon nanotubes. *Nano Letters* **2001,** *1* (9), 457-460.

14. Wei, D.; Liu, Y.; Wang, Y.; Zhang, H.; Huang, L.; Yu, G., Synthesis of n-doped graphene by chemical vapor deposition and its electrical properties. *Nano Letters* **2009,** *9* (5), 1752-1758.

15. Panchakarla, L. S.; Subrahmanyam, K. S.; Saha, S. K.; Govindaraj, A.; Krishnamurthy, H. R.; Waghmare, U. V.; Rao, C. N. R., Synthesis, structure, and properties of boron- and nitrogen-doped graphene. **2009,** *21* (46), 4726-4730.

16. Robertsona;, J.; Davisb;, C. A., Nitrogen doping of tetrahedral amorphous carbon. *Diamond and Related Materials* **1995,** *4*, 4.

17. Robertson, J.; O’Reilly, E. P., Electronic and atomic structure of amorphous carbon. *Physical Review B* **1987,** *35* (6), 2946-2957.

18. Zhou, Y.; Holme, T.; Berry, J.; Ohno, T. R.; Ginley, D.; O’Hayre, R., Dopant-induced electronic structure modification of hopg surfaces: implications for high activity fuel cell catalysts. *The Journal of Physical Chemistry C* **2010,** *114* (1), 506-515.

19. Perathoner, S.; Centi, G., Chapter 9 - Advanced nanocarbon materials for future energy applications. In *Emerging Materials for Energy Conversion and Storage*, Cheong, K. Y.; Impellizzeri, G.; Fraga, M. A., Eds. Elsevier: 2018; pp 305-325.

20. Ng, W.; Yang, Y.; van der Veen, K.; Rothenberg, G.; Yan, N., Enhancing the performance of 3D porous N-doped carbon in oxygen reduction reaction and supercapacitor via boosting the meso-macropore interconnectivity using the “exsolved” dual-template. *Carbon* **2018,** *129*, 293-300.

21. Zhang, H.; Cao, G.; Wang, Z.; Yang, Y.; Shi, Z.; Gu, Z., Growth of manganese oxide nanoflowers on vertically-aligned carbon nanotube arrays for high-rate electrochemical capacitive energy storage. *Nano Letters* **2008,** *8* (9), 2664-2668.

22. Niu, C.; Sichel, E. K.; Hoch, R.; Moy, D.; Tennent, H., High power electrochemical capacitors based on carbon nanotube electrodes. *Applied Physics Letters* **1997,** *70* (11), 1480-1482.

23. Frackowiak, E.; Jurewicz, K.; Delpeux, S.; Béguin, F., Nanotubular materials for supercapacitors. *Journal of Power Sources* **2001,** *97-98*, 822-825.

24. Ania, C. O.; Khomenko, V.; Raymundo-Piñero, E.; Parra, J. B.; Béguin, F., The large electrochemical capacitance of microporous doped carbon obtained by using a zeolite template. *Advanced Functional Materials* **2007,** *17* (11), 1828-1836.

25. Zhao, X. S.; Su, F.; Yan, Q.; Guo, W.; Bao, X. Y.; Lv, L.; Zhou, Z., Templating methods for preparation of porous structures. *Journal of Materials Chemistry* **2006,** *16* (7), 637-648.

26. Bertóti, I.; Mohai, M.; László, K., Surface modification of graphene and graphite by nitrogen plasma: Determination of chemical state alterations and assignments by quantitative X-ray photoelectron spectroscopy. *Carbon* **2015,** *84*, 185-196.

27. Lin, Y.-P.; Ksari, Y.; Aubel, D.; Hajjar-Garreau, S.; Borvon, G.; Spiegel, Y.; Roux, L.; Simon, L.; Themlin, J.-M., Efficient and low-damage nitrogen doping of graphene via plasma-based methods. *Carbon* **2016,** *100*, 337-344.

28. Dwivedi, N.; Kumar, S.; Rauthan, C. M. S.; Panwar, O. S., Nano indentation measurements on nitrogen incorporated diamond-like carbon coatings. *Applied Physics A* **2011,** *102* (1), 225-230.

29. Baba, K.; Hatada, R., Preparation and properties of nitrogen and titanium oxide incorporated diamond-like carbon films by plasma source ion implantation. *Surface and Coatings Technology* **2001,** *136* (1), 192-196.

30. Kalish, R.; Amir, O.; Brener, R.; Spits, R. A.; Derry, T. E., Incorporation of nitrogen into amorphous-hydrogenated carbon (diamond-like) films. *Applied Physics A* **1991,** *52* (1), 48-51.

31. Cullen, R. J.; Jayasundara, D. R.; Soldi, L.; Cheng, J. J.; Dufaure, G.; Colavita, P. E., Spontaneous grafting of nitrophenyl groups on amorphous carbon thin films: a structure–reactivity investigation. *Chemistry of Materials* **2012,** *24* (6), 1031-1040.

32. Behan, J. A.; Stamatin, S. N.; Hoque, M. K.; Ciapetti, G.; Zen, F.; Esteban-Tejeda, L.; Colavita, P. E., Combined optoelectronic and electrochemical study of nitrogenated carbon electrodes. *The Journal of Physical Chemistry C* **2017,** *121* (12), 6596-6604.

33. Rumble, J. R.; Lide, D. R.; Bruno, T. J., *CRC handbook of chemistry and physics : a ready-reference book of chemical and physical data*. 2018.

34. Díaz, J.; Paolicelli, G.; Ferrer, S.; Comin, F., Separation of the sp3 and sp2 components in the C1s photoemission spectra of amorphous carbon films. *Physical Review B* **1996,** *54* (11), 8064-8069.

35. Ferrari, A. C.; Rodil, S. E.; Robertson, J., Interpretation of infrared and Raman spectra of amorphous carbon nitrides. *Physical Review B* **2003,** *67* (15), 155306.

36. Le Normand, F.; Hommet, J.; Szörényi, T.; Fuchs, C.; Fogarassy, E., XPS study of pulsed laser deposited CNx films. *Physical Review B* **2001,** *64* (23), 235416.

37. Perini, L.; Durante, C.; Favaro, M.; Perazzolo, V.; Agnoli, S.; Schneider, O.; Granozzi, G.; Gennaro, A., Metal–support interaction in platinum and palladium nanoparticles loaded on nitrogen-doped mesoporous carbon for oxygen reduction reaction. *ACS Applied Materials & Interfaces* **2015,** *7* (2), 1170-1179.

38. Sharifi, T.; Hu, G.; Jia, X.; Wågberg, T., Formation of active sites for oxygen reduction reactions by transformation of nitrogen functionalities in nitrogen-doped carbon nanotubes. *ACS Nano* **2012,** *6* (10), 8904-8912.

39. Rodil, S. E.; Morrison, N. A.; Robertson, J.; Milne, W. I., Nitrogen incorporation into tetrahedral hydrogenated amorphous carbon. **1999,** *174* (1), 25-37.

40. Waidmann, S.; Knupfer, M.; Fink, J.; Kleinsorge, B.; Robertson, J., Electronic structure studies of undoped and nitrogen-doped tetrahedral amorphous carbon using high-resolution electron energy-loss spectroscopy. *Journal of Applied Physics* **2001,** *89* (7), 3783.

41. Ferrari, A. C.; Robertson, J., Interpretation of Raman spectra of disordered and amorphous carbon. *Physical Review B* **2000,** *61* (20), 14095-14107.

42. Shi, J. R.; Shi, X.; Sun, Z.; Lau, S. P.; Tay, B. K.; Tan, H. S., Resonant Raman studies of tetrahedral amorphous carbon films. *Diamond and Related Materials* **2001,** *10* (1), 76-81.

43. Tay, B. K.; Shi, X.; Tan, H. S.; Yang, H. S.; Sun, Z., Raman studies of tetrahedral amorphous carbon films deposited by filtered cathodic vacuum arc. *Surface and Coatings Technology* **1998,** *105* (1–2), 155-158.

44. Gilkes, K. W. R.; Prawer, S.; Nugent, K. W.; Robertson, J.; Sands, H. S.; Lifshitz, Y.; Shi, X., Direct quantitative detection of the sp3 bonding in diamond-like carbon films using ultraviolet and visible Raman spectroscopy. *Journal of Applied Physics* **2000,** *87* (10), 7283-7289.

45. Laidani, N.; Guzman, L.; Miotello, A.; Brusa, R. S.; Karwasz, G. P.; Zecca, A.; Bottani, C.; Perrière, J., Nanometric phenomena induced by laser, ion and cluster beamsnitrogen effects on the microstructural evolution of carbon films under thermal annealing. *Nuclear Instruments and Methods in Physics Research Section B: Beam Interactions with Materials and Atoms* **1997,** *122* (3), 553-558.

46. Das, D.; Chen, K. H.; Chattopadhyay, S.; Chen, L. C., Spectroscopic studies of nitrogenated amorphous carbon films prepared by ion beam sputtering. **2002,** *91* (8), 4944-4955.

47. Ferrari, A. C.; Robertson, J., Raman spectroscopy of amorphous, nanostructured, diamond–like carbon, and nanodiamond. *Philosophical Transactions of the Royal Society of London A: Mathematical, Physical and Engineering Sciences* **2004,** *362* (1824), 2477-2512.

48. Martins Ferreira, E. H.; Moutinho, M. V. O.; Stavale, F.; Lucchese, M. M.; Capaz, R. B.; Achete, C. A.; Jorio, A., Evolution of the Raman spectra from single-, few-, and many-layer graphene with increasing disorder. *Physical Review B* **2010,** *82* (12), 125429.

49. Barranco, V.; Lillo-Rodenas, M. A.; Linares-Solano, A.; Oya, A.; Pico, F.; Ibañez, J.; Agullo-Rueda, F.; Amarilla, J. M.; Rojo, J. M., Amorphous Carbon Nanofibers and Their Activated Carbon Nanofibers as Supercapacitor Electrodes. *The Journal of Physical Chemistry C* **2010,** *114* (22), 10302-10307.

50. Vaquero, S.; Díaz, R.; Anderson, M.; Palma, J.; Marcilla, R., Insights into the influence of pore size distribution and surface functionalities in the behaviour of carbon supercapacitors. *Electrochimica Acta* **2012,** *86*, 241-247.

51. Vlad, A.; Balducci, A., Porous materials get energized. *Nature Materials* **2017,** *16*, 161.

52. Fic, K.; Platek, A.; Piwek, J.; Frackowiak, E., Sustainable materials for electrochemical capacitors. *Materials Today* **2018,** *21* (4), 437-454.

53. Memos, G.; Lidorikis, E.; Kokkoris, G., Roughness evolution and charging in plasma-based surface engineering of polymeric substrates: the effects of ion reflection and secondary electron emission. *Micromachines* **2018,** *9* (8), 415.

54. Colavita, P. E.; Sun, B.; Tse, K.-Y.; Hamers, R. J., Photochemical grafting of n-alkenes onto carbon surfaces: the role of photoelectron ejection. *Journal of the American Chemical Society* **2007,** *129* (44), 13554-13565.

55. Wiggins-Camacho, J. D.; Stevenson, K. J., Effect of nitrogen concentration on capacitance, density of states, electronic conductivity, and morphology of n-doped carbon nanotube electrodes. *The Journal of Physical Chemistry C* **2009,** *113* (44), 19082-19090.

56. Memming, R., Semiconductor electrochemistry, Weinheim: Wiley–VCH, 2001 %J Russian Journal of Electrochemistry. **2003,** *39* (9), 1011-1012.

57. Pajkossy, T., Impedance of rough capacitive electrodes. *Journal of Electroanalytical Chemistry* **1994,** *364* (1), 111-125.

58. Kerner, Z.; Pajkossy, T., On the origin of capacitance dispersion of rough electrodes. *Electrochimica Acta* **2000,** *46* (2), 207-211.

Chapter 6

Conclusions and Future Work

This chapter presents concluding remarks based on the results of the previous three chapters. Future work involves building a sample holder for carbon nanoparticles for nitrogen incorporation using RF plasma chamber. These synthesized materials could be used for energy conversion applications.

6.1 Conclusions

Nitrogen incorporated carbon materials plays an important role on the development of energy storage technologies. The aim of this thesis is to synthesize different levels of nitrogen-incorporated amorphous carbon films and to investigate the effects of nitrogen incorporation into carbon matrix as well as the effects on its electronic and capacitive properties. The effects of N doping on the electronic properties of amorphous carbon scaffolds were studied through a combination of x-ray photoelectron spectroscopy, ultraviolet photoelectron spectroscopy and Raman spectroscopy. Electrochemical capacitive properties determination via impedance were carried out in aqueous and organic supporting electrolytes.

It is shown that low level of nitrogenation significantly increases the capacitance in aqueous electrolyte where in organic electrolyte, which are dominated by the double layer capacitance, shows reduction of p-type properties of amorphous carbon, resulting in an increased metallic character. Greater level of nitrogen incorporation results in an increase in structural disorder and bandgap of the carbon material. Therefore, the effect of nitrogen doping is limited to low levels of nitrogenation as it enhances graphitisation; on the other hand higher N/C concentrations promote the creation of defects and localised N-sites.

Furthermore , electrochemical capacitance responses were investigated on topographically smooth nitrogen doped and nitrogen free graphitized amorphous carbon. The effect of selective N-site incorporation results in a significant difference in the organization of the carbon matrix. Electrochemical capacitance study in organic electrolyte suggests an increase of the capacitance that is due to the re-organisation of the carbon matrix and presence of defects in the carbon structure.

Finally, RF plasma system was used to incorporate nitrogen into graphitised amorphous carbon. It was observed that total N/C content and the distribution of N-sites does not vary with plasma exposure time thus suggesting that the chemical composition of the carbon surface reaches steady state within *ca.* 5 min of exposure. Nitrogen incorporation results in a significant restructure of the carbon scaffold and increased disorder and amorphization. Capacitance study in organic electrolyte suggests that nitrogen incorporation through plasma treatment increases the capacitance relative to the nitrogen-free graphitised amorphous carbon. These materials are also studied as electrocatalysts in the oxygen reduction reaction to investigate the effect of nitrogenation on the ORR performance. It is found that the ORR activity in alkaline media has an anodic shift of the onset potential and a reduction of H_2O_2 yields.

6.2 Future work

Synthesis of N doped carbon nanoparticle using RF plasma system for energy conversion applications.

Carbon nanomaterials have been widely used as electrode materials for electrochemical batteries including lithium ion batteries (LIBs), lithium–sulfur batteries, metal–air (oxygen) batteries and sodium ion batteries (SIBs),due to the possibility to produce devices that have high energy densities [1]. Nitrogen incorporation is effective way of improving physical, chemical and electrochemical properties of carbon nanomaterials because of the following reasons: firstly, N doping can provide higher electrochemical activity [2]. Secondly, N doping can increase conductivity of carbon nanomaterials [3]. There are several strategies for N-doped carbon nanomaterials in the literature divided into two main categories: in situ doping and post-treatment. For in situ doping strategies, the precursors with nitrogen and carbon atoms are used [4] and for the post-treatment strategy carbon nanomaterials are modified using in the presence of different nitrogen sources [5]. In this work the approach is to use RF plasma system in order to synthesize N doped carbon nano particles. A detail overview of RF Plasma system is given in chapter II and V. A schematic diagram of plasma chamber is presented in figure 2.3 (chapter II). We have successfully synthesised N doped amorphous carbon films which is discussed in chapter V along with the characterization of these materials. Plasma treatment on carbon particles under N_2 gas flow through the plasma chamber is a great challenge. A thin film or pellet can be made from these carbon powders and nitrogen can be incorporated on it by using this plasma chamber. Another approach is proposed here where a sample holder can be designed in order to have an inlet and an outlet. Inlet and outlet should cover with gas filter which can only permit gas to go in or go out, but the materials cannot. A schematic diagram of sample holder for carbon nanoparticles is shown in figure 6.1. This sample holder will be suitable for powders, especially for carbon nanoparticles. Carbon nanoparticles can be synthesized by using Ultrasonic spray pyrolysis [6] and further modifications as proposed in the protocol of chapter V. Nitrogen incorporated carbon nanoparticles could be characterized using different spectroscopic techniques including XPS, Raman, SEM, AFM and finally performance of these materials will be analysed by using electrochemical characterization techniques such as CV, EIS,RDE and RRDE. Physico-chemical proposed characterisations will allow to identify the best synthesis strategies for carbon-based materials to be employed in batteries in order to produce devices with high energy densities.

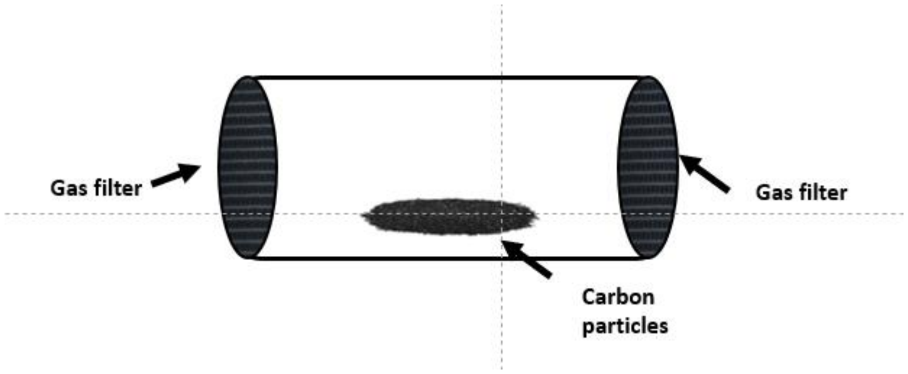

Figure 6.1: A schematic diagram of sample holder for plasma chamber where inlet and outlet are sealed with filter which allow only gas to in and out from this holder. The sample holder is made of glass materials.

6.3 References

1. Wu, J.; Pan, Z.; Zhang, Y.; Wang, B.; Peng, H., The recent progress of nitrogen-doped carbon nanomaterials for electrochemical batteries. *Journal of Materials Chemistry A* **2018,** *6* (27), 12932-12944.

2. He, Z.; Shi, L.; Shen, J.; He, Z.; Liu, S., Effects of nitrogen doping on the electrochemical performance of graphite felts for vanadium redox flow batteries. *International Journal of Energy Research* **2015,** *39* (5), 709-716.

3. Ismagilov, Z. R.; Shalagina, A. E.; Podyacheva, O. Y.; Ischenko, A. V.; Kibis, L. S.; Boronin, A. I.; Chesalov, Y. A.; Kochubey, D. I.; Romanenko, A. I.; Anikeeva, O. B.; Buryakov, T. I.; Tkachev, E. N., Structure and electrical conductivity of nitrogen-doped carbon nanofibers. *Carbon* **2009,** *47* (8), 1922-1929.

4. Shin, W. H.; Jeong, H. M.; Kim, B. G.; Kang, J. K.; Choi, J. W., Nitrogen-doped multiwall carbon nanotubes for lithium storage with extremely high capacity. *Nano Lett* **2012,** *12* (5), 2283-8.

5. Wu, Z.-S.; Ren, W.; Xu, L.; Li, F.; Cheng, H.-M., Doped Graphene Sheets As Anode Materials with Superhigh Rate and Large Capacity for Lithium Ion Batteries. *ACS Nano* **2011,** *5* (7), 5463-5471.

6. Wang, Q.; Cui, X.; Guan, W.; Zhang, L.; Fan, X.; Shi, Z.; Zheng, W., Shape-dependent catalytic activity of oxygen reduction reaction (ORR) on silver nanodecahedra and nanocubes. *Journal of Power Sources* **2014,** *269*, 152-157.

List of Publications

James A. Behan, Eric Mates-Torres, Serban N. Stamatin, Carlota Domínguez, Alessandro Iannaci, Karsten Fleischer, Md. Khairul Hoque, Tatiana S. Perova, Max García-Melchor and Paula E. Colavita. *Small* **2019,** 1902081.

James A. Behan, Alessandro Iannaci, Carlota Dominguez, Serban N. Stamatin, Md. Khairul Hoque, Joana M. Vasconcelos, Tatiana S. Perova, and Paula E. Colavita. *Carbon* **2019** 148:224-230

Md. Khairul Hoque†, James A. Behan, Serban N. Stamatin, Zen Federico , Tatiana S. Perova, and Paula E. Colavita. *RSC Advances*, **2019** 9(7):4063-4071.

James A. Behan, Md. Khairul Hoque†, Serban N. Stamatin, Tatiana S. Perova, Laia Vilella-Arribas, Max García-Melchor, and Paula E. Colavita. *J. Phys. Chem. C*, **2018**, *122* (36), pp 20763–20773.

Adam Myles, Damien Haberlin, Leticia Esteban-Tejeda, M. Daniela Angione, Michelle P. Browne, Md. Khairul Hoque, Thomas K. Doyle, Eoin M. Scanlan, and Paula E. Colavita:*ACS Sustainable Chem. Eng*. 6, 1, 1141-1151.

Carlota Dominguez, Kevin Metz, Md. Khairul Hoque, Michelle Phillippa Browne, Leticia Esteban-Tejeda, Corbin Livingston, Suoyuan Lian, Tatiana Perova, Paula E. Colavita. *ChemElectroChem* **2018**, 5, 62.

James A. Behan, Serban N. Stamatin, Md Khairul Hoque, Guido Ciapetti, Zen Federico, Esteban-Tejeda, Leticia Paula Colavita. *J. Phys. Chem. C*, **2017**, *121* (12), pp 6596–6604.

List of Communications

2018 – International Society of Electrochemistry Student Satellite Meeting, Bernal Institute-University of Limerick, Ireland – *A Study of the Electrochemical Capacitance of Nitrogen Doped Amorphous Carbon Thin Film Electrodes* (Oral Presentation)

2017 – International Society of Electrochemistry Student Satellite Meeting, Tyndall Institute, Cork, Ireland – *Capacitive Properties of Nitrogen Doped Amorphous Carbon Materials for Electrocatalytic Application* (Oral Presentation)

2018 - Electrochem 25th Annual Conference, Lancaster, United Kingdom – *Effect of Nitrogen Concentration on capacitive properties of Nitrogen Doped Amorphous Carbon* (Poster Presentation).

2017- Electrochem 24th Annual Conference, Birmingham, United Kingdom – *Capacitive Properties of Nitrogen Doped Amorphous Carbon Materials for Electrocatalytic Applications* (Poster Presentation).

RSC Advances

PAPER

View Article Online
View Journal | View Issue

Cite this: *RSC Adv.*, 2019, **9**, 4063

Capacitive storage at nitrogen doped amorphous carbon electrodes: structural and chemical effects of nitrogen incorporation†

Md. Khairul Hoque,[a] James A. Behan,[a] Serban N. Stamatin,[ab] Federico Zen,[a] Tatiana S. Perova[cd] and Paula E. Colavita *[a]

Received 12th December 2018
Accepted 21st January 2019

DOI: 10.1039/c8ra10187f

rsc.li/rsc-advances

Nitrogen incorporated carbon materials play an important role in electrochemical energy conversion technologies from fuel cells to capacitive storage devices. This work investigates the effects of nitrogen incorporation on capacitance, work function and semiconductor properties of amorphous carbon thin film electrodes. Nitrogenated electrodes (a-C:N) electrodes were synthesized *via* magnetron sputtering and characterized using X-ray photoelectron spectroscopy, ultraviolet photoelectron spectroscopy (UPS), Raman spectroscopy, cyclic voltammetry (CV), and electrochemical impedance spectroscopy (EIS). EIS was carried in both aqueous (0.1 M KCl) and organic (0.1 M TBAPF$_6$/acetonitrile) electrolytes to discriminate between pseudocapacitive contributions and changes to semiconductor properties of the materials arising from structural and chemical disruption of the graphitic carbon scaffold. Raman and UPS spectroscopy both suggest that nitrogen incorporation increases the metallic character of the disordered carbon matrix at low-intermediate concentrations, whereas further nitrogen incorporation results in significantly more defective carbon with small graphitic cluster size. EIS studies in 0.1 M KCl indicate that the capacitance of a-C:N electrodes increases relative to nitrogen-free a-C electrodes due to a combination of microroughness and pseudocapacitive contributions in parallel to those of the double layer capacitance. Results in 0.1 M TBAPF$_6$ in acetonitrile which are dominated by the interfacial capacitance, show that initial nitrogen incorporation into the disordered carbon scaffold compensates for p-type properties in the disordered carbon matrix, resulting in an increase in metallic character. Greater levels of nitrogenation, are instead disruptive and increase defect density while decreasing the double layer capacitance.

1. Introduction

Carbon materials and nanomaterials play an important role in electrochemical energy conversion technologies and are envisioned to remain important for our ability to transition to a more sustainable energy economy. Carbon is ubiquitous as an electrode material and its electronic, surface chemistry and capacitive properties are critical for the design of electrodes in a variety of applications, from fuel cells to capacitive storage devices. Highly graphitic forms of carbon such as carbon blacks and graphite powders are typically used for energy applications due a combination of low cost, good conductivity and reasonable resistance to corrosion. Furthermore, successful development of porous carbon structures has enabled applications in *e.g.* fuel cell electrocatalysis and supercapacitors due to their high specific surface areas and high density of reactive edge sites.

Some of the best performing carbon materials for electrochemical capacitive storage consist of carbon with low or no long-range order.[1] Nanostructured carbons such as activated carbon, alone or in combination with carbon blacks can display excellent capacitive properties,[2] that can be comparable to those of more costly "ordered" materials such as graphene or nanotubes.[1] A high proportion of amorphous regions in these carbon materials enables the development of a pore structure and the presence of high-energy sites resulting from bond distortions and crystallite boundaries. However, the presence of disorder can also result in an undesirable reduction in conductivity and there is consequently great interest in understanding how best to tailor the interplay between interfacial capacitance, surface functionalities and bulk electronic properties in amorphous carbon materials.[1,3]

---

[a] *School of Chemistry, CRANN, AMBER Research Centres, Trinity College Dublin, Dublin 2, Ireland. E-mail: colavitp@tcd.ie*

[b] *University of Bucharest, Faculty of Physics, 3Nano-SAE Research Centre, 405 Atomistilor Str, Magurele 077125, Bucharest, Romania*

[c] *Department of Electronic and Electrical Engineering, Trinity College Dublin, Dublin 2, Ireland*

[d] *ITMO University, 49 Kronverskiy pr., Saint Petersburg, 197101, Russia*

† Electronic supplementary information (ESI) available. See DOI: 10.1039/c8ra10187f

In this work we focus on a study of the effect of nitrogen incorporation on the capacitive properties of amorphous carbon (a-C) thin-film electrodes. Incorporation of nitrogen functional sites has emerged as one of the important tools available to modulate both electronic and interfacial chemistry of carbon electrodes. Nitrogenation has complex and multifaceted effects on the physico-chemical properties of carbons, resulting in changes in metallic/semiconducting character,[4] surface free energy and wettability,[5,6] type of reactive sites and Lewis acid/base behaviour.[7,8] The effect of nitrogenation on the electrochemical double-layer and redox-capacitance of carbons and nanocarbons has therefore received considerable attention with the objective of designing improved energy storage devices.[9,10] For instance, the effects of nitrogenation on the capacitance of carbon nanomaterials with long-range order such as carbon nanotubes[11,12] and graphite[13] have been studied by various groups.

Recent work from our group studied the effects that heteroatom incorporation has on the kinetics of interfacial charge-transfer at nitrogenated amorphous carbon (a-C:N) electrodes; our work examined to what extent the electrochemical redox response is correlated to the bulk electronic properties or is instead dominated by surface effects.[14] Herein, we study the effect of N-site incorporation on the organisation of the carbon scaffold and how this determines the capacitive properties of a-C:N electrodes as a result of both surface chemical and electronic effects. a-C:N film electrodes were synthesized with varying nitrogen content *via* DC magnetron sputtering and the materials were characterized using X-ray photoelectron spectroscopy (XPS), ultraviolet photoelectron spectroscopy (UPS), Raman spectroscopy, cyclic voltammetry (CV), and electrochemical impedance spectroscopy (EIS). EIS in both aqueous and organic media enabled the discrimination of electronic and pseudocapacitive contributions to the overall response. Our results show that n-doping can be achieved even with modest additions of N_2 during carbon deposition; greater concentrations in the deposition gas contribute mostly to the formation of functional groups and the disruption of the carbon scaffold with consequent loss of metallic character.

2. Materials and methods

Tetrabutylammonium hexafluorophosphate ($TBAPF_6$) (≥99.0%, electrochemical analysis), acetonitrile (MeCN, 99.8%, anhydrous), potassium chloride (Bioxtra, >99.0%), sulfuric acid (95–97%), hydrogen peroxide (>30% w/v), lithium chloride (>99%) were purchased from Sigma Aldrich. Glassy carbon (GC) discs (HTW Sigradur® radius 2.5 mm) and B-doped Si wafers (MicroChemicals; resistivity 5–10 Ω cm) were used as substrates for carbon deposition.

GC disks were polished first with 1200 grit sandpaper, then with 1 μm and 0.3 μm alumina slurries (Buehler) on nylon paper; disks were subsequently polished to a mirror finish using 0.3 and 0.05 μm slurries on MicroCloths® pads (Buehler). Clean disks were mounted in a custom-made Teflon® holder and placed in the vacuum chamber for deposition of thin film carbon electrodes on their surfaces. Si wafers were cleaned with piranha solution ($3:1 H_2SO_4:H_2O_2$; CAUTION piranha solutions are explosive in contact with organics), rinsed with plenty of Millipore water and dried with Ar prior to deposition. Amorphous carbon films were obtained *via* DC-magnetron sputtering (Torr International) from a graphite target (99.999%) at base pressures $<2 \times 10^{-6}$ mbar, deposition pressures $2–7 \times 10^{-3}$ mbar and total gas flow of 50 mL min^{-1}, following previously reported protocols.[14,15] Briefly, nitrogenated amorphous carbon films (a-C:N) were obtained by using N_2/Ar gas at flow ratios of 2%, 5% and 10% while keeping deposition time constant at 40 min, whereas non-nitrogenated amorphous carbon (a-C) was obtained by carrying out the deposition using 100% Ar during deposition. Electrodes thus deposited are topographically smooth; the mean thickness was determined *via* spectroscopic ellipsometry, following methods detailed in our previous work,[14,16,17] to be 74, 83, 114 and 123 nm for a-C, a-C:N-2%, 5% and 10%, respectively (see ESI†).

XPS and UPS measurements of a-C and a-C:N films were performed in an Omicron system at 1×10^{-10} mbar base pressure, using monochromatic Al Kα source (1486.6 eV) and equipped a multichannel array detector. XPS spectra were collected at 45° take-off angle and 0.5 eV resolution. Peaks were fitted with Voigt functions after Shirley background subtraction using commercial software (CasaXPS); at% composition was obtained from peak area ratios after correction by Scofield relative sensitivity factors (C = 1.0, N = 1.8, O = 2.93). UPS spectra were collected using He(I) excitation source (21.22 eV) at 90° take-off, with 0.02 eV analyser resolution. Negative bias were applied to the sample (0–12 V) to measure the high binding energy edge of the photoelectron spectrum; spectra were then corrected to account for bias and referenced to the Fermi energy measured on a Ag surface in contact with the carbon.[18] Work function (ϕ) values were calculated using the intercept at the binding energy axis of linear fits of the cut-off edge, as $\phi = 21.22$ – intercept. Raman spectra were measured in backscattering configuration using a Renishaw 1000 micro-Raman system equipped with an Ar^+ laser for 488 nm excitation and a HeNe laser for 633 nm excitation. The incident beam was focused by a Leica microscope with a 50× magnification objective and short-focus working distance; incident power was kept <2 mW to avoid sample damage. Spectra were baseline corrected using commercial software prior to analysis (Wire 3.2).

Electrochemical measurements were carried using a three-electrode cell controlled by a potentiostat with a graphite rod as counter electrode and Ag/AgCl (sat.) and Ag/Ag^+ reference electrodes (IJCambria) for characterisation in aqueous and organic electrolyte, respectively. The Ag/Ag^+ reference 1.0 mM $AgNO_3$ in 0.1 M $TBAPF_6$ in acetonitrile yielded $E^{0\prime} = 0.080$ V for 0.001 M Fc/Fc^+ in the same electrolyte, thus placing the Ag/Ag^+ potential at 0.320 V *vs.* SHE.[19] A Teflon static disk holder (Pine Instruments) enclosing a GC disk coated with the sputtered carbon film was used as a working electrode; all contacts were confirmed to be ohmic with <8 Ω resistance. Cyclic voltammetry was carried out in aqueous 0.1 M KCl solutions and in 0.1 M $TBAPF_6$ solutions in MeCN, at 25 °C, 50 mV s^{-1} and using iR compensation. EIS was carried out over the range 0.1–100 kHz using a 10 mV AC amplitude. Spectra were collected at either open circuit potential (OCP) or at varying DC offsets in 0.2 V steps as indicated in the text; 300 s equilibration time was allowed between each potential step. The specific capacitance was obtained *via* normalisation by the geometric area of the electrodes; this was determined in aqueous solution *via* a Randles–Sevcik plot,[14,20] and in 0.1 M TBAPF$_6$/MeCN *via* capacitance measurements on a reference GC disk of known area to account for any capillary wetting within the Teflon shielding in MeCN.[21]

3. Results and discussion

Nitrogenated carbon electrodes were prepared in the form of thin films *via* magnetron sputtering and characterised as described in previous work from our group.[14] Briefly, introduction of N$_2$ in the gas deposition at varying % flow ratios of 2%, 5% and 10% results in materials referred to as a-C:N-2%, a-C:N-5% and a-C:N-10%, respectively. Table 1 summarises XPS and Tauc gap results from previous work: the nitrogen content in the carbon scaffold increases with increasing N$_2$ flow% and the increase is accompanied by an increase in semiconducting character, as indicated by Tauc gap values. All a-C:N surfaces have been shown to possess a mixture of pyridinic-N, pyrrolic-N and graphitic-N, and they were found to be smooth and conformal to the substrate surface.[14]

Raman spectroscopy was used to characterise the structural properties of the amorphous carbon phase.[22–24] Fig. 1a shows baseline-corrected Raman spectra in the 900–1900 cm^{-1} range of a-C and a-C:N electrodes deposited on silicon wafers, obtained using 488 nm excitation. Spectra display two broad peaks characteristic of amorphous carbon materials, assigned to the G and D bands at approximately 1580 cm^{-1} and 1380 cm^{-1}, respectively. The G band is associated with an optically allowed E$_{2g}$ mode of sp^2 centres, while the D band is associated with a disorder-allowed A$_{1g}$ mode of six-membered carbon rings in graphite.[24–27] Although it is not possible to exclude contributions from C–N and N–N modes in the same spectral region, Raman spectra of a-C:N materials is typically interpreted without an attempt to discriminate contributions from heterocyclic structures to these two main vibrational modes in the carbon matrix.[26]

The spectral profile changes significantly after the introduction of N$_2$ in the deposition gas, as the D band increases in intensity relative to the G peak, suggesting a significant restructuring of the carbon matrix due to nitrogen incorporation. Spectra were deconvoluted using two Gaussian peaks[28–30] and the main peak parameters were used to generate the data in Fig. 1b–d. Peak heights from best fits were used to calculate the I_D/I_G ratio of each spectrum, which is diagnostic for amorphous carbon materials.[22,25,26,31,32] Fig. 1b shows the change in I_D/I_G *vs.* N$_2$%-content in the deposition and its corresponding N/C concentration at the surface. Upon introduction of 2% N$_2$ the relative height of the D band increases when compared with the nitrogen-free a-C material, which indicates an increase in the concentration of six-membered rings within the amorphous carbon scaffold.[26] The I_D/I_G ratio is known to increase as the average graphitic cluster size L_a increases in amorphous carbons, as discussed by Ferrari and Robertson;[25] therefore, the increase of I_D/I_G for a-C:N-2% relative to a-C confirms the important effect of nitrogenation on the clustering of sp^2 centres. However, higher concentrations of N$_2$ (>25% N/C at%) result in a decrease of the I_D/I_G value, suggesting that at high concentrations, the dominant effect of these heteroatoms is that of disrupting the graphitic network in a-C:N, leading to greater defect density. This is supported by an analysis of the full width half maximum (FWHM) of the G band shown on Fig. 1c; this FWHM is diagnostic of the distribution of bond angles at excited sp^2 centres and therefore tracks the local carbon disorder.[26] It is evident from the figure that a slight increase in FWHM is observed for a-C:N-2% and −5% relative to a-C, whereas a-C:N-10% shows a major increase in FWHM that indicates a broad distribution of bonding geometries for sp^2 centres.

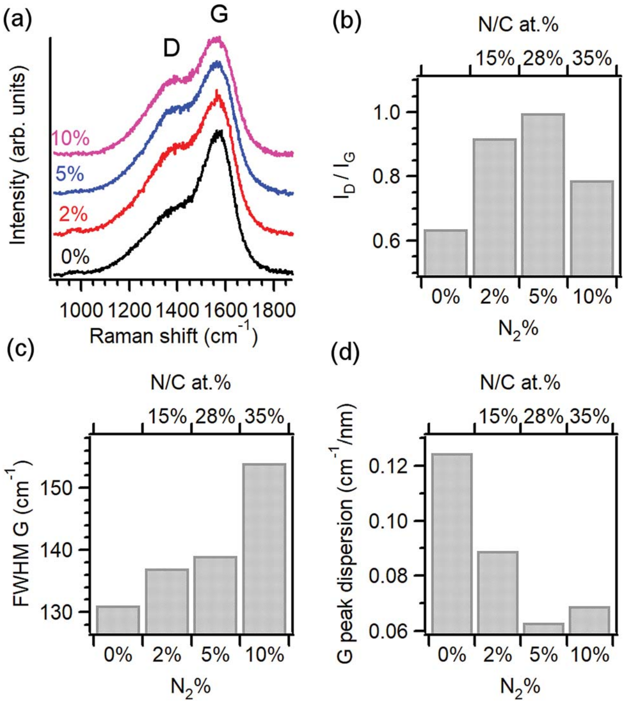

Fig. 1 (a) Raman spectra of amorphous carbon electrodes prepared with varying N$_2$% content in the deposition gas mixture: 0% (a-C), 2% (a-C:N-2%), 5% (a-C:N-5%) and 10% (a-C:N-10%); excitation 488 nm. Spectra are normalised relative to the G band intensity. (b) Variation of D to G peak height ratio (I_D/I_G), (c) G peak full width at half-maximum (FWHM) and (d) G peak dispersion *vs.* N$_2$% content in the deposition gas (bottom axis) or *vs.* surface N/C% content (top axis).

Table 1 Summary of properties of sputtered a-C:N electrodes used in our studies

Sample	N$_2$%	N^a at%	N/C^a at%	Tauc gap^a	Φ^b (eV)
a-C	0%	n/a	n/a	0.66 ± 0.01	4.69 ± 0.03
a-C:N-2%	2%	8.3	15	0.25 ± 0.07	4.94 ± 0.02
a-C:N-5%	5%	15.6	28	0.19 ± 0.09	4.82 ± 0.01
a-C:N-10%	10%	19.5	35	0.7 ± 0.1	4.84 ± 0.02

^{a} Values of N at% and Tauc gap determined *via* XPS and ellipsometry, respectively, from 14 and 16. ^{b} Obtained from UPS in this work.

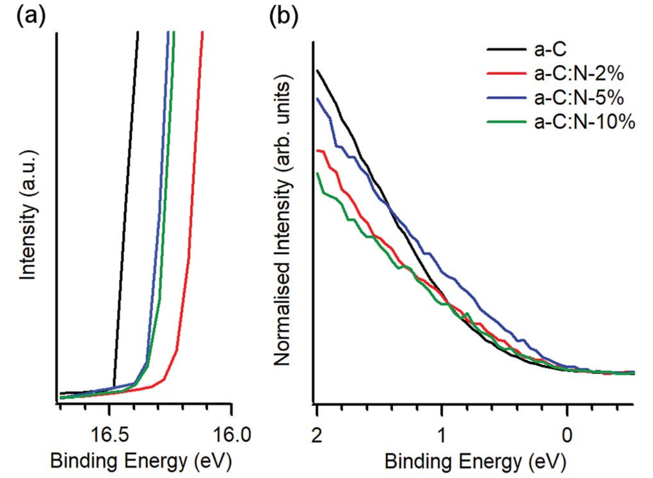

Fig. 2 UPS of a-C and a-C:N electrodes. (a) High binding energy cutoff obtained at 10 V bias, showing the change in work function due to nitrogen incorporation. (b) Low binding energy region of N-free a-C and a-C:N materials showing photoemission near E_F; spectra are shown normalised by the total photoemission intensity.

The trends observed are in good agreement with those reported by Ferrari and co-workers for amorphous carbon films with increasing nitrogen content deposited using a variety of methods. Raman results for nitrogenated a-C:N films are generally more complex to interpret than for nitrogen-free a-C, due to the non-uniqueness of sp^3-centre content and sp^2 structuring that results from nitrogen incorporation.[26] However, the dispersion of the G peak position is unequivocally associated with disordering as a result of nitrogenation; for this purpose, Raman spectra obtained at 633 nm excitation were also analysed to obtain the values of G-peak dispersion summarised in Fig. 1d. G peak dispersion falls sharply upon incorporation of nitrogen indicating an ordering effect resulting from nitrogenation.[25] However, further nitrogen incorporation in a-C:N-10% does not result in greater ordering and a slight increase in dispersion is registered, in agreement with trends in Fig. 1b and c. In summary, analysis of Raman spectra indicates that a-C:N-2% and a-C:N-5% possess a more graphitic structure than nitrogen-free a-C; this is in agreement with previous determinations of Tauc gaps, which indicate an increase in metallic character for these two materials *vs.* a-C. Further incorporation of nitrogen to form a-C:N-10% however results in carbon materials that are significantly more defective, and that likely possess smaller graphitic cluster sizes. This confirms that using the range 0–10% N_2 concentration in our deposition system it is possible to explore both the ordering and the defect-inducing effects of nitrogen incorporation on the electrochemical performance of non-crystalline carbon electrodes.

UPS was used to investigate the valence electronic properties of a-C:N electrodes. Fig. 2a and b show the UPS spectra in the high-binding and low-binding energy regions, respectively. The high binding energy edge was used to calculate work function values (ϕ), which are summarised in Table 1. The work function of a-C at 4.69 eV is in good agreement with previous reports on magnetron sputtered carbon[18,33] and close to values quoted for graphitic nitrogen-free materials such as graphite (4.4 eV)[34,35] and glassy carbon (4.6 eV).[35] Incorporation of nitrogen results in an increase of work function values which fall in the range 4.82–4.94 eV; these values are above those of a-C but below those reported for O-terminated sputtered carbons (5.1 eV).[36] The observed increase of ϕ upon N-modification is in agreement with experimental results by Wiggins-Camacho and Stevenson[12] obtained from nitrogenated and N-free carbon nanotubes. Nitrogen incorporation can result in both an increase[12,37] or a decrease[38,39] in the work function of carbons arising from changes to semiconducting properties (*e.g.* n-type doping) and from the creation of surface functional groups. The observed increase suggests the presence of C–N terminations that add a positive contribution from surface dipoles to the work function,[18,37] as observed for O-containing groups[36,38,40] and as argued in the case of N-modified carbon nanotubes.[12] No clear trend could be identified over the 2–10% deposition range, however it is possible that reorganisation of the carbon scaffold, *e.g.* due to defect creation[12] or to clustering of sp^2 centres,[26] might further contribute to the net change in ϕ, thus resulting in a non-linear trend *vs.* N-content.

Fig. 2b shows details of the photoemission intensity of a-C:N samples and that of N-free a-C near E_F. The intensity changes suggest that incorporation of nitrogen results in a slight increase in occupied states near the E_F for a-C:N-2% (N/C = 15 at%) and to a larger extent for a-C:N-5% (N/C = 28 at%); further incorporation in a-C:N-10% (N/C = 35 at%) appears to result in a decrease in occupied states. These observations are consistent with metallic/semiconducting character inferred from Tauc gap values (Table 1). Interestingly, the photoemission near E_F is maximised for a-C:N-5% which is also the sample that appears to be richest in graphitic clusters based on Raman results.

Electrochemical characterisation *via* CV and EIS was carried out using a three-electrode system. Typical CVs of a-C and a-C:N electrodes over the −0.3–0.7 V potential window at 50 mV s^{-1} in 0.1 M KCl are shown in Fig. 3; the response of a polished GC substrate disk is included for comparison. The curves show the characteristic shape of a capacitive response, with all capacitive currents being larger than that of the GC substrate disk. Incorporation of nitrogen into the carbon scaffold leads to increased capacitance with progressively higher currents over a-C:N-2%-10%.

A study of the electrochemical response was carried out using EIS over the 0.1–10^5 Hz range in the same solution. Fig. 4a and b show Bode plots of absolute impedance ($|Z|$) and phase angle obtained at OCP (0–0.05 V *vs.* Ag/AgCl), respectively, for nitrogen-free a-C electrodes and for GC as a reference graphitic electrode material. Results for the GC substrate are in good agreement with those reported for planar GC electrodes under similar conditions.[41] The GC sample yields a response characteristic of an equivalent series RC circuit, thus consistent with a double layer capacitance (C_{dl}) contribution with close to ideal behaviour. At 0.1 Hz the phase angle is approximately −83°, slightly below the ideal capacitor value of −90°, while at high frequency the response is resistive (phase ≈ 0°) with $|Z|$ determined by the solution resistance (R_s). a-C electrodes

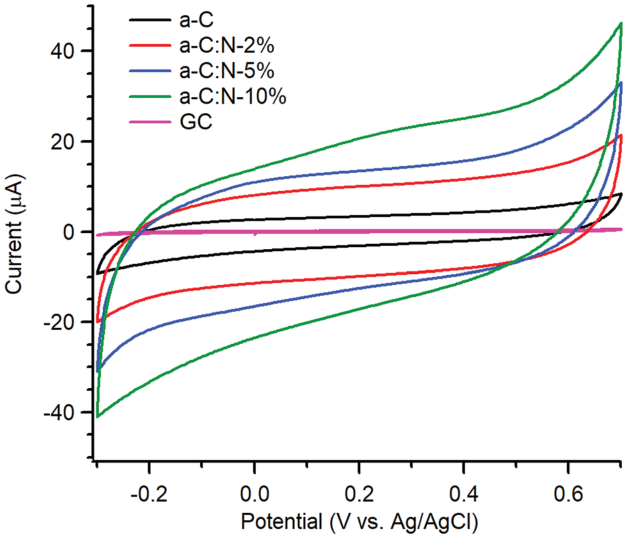

Fig. 3 Cyclic voltammograms of GC, a-C, a-C:N-2%-10% in Ar-saturated 0.1 M KCl at 50 mV s^{-1}.

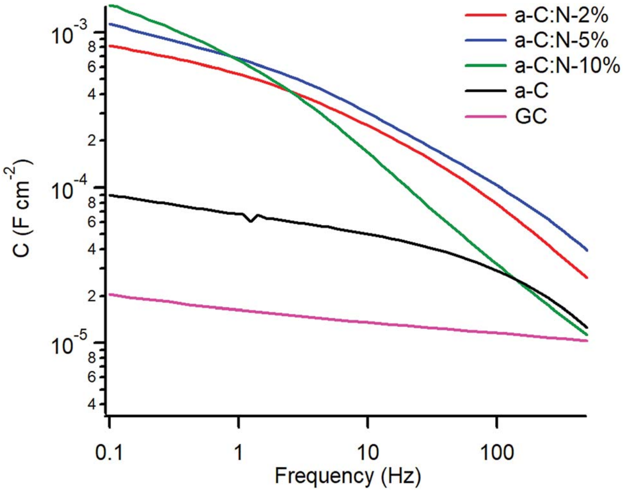

Fig. 5 Equivalent series capacitance at OCP in 0.1 M KCl.

display a lower impedance at low frequency compared to that of GC and a phase angle of −77°, indicating a mainly capacitive response; however the appearance of an additional time constant evident from the phase plot at high frequency (~600 Hz) suggests the presence of at least two distinct capacitive contributions. Fig. 4c and d show Bode plots obtained for a-C:N-2%-10% electrodes. The curves indicate that nitrogenation results in a further reduction in $|Z|$ and greater deviations from ideal capacitive behaviour, while at high frequency the plots show evidence of additional capacitive contributions to the overall response.

The effective or equivalent series capacitive contribution to EIS spectra was calculated as a function of frequency f from the imaginary part of the complex impedance Z_{im} according to:

$$C = -(2\pi f Z_{\text{im}})^{-1} \tag{1}$$

Fig. 5 shows a plot of the specific capacitance extracted over the 0.1–500 Hz range at OCP. The capacitance for the GC electrode was found to be 16 μF cm^{-2} at 1 Hz, in good agreement with reference values of C_{dl} in aqueous KCl,[20] while the capacitance for nitrogen-free a-C is 4.4 times larger at *ca.* 70 μF cm^{-2}. A very significant increase in capacitance is observed for a-C:N materials which yielded values in the mF cm^{-2} range. In the case of a-C:N samples there is also clear evidence of frequency dispersion, which is related to disorder and inhomogeneity in electrode surfaces,[42,43] and this is seen to be particularly pronounced for a-C:N-10%.

The capacitance of a-C:N materials as a function of potential was further investigated using EIS at varying DC offsets (see

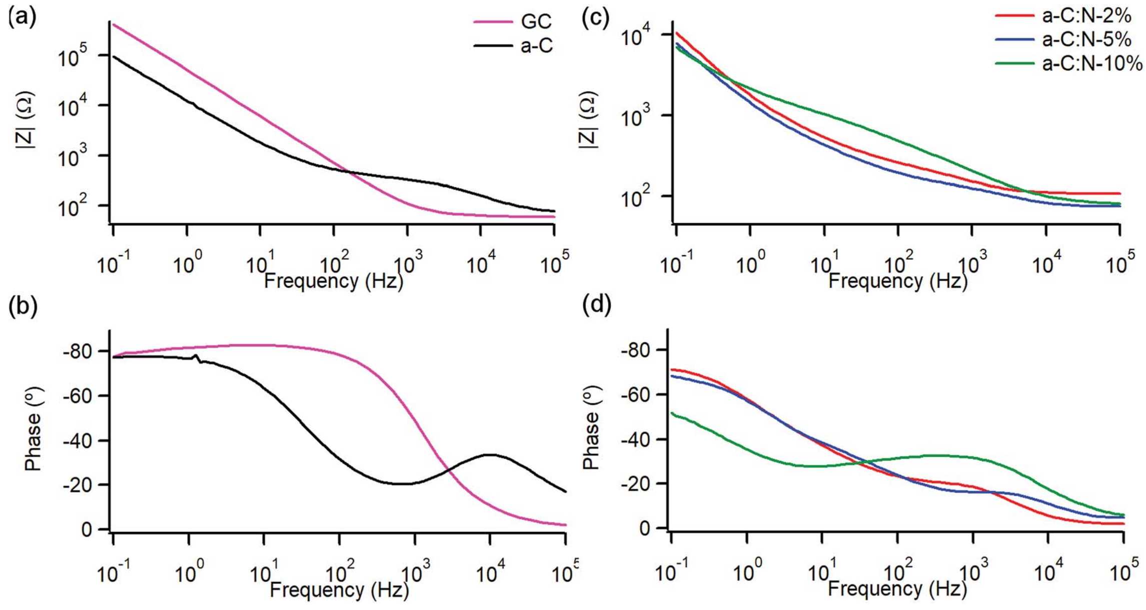

Fig. 4 Bode plots of impedance module $|Z|$ and phase angle of (a and b) nitrogen-free GC and a-C electrodes and (c and d) of nitrogenated a-C:N-2%, a-C:N-5% and a-C:N-10%. EIS spectra obtained in 0.1 M KCl at open circuit potential (OCP, 0.01–0.05 V *vs.* Ag/AgCl).

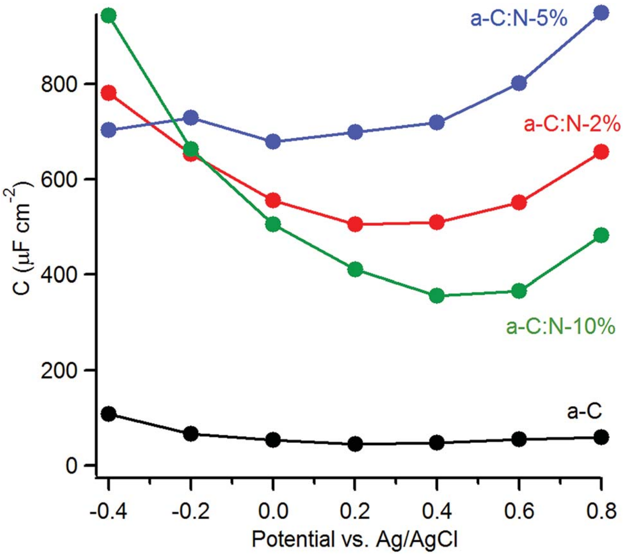

Fig. 6 Equivalent series capacitance as a function of potential in 0.1 M KCl calculated at 1 Hz.

ESI†). Fig. 6 shows the change in the series equivalent capacitance at 1 Hz as a function of the DC offset over the range −0.4–0.8 V *vs.* Ag/AgCl in 0.1 M KCl. The nitrogen-free a-C electrode shows a shallow minimum in the capacitance that suggests a potential of zero charge (pzc) of 45 μF cm^{-2} at *ca.* 0.2 V. Nitrogenation leads to a considerable increase in the area-normalised capacitance. There is no detectable shift in the potential at the minimum capacitance for a-C:N-2% (*ca.* 0.5 mF cm^{-2}) and 5% (*ca.* 0.7 mF cm^{-2}), however, a significant positive shift is observed for a-C:N-10%, whose minimum (*ca.* 0.3 mF cm^{-2}) falls in the range 0.4–0.6 V.

The capacitance values of nitrogenated a-C:N electrodes in Fig. 6 are large compared to those typical of planar carbon electrodes (1–70 μF cm^{-2} (ref. 20, 44 and 45)). This indicates that a-C:N materials possess intra-film capacitance due to porosity and/or pseudo-capacitive contributions. The presence of both such contributions is reasonable as a result of nitrogen incorporation. Previous work had shown that these a-C:N films are topographically smooth and featureless, however they might still allow for the presence of small cavities or "fissures" accessible to the electrolyte.[46] As the capacitive response at low frequency results from probing by the AC signal deep into any pores present in the material,[47–49] the large values observed could arise from intra-film porosity in all three a-C:N electrodes. This appears possible when considering the structurally disruptive effect of nitrogenation at high concentrations on the graphitic matrix.[14,26] Beyond the development of a pore structure, nitrogenation can also introduce local surface states due to structural disorder in the carbon scaffold which are known to result in increased capacitance at low frequency.[46] Finally, the presence of N-containing functional groups at the a-C:N surface in a protic solvent can promote specific adsorption[50] and redox reactions at these sites (*e.g.* amine/hydroxylamine, amine/imine or pyridine/pyridone),[51–53] thus introducing a pseudo-capacitive contribution in parallel to that of the double layer capacitance.

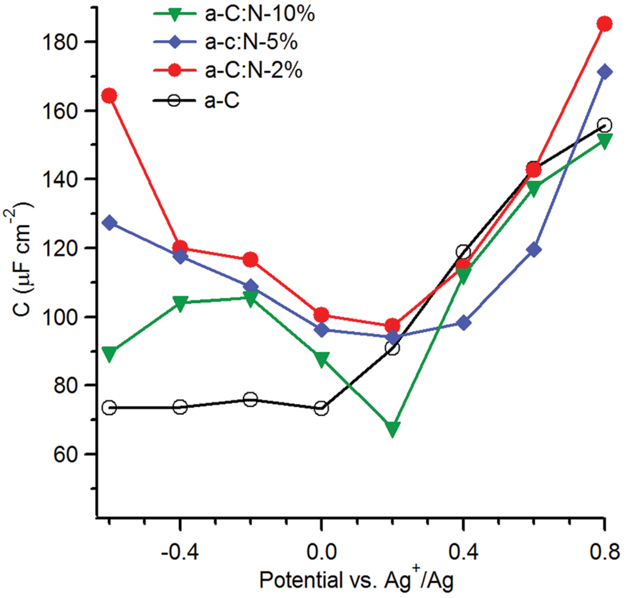

Fig. 7 Equivalent series capacitance as a function of potential in 0.1 M TBAPF$_6$ calculated at 1 Hz.

With the aim of investigating the effects of nitrogenation on the capacitive properties, while minimising complications arising from pseudo-capacitive effects, we carried out EIS studies in organic aprotic solvent using a 1 : 1 electrolyte with large ionic radii.[12,54,55] Fig. 7 shows the series equivalent capacitance at 1 Hz as a function of potential over the range −0.6–0.8 V *vs.* Ag$^+$/Ag in 0.1 M TBAPF$_6$ in acetonitrile for a-C and a-C:N electrodes. Cyclic voltammograms and representative EIS data over potentials close to the capacitance minima are reported in the ESI.† The capacitance curve of the a-C electrode is asymmetric with a capacitance at pzc of 73 μF cm^{-2} at 0 V *vs.* Ag$^+$/Ag. This value is 3.5 times larger than that of a GC electrode disk measured under identical conditions (data not shown). The $C_{\mathrm{aC}}/C_{\mathrm{GC}}$ ratio is very close to that observed in aqueous electrolyte, therefore indicating that the larger capacitance of a-C electrodes relative to GC is mostly due to microroughness effects. Remarkably, while the capacitance at the potential of zero charge for the a-C:N samples in KCl are 5–10 times larger than that of a-C, the difference is instead small when the materials are tested in TBAPF$_6$ solutions. The capacitances at pzc are remarkably close to each other and to the a-C value, being in a ratio $C_{\mathrm{aCN10}} : C_{\mathrm{aC}} : C_{\mathrm{aCN5}} : C_{\mathrm{aCN2}} = 1 : 1.1 : 1.4 : 1.4$. This strongly suggests that the large differences observed between a-C:N and a-C in KCl arise from pseudo-capacitive effects brought about by the presence of surface N-sites. Although it is not possible to exclude that intra-film porosity also contributes to the values in Fig. 5, protonation and faradaic activity of N-sites can be identified as the dominant contribution to the capacitive response of a-C:N electrodes in aqueous KCl.

The capacitance in TBAPF$_6$/acetonitrile on the other hand is dominated by the double layer (C_{dl}); furthermore, use of a high electrolyte concentration also ensures that the series contribution to the double layer capacitance arising from the diffuse layer (C_{diff}) can be neglected. Under such conditions the observed capacitance is modulated by the electronic properties of a-C/a-C:N materials and by any differences in microroughness among the electrodes, thus enabling an analysis of the effects of nitrogen incorporation beyond those of surface chemical reactivity. The asymmetry in the a-C curve is consistent with an accumulation region at potentials anodic to 0 V *vs.* Ag^+/Ag, which agrees with previous reports of p-type behaviour in nitrogen-free sputtered a-C.[18,56] All of the plots for a-C:N materials display relatively symmetric minima at 0.2 V *vs.* Ag^+/Ag, thus indicating that nitrogen incorporation into a-C results in an increase in the pzc.[57] The shift in pzc relative to a-C is in good agreement with UPS data, which show that nitrogenation of a-C results in work function increases of 0.1–0.2 eV (Table 1). The minimum capacitance of a-C:N-10% is the lowest among a-C:N materials, while a-C:N-2% and a-C:N-5% display the largest ones; assuming that the microroughness factor remains constant across all sputtered electrodes, this finding is consistent with a-C:N-10% having the largest Tauc gap (Table 1) and greatest semiconducting character. The largest carrier density is achieved instead at low N/C contents.

The effects of nitrogen incorporation on the interfacial capacitance have been previously studied using carbon nanomaterials with long range order, such as graphene and nanotubes. Capacitance determinations in $TBAPF_6$/acetonitrile of N-doped graphene with low N-content (<3 at%) show significant increases in capacitance as a result of doping. For instance, Jeong *et al.*[50] observed a *ca.* 4-fold enhancement after N-doping *via* plasma treatment, while Zhang *et al.*[58] reported a *ca.* 2-fold increase in the specific capacitance after N-doping during graphene growth. Interestingly, Zhu *et al.*[59] investigated the effects of combined graphene N-doping (*ca.* 2%) and controlled defect introduction *via* Ar^+ bombarding, achieving very significant increases in capacitance. In the case of carbon nanotubes, Wiggins-Camacho and Stevenson[12] also reported a progressive enhancement of the C_{pzc} in $TBAPF_6$/acetonitrile up to a factor of *ca.*3 for N-content <8 at%. In the case of our a-C:N materials the enhancement observed is comparatively modest (<40%), while for a-C:N-10% it is possible to actually observe a reduction in interfacial capacitance. This might be explained by the N-content being higher in our materials (15–35%) than in graphene/nanotube studies and by the concomitant presence of amorphous/non-crystalline regions. A higher N-content than 3–7% is frequently obtained for non-crystalline materials, and the data suggests that capacitive enhancements resulting from N-doping might be smaller once the N-content rises and/or the disorder increases. For instance, Zeng *et al.*[60,61] observed marginal changes in the capacitance minimum of a-C:N electrodes deposited *via* filtered cathodic vacuum arc when N/C% increased from 8 to 17%, albeit in aqueous solutions. In $TBAPF_6$/acetonitrile, Hulicova-Jurcakova *et al.*[62] characterised the effect of N-content increases in porous nanocarbons and observed no increase in capacitance for N-content >10%. Literature results with non-crystalline materials support our observations; our previous work using redox couples and high N-content sputtered a-C:N electrodes[14] showed that progressive inclusion of N-sites results in increased localisation of graphitic clusters within. It would therefore appear that capacitive enhancements can only be expected to result from N-doping when the nitrogenation process preserves a sufficient concentration of extended graphitic clusters in the carbon scaffold.

Table 2 Capacitance at potential of zero charge (C_{pzc}) and comparison with resistance to charge transfer (R_{ct}) reported[14] for $Ru(NH_3)_6^{+2/+3}$

Sample	C_{pzc} (μF cm^{-2})	R_{ct} (Ω)[14]
a-C	73	256
a-C:N-2%	97	46
a-C:N-5%	94	21
a-C:N-10%	67	197

In the absence of an experimental determination of the microroughness factor for each electrode, it is not possible to obtain estimates of the density of states from values of C_{pzc}, as previously done by other groups in the case of nanocarbon electrodes.[12,54] However, it is interesting to note that C_{pzc} values are strongly correlated to the resistance to charge transfer (R_{ct}) obtained in our previous work[14] with the same electrode materials using $Ru(NH_3)_6^{+2/+3}$, an outer-sphere redox couple, as shown in Table 2. The highest R_{ct} values correspond to the lowest C_{pzc} values; a similar trend is observed when the effective capacitance values are considered at −0.20 V, close to the formal potential of $Ru(NH_3)_6^{+2/+3}$ (0.10 V *vs.* SHE,[19] or −0.22 *vs.* Ag/Ag^+). As the R_{ct} had been found to be inversely correlated to the density of states near the Fermi energy in these materials, this observation supports that the trends observed in Fig. 7 are controlled by the space-charge properties of a-C/a-C:N electrodes (albeit for small differences in microroughness). On the basis of the asymmetry observed in the curves, it is therefore possible to conclude that N-free a-C materials start as p-doped in character; a small amount of nitrogen incorporation as in a-C:N-2% has a drastic effect in reducing the p-character, as expected from the role of group V atoms as n-type donors. This is evident from the greater symmetry in the C *vs.* E curve and the increase in its C_{pzc} value, which are also consistent with the graphitizing effect of nitrogen incorporation observed from Raman. Further nitrogen incorporation, beyond ∼15 at% results in no apparent further increases in n-type character in the materials. This is likely due to rapid saturation of sites in the carbon matrix suitable for N-doping (graphitic-N); further increase in N/C at% involve the creation of functional groups that instead contribute to pseudocapacitance in aqueous solutions.

4. Conclusion

In this work we have used sputtered thin films of amorphous carbon to investigate the effects of gradual nitrogen incorporation into the graphitic scaffold and its effects on the electronic and capacitive properties. The materials investigated varied in their total N/C content but all displayed a mixture of N-sites including pyridinic-N, pyrrolic-N, graphitic-N and N-oxides, and a combination of methods that are sensitive to both bulk and surface properties, was used for this purpose. Importantly, a comparison of capacitive storage of the same materials in aqueous and organic supporting electrolytes was carried out. Our results show that nitrogen incorporation significantly increases the capacitive storage in aqueous media relative to the N-free parent material. However, most of this increase can be attributed to pseudocapacitive contributions from redox-active N-sites. Measurements in organic electrolyte, which are dominated by the double layer capacitance, show that initial nitrogen incorporation into the disordered carbon scaffold compensates for p-type properties in the disordered carbon matrix, resulting in an increase in metallic character. Greater levels of nitrogenation, however, are disruptive and progressively increase the disorder and bandgap of the carbon material. It therefore appears that the effect of nitrogen as an n-type dopant is limited to low levels of nitrogenation that preserve graphitization in the carbon matrix, while higher N/C concentrations largely involve creation of defects and localised N-sites. This interpretation is consistent with bandgap results, work function and valence photoemission results. This combined experimental approach offers an effective strategy to discriminate between the local chemical effects of N-sites and those that impart a long-range effect on the metallic character of nitrogenated disordered carbon materials.

Conflicts of interest

The authors declare no conflict of interest.

Acknowledgements

This publication has emanated from research conducted with the financial support of Science Foundation Ireland under Grant No. 13/CDA/2213. JAB gratefully acknowledges support from the Irish Research Council under Grant No. GOIPG/2014/399. Use of the XPS of I. V. Shvets and C. McGuinness provided under SFI Equipment Infrastructure funds.

References

1 P. Simon and Y. Gogotsi, *Acc. Chem. Res.*, 2013, **46**, 1094–1103.
2 L. Wei, M. Sevilla, A. B. Fuertes, R. Mokaya and G. Yushin, *Adv. Energy Mater.*, 2011, **1**, 356–361.
3 G. Moussa, S. Hajjar-Garreau, P.-L. Taberna, P. Simon and C. Matei Ghimbeu, *C*, 2018, **4**, 20.
4 J. Robertson, *Mater. Sci. Eng.*, 2002, **37**, 129–281.
5 *Carbon Materials for Catalysis*, ed. P. Serp and J. L. Figueiredo, John Wiley & Sons, Hoboken, New Jersey, 2009.
6 *Properties of amorphous carbon*, ed. S. R. P. Silva, INSPEC, Inc., The Institution of Electrical Engineers, London, 1st edn, 2003.
7 D. Guo, R. Shibuya, C. Akiba, S. Saji, T. Kondo and J. Nakamura, *Science*, 2016, **351**, 361–365.
8 Y. Shao, J. Sui, G. Yin and Y. Gao, *Appl. Catal., B*, 2008, **79**, 89–99.
9 S. L. Candelaria, Y. Shao, W. Zhou, X. Li, J. Xiao, J.-G. Zhang, Y. Wang, J. Liu, J. Li and G. Cao, *Nano Energy*, 2012, **1**, 195–220.
10 Y. Deng, Y. Xie, K. Zou and X. Ji, *J. Mater. Chem. A*, 2016, **4**, 1144–1173.
11 S. Latil, S. Roche, D. Mayou and J.-C. Charlier, *Phys. Rev. Lett.*, 2004, **92**, 256805.
12 J. D. Wiggins-Camacho and K. J. Stevenson, *J. Phys. Chem. C*, 2009, **113**, 19082–19090.
13 Y. Zhou, T. Holme, J. Berry, T. R. Ohno, D. Ginley and R. O'Hayre, *J. Phys. Chem. C*, 2010, **114**, 506–515.
14 J. A. Behan, S. N. Stamatin, M. K. Hoque, G. Ciapetti, F. Zen, L. Esteban-Tejeda and P. E. Colavita, *J. Phys. Chem. C*, 2017, **121**, 6596–6604.
15 R. J. Cullen, D. R. Jayasundara, L. Soldi, J. J. Cheng, G. Dufaure and P. E. Colavita, *Chem. Mater.*, 2012, **24**, 1031–1040.
16 F. Zen, V. D. Karanikolas, J. A. Behan, J. Andersson, G. Ciapetti, A. L. Bradley and P. E. Colavita, *Langmuir*, 2017, **33**, 4198–4206.
17 F. Zen, M. D. Angione, J. A. Behan, R. J. Cullen, T. Duff, J. M. Vasconcelos, E. M. Scanlan and P. E. Colavita, *Sci. Rep.*, 2016, **6**, 24840.
18 P. E. Colavita, B. Sun, K.-Y. Tse and R. J. Hamers, *J. Am. Chem. Soc.*, 2007, **129**, 13554–13565.
19 J. Kerr and D. Lide, *CRC Handbook of Chemistry and Physics*, 2000.
20 P. Kissinger and W. R. Heineman, *Laboratory Techniques in Electroanalytical Chemistry*, Taylor & Francis, 2nd edn, revised and expanded, 1996.
21 R. De Levie, *J. Electroanal. Chem.*, 1965, **9**, 117–127.
22 P. K. Chu and L. Li, *Mater. Chem. Phys.*, 2006, **96**, 253–277.
23 A. C. Ferrari and J. Robertson, *Philos. Trans. R. Soc. London, A*, 2004, **362**, 2477–2512.
24 A. C. Ferrari, S. E. Rodil and J. Robertson, *Diamond Relat. Mater.*, 2003, **12**, 905–910.
25 A. C. Ferrari and J. Robertson, *Phys. Rev. B*, 2000, **61**, 14095–14107.
26 A. C. Ferrari, S. E. Rodil and J. Robertson, *Phys. Rev. B*, 2003, **67**, 155306.
27 K. W. R. Gilkes, S. Prawer, K. W. Nugent, J. Robertson, H. S. Sands, Y. Lifshitz and X. Shi, *J. Appl. Phys.*, 2000, **87**, 7283–7289.
28 M. I. Nathan, J. E. S. Jr and K. N. Tu, *J. Appl. Phys.*, 1974, **45**, 2370.
29 J. Robertson, *Surf. Coat. Technol.*, 1992, **50**, 185–203.
30 F. C. Tai, S. C. Lee, J. Chen, C. Wei and S. H. Chang, *J. Raman Spectrosc.*, 2009, **40**, 1055–1059.
31 M. A. Tamor and W. C. Vassell, *J. Appl. Phys.*, 1994, **76**, 3823–3830.
32 M. Yoshikawa, G. Katagiri, H. Ishida, A. Ishitani and T. Akamatsu, *J. Appl. Phys.*, 1988, **64**, 6464–6468.
33 D. M. Murphy, R. J. Cullen, D. R. Jayasundara, R. L. Doyle, M. E. G. Lyons and P. E. Colavita, *J. Phys. Chem. C*, 2013, **117**, 22768–22777.

34 E. C. M. Chen and E. S. D. Chen, in *The Electron Capture Detector and the Study of Reactions with Thermal Electrons*, John Wiley & Sons, Inc., 2004, pp. 47–74.

35 H. J. Lipkin, *Phys. Rev.*, 1949, **76**, 567.

36 P. E. Colavita, B. Sun, X. Wang and R. J. Hamers, *J. Phys. Chem. C*, 2009, **113**, 1526–1535.

37 M. Kaukonen, R. M. Nieminen, S. Pöykkö and A. P. Seitsonen, *Phys. Rev. Lett.*, 1999, **83**, 5346–5349.

38 N. Yang, D. Yang, L. Chen, D. Liu, M. Cai and X. Fan, *Nanoscale Res. Lett.*, 2017, **12**, 642.

39 J. Xu, J. Mei, X. H. Huang, X. Li, Z. Li, W. Li and K. Chen, *Appl. Phys. A*, 2005, **80**, 123–126.

40 H. Ago, T. Kugler, F. Cacialli, W. R. Salaneck, M. S. P. Shaffer, A. H. Windle and R. H. Friend, *J. Phys. Chem. B*, 1999, **103**, 8116–8121.

41 K. M. Metz, P. E. Colavita, K.-Y. Tse and R. J. Hamers, *J. Power Sources*, 2012, **198**, 393–401.

42 T. Pajkossy, *J. Electroanal. Chem.*, 1994, **364**, 111–125.

43 Z. Kerner and T. Pajkossy, *Electrochim. Acta*, 2000, **46**, 207–211.

44 D. T. Fagan, I. F. Hu and T. Kuwana, *Anal. Chem.*, 1985, **57**, 2759–2763.

45 S. Ranganathan, T.-C. Kuo and R. L. McCreery, *Anal. Chem.*, 1999, **71**, 3574–3580.

46 J.-P. Randin and E. Yeager, *J. Electroanal. Chem. Interfacial Electrochem.*, 1975, **58**, 313–322.

47 S. Fletcher, V. J. Black and I. Kirkpatrick, *J. Solid State Electrochem.*, 2014, **18**, 1377–1387.

48 H. D. Yoo, J. H. Jang, J. H. Ryu, Y. Park and S. M. Oh, *J. Power Sources*, 2014, **267**, 411–420.

49 F. Lufrano and P. Staiti, *Electrochem. Solid-State Lett.*, 2004, **7**, A447–A450.

50 H. M. Jeong, J. W. Lee, W. H. Shin, Y. J. Choi, H. J. Shin, J. K. Kang and J. W. Choi, *Nano Lett.*, 2011, **11**, 2472–2477.

51 J.-I. Kim and S.-J. Park, *J. Solid State Chem.*, 2011, **184**, 2184–2189.

52 F. Béguin, K. Szostak, G. Lota and E. Frackowiak, *Adv. Mater. (Weinheim, Ger.)*, 2005, **17**, 2380–2384.

53 D.-W. Wang, F. Li, L.-C. Yin, X. Lu, Z.-G. Chen, I. R. Gentle, G. Q. Lu and H.-M. Cheng, *Chem. – Eur. J.*, 2012, **18**, 5345–5351.

54 H. Gerischer, R. McIntyre, D. Scherson and W. Storck, *J. Phys. Chem.*, 1987, **91**, 1930–1935.

55 M. Hahn, M. Baertschi, O. Barbieri, J.-C. Sauter, R. Kötz and R. Gallay, *Electrochem. Solid-State Lett.*, 2004, **7**, A33–A36.

56 N. A. Hastas, C. A. Dimitriadis, Y. Panayiotatos, D. H. Tassis, P. Patsalas and S. Logothetidis, *J. Appl. Phys.*, 2000, **88**, 5482–5484.

57 S. Trasatti and R. Parsons, in *Pure Appl. Chem.*, 1986, vol. 58, p. 437.

58 L. L. Zhang, X. Zhao, H. Ji, M. D. Stoller, L. Lai, S. Murali, S. McDonnell, B. Cleveger, R. M. Wallace and R. S. Ruoff, *Energy Environ. Sci.*, 2012, **5**, 9618–9625.

59 J. Zhu, A. S. Childress, M. Karakaya, S. Dandeliya, A. Srivastava, Y. Lin, A. M. Rao and R. Podila, *Adv. Mater. (Weinheim, Ger.)*, 2016, **28**, 7185–7192.

60 A. Zeng, M. M. M. Bilek, D. R. McKenzie and P. A. Lay, *Diamond Relat. Mater.*, 2009, **18**, 1211–1217.

61 A. Zeng, V. F. Neto, J. J. Gracio and Q. H. Fan, *Diamond Relat. Mater.*, 2014, **43**, 12–22.

62 D. Hulicova-Jurcakova, M. Kodama, S. Shiraishi, H. Hatori, Z. H. Zhu and G. Q. Lu, *Adv. Funct. Mater.*, 2009, **19**, 1800–1809.